

# Perovskite Interlayers For Mass Manufacture Using Roll-To-Roll Compatible Deposition Methods

**David James Richards**

Supervisor: **Professor Trystan M. Watson**



Swansea University  
Prifysgol Abertawe

Submitted to Swansea University in fulfilment of the requirements for  
the Degree of Doctor of Engineering  
Department of Materials Engineering  
Swansea University

2021



Engineering and  
Physical Sciences  
Research Council



*"The living world is essentially solar powered. The earth's plants capture 3 trillion kW h of solar energy each day, that's almost 20 times the energy we need, from sunlight. Imagine, if we phased out fossil fuels and run our world on the eternal energies of nature too."*

*-David Attenborough*

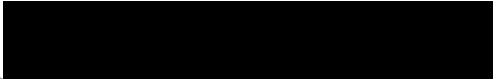
*Natural historian*

# Abstract

Organic-inorganic perovskites have been used as the light absorbing layer in solar cells since 2009 and have since seen a ground breaking rise in efficiency in a relatively short period of time. Today, perovskite based solar cells have reached efficiencies of over 24% making them a potential competitor to conventional solar cells such as silicon. However, unlike silicon, perovskites can essentially be "printed" as the layers can all be solution processed and prepared at low temperatures, giving them a huge advantage in terms of cost and process-ability. Nonetheless, before perovskites are commercially viable, significant work must be undertaken to ensure they are ready for mass manufacture. This work was aimed at developing large scale compatible (roll-to-roll), flexible perovskite solar cells utilising an Indium doped Tin Oxide (ITO) coated PET substrate. Due to the nature of the substrate, the processing temperatures of each layer had to be low and ideally less than 150 °C. Significant work has been undertaken to make perovskite layers roll-to-roll compatible, but the interlayers which it is sandwiched between require further investigation. Therefore, the following work presents the development and application of a roll-to-roll compatible electron transport layer (ETL) and hole transport layer (HTL). For the deposition of each layer in a roll-to-roll setting, slot-die coating was employed due to its compatibility with solution deposition and small material wastage. In addition, care was taken to focus on low-toxicity alternatives removing barriers that would otherwise be in place for toxic substances which would hinder large scale manufacturing from a health and safety point of view.

# Declaration

This work has not previously been accepted in substance for any degree and is not being concurrently submitted in candidature for any degree.

Signed: 

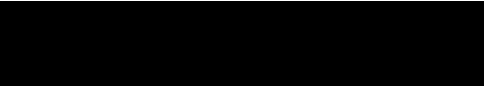
Date:.....09/12/2022.....

This thesis is the result of my own investigations, except where otherwise stated. Other sources are acknowledged by footnotes giving explicit references. A bibliography is appended.

Signed: 

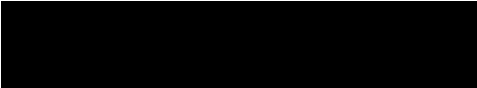
Date:.....09/12/2022.....

I hereby give consent for my thesis, if accepted, to be available for photocopying and for inter- library loan, and for the title and summary to be made available to outside organisations.

Signed: 

Date:.....09/12/2022.....

The University's ethical procedures have been followed and, where appropriate, that ethical approval has been granted.

Signed: 

Date:.....09/12/2022.....

# Contents

<b>Abstract</b>	<b>iii</b>
<b>Acknowledgments</b>	<b>viii</b>
<b>List of Figures</b>	<b>ix</b>
<b>List of Tables</b>	<b>xvii</b>
<b>Abbreviations</b>	<b>xix</b>
<b>1 Introduction</b>	<b>1</b>
1.1 Why Perovskite . . . . .	2
1.2 Perovskite Solar Cells . . . . .	2
1.3 How a Perovskite Solar Cell Operates . . . . .	4
1.3.1 Band Structures . . . . .	4
1.3.2 Electron Generation Mechanisms in Perovskite Devices . . . . .	5
1.3.3 Recombination Reactions . . . . .	6
1.3.4 Equivalent Circuit . . . . .	7
1.4 Perovskite Device Architectures . . . . .	7
1.4.1 Semiconductors . . . . .	8
1.4.1.1 n-type . . . . .	9
1.4.1.2 p-type . . . . .	9
1.4.2 Metal oxide semiconductors . . . . .	10
1.4.3 n-i-p and p-i-n architectures . . . . .	11
1.4.4 Electron-transport Layers . . . . .	11
1.4.5 Perovskite Layers . . . . .	14
1.4.5.1 Single-Step Deposition . . . . .	14
1.4.5.2 Two-Step Deposition . . . . .	15
1.4.5.3 Anti-Solvent Method . . . . .	16
1.4.6 Hole-transport Layers . . . . .	17
1.4.7 Conductive Electrodes . . . . .	20
1.5 Scaling up of perovskite devices . . . . .	22
1.5.1 Slot-die Coating . . . . .	22
1.5.1.1 Slot-Die Coating Modelling . . . . .	24
1.5.2 Scale up of N-I-P architectures . . . . .	27

1.5.3	Scale up of P-I-N structures . . . . .	29
1.6	Perovskite Solar Cell Characterisation . . . . .	32
1.6.1	Current-Voltage Measurements . . . . .	32
1.6.2	The Ideality Factor . . . . .	34
1.6.3	Hysteresis . . . . .	37
1.7	Conclusion . . . . .	38
1.8	References . . . . .	39
<b>2</b>	<b>Experimental methods</b>	<b>55</b>
2.1	Spin Coating . . . . .	55
2.1.1	Glass cleaning . . . . .	56
2.1.2	Plasma cleaning . . . . .	57
2.1.3	Perovskite Deposition . . . . .	57
2.1.4	Hole-transport Layers . . . . .	57
2.1.5	Electron-transport Layers . . . . .	58
2.1.6	Glass based device layout . . . . .	58
2.1.7	Manufacturing of flexible devices . . . . .	59
2.2	Slot-Die Meniscus Coating . . . . .	60
2.2.1	Slot-Die Coating and Visco-Capillary Model Calculations . . . . .	62
2.3	Thermal Evaporation . . . . .	62
2.4	Rheological Measurements . . . . .	63
2.4.1	Viscosity Measurements . . . . .	63
2.4.2	Surface Tension Measurements . . . . .	63
2.4.3	Contact Angle Measurements . . . . .	63
2.5	Optical Measurements . . . . .	64
2.5.1	Ultraviolet-Visible-Near Infrared Spectroscopy (UV-Vis-NIR) . . . . .	64
2.5.2	Fourier Transform Infrared Spectroscopy (FTIR) . . . . .	64
2.5.3	Optical Imaging . . . . .	65
2.6	Other Characterisation Methods . . . . .	65
2.6.1	Scanning Electron Microscopy (SEM) . . . . .	65
2.6.2	Transmission Electron Microscopy . . . . .	65
2.6.3	Cyclic Voltammetry . . . . .	65
2.6.4	ThermoGravimetric Analysis (TGA) and Differential Scanning Calorimetry (DSC) . . . . .	67
2.6.5	Atomic Force Microscopy . . . . .	68
2.6.6	X-ray Photoelectron Spectroscopy . . . . .	68
2.7	Device Characterisation . . . . .	69
2.7.1	Current-Voltage Measurements . . . . .	69
2.7.2	External Quantum Efficiency Measurements (EQE) . . . . .	69
2.8	Alternative Processing Methods . . . . .	69
2.8.1	Near Infra-Red Annealing (NIR) . . . . .	69
2.8.2	UltraViolet-Ozone (UVO) . . . . .	70
2.8.3	Photonic Curing . . . . .	70

2.9	References . . . . .	71
<b>3</b>	<b>Tin Oxide Electron Transport Layer, Optimisation, Coating and Device Characterisation</b>	<b>72</b>
3.1	Introduction . . . . .	72
3.2	Experimental Methods . . . . .	74
3.3	Results and Discussion . . . . .	74
3.3.1	Low-temperature spin coated tin oxide optimisation . . . . .	74
3.3.2	Slot-die coating of tin oxide . . . . .	91
3.4	Conclusions . . . . .	117
3.5	References . . . . .	117
<b>4</b>	<b>Roll-to-Roll Coating Of Tin Oxide</b>	<b>120</b>
4.1	Introduction . . . . .	120
4.2	Experimental Methods . . . . .	121
4.3	Results and Discussion . . . . .	124
4.3.1	Corona treatment . . . . .	125
4.3.2	Film optimisation . . . . .	132
4.4	Conclusions . . . . .	135
<b>5</b>	<b>Nickel Oxide Hole Transport Layer, Optimisation, Coating and Device Characterisation</b>	<b>136</b>
5.1	Introduction . . . . .	136
5.2	Experimental Methods . . . . .	137
5.3	Results and Discussion . . . . .	138
5.3.1	Sol-Gel Based Nickel Oxide . . . . .	138
5.3.2	Photonic Curing of NiAc . . . . .	141
5.3.3	Nickel Oxide Nanoparticles . . . . .	148
5.3.4	Stability of NiOx nanoparticles . . . . .	166
5.3.5	Slot-die coating of NiOx nanoparticles . . . . .	168
5.4	Conclusions . . . . .	171
5.5	References . . . . .	172
<b>6</b>	<b>Low-temperature processing options for NiOx HTL</b>	<b>175</b>
6.1	Introduction . . . . .	175
6.2	Experimental Methods . . . . .	175
6.3	Results and Discussion . . . . .	176
6.3.1	Near-infrared annealing of NiOx nanoparticles . . . . .	176
6.3.2	UltraViolet-Ozone treatment of NiOx nanoparticles . . . . .	185
6.3.3	Photonic curing of NiOx nanoparticles . . . . .	192
6.4	Conclusions . . . . .	195
6.5	References . . . . .	197
<b>7</b>	<b>Conclusions and Future Work</b>	<b>198</b>

# Acknowledgments

I would firstly like to thank Swansea University, all of the team in the Materials and Manufacturing Academy (M2A), the European Social Fund and TATA steel for the generous financial support over the course of my research.

Secondly I would like to express my sincere gratitude to my academic supervisors, Professor Trystan Watson and Dr Eifion Jewell for their guidance and enthusiasm throughout my project. Further gratitude goes to my industrial supervisors, Dr Ricardo Bouwer and Dr Berend Bolend for their help during the project and monthly meetings to keep me on track.

I would also like to thank and acknowledge certain colleagues for their help in providing measurements for me. Dr James McGettrick for his XPS analysis, Dr Vasil Stoichkov for providing AFM measurements, Dr Matt Burton for TEM images and finally Dr Daniel Burkitt for helping me obtain SEM images.

Finally, an enormous thank you to all of the team at SPECIFIC PV for making me feel welcomed from the first day and providing a fun work environment. Special thanks go to Daniel Burkitt, David Beynon, Vasil Stoichkov, Katherine Hooper, Ben Smith, James McGettrick and Peter Greenwood for giving me their time knowledge and patience throughout my research.



# List of Figures

1.1	A schematic diagram of a material employing the $ABX_3$ perovskite structure. . . . .	2
1.2	Electronic band structures in solid materials. . . . .	5
1.3	Schematic diagram of electron and hole generation in a direct bandgap semiconductor as well as an indirect bandgap semiconductor. . . . .	6
1.4	equivalent circuit of a photovoltaic cell. . . . .	8
1.5	Schematic representation of a typical perovskite solar cell architecture. . . . .	8
1.6	Schematic representation n-type silicon doping and its representative band diagram. . . . .	9
1.7	Schematic representation p-type silicon doping and its representative band diagram. . . . .	10
1.8	Schematic illustration of single-step and two-step perovskite depositions. . . . .	16
1.9	Schematic illustration of the anti-solvent method. . . . .	17
1.10	(a) Schematic representation of a metal mounted perovskite solar cell and associated target layer thickness. (b) A photograph of a flexible perovskite solar cell on titanium foil [99] . . . . .	21
1.11	Schematic diagram of a typical slot-die coating head. . . . .	23
1.12	Slot-die coating head schematic where $W$ is the width of the feed slot, $H_0$ is the head-substrate gap, $t_{min}$ is the minimum wet film thickness and $R$ is radius of the curvature of the downstream meniscus. . . . .	25
1.13	Example viscocapillary model showing the stable region (Green) and the unstable region (Red). . . . .	26
1.14	Photograph of the R2R coating setup used in Galagan et al’s work [119] . . . . .	28
1.15	Photograph of the R2R coating of a two-step perovskite film used in work by Burkitt et al [128] . . . . .	30
1.16	Schematic of the R2R coating set up used in Burkitt et al’s slot-die coated p-i-n device architecture [129] . . . . .	31
1.17	Schematic of a simple solar J-V testing rig. The current and voltage are measured separately to overcome contact resistance issues. . . . .	33
1.18	Spectral characteristics of AM1.5G. . . . .	33
1.19	A typical J-V curve for a perovskite solar cell. . . . .	34
1.20	Ideal Current-Voltage diode curve. . . . .	35
1.21	Example J-V curve of a solar cell with no illumination (black) and under illumination (Red). . . . .	36

1.22	Example current-density plots demonstrating the effect that series and shunt resistances have on the curve. . . . .	36
1.23	J-V curve of a perovskite solar cell exhibiting hysteresis. . . . .	37
1.24	Example of a stabilised current measurement for a perovskite solar cell [134] . . . . .	39
2.1	Diagram of spin coating procedure . . . . .	55
2.2	Schematic of the ITO coated glass substrates used in this work as well as a schematic of an individual perovskite solar cell showing the working electrode and 8 counter-electrode "pixels". . . . .	59
2.3	Schematic illustration of the pre-patterned PET/ITO provided by Meko print and the method used to cut into smaller samples. . . . .	59
2.4	Schematic diagram of the bench-top FOM slot-die coater used in this work with the key parts labelled. . . . .	60
2.5	Schematic diagram of the slot-die head used in this work with the key components labelled. . . . .	61
2.6	Schematic diagram showing how the slot-die head is assembled. . . . .	61
2.7	Example of an image taken for surface tension calculation. . . . .	63
2.8	Schematic representation of the contact angle formed between a liquid and a substrate. . . . .	64
2.9	Schematic diagram of the CV setup used in this work. . . . .	66
2.10	A typical cyclic voltammogram produced from an ITO coated glass working electrode with a potassium ferri/ferrocyanide redox couple and Calomel reference electrode. $I_p^a$ is the peak anodic current, $I_p^c$ is the peak cathodic current and $\Delta E$ is the peak-to-peak separation. Also included are the respective single electron reduction and oxidation reactions. . . . .	68
2.11	Heraeus NIR system . . . . .	70
3.1	Tin oxide perovskite device structure . . . . .	75
3.2	Statistical analysis of J-V data from perovskite solar cells prepared from spin coating of Avantama tin oxide nanoparticle ETLs at different spin speeds (Reverse scans). Data presented from 15 devices. . . . .	76
3.3	J-V curves showing the forward (dashed lines) and reverse (solid lines) scans for best performing devices prepared from spin coating of the Avantama tin oxide nanoparticles. . . . .	77
3.4	Cyclic voltammograms of spin coated Avantama tin oxide nanoparticles vs. bare ITO substrate vs. tin chloride-based control film. . . . .	78
3.5	Statistical analysis of J-V data from spin coated perovskite solar cells prepared using spin coated Avantama tin oxide nanoparticle ETLs at different spin speeds, including double layers at each spin speed (Reverse scans). Data presented from 21 devices. . . . .	79
3.6	SEM image of a spin coated double layer of Avantama tin oxide nanoparticles showing a large amount of pinholes . . . . .	81

3.7	Cyclic voltammograms of spin coated Avantama tin oxide nanoparticles after sonication. . . . .	82
3.8	Cyclic voltammograms of spray coated Avantama tin oxide films. . . . .	83
3.9	Cyclic voltammograms for spin coated Alfa Aesar tin oxide nanoparticles at different weight% suspensions. . . . .	85
3.10	Statistical analysis of J-V data from spin coated perovskite solar cells employing increasing weight percentages of Alfa Aesar tin oxide nanoparticles as the ETL (Reverse scans). Data presented from 18 devices. . . . .	86
3.11	Statistical analysis of J-V data from the second optimisation of spin coated perovskite solar cells employing increasing weight percentages of Alfa Aesar tin oxide nanoparticles as the ETL (Reverse scans). Data presented from 24 devices. . . . .	87
3.12	SEM images for the perovskite layers formed on different SnO <sub>2</sub> layers. SnO <sub>2</sub> colloid solutions of different concentrations: (a) 10 wt.%, (b) 6.67 wt.%, (c) 5 wt.%, (d) 4 wt.%, and (e) 3.33 wt.%.[8] . . . . .	87
3.13	Hero device J-V curves for perovskite solar cells employing a tin chloride based tin oxide ETL and a 50nm thick tin oxide nanoparticle ETL (Alfa Aesar). Corresponding device performances are shown in Table 3.5 . . . . .	88
3.14	SEM micrographs comparing Alfa Aesar and Avantama SnO <sub>2</sub> nanoparticle films on top of ITO coated glass. Scratches were made on the films to differentiate the ITO from the SnO <sub>2</sub> . . . . .	89
3.15	Forward and reverse scans for SnO <sub>2</sub> nanoparticle ETL showing hysteresis. . . . .	91
3.16	Photograph of dry slot-die coated tin oxide nanoparticle film on plasma cleaned soda glass. . . . .	92
3.17	Photographs of tin oxide nanoparticles diluted to 1.2wt% using IPA, and ethanol. . . . .	93
3.18	Photographs showing the change in PH of the nanoparticle suspension before and after dilution with IPA. . . . .	94
3.19	Photographs of tin oxide nanoparticles diluted to 1.2 wt% using increasing volume percentages of IPA and ethanol. . . . .	94
3.20	Contact angles of both tin oxide nanoparticle solvent system as a function of increasing volume% additions of IPA and ethanol. Inset is an image taken during the measurement of a 5 volume% IPA solution . . . . .	95
3.21	TGA of a 1.2 weight% tin oxide nanoparticle solvent system with a 10 volume% addition of IPA. . . . .	96
3.22	Visco-capillary model of Alfa Aesar tin oxide nanoparticle IPA and ethanol solvent systems. . . . .	97
3.23	Visco-capillary verification. Inserted images are dried films taken with a flat-bed scanner. . . . .	99
3.24	Cyclic voltammograms comparing slot-die coated IPA and ethanol tin oxide nanoparticle solvent systems on glass and PET substrates. . . . .	100
3.25	Scanned images of the slot-die coated tin oxide films deposited from IPA and Ethanol solvents. . . . .	101

3.26	Statistical analysis of J-V data from slot-die coating of two different tin oxide nanoparticle solvent systems coated onto ITO coated glass, and PET substrates. Data presented from 20 devices. . . . .	102
3.27	Hero device J-V curves for perovskite solar cells using slot-die coated tin oxide nanoparticle ETLs in IPA and ethanol solvent systems. Corresponding device performances are shown in Table 3.8 . . . . .	103
3.28	Flat-bed scanner image of a slot-die coated tin oxide nanoparticle layer from an IPA based solvent system. . . . .	104
3.29	Flat-bed scanner images of a slot-die coated tin oxide nanoparticle layer from an IPA based solvent system, dried via: a) a hot plate at 140 °C, and b) in coater ovens with fans off at 140 °C. . . . .	104
3.30	TGA graph showing weight loss as a percentage of a tin oxide nanoparticle solvent system with a 40 volume % addition of IPA. . . . .	105
3.31	Images of each tin oxide solvent system with increasing volume percentage addition of solvent labelled for each vial. Also included are the same solvent systems after 24 hours storage. Images on the bottom row of each solvent system are after 24 hours . . . . .	106
3.32	Surface tension measurements for each of the volume% additions of IPA, ethanol, 1-propanol and 1-butanol to the water based tin oxide nanoparticles. Measurements were made at 25 °C. . . . .	107
3.33	Visco-capillary models for all four solvent systems of tin oxide nanoparticle suspensions. . . . .	108
3.34	Images of ethanol and 1-butanol tin oxide nanoparticle solvent system slot-die coated onto either: non-treated ITO coated PET, or plasma treated ITO coated PET substrates. . . . .	109
3.35	Images of IPA and 1-propanol tin oxide nanoparticle solvent system slot-die coated onto either: non-treated ITO coated PET, or plasma treated ITO coated PET substrates. . . . .	109
3.36	Cyclic voltammograms of each tin oxide nanoparticle solvent system slot-die coated onto either: non-treated ITO coated PET, or plasma treated ITO coated PET substrates. . . . .	110
3.37	TGA graphs for each tin oxide nanoparticle solvent system with the weight % derivative plotted. . . . .	111
3.38	Statistical analysis of J-V data from slot-die coating of four tin oxide nanoparticle solvent systems coated onto ITO coated PET substrates with and without plasma treatment prior to deposition. Plasma treated films are denoted via the lined boxes. (Reverse scans). Data presented from 36 devices. . . . .	113
3.39	Statistical analysis of J-V data from the thickness optimisation of a slot-die coated tin oxide ETL using a 10 volume% 1-butanol solvent system (Reverse scans). Data presented from 24 devices. . . . .	115

3.40	Hero device J-V curves for hero perovskite solar cells comparing slot-die coated and spin-coated tin oxide ETLs. Corresponding device performances are shown in Table 3.12. . . . .	116
3.41	Stabilised power conversion efficiencies of hero spin-coated and slot-die coated SnO <sub>2</sub> films. . . . .	116
4.1	Images of the Coatema smart coater used for roll-to-roll coating trials in this chapter . . . . .	121
4.2	Schematic diagram of the layout of the Coatema smart coater . . . . .	122
4.3	Image of the slot die head during coating of the tin oxide ETL in the smart coater.	123
4.4	Visco capillary models for roll-to-roll coating of SnO <sub>2</sub> at 1 m/min . . . . .	125
4.5	Temperature measured within the smart coater ovens compared to the set-point.	126
4.6	Diagram of the corona treatment unit used in this experiment and an image of the unit itself. . . . .	126
4.7	Cyclic voltammetry on bare PET/ITO substrates before and after running through the smartcoater . . . . .	127
4.8	SEM images of PET/ITO substrate before (a) and after running through the smart coater (b&c). Images taken by Rahul Patidar. . . . .	128
4.9	Contact angle measurements of tin oxide slot-die coating ink on PET/ITO substrates after different corona treatments . . . . .	129
4.10	Images of roll-to-roll, slot-die coated tin oxide films with dye added to the ink. Films were subjected to various levels of corona treatment, with powers ranging from 0 - 1.0 kW . . . . .	130
4.11	Cyclic voltammetry of a) a 7 $\mu$ m wet film of SnO <sub>2</sub> with no corona treatment compared to bare ITO and b) a comparison of increasing corona treatment power.	131
4.12	Snapshots from videos taken of dropping SnO <sub>2</sub> ink formulations onto non-treated and corona-treated PET/ITO substrates . . . . .	131
4.13	Statistical analysis of J-V data from slot-die coating of a tin oxide nanoparticle solution in a roll-to-roll setting. Data presented from 20 devices. . . . .	132
4.14	Hero device J-V data comparing a roll-to-roll slot die coated tin oxide ETL on a PET substrate compared to a spin coated control device on glass. . . . .	133
4.15	Stabilised efficiency measurements for spin-coated SnO <sub>2</sub> and roll-to-roll slot-die coated SnO <sub>2</sub> . . . . .	134
4.16	External Quantum efficiency measurements comparing the slot-die and spin-coated films. Also included is the integrated Jsc . . . . .	134
5.1	Schematic diagram of the energy level alignments of perovskite absorbers and various common HTLs, ETLs, and electrodes [13] . . . . .	137
5.2	Nickel oxide based perovskite device structure. . . . .	138
5.3	Images of full perovskite device stacks built on top of annealed NiAc films at: a) 300 °C for 30 minutes, b) 150 °C for 30 minutes, and c) 150 °C for 10 minutes.	139
5.4	Typical JV curves comparing the device performances of NiAc films annealed at 300 °C (30 mins) and 150 °C (30 mins and 10 mins). (Reverse scans) . . . .	139

5.5	FTIR spectra showing the difference between a NiAc film annealed at 300 °C for 30 minutes and at 150 °C for 30 minutes. Also included is the FTIR spectra for a neat NiAc solution . . . . .	140
5.6	TGA analysis of neat NiAc solution with a ramp rate of 10 °C/minute up to 300 °C and held for 50 minutes. . . . .	141
5.7	DSC analysis of neat NiAc solution with a ramp rate of 10 °C/minute up to 300 °C and held for 50 minutes. . . . .	142
5.8	Intensity spectra for Novacentrix Pulseforge 1300 photonic lamps using a 200 $\mu$ s pulse at three lamp voltages. @Novacentrix 2021. . . . .	142
5.9	Comparison of the PulseForge white light intensity to the absorbance spectra of NiAc on glass/ITO substrate. . . . .	143
5.10	Schematic illustration of the photonic system used in this work. . . . .	143
5.11	Statistical analysis of J-V data for the best performing photonicallly cured NiOx devices from each power setting. Data presented from 24 devices. . . . .	145
5.12	XPS data showing a) Nitrogen peaks, and b) Oxygen peaks. Data collated by Dr James McGettrick . . . . .	146
5.13	Images of perovskite films deposited on top of photonicallly cured NiAc at different power and pulses. Included diagram is the ITO pattern on the glass used for illustration of damaged areas . . . . .	148
5.14	statistical JV analysis of the spin speed optimisation of NiOx nanoparticles. Data presented from 16 devices. . . . .	149
5.15	Hero JV curves for the nanoparticle-based perovskite solar cell compared to HT-NiOx. . . . .	150
5.16	Average roughness measurements comparing HT-NiOx and NiOx nanoparticles, as well as a perovskite layer on top of each. (Each measurement was made five times over separate areas). . . . .	151
5.17	AFM images of a) NiAc based NiOx layer and b) NiOx nanoparticles. . . . .	152
5.18	SEM images of a perovskite layer on top of a) HT-NiOx, and b) a NiOx nanoparticle layer. . . . .	153
5.19	Schematic diagram of m-i-m device structure for measuring conductivity. . . . .	154
5.20	J-V Curves for conductivity measurements on HT-NiOx, compared to nanoparticles. . . . .	154
5.21	J-V Curves for conductivity measurements on HT-NiOx, compared to nanoparticles annealed at 150 and 250 °C for 30 minutes. . . . .	155
5.22	Statistical J-V analysis for NiOx nanoparticles annealed at 150 °C and 250 °C for 30 minutes compared to a HT-NiOx device. Data presented from 12 devices. . . . .	156
5.23	TGA of Avantama NiOx nanoparticle suspension held at 150 °C and 250 °C, with the insert showing the weight losses with a reduced x-axis. . . . .	158
5.24	DSC curves of Avantama NiOx nanoparticle suspension held at 150 °C and 250 °C. . . . .	158
5.25	AFM images of Avantama NiOx nanoparticle films annealed at a) 150 °C and b) 250 °C . Images taken by Dr Vasil Stoichkov. . . . .	159

5.26	SEM images of Avantama NiOx nanoparticle films annealed at a) 150 °C and b) 250 °C. Images taken by Rahul Patidar . . . . .	160
5.27	TEM images of Avantama NiOx nanoparticle films annealed at a) 150 °C and b) 250 °C. Image taken by Dr Matt Burton. . . . .	160
5.28	Average device parameters for perovskite solar cells built on top of NiOx nanoparticle films annealed at 150 and 250 °C at increasing times (averages of 12 pixels per annealing time). . . . .	161
5.29	Thermogravimetric analysis of NiOx nanoparticles pre-dried on a hot plate to remove solvent. . . . .	163
5.30	Thermogravimetric analysis of NiOx nanoparticles combined with PCE box plots at each corresponding annealing temperature. . . . .	164
5.31	PL spectroscopy comparing NiOx annealed at 150 and 250 °C. . . . .	165
5.32	XPS spectra for the Ni 2p <sub>3/2</sub> and O 1s orbitals comparing NiOx nanoparticle films annealed at 150 and 250 °C. . . . .	166
5.33	Images of perovskite devices employing a PEDOT HTL and a NiOx nanoparticle (annealed at 150 °C) HTL under constant illumination in a lightbox. . . .	166
5.34	Normalised efficiency stability measurements for a PEDOT (Blue) based perovskite device compared to perovskite devices employing NiOx nanoparticle HTLs annealed at 150 °C (Red) and 250 °C (Black). . . . .	168
5.35	Viscocapillary model for NiOx nanoparticles at 3 wet film thicknesses (5,7 and 9 micron) and with an overall head-substrate gap height set at 1200 micron. . .	169
5.36	Statistical JV data for slot-die coated NiOx nanoparticles with increasing wet film thickness and annealed at 250 °C, compared to a spin-coated control device. Data presented from 16 devices. . . . .	169
5.37	Statistical JV data for slot-die coated NiOx nanoparticles on PET/ITO with increasing wet film thickness and annealed at 150 °C, compared to a spin-coated control device. Data presented from 16 devices. . . . .	171
6.1	Schematic illustration of the difference in NIR and convection oven annealing. .	176
6.2	Intensity spectra for the Huraeus NIR emitters. Data from manufacturer . . . .	177
6.3	Absorbance spectra for ITO glass and ITO glass + NiOx. . . . .	178
6.4	Schematic illustration of the method used to calibrate the IR camera. . . . .	179
6.5	Schematic illustration of the method used to measure the temperature of the ITO film on exit . . . . .	179
6.6	Statistical J-V analysis of NIR annealed NiOx nanoparticle films on a metal plate, compared to hot plate annealed films at 150 and 250 °C. Data presented from 20 devices. . . . .	180
6.7	Statistical J-V analysis of NIR annealed NiOx nanoparticle films without a metal plate, compared to hot plate annealed films at 150 and 250 °C. Data presented from 20 devices. . . . .	182
6.8	J-V curves for highest performing perovskite solar cells employing hot plate annealed NiOx nanoparticles as well as an NIR annealed film. . . . .	183

6.9	IR measured temperatures of ITO substrates upon exiting the NIR oven at each residence exposure time. . . . .	184
6.10	Image of an ITO coated PET film exposed to 7 seconds of NIR radiation. . . . .	184
6.11	UV-Vis spectra for Avantama NiOx nanoparticle films with increasing UVO exposure times. . . . .	186
6.12	Summary of JV characteristics from perovskite solar cells built on top of Avantama NiOx nanoparticles subjected to increasing UVO exposure. Data presented from 28 devices. . . . .	187
6.13	XPS spectra for the Ni 2p <sub>3/2</sub> and O 1s orbitals comparing NiOx nanoparticle films annealed at 150 °C and exposed to 40 seconds and 5 minutes of UVO. . . . .	188
6.14	Image of UVO treated NiOx films with UVO treatment, as well as a heat treatment of 150 °C post UVO treatment. . . . .	189
6.15	UV-Vis transmittance at 500 nm for UVO treated NiOx films as well as post UVO heat treatment at 140 °C for 10 minute. . . . .	190
6.16	XPS spectra for the Ni 2p <sub>3/2</sub> and O 1s orbitals comparing NiOx nanoparticle films annealed at 150 °C and exposed to 40 seconds and 5 minutes of UVO. Also included are the same XPS spectra for the films placed on a hot plate at 150 °C for 10 minutes post UVO exposure . . . . .	191
6.17	Summary of JV characteristics from perovskite solar cells built on top of Avantama nanoparticles subjected to increasing UVO exposure with a 10 minute heat treatment at 150 °C post UVO. Data presented from 28 devices. . . . .	192
6.18	Intensity spectra for Novacentrix Pulseforge 1300 photonic lamp. . . . .	193
6.19	Absorbance spectra for ITO glass as well as ITO glass + NiOx up to 800 nm. . . . .	193
6.20	JV data for photonicallly cured NiOx nanoparticle films subjected to one pulse with increasing voltage, compared to films hot plate annealed at 150 and 250 °C. Data presented from 32 devices. . . . .	194
6.21	JV curves for best performing photonicallly cured NiOx film compared to hot-plate annelaed control devices at 150 and 250 °C. . . . .	196



# List of Tables

3.1	Table of cyclic voltammetry parameters calculated for Avantama tin oxide nanoparticles deposited via spin coating, compared to a control film deposited by thermal decomposition of tin chloride . . . . .	79
3.2	Table showing the JV characteristics from the hero device fabricated from spinning two layers of Avantama SnO <sub>2</sub> nanoparticles at 4000 rpm . . . . .	80
3.3	Table showing the approximate surface coverage calculated from CV data for each of the Avantama tin oxide nanoparticle films discussed in Chapter 4.1. . . . .	83
3.4	Averages of cell data for spin coated perovskite solar cells with increasing weight % suspensions of Alfa Aesar tin oxide nanoparticles as the ETL (Reverse scans). . . . .	88
3.5	Cell data for hero perovskite solar cells comparing tin chloride based tin oxide ETL to an Alfa Aesar based tin oxide nanoparticle layer (Reverse scans). . . . .	89
3.6	Rheological properties of tin oxide nanoparticle solvent systems using increasing volume % additions of ethanol and IPA. Viscosity and surface tensions measured at 25 °C. . . . .	95
3.7	Calculated estimate for surface coverage of slot-die coated tin oxide ETLs from IPA and ethanol solvent systems on glass and PET. . . . .	100
3.8	Cell data for hero perovskite solar cells made with slot-die coated tin oxide nanoparticle ETLs in IPA and ethanol solvent systems (Reverse scans). . . . .	102
3.9	Viscosity measurements for each of the volume% additions of IPA, ethanol, 1-propanol and 1-butanol to the water based tin oxide nanoparticles. Measurements were made at 25 °C . . . . .	106
3.10	Estimated surface coverage values for each tin oxide nanoparticle solvent system slot-die coated onto either: non-treated ITO coated PET, or plasma treated ITO coated PET substrates. . . . .	111
3.11	Averages of J-V data from slot-die coating of four tin oxide nanoparticle solvent systems coated onto ITO coated PET substrates with and without plasma treatment prior to deposition. . . . .	114
3.12	Hero device J-V characteristics comparing a slot-die coated tin oxide ETL to a spin-coated equivalent (Reverse scans). Corresponding J-V curves plotted in Figure 3.40 . . . . .	114

---

4.1	Hero device J-V characteristics comparing a roll-to-roll, slot-die coated tin oxide ETL to a spin-coated equivalent (Reverse scans). Corresponding J-V curves plotted in Figure 4.14 . . . . .	133
5.1	Parameters for photonic curing exposures on NiAc. . . . .	144
5.2	XPS compositional data of the best performing photonic NiAc films at each voltage compared to a hot-plate annealed NiAc film. (p) refers to the number of pulses . . . . .	147
5.3	Average values for series and shunt resistances of the nanoparticle and HT-NiOx based perovskite devices. . . . .	150
5.4	Roughness values measured by AFM on Avantama NiOx nanoparticle films annealed at 150 °C and 250 °C. . . . .	159
5.5	Hero device data for slot-die coated NiOx nanoparticles annealed at 250 °C compared to a spin coated equivalent. . . . .	170
6.1	J-V curves for highest performing perovskite solar cells employing hot plate annealed NiOx nanoparticles as well as an NIR annealed film. . . . .	182
6.2	Table comparing the amount of Ni(OH <sub>2</sub> ) as a % of total nickel, and carbon content of NiOx films annealed on a hot plate, and exposed to UVO . . . . .	188
6.3	Table comparing the amount of Ni(OH <sub>2</sub> ) as a % of total nickel, and carbon content of NiOx films annealed on a hot plate, treated with UVO as well as UVO treated films with a post heat treatment at 150 °C for 10 minutes . . . . .	190
6.4	Estimated peak temperature for NiOx films subjected to increasing photonic pulse power. . . . .	194

# Abbreviations

**AFM:** Atomic Force Microscopy  
**Al<sub>2</sub>O<sub>3</sub>:** Aluminium oxide  
**ALD:** Atomic Layer Deposition  
**AM:** Air Mass  
**ASTM:** American Society of the International Association for Testing and Materials  
**ATR:** Attenuated Total Reflectance  
**CBD:** Chemical Bath Deposition  
**CsI:** Cesium Iodide  
**CuSCN:** Copper Thiocyanate  
**CV:** Cyclic Voltammetry  
**CVD:** Chemical Vapor Deposition  
**DA:** Dopamine  
**DMF:** Dimethyl Formamide  
**DMSO:** Dimethyl Sulfoxide  
**DSC:** Differential Scanning Calorimetry  
**DSSC:** Dye-sensitized Solar Cell  
**EQE:** External Quantum Efficiency  
**ETL:** Electron-transport layer  
**FF:** Fill Factor  
**FTIR:** Fourier Transform Infrared Spectroscopy  
**FTO:** Fluorine-doped Tin Oxide  
**GBL:** gamma-butyrolactone  
**HTL:** Hole-transport layer  
**IPA:** Isopropyl Alcohol  
**ITO:** Indium-doped Tin Oxide  
**MAI:** Methyl Ammonium Iodide  
**MAPI:** Methyl Ammonium Lead Iodide  
**NiOx:** Nickel Oxide  
**NIR:** Near Infrared  
**P3HT:** Poly(3-hexythiophene)  
**PCBM:** phenyl-C61-butyric acid methyl ester  
**PCE:** Power Conversion Efficiency  
**PEDOT:PSS:** poly(3,4-ethene-dioxythiophene):poly(styrenesuulfonate)  
**PET:** Polyethylene terephthalate

**PSK:** Perovskite  
**PTAA:** poly[bis(4-phenyl)(2,4,6-trimethylphenyl)amine]  
**PV:** Photovoltaic  
**R2R:** Roll to Roll  
**SEM:** Scanning Electron Microscope  
**SnO<sub>2</sub>:** Tin Oxide  
**SRH:** Shockley-Read-Hall  
**STA:** Simultaneous Thermal Analysis  
**TCA:** Transparent Conductive Adhesive  
**TCO:** Transparent conductive Oxide  
**TEM:** Transmission Electron Microscopy  
**TGA:** ThermoGravimetric Analysis  
**TiO<sub>2</sub>:** Titanium Dioxide  
**UVO:** UV-Ozone  
**UV-Vis:** Ultraviolet-Visible  
**VBM:** Valence Band Minimum  
**V<sub>OC</sub>:** Open-circuit Voltage  
**XPS:** X-ray Photoelectron Spectroscopy  
**ZnO:** Zinc Oxide

# Chapter 1

## Introduction

With ever-increasing tension over the harmful effects continued use of fossil fuels has on our planet, the transition to renewable energy is becoming evermore important. Although a rise in renewable energy sources such as; solar, wind and hydro has been demonstrated over the last few years, the majority of our power still comes from burning fossil fuels. More and more studies are being released on the harmful effects using fossil fuels has on our environment. Many nations accept that global warming is the main result. Progress is being made in converting to renewable energy. However, it is paramount that we progress technologies such as solar energy harvesting.

It is estimated that 173,000 terawatts of solar energy strikes the earth continuously which is more than 10,000 times the amount of energy used worldwide [1]. This is clearly an infinite supply of energy which could be harnessed with photovoltaic (PV) technologies to convert it into electricity. In addition to this, solar energy is available practically anywhere geographically making it a readily available energy source waiting to be harnessed. The PV energy sector is rapidly growing with solar cells on commercial as well as domestic buildings becoming more commonplace. The most common PV devices used currently are silicon based, and although their cost has become significantly cheaper, the precursor materials need to be extremely pure, and as such require high energy input in their processing and mining. A possible alternative to this is the perovskite solar cell, a low cost, solution processable organometal halide.

## 1.1 Why Perovskite

Prior to the use of perovskite as the light absorbing material in a solar cell, similar technologies were already being researched, with the main influencers being dye-sensitised solar cells (DSSCs). In addition to DSSCs, other technologies such as organic polymer solar cells and thin film solar cells were also heavily researched.

## 1.2 Perovskite Solar Cells

Perovskite in nature is the name for any mineral with the same structure as an oxide called calcium titanate ( $\text{CaTiO}_3$ ). German scientist, Gustav Rose discovered calcium titanate in 1839 in the Ural Mountains. It was named in honor of Count Lev Aleksevich Von Perovski, a Russian states man and mineralogist [2]. Perovskites have a general formula of  $\text{ABX}_3$  (X = Oxygen, Carbon, Nitrogen or a Halogen). Where A and B are cations which coordinate with 12 and 6 X anions, forming a cuboctahedral and octahedral geometry [2]. This structure is shown in Figure 1.1.

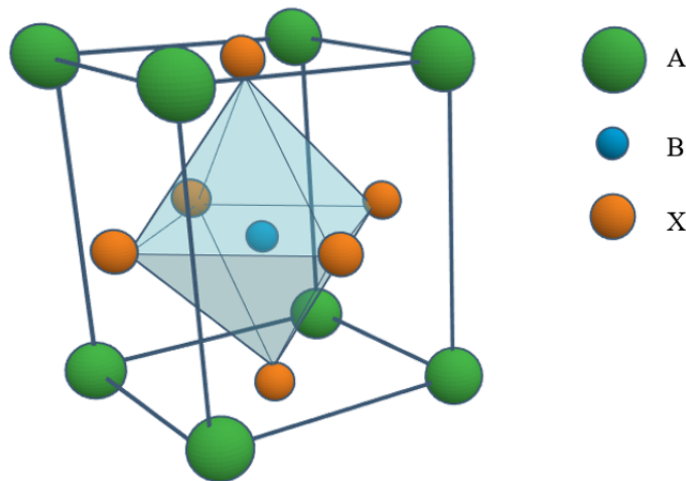


Figure 1.1: A schematic diagram of a material employing the  $\text{ABX}_3$  perovskite structure.

Since the 1970s, perovskites have attracted significant scientific research due to their structural versatilities and magnetic, optical and electric properties [3]. In the 1900s, researchers focussed on the perovskite semiconductor properties, high carrier mobilities for thin-film transistors and strong excitonic features for light emitting diodes. It wasn't until 2009 that perovskite really gained traction as a light harvesting layer in a photovoltaic device [3]. However, a paper published in 2007 by Kojima et al showed the potential of perovskite as the light

harvester in a DSSC-type device [4]. This group used  $\text{CH}_3\text{NH}_3\text{PbBr}_3$  and  $\text{CH}_3\text{NH}_3\text{PbI}_3$  perovskites as the visible light absorber on a  $\text{TiO}_2$  electrode and achieved efficiencies of 2.19 and 0.36 % respectively. It was noted that low photocurrent was due to the narrow absorption band of the  $\text{CH}_3\text{NH}_3\text{PbBr}_3$  (less than 570 nm) and the  $\text{CH}_3\text{NH}_3\text{PbI}_3$  was employed to increase the photocurrent as it has a wider absorption band, but higher efficiencies were not observed. 2 years later in 2009, a follow up paper was published by the same group achieving improved efficiencies of 3.13 and 3.81% [5].

By dissolving  $\text{CH}_3\text{NH}_3\text{Br}$  and  $\text{PbBr}_2$  in N,N-dimethylformamide, or dissolving  $\text{CH}_3\text{NH}_3\text{I}$  and  $\text{PbI}_2$  in  $\gamma$ -butyrolactone (GBL), perovskite precursors were formed and deposition achieved by spin coating onto a  $\text{TiO}_2$  film. Upon drying of the films, colour changes were observed with the  $\text{CH}_3\text{NH}_3\text{PbBr}_3$  changing from colourless to yellow and the  $\text{CH}_3\text{NH}_3\text{PbI}_3$  film changing from yellow to black indicating the formation of  $\text{CH}_3\text{NH}_3\text{PbX}_3$  in the solid state. The rest of each device was made using a typical DSSC architecture with the redox electrolyte composed of a lithium halogen and halide. Higher efficiencies were observed for the  $\text{CH}_3\text{NH}_3\text{PbI}_3$  based devices owing to their much-improved current densities of  $11 \text{ mA/cm}^2$  compared to  $5.57 \text{ mA/cm}^2$  for the  $\text{CH}_3\text{NH}_3\text{PbBr}_3$  devices.

Several other papers were published on the use of perovskites as the light harvesting material in DSSC type devices, with Nam-Gyu Park publishing efficiencies of 6.54% in 2011 by reducing the film thickness of the perovskite. This group did however come to realise that using liquid electrolytes led to severe stability issues with 80% efficiency loss in 10 minutes. This was due to the perovskite gradually dissolving into the electrolyte [6].

To overcome these stability issues solid-state devices were used with the electrolyte being replaced with an amorphous organic hole transporting layer of spiro-OMeTAD. Kim et al were first to publish this in August 2012 achieving efficiencies of 9.7% with high photocurrents exceeding  $17 \text{ mA/cm}^2$  [7]. This was achieved using a  $\text{CH}_3\text{NH}_3\text{PbI}_3$  perovskite deposited onto sub-micron thick anatase  $\text{TiO}_2$  which exhibited superior stability compared to liquid based devices. Shortly after, Lee et al published work using spiro-OMeTAD as the hole transport layer with a slightly higher efficiency of 10.9%. Interestingly, Lee et al moved away from the typical DSSC architecture and instead of using a  $\text{TiO}_2$  photoanode they used an electrically insulating porous “scaffold” of  $\text{Al}_2\text{O}_3$  nanoparticles [8]. It was discovered that rather than extracting charge by charge transfer through the  $\text{TiO}_2$  particles themselves, extraction by the perovskite material itself was much faster, with the insulating  $\text{Al}_2\text{O}_3$  scaffold serving as a

method for increasing the overall surface area of the perovskite film and not charge extraction [8].

Since the first few papers on perovskites, notable advances have been achieved by fine-tuning of all of the layers used in the device stack with the highest certified efficiency for a perovskite device now being 25.2% [9]. This huge rise in efficiency in such a short space of time outperforms any other PV technology and the efficiencies are set to overtake that of silicon in the near future. Perovskites are certainly nearing commercialisation, especially perovskite tandem devices and have a strong potential for future use in a variety of applications due to their cheap processing costs and flexible substrate compatibility.

## **1.3 How a Perovskite Solar Cell Operates**

Solar cells convert the solar radiation from the sun into electricity by the photovoltaic effect. Therefore, a solar cell requires a material which is able to absorb as much of this radiation as possible, but also have the ability to create mobile charge carriers and electron-hole pairs which are separated at each terminal without a significant loss of energy.

### **1.3.1 Band Structures**

It is important to understand the electronic band structure of a semi-conductor before explaining how a perovskite solar cell works. When two or more atoms are joined together in a molecule, their atomic orbitals overlap forming discrete energy levels. For solid materials, the number of atoms overlapping is very large and with the energy levels being so close they are considered as a continuum and form “bands” of energy levels. Figure 1.2 shows how the band energy diagram of different materials differ which determines its properties. The valence band is the highest energy band that contains electrons and can be fully or partially occupied, with the empty states in the valence band contributing to electric current. The conduction band is the lowest energy band with unoccupied states. In materials, the conducting bands can interfere with the forbidden gap, which is usually called the band gap, and is a measure of the width between the two bands [10]. The width of the band gap determines the type of material: insulator, semiconductor or metal.

In addition to this, the band gap is a measurement of the minimum amount of energy required for an electron to move from the valence to the conduction band. With respect to



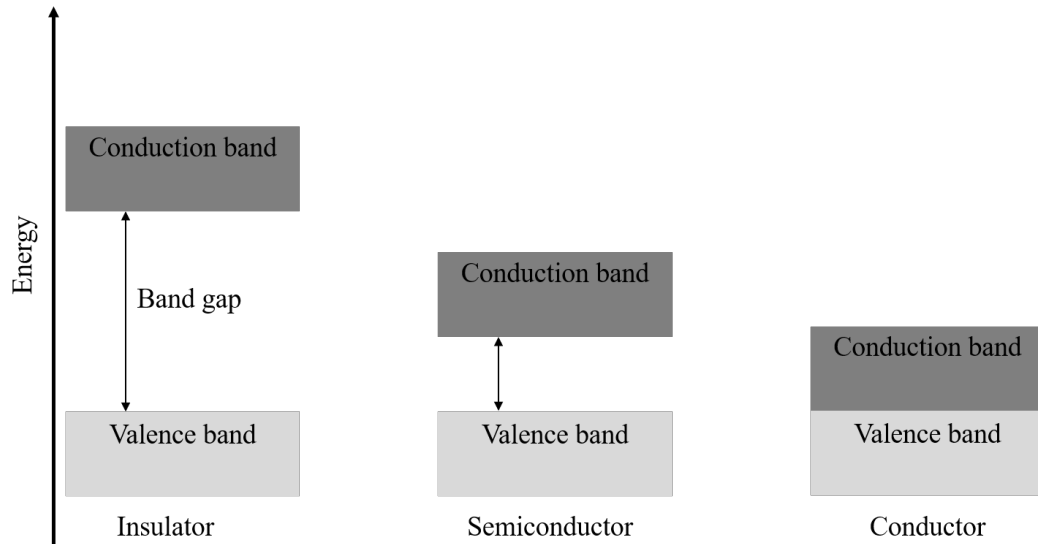


Figure 1.2: Electronic band structures in solid materials.

semiconductors, they can be classified as having direct or indirect band gaps. In a direct band gap semiconductor, the top of the valence band and bottom of the conduction band occur at the same value of momentum, whereas in an indirect band gap semiconductor the maximum energy of the valence band occurs at a different value of momentum to the minimum in the conduction band energy [11]. This influences the likeliness of a photon being absorbed by a material as well as how long electrons can exist in the conduction band.

### 1.3.2 Electron Generation Mechanisms in Perovskite Devices

Upon absorption of a photon in the perovskite material, providing the energy from said photon is equivalent to the band gap energy, an electron-hole pair is produced. The energy from the photon interacts with an electron in the valence band of the perovskite causing it to jump to the conduction band. It is said that where the electron once resided, a “hole” now occupies the empty state in the valence band. These fictitious holes are actually just missing electrons, but the concept is used to simplify calculations and understanding of the process [10]. As discussed briefly in section 1.3.1, the movement of an electron in direct and indirect semi-conductors is illustrated in Figure 1.3

In direct bandgap semiconductors, a photon of energy can produce an electron-hole pair relatively easily as the electron does not need much momentum, whereas in an indirect semiconductor and electron must undergo a significant change in its momentum for a photon to produce an electron-hole pair. This is possible, but the electron needs to interact with a photon

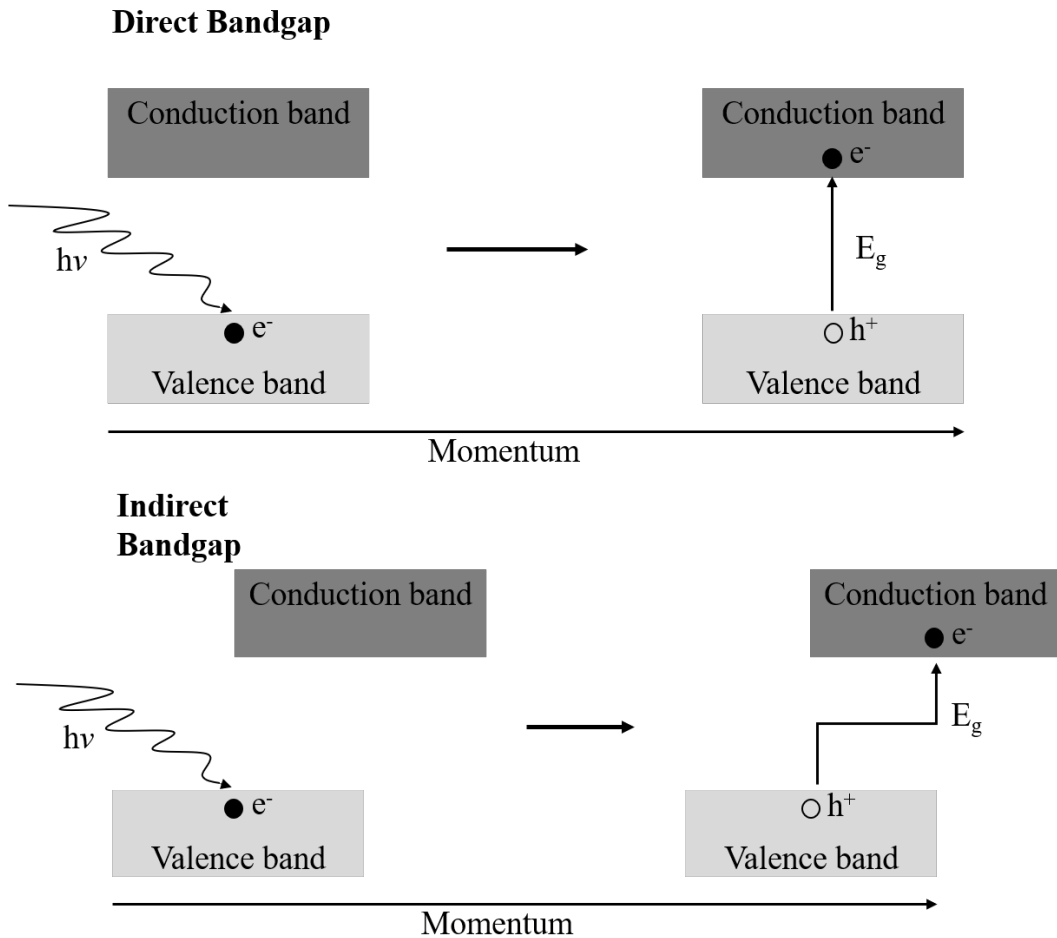


Figure 1.3: Schematic diagram of electron and hole generation in a direct bandgap semiconductor as well as an indirect bandgap semiconductor.

and a lattice vibration called a phonon to gain or lose momentum. The indirect process occurs at a slower rate compared to the direct process and can lead to recombination of electrons and holes before the electrons can be extracted for work. Recombination reactions are discussed in more detail in section 1.3.3. Once an electron has jumped into the conduction band, the electron is free to move around and termed a “charge carrier”. Similarly, the hole left in the valence band is also free to move around, with the number of electrons in the conduction band, and number of holes in the valence band termed the “intrinsic carrier concentration”. The overall conductivity of the material depends on this carrier concentration.

### 1.3.3 Recombination Reactions

When an electron and a hole meet in the perovskite layer, they recombine, and the potential energy is lost and therefore is unable to be extracted for work. Recombination reactions reduce the fill factor and open-circuit voltage ( $V_{OC}$ ) of a solar cell and thus the overall efficiency. Many

recombination processes exist in perovskite solar cells, which include; radiative recombination, nonradiative recombination, and interface recombination [12].

Radiative recombination is when an electron in the conduction band recombines with a hole in the valence band and results in the emission of a photon. Radiative recombination reactions require momentum, and therefore, indirect bandgap materials can suppress this due to the momentum mismatch between the conduction and valence bands [13].

Trap-assisted or Shockley-Read-Hall (SRH) is non-radiative and the main recombination loss mechanism which is driven by defects or trap states due to poor film qualities. These recombination mechanisms can be suppressed by the improvement of perovskite film quality, trap passivation or improvements in light outcoupling [14].

Interface recombination reactions are caused by poor interfaces between the perovskite material and the charge transport layers, so improvements of the interface whether by energy matching or reduction of defect trap states are relatively straight forward.

### **1.3.4 Equivalent Circuit**

A simple equivalent circuit for a PV cell is shown in Figure 1.4 and consists of a real diode in parallel with an ideal current source, as well as a resistor in series and shunt resistor in parallel. Series resistance can be affected by the contact resistance between the cell and the wire leads, as well as the resistance of the layers in the device. Shunt resistance represents power losses due to alternating current paths, with this diversion reducing the amount of current flowing, thus voltage produced. Therefore, it is key to have a high shunt resistance and low series resistance to maximise the cells efficiency. Effects of series and shunt resistances is further discussed in Section 1.6.2

## **1.4 Perovskite Device Architectures**

Many architecture variations exist within perovskite devices, but mostly adhere to the basic structure shown in Figure 1.5. This consists of a perovskite layer sandwiched between two charge transport layers, an electron-transport layer (ETL) which serves to collect electrons produced by the perovskite and block holes, and a hole-transport layer (HTL) which collects holes and blocks electrons. Both charge transport layers are connected to a conductive electrode which transport the electrons to an external circuit as photocurrent.

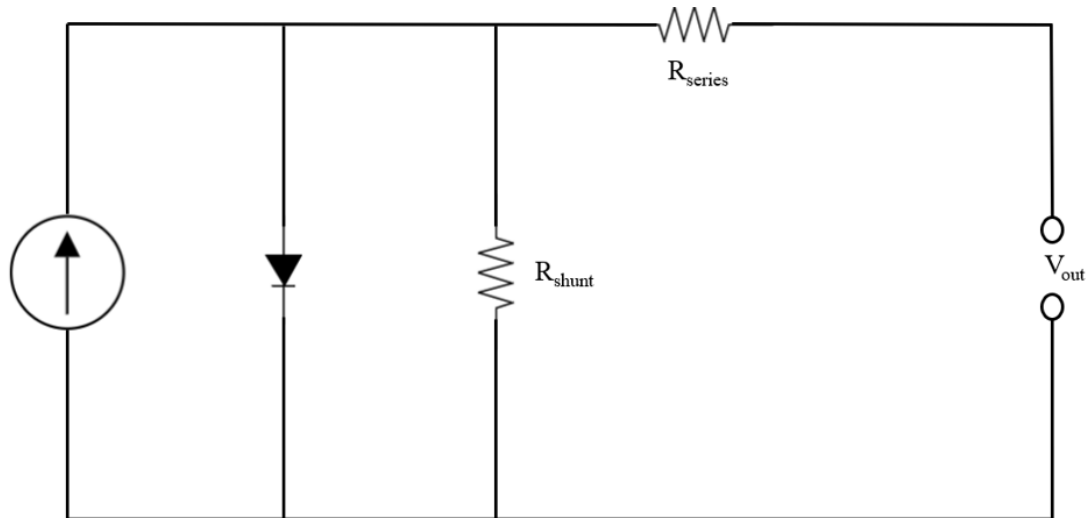


Figure 1.4: equivalent circuit of a photovoltaic cell.

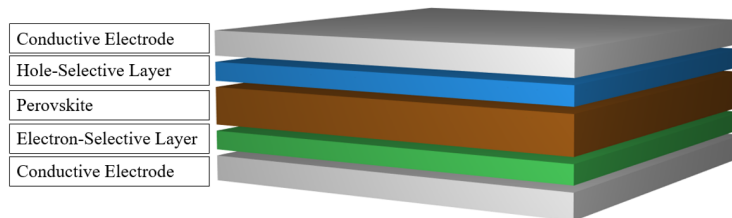


Figure 1.5: Schematic representation of a typical perovskite solar cell architecture.

### 1.4.1 Semiconductors

A semi-conductor simply implies that a materials electrical property lies between that of an insulator and a conductor. Two types of semiconductor exist; intrinsic and extrinsic (p-type and n-type). Taking pure silicon as an example of an intrinsic semiconductor, at any temperature above absolute zero there is a finite probability that an electron will be knocked out of place in its lattice, leaving behind a hole. Applying a voltage allows therefore allowed a small current flow [15]. Extrinsic semiconductors are simply intrinsic semiconductors which have been doped with impurity atoms. This doping increases the electrical conductivity of the semiconductor by introducing atoms of different elements into the lattice [16]. Intrinsic semiconductors can be doped to increase either their n-type conductivity or p-type conductivity. N-type semiconductors have been doped with atoms that can donate electrons, and p-type semiconductors have been doped with atoms that can accept electrons. In both cases, the electrical conductivity is increased when compared with its pure intrinsic form. In a perovskite device, the n-type semiconductors are more commonly named “electron transport layers” (ETLs) and the p-type

called “hole transport layers” (HTLs)

### 1.4.1.1 n-type

Using silicon as an example, n-type conductivity is achieved by doping with an element from group V in the periodic table such as phosphorus, arsenic or antimony which all have one extra valence electron per atom. The dopant enters the silicon lattice and replaces one silicon atom releasing its extra valence electron into the silicon lattice. Figure 1.6 shows a schematic representation of antimony doping as well as the energy diagram of an n-type semiconductor.

Once the dopants have been inserted into the semiconductor, the fermi level moves closer to the conduction band. The fermi level determines the probability of electron occupancy at different energy levels, and the closer it is to the conduction band the easier it becomes for electrons to move into the conduction band [17]. Therefore, increasing the conductivity of the n-type semiconductor is achieved by increasing the amount of dopant introduced.

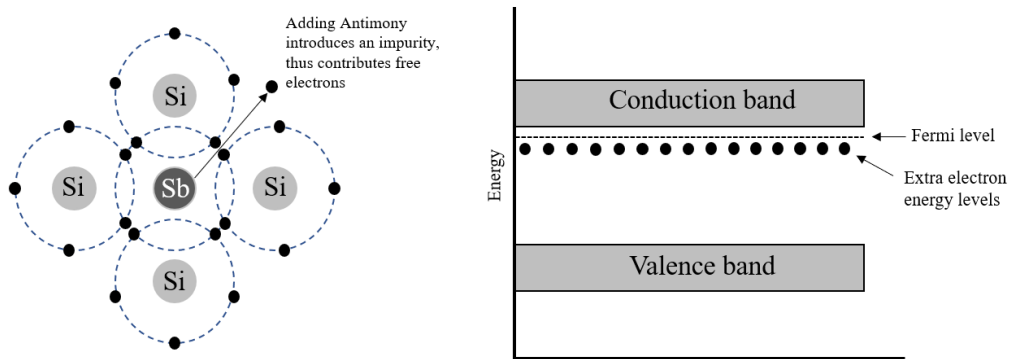


Figure 1.6: Schematic representation n-type silicon doping and its representative band diagram.

### 1.4.1.2 p-type

p-type conductivity is achieved by doping atoms of group III elements into the silicon lattice such as Boron or Gallium (Fig 1.7). These atoms have one less valence electron, thus, once bonding to four silicon atoms they accept an electron from an adjacent atom into its covalent bond. This allows movement of a hole through the valence band of the material. Via the same principle as discussed in the n-type semiconductor, the fermi level now moves closer to the valence band allowing easier movement of free holes through the valence band. Again, increasing the amount of dopant leads to an increase in electrical conductivity.

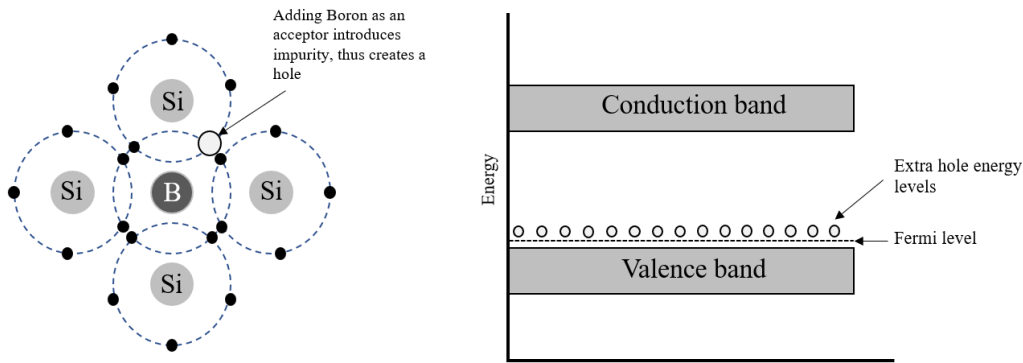


Figure 1.7: Schematic representation p-type silicon doping and its representative band diagram.

### 1.4.2 Metal oxide semiconductors

Metal oxide semiconductors are in a different class of materials when compared to silicon-based semiconductors, with the interaction between the metal and oxide orbitals resulting in a large difference in charge carrier transport. To summarise, the M ns orbitals are highly dispersive, whilst the O 2p is localised, resulting in a smaller effective mass for electrons compared to holes. This smaller electron effective mass suggests better electron transport in comparison to hole transport [18]. Due to this, typical metal oxide semiconductors have n-type conductivity. However, p-type conductivity can also be achieved in certain metal oxides such as Nickel Oxide (NiO) and Copper (I) Thiocyanate (CuSCN). P-type metal oxides are designed by introducing metal cations which occupy d or s states near the valence band minimum (VBM), resulting in p-d and p-s coupling between the metal cation and oxygen orbitals. This in-turn enhances the dispersion of VBM, reducing the hole effective mass [18]. It must be noted that although metal oxide semiconductors can facilitate electron and hole transport, high conductivity can only be achieved via extrinsic doping with controllable concentrations up to a very high level. For example, NiO in its stoichiometric form is an insulator, but by doping with Li<sup>+</sup> ions or increasing the content of Ni<sup>3+</sup> ions the p-type conductivity can be increased [19].

Most importantly, for metal oxides to be used as n-type or p-type in a perovskite device, they must be transparent, stable and have a suitable band gap. In addition to this, most metal oxides used in the literature are processed at high temperatures which is clearly unsuitable for roll-to-roll coating, thus the next two sections will be discussing the progress being made on the low-temperature deposition of ETLs and HTLs. Furthermore, there are a variety of organic semiconductors used in perovskite architectures which will also be included in the following

sections.

### 1.4.3 n-i-p and p-i-n architectures

In the literature, perovskite devices are usually categorised into two types; n-i-p (n-type, intrinsic, p-type) and p-i-n (p-type, intrinsic, n-type), which simply states the configuration of the device stack with the first letter corresponding to the layer which is positioned at the bottom. Generally, the majority of devices in the literature are n-i-p based as shown in Figure 1.5, however, publications using the p-i-n architecture are becoming increasingly more common. The architecture used is usually pre-determined by the ETL and HTL used due to the deposition requirements of said layer. A significant portion of ETLs require high-temperature processing (usually inorganic metal oxides), which would damage the perovskite layer if deposited on top. In addition, some ETLs are dissolved in solvents which dissolve the perovskite layer, thus cannot be used in a p-i-n structure. Significant advances in ETL and HTL materials have led to a variety of architectures which will be discussed in the next section.

### 1.4.4 Electron-transport Layers

This section aims to cover the literature based on the low-temperature deposition of ETLs for use in a perovskite device. Although there are several low-temperature deposition methods, only the methods deemed to be potentially roll-to-roll compatible will be discussed. Methods such as atomic layer deposition (ALD), chemical bath deposition (CBD) and chemical vapor deposition (CVD) were not included as although they are low-temperature, they would be difficult to incorporate into a roll-to-roll coating line and would lead to impractical capital costs.

In addition to being transparent, ETLs must also be compact and pin-hole free. Thickness of the layer is also paramount to device performance, firstly as to not hinder the series resistance of the device, and secondly to provide full coverage of the underlying substrate.

With respect to ETLs used in perovskite devices, these usually consist of inorganic materials and occasionally organic semiconductors. Inorganic ETLs in the literature are predominately metal oxides, with the main candidates being titanium dioxide ( $\text{TiO}_2$ ), Zinc Oxide ( $\text{ZnO}$ ) and Tin Oxide ( $\text{SnO}_2$ ). Organic ETLs are less common than their HTL counterparts with the most frequent organic ETL being phenyl-C61-butyric acid methyl ester (PCBM).

Titanium dioxide ( $\text{TiO}_2$ ) is perhaps the most common electron transport layer used in per-

ovskite solar cells and is usually used in two forms; mesoporous TiO<sub>2</sub> scaffolds and compact TiO<sub>2</sub>. The two types are usually used in conjunction with one another, however, compact TiO<sub>2</sub> is commonly used on its own.

Two types of TiO<sub>2</sub> based devices are seen frequently in the literature, one being the mesoporous architecture, and the other being the planar architecture. Mesoporous architectures either employ a TiO<sub>2</sub> or Al<sub>2</sub>O<sub>3</sub> scaffold which were discussed briefly in section 1.2, however the vast majority of n-i-p based architectures also employ a compact TiO<sub>2</sub> hole blocking layer [20, 21, 22].

Many deposition methods have been explored for TiO<sub>2</sub> compact layers with the majority requiring relatively high annealing temperatures. Most commonly compact TiO<sub>2</sub> layers are deposited via spray pyrolysis [23, 24, 25] or spin-coating [26, 21, 27] with other methods such as atomic layer deposition (ALD) [28] or sputtering [20]. Burkitt et al also managed to slot-die coat a mesoporous and compact layer of TiO<sub>2</sub> onto glass substrates [29]. Nonetheless, these compact layers require high temperature annealing at temperatures of 400 - 500 °C and above due to the requirement of converting the TiO<sub>2</sub> precursors into n-type TiO<sub>2</sub> making their application in a roll-to-roll setting unachievable unless suitable substrates such as steel foils are used, whereas in the case of this work, plastic substrates were used.

One-method to alleviate the high temperatures necessary for the deposition of a compact layer of TiO<sub>2</sub> is to use a nanoparticle suspension. Instead of forming the TiO<sub>2</sub> in situ via the annealing of a precursor, the nanoparticles can be pre-synthesised and dispersed into a chosen solvent. This method also offers more control over the doping and particle sizes. In 2014 Conings et al used an in-house prepared TiO<sub>2</sub> nanoparticle suspension for use as an ETL achieving an efficiency of 13.6% [30]. The TiO<sub>2</sub> layer was deposited via spin coating and thermally treated at 135 °C making it a suitable candidate for roll-to-roll deposition onto temperature-sensitive substrates. Hossain et al also reported the use of a low-temperature processed TiO<sub>2</sub> nanoparticle ETL with spin-coated efficiencies reaching 19.5% [31]. In addition to this, the group also managed to deposit the TiO<sub>2</sub> via inkjet and slot-die coating managing a respectable 15% PCE, confirming their compatibility with not only low-temperature substrates, but also roll-to-roll compatible deposition techniques [31]. Several other papers have since been published employing TiO<sub>2</sub> nanoparticle ETLs with similar efficiencies [32, 33, 34].

Alleviating or replacing a thermal treatment is also a possible course for low-temperature films to be processed. Das et al used photonic-curing to produce crystalline anatase-phase TiO<sub>2</sub>



films from a sol-gel on PET substrates achieving efficiencies up to 11.2% [35][36]. Photonic curing uses high-intensity photonic light pulses to anneal/sinter thin films, and does so in such a short space of time (in the order of milliseconds) that the underlying substrate is not damaged [37]. A total exposure time of 13 seconds was reported and certainly has the potential to be incorporated into a roll-to-roll coating set-up.

Tin oxide ( $\text{SnO}_2$ ) has also become a common hole blocking layer in the literature and may be a better option for use in perovskite solar cells than  $\text{TiO}_2$ .  $\text{SnO}_2$  has a wide bandgap ranging from 3.6 to 4.1 eV and has a higher electron mobility than  $\text{TiO}_2$  [38]. Tin oxide has been deposited using relatively low temperatures of 200 °C by thermal decomposition of tin based salt precursors ( $\text{SnCl}_2$  or  $\text{SnCl}_4$ ), or their hydrates ( $\text{SnCl}_2 \cdot 2\text{H}_2\text{O}$  or  $\text{SnCl}_4 \cdot 5\text{H}_2\text{O}$ ) dissolved in an appropriate solvent such as ethanol with annealing converting them into  $\text{SnO}_2$  [39, 40, 41]. Zuo et al managed to manufacture a perovskite device using this method with an efficiency of 20.2%, however, the annealing conditions were lengthy (150 °C for 30 minutes followed by 60 minutes at 180 °C) [42]. Nonetheless, this proves that high performance devices can be made using  $\text{SnO}_2$  as the ETL annealed at relatively low temperatures. The temperature and annealing time do however require reducing should roll-to-roll coating on flexible substrates be realised. Reduction of the annealing temperature and time is unlikely as the crystallinity of the final film is heavily reliant on these conditions.

Much like  $\text{TiO}_2$ , synthesised nanoparticles are an obvious avenue to achieve quality films at low temperature. Jiang et al presented a commercially bought  $\text{SnO}_2$  nanoparticle ETL (spin-coated) based perovskite device with a certified efficiency of 19.9% [43]. More importantly, this layer was dried on a hot plate at 150 °C for 30 minutes making it suitable for flexible, temperature sensitive substrates. Since Jiang et al's publication, numerous papers have employed this nanoparticle suspension, all with excellent efficiencies [38, 44, 45, 46, 47] and appears to be a new standard for producing high performance, low temperature  $\text{SnO}_2$  ETLs. One thing to note is that more or less all of these publications employ an annealing time of 30 minutes at 150 °C, which would be a bottleneck in large scale manufacture, thus reducing the time would be hugely advantageous.

Another inorganic electron transport layer used in perovskite devices is zinc oxide ( $\text{ZnO}$ ), which also has the advantage of low-temperature compatible processing, either from a sol-gel [48] or nanoparticle suspensions [49]. Unfortunately, zinc oxide causes severe instability issues when used in perovskite devices and is due to the basic nature of the  $\text{ZnO}$  surface which leads

to proton-transfer reactions at the ZnO/perovskite interface degrading the perovskite itself [50]. This decomposition is accelerated by surface hydroxyl groups and residual acetate ligands, if any are present from the precursor materials [50]. It is not yet clear whether the stability issues are present in all the metal halide perovskites, but research is being conducted to determine this.

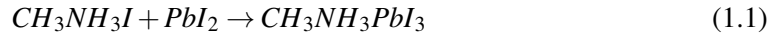
One other common electron transport layer used throughout literature is the organic fullerene derivative phenyl-C61-butyric acid methyl ester (PCBM). Unlike the inorganic hole blocking layers discussed in this section, PCBM is frequently used in p-i-n (p-type, intrinsic, n-type) architecture, usually referred to as the “inverted” architecture. In these devices the electron transport layer is deposited on top of the perovskite layer instead of before it, mainly owing to PCBM's ability to dissolve in many solvents. Chlorobenzene or toluene are the main solvents used to dissolve PCBM, and spin-coated straight on to the perovskite layer, with no further drying steps required, making it a popular choice for low-temperature applications. PCBM has enabled the fabrication of high efficiency, low-temperature perovskite devices with efficiencies exceeding 20% [51][52][53]

### **1.4.5 Perovskite Layers**

There have been many different methods utilised in the deposition of perovskite films throughout the literature, and the most common will be discussed in this section. There are three main methods for depositing perovskite films, irrespective of the precursor; single-step, two-step and the anti-solvent method. All three have been demonstrated to produce high quality perovskite films, with each having advantages and disadvantages. Vapour deposition has also been demonstrated but not included in this review due to the difficulties that would originate for scale up.

#### **1.4.5.1 Single-Step Deposition**

The method employed by Lee et al [6] and Kim et al [7] was that of a single-step perovskite deposition, in which a precursor solution was made up by dissolving methyl ammonium iodide ( $\text{CH}_3\text{NH}_3\text{I}$ ) and lead iodide ( $\text{PbI}_2$ ) in a solvent, usually N,N-Dimethylformamide (DMF). This is then spin coated onto a substrate and annealed on a hot plate (100 °C for 10 minutes) to convert it into methyl ammonium lead iodide ( $\text{CH}_3\text{NH}_3\text{PbI}_3$ ) via the following equation.



Different lead halides are commonly used in the literature such as lead bromide ( $PbBr_2$ ) or lead chloride ( $PbCl_2$ ), but the method is essentially the same. More recently, further iterations of perovskite precursors have gained traction in the literature with reports of them being more stable or reaching higher efficiencies. Replacing the methylammonium cation with a larger formamidinium cation, the band gap becomes more tuneable (1.48 to 2.23 eV) [54]. Li et al reported that by mixing the formamidinium and methylammonium cations together leads to greater stability, very long diffusion lengths and improvements on carrier mobility [55]. It is clear that numerous choices are available for the perovskite precursor, and choices depend on the properties desired, processing methods and the environment they are deposited within. Annealing temperature of these films has a strong impact on the overall film morphology and power conversion efficiency of the subsequent device. Dualeh et al conducted a study on the effect of temperature on the film morphology of a methyl ammonium lead iodide (MAPI) perovskite and found that a minimum temperature of 80 °C was required for conversion into perovskite and increasing this temperature lead to formation of islands of perovskite material and is accompanied by an increase in  $PbI_2$  content. This group found that an annealing temperature of between 80 and 100 °C was optimal [56]. It did, however, take 45 minutes for full conversion at 100 °C which is a large bottleneck in large scale processing.

#### 1.4.5.2 Two-Step Deposition

Two-step deposition involves the deposition of a lead halide containing solution, usually DMF with a drying stage, and then depositing a methyl ammonium halide solution (usually in IPA) on top either by spin coating or dip coating to form the perovskite. A comparison of the single-step and two-step deposition methods is illustrated in Figure 1.8

Crystal sizes and morphology of the perovskite films are easier to control using the two-step method [57]. The crystal sizes of the perovskite can be altered by changing the concentration of MAI in the second step, with the crystal sizes increasing as the concentration of MAI decreases [58]. Formation of the perovskite using two-step deposition differs between planar and mesoporous architectures, where conversion is relatively fast in mesoporous devices, and much slower in planar architectures. Crystal sizes on planar architectures are difficult to con-

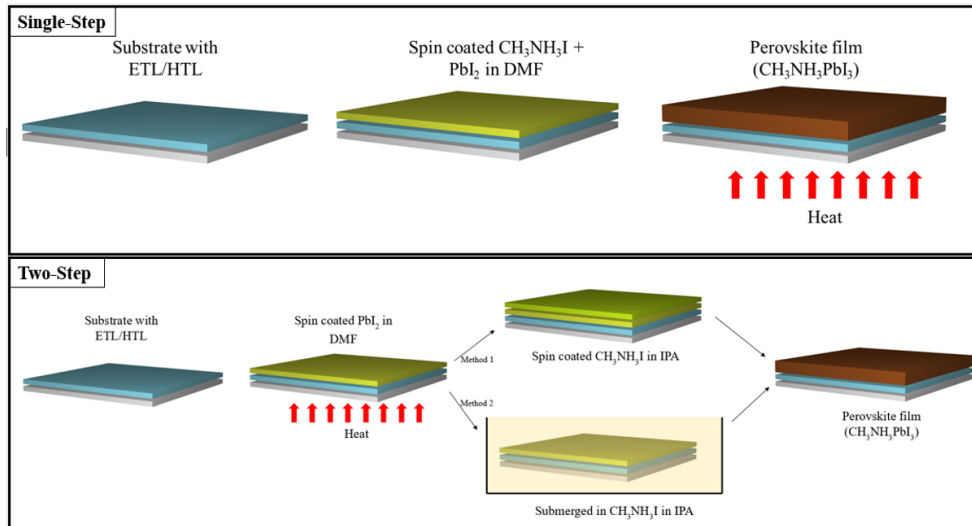


Figure 1.8: Schematic illustration of single-step and two-step perovskite depositions.

control, which hinders device reproducibility and is caused by the ease of  $\text{PbI}_2$  crystallisation. Wu et al overcame this by inhibiting the crystallisation by use of DMSO as the solvent instead of DMF due to DMSO having a stronger coordination ability with  $\text{PbI}_2$  compared to DMF [59]. Using this method Wu et al were able to fully convert the  $\text{PbI}_2$  into perovskite in 10 minutes with efficiencies of upto 13.5% [59].

### 1.4.5.3 Anti-Solvent Method

The anti-solvent method was first demonstrated by Jeon et al, in which they spin coated a layer of  $\text{CH}_3\text{NH}_3\text{Pb}(\text{I}_{1-x}\text{Br}_x)_3$  dissolved in  $\gamma$ -butyrolactone (GBL) and DMSO onto a substrate, followed by a toluene drip dropped sequentially onto the spinning substrate. This toluene drip does not dissolve the perovskite constituents, but is miscible with DMSO and GBL and serves to remove any residual DMSO or GBL which is not removed by the centripetal forces of the spin coating procedure. This, in turn leads to an intermediate phase of  $\text{PbI}_2\text{-CH}_3\text{NH}_3\text{I-DMSO}$  [60]. Upon annealing at  $100\text{ }^\circ\text{C}$  any residual solvent is removed, and an extremely smooth and homogenous perovskite film is produced. This is now an established method in the literature for producing high quality reproducible perovskite films and is compatible with all of the common precursors [61][62][63]. Several other anti-solvents have been investigated including; chlorobenzene and ethyl acetate with the anti-solvent used depending on the type of perovskite and the conditions [61].

Although reproducible high-quality films are easily achievable using this method, it relies on the spinning motion of a spin coater which would be extremely difficult to scale-up and no

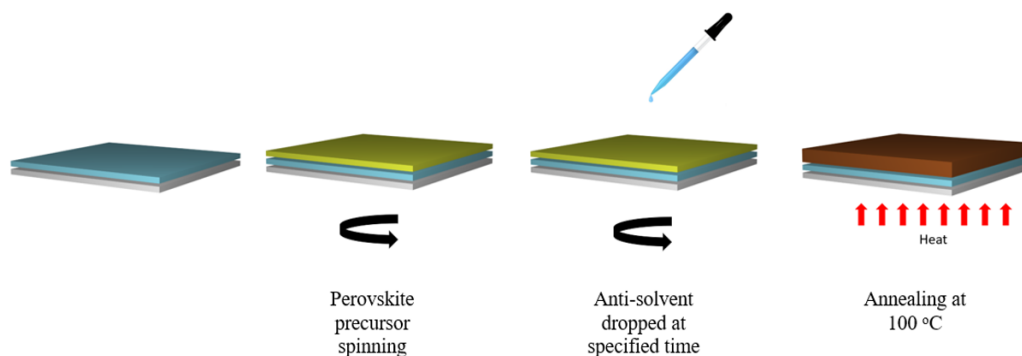


Figure 1.9: Schematic illustration of the anti-solvent method.

work has yet been published on the scale up of this method. However, as this work is aimed at the scale up of the ETL and HTL layers, these were deposited using scalable coating techniques and the perovskite layer always spin coated for reliability purposes.

#### 1.4.6 Hole-transport Layers

Hole-transport layers or hole-transport material (HTM) serve to transport holes to an external circuit whilst simultaneously blocking the transfer of electrons. Certainly, the most common HTL seen in the literature is an organic molecule named spiro-OMeTAD (2,2',7,7'-tetrakis-(N,N-di-pmethoxyphenylamine)9,9'-spirobifluorene) and leads to great efficiencies in excess of 20% due to its well matched HOMO level of -5.22 eV [64][22]. Hole mobilities of spiro-OMeTAD are increased by p-doping with various molecules, usually Li-TFSI (lithium bis(trifluoromethanesulfonyl)-imide), tBP (4-tert-Butylpyridine) and different cobalt (III) complexes. Spiro-OMeTAD and its dopants are usually dissolved in chlorobenzene and deposited directly on top of the perovskite layer with no further drying/annealing processes required. Although Spiro-OMeTAD appears to be the perfect HTL for perovskite devices, it suffers from two main issues. Firstly, it is extremely expensive and at the time of writing the cost for 1 g of Spiro-OMeTAD powder is £347 on Sigma Aldrich (April 2020) and using this in large quantities would prove tremendously expensive. Secondly, it requires oxidation (in air) for efficient functionality which could prove to be a significant bottleneck in large scale manufacturing.

Several replacement HTLs have been successfully employed in high efficiency perovskite solar cells, with P3HT (Poly(3-hexythiophene)) a promising cheaper alternative to Spiro-OMeTAD [65][66]. Efficiencies have not yet reached that of Spiro-OMeTAD equivalent devices which is due to low open-circuit voltage ( $V_{OC}$ ) caused by non-radiative recombination at the perovskite/P3HT interface. In addition to this, molecules of P3HT are flat which results in strong

electronic coupling between the perovskite and P3HT causing lower electron lifetime compared with Spiro-OMeTAD [65].

PTAA (poly[bis(4-phenyl)(2,4,6-trimethylphenyl)amine]) is another HTL popular in the literature with efficiencies reaching 20% and above [67][68]. PTAA is typically doped with similar additives to Spiro-OMeTAD but suffers from even higher costs than Spiro-OMeTAD which, at the time of writing costs over £2000/g (Sigma Aldrich April 2020) clearly preventing its use in large scale deposition.

One of the most widely used polymer HTLs for inverted perovskite devices is poly(3,4-ethene-dioxythiophene):poly(styrenesulfonate), more commonly known as PEDOT:PSS. PEDOT:PSS has high transparency in the visible region, high mechanical flexibility, good wettability of the perovskite film and can be processed at low-temperatures [69, 70]. The first p-i-n perovskite device adopted PEDOT:PSS as the HTL with an efficiency of 3.9% in 2013 [71]. Since then, improvements to efficiencies have been achieved by doping of the film and the highest efficiency found so far to be 20.22% [72]. By doping with CsI (Cesium Iodide), Jiang et al enhanced the hole extraction properties of PEDOT:PSS as well as suppressing charge recombination leading to no hysteresis [72]. Doping of PEDOT:PSS with dopants such as; other polymers [73, 74], sodium citrate [75] and graphene oxide [76] has become commonplace in the literature, all improving upon the efficiency of a PEDOT:PSS only HTL. PEDOT:PSS has also been used successfully in R2R devices, which will be discussed further on in section 1.5.3. Despite the fact that PEDOT:PSS appears to be the perfect candidate for a R2R compatible HTL, its main drawback is the stability of the devices made upon it; PEDOT:PSS is highly hygroscopic, has high acidity and a low work function [77, 78]. Its hygroscopic nature leads to the absorption of atmospheric water, inevitably inducing degradation of the perovskite layer. Doping of PEDOT:PSS has been reported to vastly improve the stability of perovskite devices. Huang et al doped the PEDOT:PSS with dopamine (DA), which is basic in nature, thus reducing the acidity of the PEDOT as well as increasing its work function. Devices made using the DA-PEDOT led to a significant increase in device stability when compared to un-doped PEDOT:PSS as well as overall device performance [77]. Redondo-Obispo et al employed a hydrophobic dopant of graphene to counteract the hygroscopic nature of PEDOT:PSS leading to enhanced stability as well as performance [78]. Clearly the stability issue of PEDOT:PSS can be somewhat eradicated, and are a promising candidate for use in R2R perovskites.

Inorganic HTLs have also paved the way for cheaper, more stable perovskite devices, with

NiOx (Nickel Oxide) [79][80] and CuSCN (Copper(I) thiocyanate) [81][82] exhibiting high efficiencies. Pure stoichiometric nickel oxide (NiO) is an excellent insulator so doping with excess oxygen is simple and enables p-type conductivity by introducing Ni<sup>+</sup> vacancies, thus holes. NiOx is also highly transparent with band gaps compatible with perovskites making it a promising alternative to the more expensive inorganic HTLs. Most commonly, NiOx is deposited by thermal degradation of a nickel based salt precursor such as nickel acetate tetrahydrate dissolved in an appropriate solvent [83, 84] and annealed at temperatures of 300 – 500 °C [85, 86] clearly making this inappropriate for roll-to-roll coating. With the recent rise in nanoparticle suspensions being used in perovskite applications, numerous papers have been published employing NiOx nanoparticles (both commercial and in-house) for low-temperature processed HTLs. Kwon et al reported a solution processable NiOx nanoparticle HTL with an efficiency of 15.4%, however, these nanoparticles were suspended in tetradecane which required drying at 270 °C [87]. Hou et al prepared a NiOx nanoparticle suspension dispersed in methanol achieving an initial efficiency of 11.7% after drying the film at 140 °C making it roll-to-roll compatible [88]. In addition to this, the group noticed that the low performance was down to a poor fill factor, directly related to the series resistance of the device. They overcame this by employing a 2,9-Bis[3-(dimethyloxidoamino)propyl]anthra[2,1,9-def:6,5,10-d'e'f']diisoquinoline-1,3,8,10(2H,9H)-tetrone (PDINO) buffer layer between the PCBM ETL and the Ag electrode. This vastly increased the fill factor from 50 to 77% and subsequently the efficiency from 11.7 to 17.5% [88]. High series resistance in NiOx nanoparticle based devices appears to be a common theme among the publications owing to the overall low conductive nature of NiOx [89]. Many publications on using UV-Ozone to increase the conductivity of sol-gel based NiOx have been made. UV-Ozone not only increases the conductivity of the NiOx film, but also increases the wettability and valence band energy [83]. Islam et al investigated the effect of UV-Ozone on NiOx surfaces and found that it changes the film stoichiometry by introducing Ni vacancy defects, with oxygen-rich NiOx behaving as a p-type semiconductor, thus increasing the p-type conductivity and overall reducing the resistance [90]. Liu et al employed this technique on a NiOx nanoparticle layer and witnessed the same effects, which in turn improved their device performance from 12.0 to 15.9% [80]. This group confirmed by XPS that an increase in Ni<sup>3+</sup> vacancies was responsible for an increase in overall film conductivity. Interestingly, Liu et al also reported that their nanoparticle suspension could be deposited directly on top of a perovskite layer without damaging it, and prepared a flexible n-i-p device

with a champion efficiency of 11.84% [80]. One other issue arises from the use of nanoparticle suspensions; the ligands used to stabilise the solution negatively effects the conductivity of the coated layer as they are not removed at the low temperatures used to dry the films [91]. Qiu et al used oxygen plasma treatment to remove residual ligands from the NiOx film leading to an increase in PCE from 4.2 to 6.10% when compared to an untreated film [91]. It must be noted that the low efficiencies reported by Qui et al were due to the NiOx being deposited on top of the perovskite, but nonetheless proved that NiOx is an excellent contender for a roll-to-roll HTL in an n-i-p or p-i-n stack.

CuSCN is an intrinsic p-type semiconductor with high hole mobility and has been proven to achieve 20% efficiencies in an n-i-p configuration [81]. It is also cheap and earth abundant making it an excellent replacement for organic HTLs (£1.65/g Sigma Aldrich April 2020). Although high efficiencies have been realised in an n-i-p architecture, the minimal choice of solvents that dissolve CuSCN but not perovskite are a main drawback for large scale deposition.

#### **1.4.7 Conductive Electrodes**

Perovskite devices are made up of the charge transport layers and the perovskite sandwiched between two conductive electrodes. At least one of these electrodes must be transparent as to allow light to pass through and be absorbed by the perovskite layer. Typically, the transparent electrode is glass coated in a transparent conductive oxide (TCO) such as fluorine-doped tin oxide (FTO) or indium-doped tin oxide (ITO), with the former being the more thermally stable of the two. Each of these TCOs has high optical transparency and good electrical conductivity of around 15 Ohms/sq. Main differences between FTO and ITO are that ITO is much smoother than FTO allowing for extremely thin homogenous layers to be deposited where this is critical. ITO can also be deposited onto temperature sensitive substrates such as PET (polyethylene terephthalate), making it roll-to-roll compatible. PET substrates are however limited by their processing temperatures due to their low melting point of around 150 °C, limiting the use of high temperature annealed HTLs or ETLs. In the last few years an influx of papers using flexible PET-ITO substrates for perovskite devices have appeared with efficiencies comparable to their rigid substrate counterparts [92][93][94][95].

Top electrodes are almost always made up of an evaporated metal such as silver or gold, which clearly inhibits the conversion from small scale devices to large printed devices due to the vacuum process required to deposit the metal electrodes. Recent advances on using screen



printed silver electrodes have been promising [96], but the long term stability of perovskite solar cells using silver electrodes is challenging. Degradation of perovskite devices using a silver electrode was thoroughly investigated by Li et al, and it was found that iodide and methylammonium ions from the perovskite diffuse through the HTL and accumulate at the silver electrodes inner surface [97]. This forms silver iodide (AgI) and results in degradation of the perovskite, observed by a gradual colour change from brown/black to yellow.

It would be advantageous for future perovskite solar cells to be deposited onto opaque substrates such as metals, which could be used as integrated building components. This does, however, require a transparent top electrode for light absorption. Troughton et al managed to create a perovskite device on a titanium foil with an efficiency of 10.3% (Figure 1.10) which used a transparent PET with embedded Nickel mesh as a top electrode [98]. Another paper published by this group discussed the use of a transparent conductive adhesive (TCA) to establish a connection between the Ni mesh and the HTL, which was made up of PEDOT:PSS [99]. Stability of these devices were not discussed in the papers which would be of concern due to the hygroscopic and basic nature of the PEDOT:PSS. Nonetheless, the research demonstrated that using an opaque substrate for high efficiency perovskite solar cells was possible.

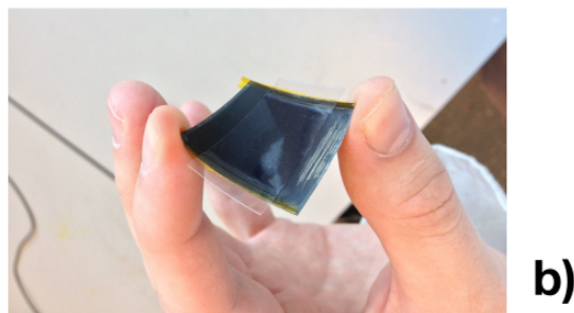
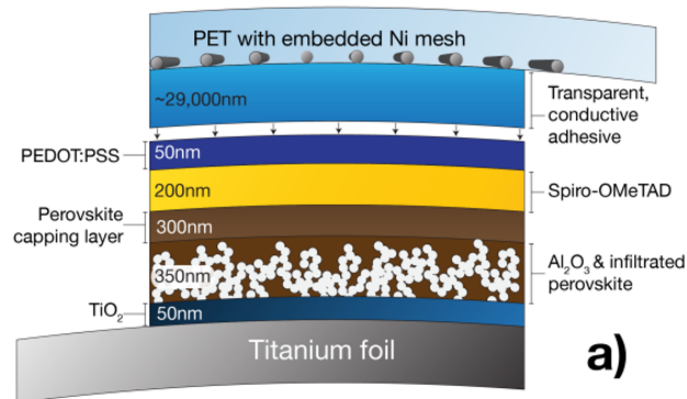


Figure 1.10: (a) Schematic representation of a metal mounted perovskite solar cell and associated target layer thickness. (b) A photograph of a flexible perovskite solar cell on titanium foil [99]

Many perovskite devices have been reported using solution-processed silver nanowires as top electrodes [100][101]. These nanowire solutions are sprayed on using ultrasonic spray coating and have led to efficiencies of 13.93%. In addition to this, more scalable deposition methods such as ink-jet printing have been successfully used to deposit silver nanowires [102], however, these devices were all made on TCO coated glass substrates and illuminated through this layer and not the top electrode. Illuminating through the silver nanowire would inevitably lead to efficiency losses due to lower light transmission. Further intensive research is required before a roll-to-roll compatible transparent top electrode is realised.

## **1.5 Scaling up of perovskite devices**

This section will discuss the current advancements on the scaling up from spin-coating to roll-to-roll compatible deposition methods of various layers in a perovskite device. Particular focus will be on methods for ETL and HTLs, paying attention to the temperatures used and the overall toxicity, thus safety aspects involved with each layer. A number of deposition methods have been employed for scale up of various layers perovskite devices, mainly the ETL, HTL and perovskite. These deposition methods consist of; slot-die [103, 104, 105, 106], gravure [107], inkjet [108, 109], blade [110, 111] and screen printing [112, 113]. However, the most prevalent deposition method in the literature is undoubtedly slot-die coating and will therefore be the focus of the following review.

### **1.5.1 Slot-die Coating**

Slot-die coating is a pre-metered process used in many industrial coating lines. Figure 1.11 shows a typical slot-die coating head which comprises of two precision made “heads”, which are bolted tightly together separated by a “shim” which is used to create a small gap for the ink to pass through as well as defining the printing pattern. Only simple 2D shapes are currently possible with slot-die coating, but this is all that’s needed for perovskite solar cell deposition. Ink leaving the head at the slot-die lips is what forms the meniscus between the head and the substrate and this can be aided in the form of a meniscus guise inserted between the shim and the head, with this called “meniscus guide slot-die coating”.

The coating thickness is defined by the flow rate of the ink fed into the slot-die head and therefore highly tuneable. In summary, ink is fed into the slot-die head and fills the ink channel.

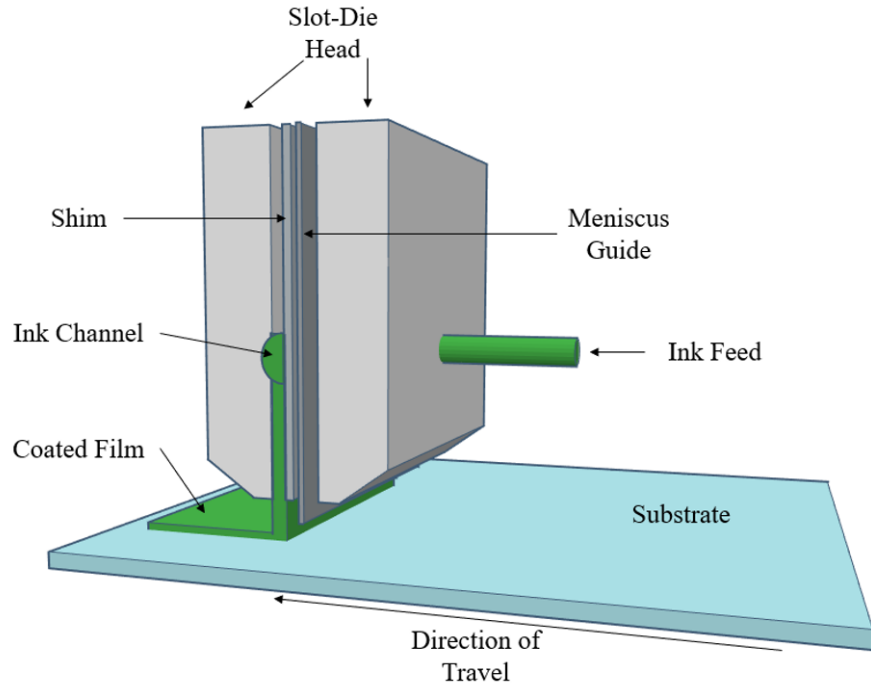


Figure 1.11: Schematic diagram of a typical slot-die coating head.

Ink then flows down the gap between the two heads which is separated by a shim and sometimes a meniscus guide, with the shim determining the coating pattern and width. Upon the ink exiting the head at the slot-die lips, a bead of liquid is held between the lips and the moving substrate by capillary forces, which are dependant on; surface tension, the gap between the slot-die lips/meniscus guide and the substrate and the contact angle of the ink. Viscosity of the ink, coating thickness and the externally applied pressure difference also contribute to these forces [114].

As slot-die coating is a pre-metered process, calculation of wet film thicknesses are simple and calculated using equation 1.2. Where  $D_w$  is the wet film thickness in cm,  $f$  is the flow rate of the ink in  $\text{cm}^3/\text{min}$ ,  $v$  is the velocity of the moving substrate in  $\text{cm}/\text{min}$  and  $w$  being the total coating width in cm.

$$D_w = \frac{f}{vW} \quad (1.2)$$

The subsequent dry film thickness can then be calculated from knowledge of the solids content in the ink as well as the dry film density. Equation 1.3 shows the dry film thickness calculation in which  $D_d$  is the dry film thickness in cm,  $D_w$  is the wet film thickness in cm,  $c$  being the concentration of solids in the ink in  $\text{g}/\text{cm}^3$  and  $\rho$  is the density of the dry film in  $\text{g}/\text{cm}^3$ .

$$D_d = D_w \left( \frac{c}{\rho} \right) \quad (1.3)$$

These equations show that the thickness of the dry film can be carefully controlled by varying the solids content of the ink and the wet film thickness deposited. Sometimes, control of the ink properties can be difficult whether that be due to solubility issues or a severe change in fluid dynamics which could lead to poor film qualities. This can be overcome by changing the substrate velocity or the flow rate of the ink, allowing high precision wet film thicknesses, and very thin dry films.

Issues can also arise when coating films that are too thick or too thin; thicker films may lead to poor morphologies due to drying inconsistencies, whereas, films that are too thin can lead to coating failure from small variations in slot-die lips and substrate height differences. It is therefore important to take all these factors into account when choosing the ink properties and the conditions in which they are coated. Use of a meniscus guide within the slot-die head can help to force the ink to travel down the guide and aid in the formation of a meniscus, leading to more stable coatings. Burkitt et al successfully employed meniscus guide slot-die coating for the deposition of 4 layers in a slot-die coated perovskite device with low weight% precursors achieving dry film thicknesses of less than 50 nm [29].

### 1.5.1.1 Slot-Die Coating Modelling

The parameters of a coating procedure that produces a stable coating from an ink is known as the “coating window”. It is useful to know the coating window to predict whether a given ink will provide stable coatings in the deposition parameters chosen, which will prevent extensive “trial and error” type experiments to find the coating window manually. Many methods exist to determine the coating window, with some being more complicated than others, however, regardless of the method used, it is still good practice to back up the model with some experimental procedures.

Figure 1.12 shows a 3D cross section of a slot-die coating head with a coating bead and the main parameters required for modelling. Upon exiting the slot-die head, the ink forms a bridge between the head and substrate which is called the head-substrate gap ( $H_0$ ) and forms a coating bead and is bound by two liquid-gas interfaces. Clearly, physics sets the operating parameters at which this flow exists which can be modelled. Understanding all of the physical parameters

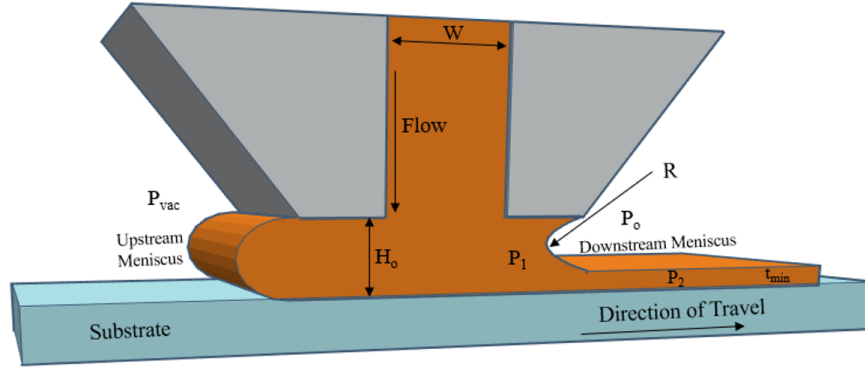


Figure 1.12: Slot-die coating head schematic where  $W$  is the width of the feed slot,  $H_o$  is the head-substrate gap,  $t_{min}$  is the minimum wet film thickness and  $R$  is radius of the curvature of the downstream meniscus.

involved in modelling a slot-die coating process is difficult, and beyond the scope of this work, however, simpler models such as the viscocapillary model can be used as a good estimation of coating stability [114].

A highly important limit in slot-die coating is the low flow limit, which corresponds to the maximum coating speed possible for a desired coating thickness, or the minimum film thickness at a given web speed at which a coating should be stable. This low flow limit can be determined using the viscocapillary model which relates the capillary number and the head-substrate gap ( $H_o$ ). The minimum film thickness ( $t_{min}$ ) is determined by the maximum pressure gradient possible at the downstream meniscus and is approximated from the radius of the downstream meniscus ( $R$ ), and the surface tension of the ink ( $\sigma$ ):

$$P_o - P_1 = \frac{\sigma}{R} \quad (1.4)$$

With  $R$  being determined by:

$$R = \frac{H_o - t_{min}}{2} \quad (1.5)$$

And the capillary number defined as:

$$Ca = \frac{\mu V}{\sigma} \quad (1.6)$$

Where  $\mu$  is the viscosity of the ink and  $V$  the velocity of the substrate. Combining the capillary number with equation 1.4 and equation 1.5 allows relation of the minimum wet film thickness ( $t_{min}$ ):

$$Ca = 0.65 \left( \frac{2}{\frac{H_o}{t_{min}} - 1} \right)^{\frac{3}{2}} \quad (1.7)$$

Plotting the capillary number against  $H_o/t_{min}$  (also known as the "dimensionless gap") shows the maximum stable coating speed possible for a given wet film thickness of an ink with a set gap height. An example of the viscocapillary model is given in Figure 1.13.

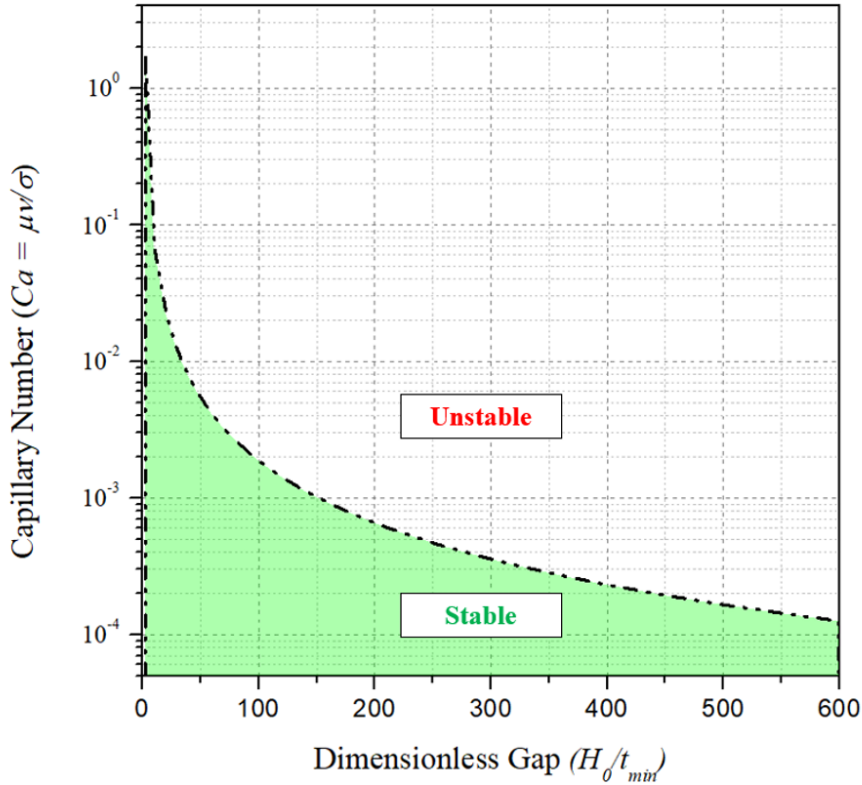


Figure 1.13: Example viscocapillary model showing the stable region (Green) and the unstable region (Red).

The area shaded green represents the “stable” coating area and crossing the line in a coating experiment would lead to unstable coatings with defects such as rivulets a common problem. Clearly, the viscocapillary model shows that the minimum possible coating thickness increases as the viscocapillary number increases. This means that the faster the coating speed, the thicker the minimum thickness becomes. Manipulation of the ink fluid properties can also lead to a change in the capillary number, where process engineering of an unstable ink can lead to stable coatings, whether by solvent engineering or by the addition of binders or surfactants to the ink.

A noteworthy mention is that the viscocapillary model is only valid at low capillary numbers, typically low speed coating or a low viscosity of the ink. However, inks used in the deposition of the layers in a perovskite device are usually of low viscosity so the viscocapillary

model should be applicable.

### 1.5.2 Scale up of N-I-P architectures

Although a large number of publications have been written on the use of slot-die coating for N-I-P perovskite devices, the majority have been on glass and employed high sintering/annealing temperatures or used highly toxic solvents such as DMF [29, 115, 103, 105, 106]. These methods have been useful to confirm that slot-die coating is a promising deposition method for industrial scale manufacture realisation. However, this section will focus on low-temperature ETL and HTLs, in order to illustrate roll to roll and flexible substrate compatibility.

Most papers published currently employ the P-I-N structure due to the difficulty in printing the HTL on top of the perovskite layer due to lack of uniformity and poor morphology [116]. There are however, a small number of reports on R2R slot-die coated N-I-P device stacks.

Although  $\text{TiO}_2$  is arguably the most popular ETL in the literature, low-temperature R2R deposition has to the best of my knowledge not been yet realised. Hossain et al have reported the use of slot-die coated  $\text{TiO}_2$  nanoparticles processed at  $100\text{ }^\circ\text{C}$  and achieving an efficiency of 15.7% but were manufactured on glass substrates [31].

As discussed in Section 1.4.4,  $\text{SnO}_2$  is a popular ETL and at the time of writing appears to be the most promising candidate for R2R deposition. Dou et al reported a R2R coated  $\text{SnO}_2$  ETL and perovskite layer achieving a PCE of 14.7% (with the rest of the device stack spin-coated), however this was on a flexible glass substrate and they opted to use a  $\text{Sn}(\text{OCH}(\text{CH}_3)_2)_4$  in IPA solution to avoid wettability problems. The temperature used to anneal the tin oxide precursor was not included, but was expected to be higher than  $150\text{ }^\circ\text{C}$  [117]. Also R2R coated was a  $\text{MAPbI}_3$  layer utilising a non-toxic solvent system of methylamine (MA) and acetonitrile (ACN), leading to a highly-crystalline perovskite film.

Papers by Bu et al [118] and Galagan et al [119] have accomplished R2R compatible deposition of  $\text{SnO}_2$  ETLs in an n-i-p architecture, both employing the same nanoparticle suspension from Alfa Aesar. Bu et al used the nanoparticle suspension and diluted using  $\text{H}_2\text{O}$  and IPA in a 1:1 ratio with a final concentration of about 10 mg/mL.  $\text{SnO}_2$  was then slot-die coated using a benchtop coater onto flexible PET/ITO substrates for three cycles, subsequently annealing for 1 hour at  $140\text{ }^\circ\text{C}$ . The remainder of the device stack was spin-coated with a champion efficiency of 15.22% confirming the suitability of the nanoparticles for a low-temperature, roll-to-roll compatible ETL. However, although the annealing temperature was low, the length at which

it was carried out (1 hour) is far too long for industrial scale and would require an immensely long oven if it were to be coated at industrial speeds. In addition to this, although feasible, coating the layer three times would introduce a large bottleneck in processing time, with one layer being much more suitable. Nonetheless, with some process engineering, the coating and annealing times should be possible to reduce.

Galagan et al reported R2R slot-die coated perovskite devices on PET/ITO substrates, with the ETL ( $\text{SnO}_2$ ) and perovskite layers deposited in ambient atmosphere, with non toxic industrially compatible solvents, achieving a best PCE of 13.5% [119]. This paper mainly focused on the deposition of the perovskite layer itself, and was achieved using a mixed cation and halide perovskite ( $\text{Cs}_{0.15}\text{FA}_{0.85}\text{PbI}_{3-x}\text{Br}_x$ ) in a mixture of DMSO and 2-butoxyethanol. With regards to the  $\text{SnO}_2$  itself, an Alfa Aesar colloidal suspension of  $\text{SnO}_2$  nanoparticles was used and diluted with 10 volume% 1-butanol to aid in wetting. This was then slot-die coated in a R2R coater at a speed of 5 m/min, with subsequent drying at 140 °C in a 20 m long oven at the same speed, giving an overall residence time of 4 minutes. The remainder of the device was spin-coated offline with evaporated contacts, achieving a maximum PCE of 15.2% in the reverse direction (13.5% stabilised). This paper is a good example of the potential for roll-to-roll coated n-i-p perovskite devices with low-temperature and low-toxicity processes. The set-up that Galagan et al used is shown in figure 1.14.



Figure 1.14: Photograph of the R2R coating setup used in Galagan et al's work [119]

Slot-die coated Zinc Oxide ( $\text{ZnO}$ ) layers have been widely used in organic photovoltaic devices [120]. Hwang K et al. used this knowledge and made a fully R2R coated perovskite device, apart from evaporated contacts, using a  $\text{ZnO}$  nanoparticle solution made in house [121]. No difference was noted when comparing the slot-die coated zinc oxide to the spin coated equivalent. Slot-die coated zinc oxide layers required a relatively short drying time of 10 minutes at 120 °C, demonstrating compatibility with a R2R processes on temperature sensitive



substrates. However, zinc oxide has been reported on numerous occasions to cause stability problems with perovskite devices and induce rapid degradation of the perovskite layer. It is well reported that thermal annealing of perovskite on top of ZnO causes the perovskite to decompose and is due to the basic properties of the ZnO, causing deprotonation of the methyl ammonium cations. Krebs et al. also used low-temperature (110 °C) dried, slot-die coated ZnO on flexible ITO coated PET substrates with n-i-p device stack, with a PCBM interlayer between the ZnO and perovskite [122]. Krebs et al. also found that annealing the perovskite precursor on top of the ZnO caused issues with perovskite formation, and overcame this by using a two-step perovskite deposition, which gave a champion efficiency of 2.6%. Although the device performance is relatively low due to the use of a printed top electrode, it does demonstrate the compatibility of ZnO in a R2R compatible process. In addition to this, they demonstrated full R2R compatibility of all of the layers in the device stack, whereas in the majority of other publications the films post perovskite are spin-coated. It must be noted that the printed electrodes were screen printed on a S2S basis, but does demonstrate the compatibility for a R2R coating should a rotary screen printer or similar be employed. The instability of ZnO based devices can, to an extent, be reduced by depositing the ZnO on top of the perovskite, usually using a nanoparticle formulation, firstly by negating the need for thermal annealing of the perovskite on the ZnO surface, and secondly as ZnO has a strong resistance to oxygen and humidity [123].

Throughout the literature on R2R coated n-i-p architectures there is a common theme in that the HTL is almost always spin-coated. This is due to difficulties in film morphology, however, Burkitt et al reported the slot-die coating of a spiro-OMeTAD HTL layer in a n-i-p architecture (albeit, this included glass substrates and a high-temperature annealed TiO<sub>2</sub> ETL), replacing the common chlorobenzene solvent with a lower toxicity toluene [29]. A champion efficiency of 11.99% was achieved, however, a large spread in data was present suggesting poor film morphology. Overcoming the issues with the HTL deposition is paramount for R2R n-i-p architectures to be realised.

### **1.5.3 Scale up of P-I-N structures**

Roll-to-roll coating of p-i-n architectures has become more common in the literature compared with n-i-p due to the more compatible HTLs. PEDOT:PSS is perhaps the most prevalent layer employed which has been well documented in organic photovoltaics, due to its good flexibility, high transparency, tuneable conductivity and easy solution processing [124, 125].

In 2017, Ciro et al reported a low-temperature, R2R compatible p-i-n device architecture using a PEDOT:PSS HTL deposited by slot-die coating in ambient conditions. All of the layers in the device stack consisting of: PET/ITO/PEDOT:PSS/MAPbI<sub>3-x</sub>Cl<sub>x</sub>/PCBM/Ag were slot-die coated, apart from the evaporated silver electrode [126]. A low champion efficiency of 2.9% was achieved, but paved the way for p-i-n structures to be realised, and much higher efficiencies are now being accomplished. Schmidt et al also reported a R2R compatible p-i-n structure using PEDOT:PSS as the HTL, managing a respectable champion efficiency of 4.9%. More importantly, Schmidt et al slot-die coated all of the layers in the stack consisting of: PET/ITO/PEDOT:PSS/CH<sub>3</sub>NH<sub>3</sub>PbI<sub>3-x</sub>PbCl<sub>x</sub>/PCBM/ZnO/Ag, apart from the silver electrode which was screen printed [122].

Sears et al used a slot-die coated PEDOT:PSS layer on flexible PET substrates with a champion efficiency of 11% [127]. This group focused on replacing the ITO electrode with slot-die coated silver nanowires, followed by slot-die coated PEDOT:PSS, with the remainder of the device spin-coated. The Ag nanowire electrode was incredibly robust, showing a negligible change in efficiency after 10000 compressive bending tests to a 5 mm radius.

Further work on R2R p-i-n structures employing PEDOT:PSS have shown a great rise in efficiency, with Burkitt et al producing a large area, R2R coated PEDOT:PSS HTL and perovskite layer (two-step) on a PET/ITO substrate, with a champion efficiency of 9.4% (rest of device stack spin-coated). The spread in efficiency data was, however, sporadic owing to poor film morphology of the perovskite layer and damage to the PET on drying of the lead iodide layer (Figure 1.15) [128].

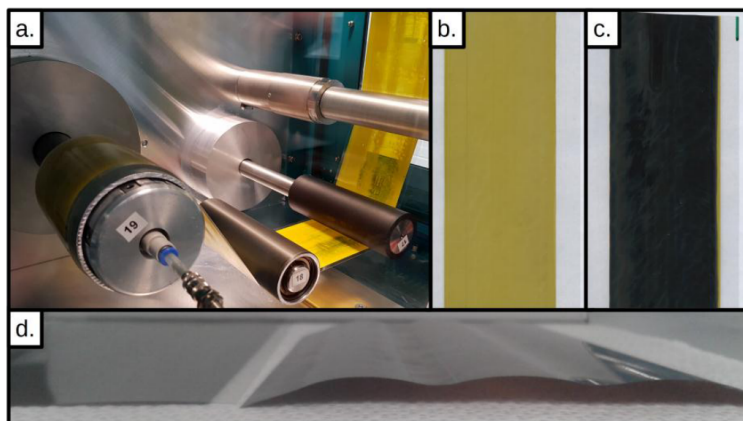


Figure 1.15: Photograph of the R2R coating of a two-step perovskite film used in work by Burkitt et al [128]

2020 saw another publication from Burkitt et al improving upon their results in 2018 [129].

In this paper, an ACN based, single-step perovskite layer was used which when coupled with an  $N_2$  air knife allows fast drying and annealing of the film leading to excellent morphology. An overall device architecture of PET/ITO/PEDOT:PSS/PSK/PCBM/BCP/Ag was used, in which every layer was R2R slot-die coated apart from the evaporated silver electrode. A champion stabilised PCE of 12.2% was demonstrated, which at the time of writing is the highest reported for a device with all layers R2R coated apart from the top electrode. Firstly, the PEDOT:PSS layer was coated onto a PET/ITO substrate and corona surface treatment was used to aid in the wetting of the film and overall film morphology. For the perovskite layer, a  $CH_3NH_3PbI_3$  was made using an acetonitrile/methylamine solvent mixture with a HCl additive, and an air knife to control solvent evaporation and film uniformity. Perovskite films were slot-die coated onto the PEDOT:PSS film at 1 m/min and dried in an in-line oven at 122 °C with an overall residence time of 1 minute. PCBM was then slot-die coated at the same speed, and the typical chlorobenzene solvent replaced with a mixture of toluene and methylanisole to aid in deposition and film formation. Finally BCP was slot-die coated at 1 m/min in ethanol and silver electrodes evaporated on top. A schematic of the set up used in this work is presented in Figure 1.16

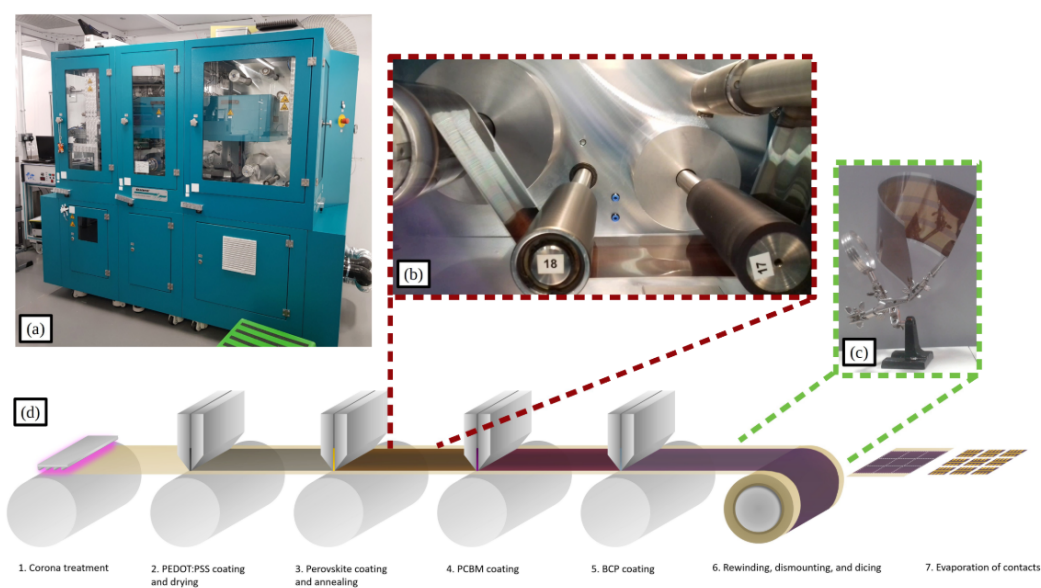


Figure 1.16: Schematic of the R2R coating set up used in Burkitt et al's slot-die coated p-i-n device architecture [129]

This work confirms the potential of R2R coated perovskite devices at low-temperature using low-toxicity solvents. Although good efficiencies were recorded, the replacement of PEDOT:PSS is the next challenge due to its poor stability. Replacement with more stable metal oxides such as NiOx, has been realised on small scale spin-coated flexible devices as discussed

in section 1.4.6, however, there is only one report to date on the R2R deposition of NiOx in a perovskite device. A conference proceeding report from Giacomo et al stated that R2R slot-die coating of p-i-n modules including a NiOx HTL was achieved on flexible substrates with efficiencies up to 16% [130]. Unfortunately no indication of the NiOx precursor was included, nor the annealing conditions.

Huang et al reported a slot-die coated NiOx layer on glass substrates in which they thermally annealed a nickel acetate tetrahydrate precursor using NIR [131], also replacing the common toxic 2-methoxyethanol solvent with ethanol and Tetramethylammonium hydroxide (TMAOH). This could potentially be processed on flexible substrates using NIR, but the temperature for conversion of the precursor into NiOx requires temperatures over 300 °C and would most likely damage any flexible substrates.

## 1.6 Perovskite Solar Cell Characterisation

### 1.6.1 Current-Voltage Measurements

The most fundamental characterisation technique for a perovskite solar cell is the Current-voltage measurement (J-V sweep), which is a measurement that shows the efficiency of a device. This testing procedure is a standardised technique which allows comparison of devices manufactured in different companies and laboratories. This measurement applies a sweeping voltage bias to the solar cell whilst simultaneously measuring the current output when the cell is exposed to a light source with known intensity. The standardised light intensity is 1000  $\text{Wm}^{-2}$  (“1 Sun” of illumination) in which the spectral characteristics conform to ASTM G173-03, also referred to as AM1.5G (Air Mass 1.5 Global). Cell temperature must also be 25 °C. A Schematic illustration of a typical solar simulation unit is shown in Figure 1.17.

Light sources are usually a xenon arc lamp with filters installed to irradiate at the standard AM1.5G spectrum. AM1.5G is set to closely represent sunlight, with the intensity and spectrum used set as a standard for all solar cell device testing. The spectral characteristics of AM1.5G is shown in Figure 1.18.

Complete replication of AM1.5G on samples is difficult, and calibration of the light source is achieved by a calibration cell prior to device testing.

Whilst testing a device, a J-V curve is plotted with voltage on the x-axis and the current produced on the y-axis. Figure 1.19 shows a typical J-V curve for a perovskite solar cell which

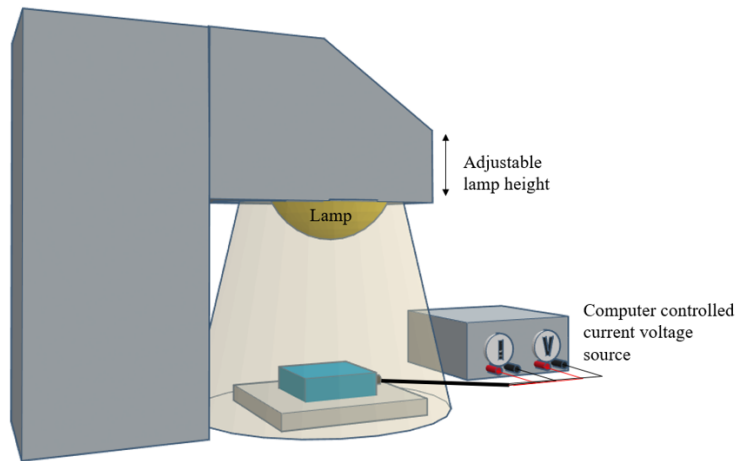


Figure 1.17: Schematic of a simple solar J-V testing rig. The current and voltage are measured separately to overcome contact resistance issues.

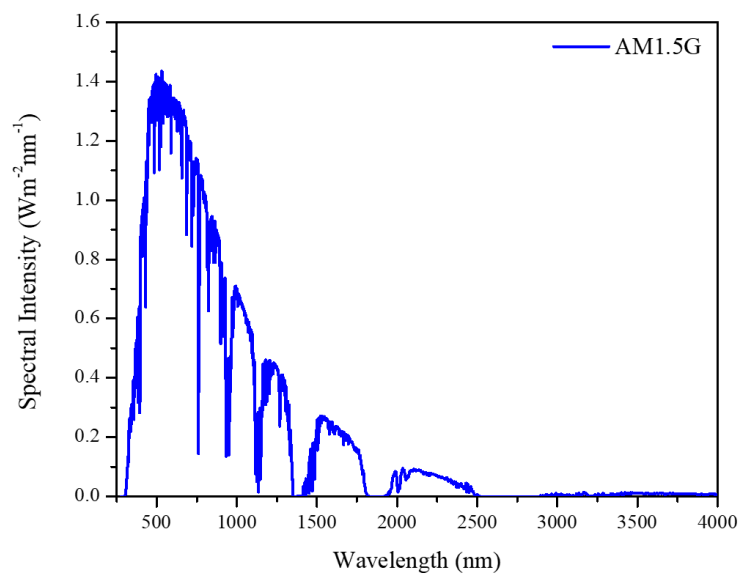


Figure 1.18: Spectral characteristics of AM1.5G.

contains some useful information about the device:

- VOC refers to the “Open Circuit Voltage” which is the voltage measured when the current is zero.
- ISC is the “Short Circuit Current” and is the maximum current from a device and occurs when the voltage across the device is zero.
- P<sub>MAX</sub> is the point at which the power output of the cell is at maximum power. And is calculated via Equation 1.8.

$$P_{\text{MAX}} = I_{\text{MAX}} * V_{\text{MAX}} \quad (1.8)$$

The Fill Factor (FF) is a common parameter used and is a measure of the maximum power from a solar cell and is defined as the ratio of maximum power from the cell to the product of  $V_{OC}$  and  $I_{SC}$  and is calculated as follows:

$$FF = \frac{P_{MAX}}{V_{OC} * I_{SC}} \quad (1.9)$$

The solar cells ability to turn sunlight into useable electricity is defined by its Power Conversion Efficiency (PCE). The PCE is determined from equation 1.10 and determined by the fraction of incident power which is converted to electricity.

$$PCE = \frac{V_{OC} * I_{SC} * FF}{P_{in}} \quad (1.10)$$

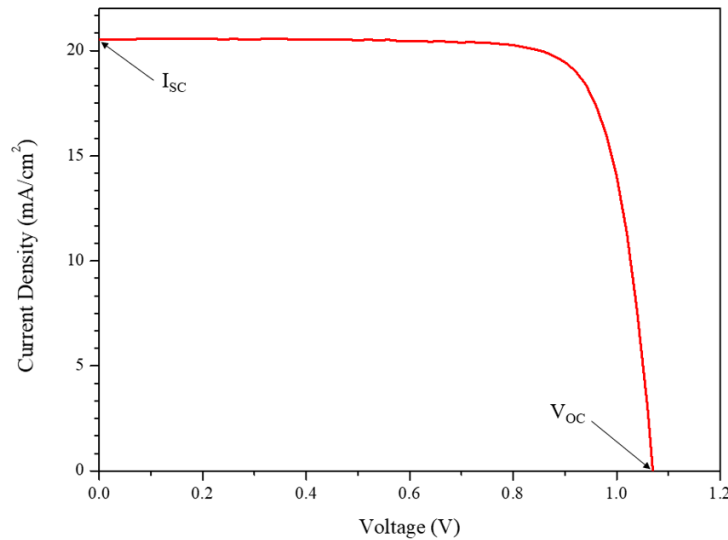


Figure 1.19: A typical J-V curve for a perovskite solar cell.

## 1.6.2 The Ideality Factor

As discussed in Section 1.3.4 A solar cell can be considered a diode in parallel with a current source, with two resistors representing series and shunt resistances. If the solar cell is not illuminated it will not produce a current and a “dark” current scan shows the cell acting as a diode. A measure of how closely a diode follows the ideal diode equation is named the “ideality factor” with the ideal diode equation shown in Equation 1.11. Where  $I_0$  is the reverse saturation current (A),  $q$  is the elementary charge,  $V$  is the voltage (V),  $n$  is the ideality factor,  $k$  is the Boltzmann constant with a value of  $1.38 \times 10^{-23}$ , and  $T$  is the device temperature (K).

$$I = I_0 \left[ \exp\left(\frac{qV}{nKT}\right) - 1 \right] \quad (1.11)$$

The ideal diode equation assumes that all recombination reactions occur via band to band recombination via traps in the bulk of the device. This leads to the ideality factor being one. A plot of the ideal diode equation where  $n=1$  can be seen in Figure 1.20.

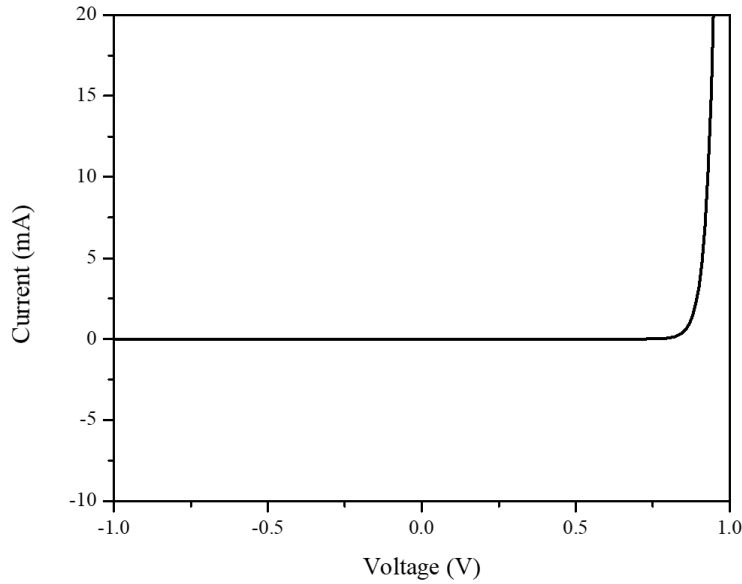


Figure 1.20: Ideal Current-Voltage diode curve.

However, the diode equation for a solar cell is more complex than the ideal diode where the photogenerated current ( $I_L$ ) must be included and is shown in Equation 1.12

$$I = I_0 \left[ \exp\left(\frac{qV}{nKT}\right) - 1 \right] - I_L \quad (1.12)$$

Plotting the curve from Equation 1.12 where the cell is illuminated and producing a photo-generated current of 5 mA produces a plot as shown in Figure 1.21.

When reporting J-V curves of perovskite solar cells, the consensus is to flip the current axis which is achieved by modifying Equation 1.12 to Equation 1.13.

$$I = I_L - I_0 \left[ \exp\left(\frac{qV}{nKT}\right) - 1 \right] \quad (1.13)$$

The plot in Figure 1.21 shows an ideal PV cell, however, in reality this is not true with shunt and series resistances effecting the overall J-V curve. Inputting these two resistances to the diode equation leads to Equation 1.14

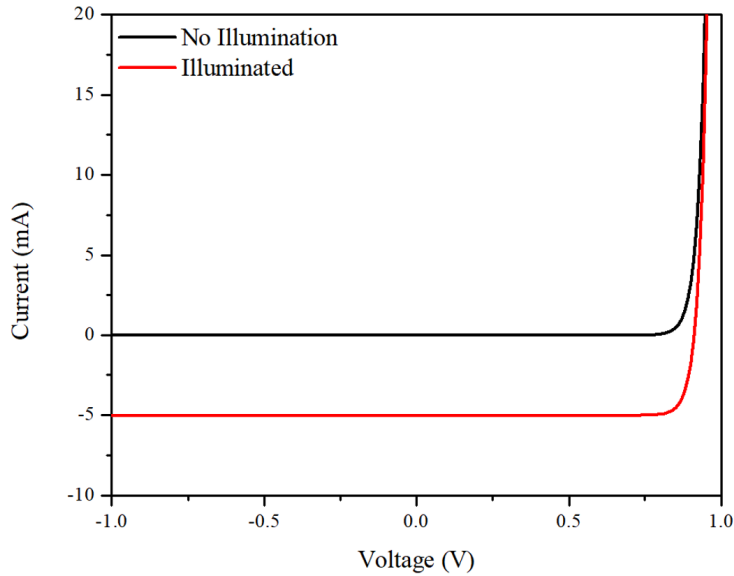


Figure 1.21: Example J-V curve of a solar cell with no illumination (black) and under illumination (Red).

$$I = I_L - I_0 \left[ \exp\left(\frac{q(V + IR_{\text{series}})}{nkT}\right) - \frac{V + IR_{\text{series}}}{R_{\text{shunt}}}\right] \quad (1.14)$$

The effect series and shunt resistances have on the J-V curve is demonstrated in Figure 1.22.

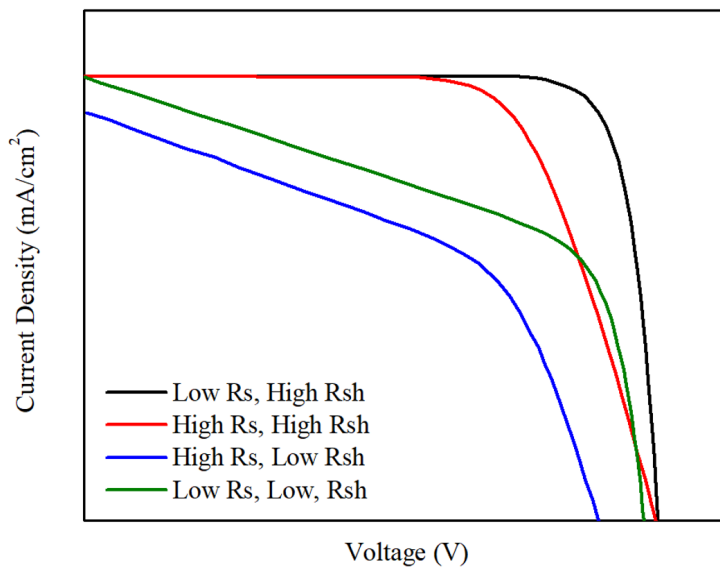


Figure 1.22: Example current-density plots demonstrating the effect that series and shunt resistances have on the curve.

As Figure 1.22 shows, a decrease in the cells shunt resistance, or an increase in its series resistance leads to a drop in fill factor, thus the devices overall efficiency. Decreases in shunt resistances can originate from pinholes in the device layers or short-circuiting of the device by



means of unwanted contact between layers. Increase in series resistances are usually due to low conductivity of electron or hole transport layers, whether it's down to the intrinsic nature of the material or the film being too thick, or the electrode conductivity may be too low. Ideally, a solar cell should have high shunt resistance and low series resistance.

### 1.6.3 Hysteresis

Hysteresis is a term used when there is a difference in the solar cell performance between forward and reverse scans, and this makes it difficult to authenticate the real performance of the cell. Figure 1.23 shows a J-V curve for a perovskite solar cell exhibiting severe hysteresis.

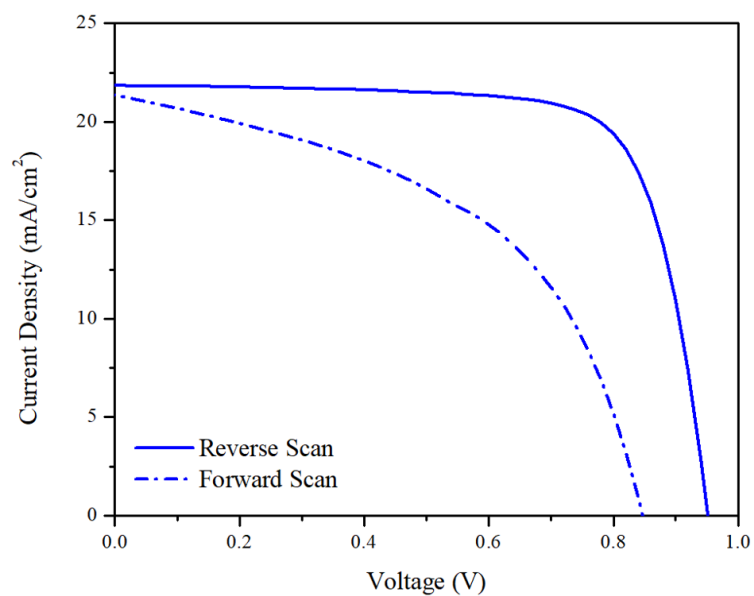


Figure 1.23: J-V curve of a perovskite solar cell exhibiting hysteresis.

It is clear from the J-V curve that upon scanning in the forward direction ( $J_{SC}$  to  $V_{OC}$ ), the J-V curve differs significantly compared to the reverse scan direction ( $V_{OC}$  to  $J_{SC}$ ). This leads to a drop in fill factor and  $V_{OC}$ , and appears to suffer from lower shunt resistance and higher series resistance, inevitably having a lower efficiency. Many factors can cause hysteresis in perovskite devices which include; cell architecture, materials used and cell testing conditions [132].

Generally, mesoporous based devices exhibit less hysteresis compared to planar architectures which can be attributed to the larger surface area and more efficient charge extraction. When comparing a  $TiO_2$  based device with and without a mesoporous layer, hysteresis is much more prevalent in the device without the mesoporous layer. Interestingly, n-i-p architectures show a much higher degree of hysteresis than p-i-n structures, which shows that selection of

the cell architecture plays a factor in achieving hysteresis free devices.

With respect to the materials used, these can all effect the hysteresis in a perovskite device, for example, the crystal sizes in the perovskite layer can improve hysteresis [132]. Also, the thickness of a mesoporous TiO<sub>2</sub> layer can lead to hysteresis, where optimisation of the thickness of a mp-TiO<sub>2</sub> layer by Snaith et al showed a 440nm lead to the smallest amount of hysteresis compared to 220 and 750 nm [133]. Thicknesses of the ETL itself also leads to changes in hysteresis so engineering of layer thicknesses is an important factor. The interface between the charge transport layers and the perovskite layer, as well as the electrodes can have a detrimental effect on the hysteresis as the charge separation at the interfaces depend strongly on the interfaces.

Finally, the cell testing conditions, namely the scan rates can alter the hysteresis. Generally, in planar architectures a slower scan rate leads to higher degrees of hysteresis, however for mp-TiO<sub>2</sub> based devices this seems to be the opposite with slower scan rates reducing the hysteresis.

All these effects on the hysteresis make it difficult to determine the true efficiency of a device, especially as there is no standard measuring procedure with respect to scan rates, light soaking times etc. Scans at very low speeds should eventually match in the forwards and reverse directions, however, this leads to scans taking many minutes and testing a whole batch of cells very laborious. To overcome this, stabilised current measurements are taken for best performing cells to get a more accurate reading of the device's efficiency. This involves holding the device at a particular voltage (usually the  $V_{mp}$  of the scan in one direction) and monitoring the current output over time. Normally the current will start at a high value and stabilise at a lower level as seen in Figure 1.24 This method is a more standardised way of determining a "hero" cell performance.

## 1.7 Conclusion

In conclusion, promising progress has been made on the road to industrial scale manufacturing techniques for HTL and ETLs. However, many issues must still be overcome such as lower temperature annealing processes for plastic substrate compatibility and further clarification of the viscopillary model.

Slot die coating was used in this work to demonstrate the compatibility of the process for use in large scale manufacture on flexible substrates and good quality, low temperature ETL

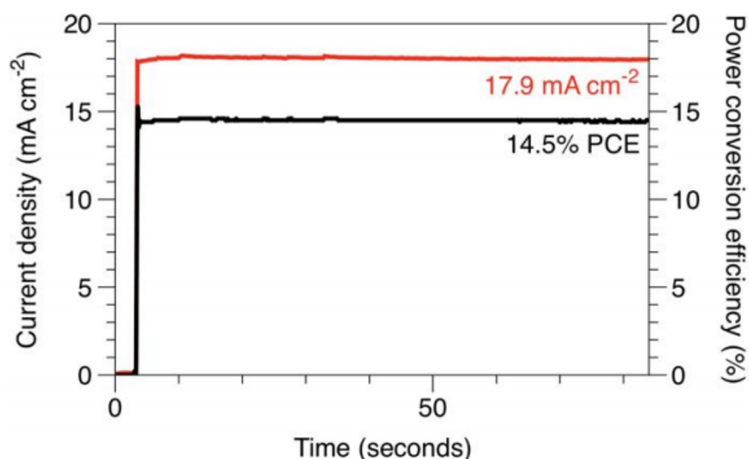


Figure 1.24: Example of a stabilised current measurement for a perovskite solar cell [134]

and HTLs were deposited with excellent reproducibility.

Although the viscocapillary model appears to be an excellent way to predict the coating stability when using slot-die coating, no publication has been made on its validation. In this work the viscocapillary models accuracy was confirmed by experimental procedures validating the coating quality when inks were said to be in the stable and unstable regions.

## 1.8 References

- [1] David L. Chandler. “Vast amounts of solar energy radiate to the Earth”. In: *Phys.org* October (2011), pp. 1–3. URL: <http://news.mit.edu/2011/energy-scale-part3-1026>.
- [2] P. C. Reshmi Varma. *Low-dimensional perovskites*. Elsevier Inc., 2018, pp. 197–229. ISBN: 9780128129159. DOI: 10.1016/B978-0-12-812915-9.00007-1. URL: <http://dx.doi.org/10.1016/B978-0-12-812915-9.00007-1>.
- [3] Xiangye Liu et al. “Organic-inorganic halide perovskite based solar cells-revolutionary progress in photovoltaics”. In: *Inorganic Chemistry Frontiers* 2.4 (2015), pp. 315–335. ISSN: 20521553. DOI: 10.1039/c4qi00163j.
- [4] E C S Meeting Abstracts. “Novel Photoelectrochemical Cell with Mesoscopic Electrodes Sensitized by Lead-halide Compounds (11)”. In: *ECS Meeting Abstracts* 2 (2008). DOI: 10.1149/ma2008-02/1/27.

- [5] Akihiro Kojima et al. “Organometal halide perovskites as visible-light sensitizers for photovoltaic cells”. In: *Journal of the American Chemical Society* 131.17 (May 2009), pp. 6050–6051. ISSN: 00027863. DOI: 10.1021/ja809598r.
- [6] Jeong Hyeok Im et al. “6.5% Efficient Perovskite Quantum-Dot-Sensitized Solar Cell”. In: *Nanoscale* 3.10 (2011), pp. 4088–4093. ISSN: 20403364. DOI: 10.1039/c1nr10867k.
- [7] Hui Seon Kim et al. “Lead iodide perovskite sensitized all-solid-state submicron thin film mesoscopic solar cell with efficiency exceeding 9%”. In: *Scientific Reports* 2 (2012), pp. 1–7. ISSN: 20452322. DOI: 10.1038/srep00591.
- [8] Michael M. Lee et al. “Efficient Hybrid Solar Cells Based on Meso-Superstructured Organometal Halide Perovskites”. In: 338.November (2012), pp. 643–648.
- [9] *Best Research-Cell Efficiencies*. URL: <https://www.nrel.gov/pv/insights/assets/pdfs/cell-pv-eff-emergingpv.20200406.pdf>.
- [10] John Singleton. *Band theory and electronic properties of solids*. Oxford University Press, 2001, p. 222. ISBN: 0198506449.
- [11] *DoITPoMS - TLP Library Introduction to Semiconductors - Direct and Indirect Band Gap Semiconductors*.
- [12] Jiangzhao Chen and Nam Gyu Park. “Causes and Solutions of Recombination in Perovskite Solar Cells”. In: *Advanced Materials* 31.47 (2019), pp. 1–56. ISSN: 15214095. DOI: 10.1002/adma.201803019.
- [13] Xie Zhang et al. “First-Principles Analysis of Radiative Recombination in Lead-Halide Perovskites”. In: *ACS Energy Letters* 3.10 (2018), pp. 2329–2334. ISSN: 23808195. DOI: 10.1021/acsenergylett.8b01297.
- [14] Luis M. Pazos-Outón, T. Patrick Xiao, and Eli Yablonovitch. “Fundamental Efficiency Limit of Lead Iodide Perovskite Solar Cells”. In: *Journal of Physical Chemistry Letters* 9.7 (2018), pp. 1703–1711. ISSN: 19487185. DOI: 10.1021/acs.jpcllett.7b03054.
- [15] *Intrinsic Semiconductors*. URL: <http://hyperphysics.phy-astr.gsu.edu/hbase/Solids/intrin.html>.

- [16] Roberto Hernandez Sampieri. *Extrinsic semiconductors*, p. 634. ISBN: 9783540773405. URL: [https://batch.libretexts.org/print/url=https://eng.libretexts.org/Bookshelves/Materials\\_Science/Supplemental\\_Modules\\_\(Materials\\_Science\)/Semiconductors/Extrinsic\\_Semiconductors.pdf](https://batch.libretexts.org/print/url=https://eng.libretexts.org/Bookshelves/Materials_Science/Supplemental_Modules_(Materials_Science)/Semiconductors/Extrinsic_Semiconductors.pdf).
- [17] *Electrons and holes in a semiconductor*. 2014, pp. 1–49. ISBN: 9781782422242. DOI: 10.1533/9781782422242.1.
- [18] Haiping He. *Metal oxide semiconductors and conductors*. Elsevier Inc., 2020, pp. 7–30. ISBN: 9780128149300. DOI: 10.1016/b978-0-12-814930-0.00002-5. URL: <http://dx.doi.org/10.1016/B978-0-12-814930-0/00002-5>.
- [19] Jong H. Kim et al. “High-performance and environmentally stable planar heterojunction perovskite solar cells based on a solution-processed copper-doped nickel oxide hole-transporting layer”. In: *Advanced Materials* 27.4 (2015), pp. 695–701. ISSN: 15214095. DOI: 10.1002/adma.201404189.
- [20] Weijun Ke et al. “Perovskite solar cell with an efficient TiO<sub>2</sub> compact film”. In: *ACS Applied Materials and Interfaces* 6.18 (2014), pp. 15959–15965. ISSN: 19448252. DOI: 10.1021/am503728d.
- [21] Jianqiang Qin et al. “The optimum titanium precursor of fabricating TiO<sub>2</sub> compact layer for perovskite solar cells”. In: *Nanoscale Research Letters* 12.1 (2017). ISSN: 1556276X. DOI: 10.1186/s11671-017-2418-9.
- [22] Yan Li et al. “Over 20% Efficiency in Methylammonium Lead Iodide Perovskite Solar Cells with Enhanced Stability via “in Situ Solidification” of the TiO<sub>2</sub> Compact Layer”. In: *ACS Applied Materials and Interfaces* 12.6 (2020), pp. 7135–7143. ISSN: 19448252. DOI: 10.1021/acscami.9b19153.
- [23] Aibin Huang et al. “One step spray-coated TiO<sub>2</sub> electron-transport layers for decent perovskite solar cells on large and flexible substrates”. In: *Nanotechnology* 28.1 (2017). ISSN: 13616528. DOI: 10.1088/0957-4484/28/1/01LT02.
- [24] Peng Zhou et al. “Ultrasonic spray-coating of large-scale TiO<sub>2</sub> compact layer for efficient flexible perovskite solar cells”. In: *Micromachines* 8.2 (2017), pp. 1–12. ISSN: 2072666X. DOI: 10.3390/mi8020055.

- [25] Paola Vivo et al. “Influence of TiO<sub>2</sub> compact layer precursor on the performance of perovskite solar cells”. In: *Organic Electronics* 41 (2017), pp. 287–293. ISSN: 15661199. DOI: 10.1016/j.orgel.2016.11.017.
- [26] Inyoung Jeong et al. “Solution-Processed Ultrathin TiO<sub>2</sub> Compact Layer Hybridized with Mesoporous TiO<sub>2</sub> for High-Performance Perovskite Solar Cells”. In: *ACS Applied Materials and Interfaces* 9.42 (2017), pp. 36865–36874. ISSN: 19448252. DOI: 10.1021/acsami.7b11901.
- [27] Takeo Oku et al. “Fabrication and characterization of perovskite photovoltaic devices with TiO<sub>2</sub> nanoparticle layers”. In: *AIP Conference Proceedings* 1807. January (2017). ISSN: 15517616. DOI: 10.1063/1.4974796.
- [28] In Soo Kim et al. “Amorphous TiO<sub>2</sub> Compact Layers via ALD for Planar Halide Perovskite Photovoltaics”. In: *ACS Applied Materials and Interfaces* 8.37 (2016), pp. 24310–24314. ISSN: 19448252. DOI: 10.1021/acsami.6b07658.
- [29] Daniel Burkitt, Justin Searle, and Trystan Watson. “Perovskite solar cells in N-I-P structure with four slot-die-coated layers”. In: *Royal Society Open Science* 5.5 (2018). ISSN: 20545703. DOI: 10.1098/rsos.172158.
- [30] B. Conings et al. “An easy-to-fabricate low-temperature TiO<sub>2</sub> electron collection layer for high efficiency planar heterojunction perovskite solar cells”. In: *APL Materials* 2.8 (2014). ISSN: 2166532X. DOI: 10.1063/1.4890245.
- [31] Ihtez M. Hossain et al. “Scalable processing of low-temperature TiO<sub>2</sub> nanoparticles for high-efficiency perovskite solar cells”. In: *ACS Applied Energy Materials* 2.1 (2019), pp. 47–58. ISSN: 25740962. DOI: 10.1021/acsaem.8b01567.
- [32] Md Shahiduzzaman et al. “Low-Temperature-Processed Brookite-Based TiO<sub>2</sub> Heterophase Junction Enhances Performance of Planar Perovskite Solar Cells”. In: *Nano Letters* (2019). ISSN: 15306992. DOI: 10.1021/acs.nanolett.8b04744.
- [33] Dong Wei et al. “A TiO<sub>2</sub> embedded structure for perovskite solar cells with anomalous grain growth and effective electron extraction”. In: *Journal of Materials Chemistry A* (2017). ISSN: 20507496. DOI: 10.1039/c6ta10418e.

- [34] Peng Chen et al. “TiO<sub>2</sub> nanoparticle-based electron transport layer with improved wettability for efficient planar-heterojunction perovskite solar cell”. In: *Journal of Energy Chemistry* (2015). ISSN: 20954956. DOI: 10.1016/j.jechem.2015.10.014.
- [35] Sanjib Das et al. “Low thermal budget, photonic-cured compact TiO<sub>2</sub> layers for high-efficiency perovskite solar cells”. In: *Journal of Materials Chemistry A* (2016). ISSN: 20507496. DOI: 10.1039/c6ta02105k.
- [36] Joel Troughton et al. “Photonic flash-annealing of lead halide perovskite solar cells in 1 ms”. In: *Journal of Materials Chemistry A* 4.9 (2016), pp. 3471–3476. ISSN: 20507496. DOI: 10.1039/c5ta09431c.
- [37] Ji Hye Kwak et al. “Back-irradiation photonic sintering for defect-free high-conductivity metal patterns on transparent plastic”. In: *Applied Physics Letters* (2018). ISSN: 00036951. DOI: 10.1063/1.5022847.
- [38] Yonghui Lee et al. “Efficient Planar Perovskite Solar Cells Using Passivated Tin Oxide as an Electron Transport Layer”. In: *Advanced Science* 5.6 (2018), pp. 1–6. ISSN: 21983844. DOI: 10.1002/advs.201800130.
- [39] Yi Li et al. “Mesoporous SnO<sub>2</sub> nanoparticle films as electron-transporting material in perovskite solar cells”. In: *RSC Advances* 5.36 (2015), pp. 28424–28429. ISSN: 20462069. DOI: 10.1039/c5ra01540e.
- [40] Qingshun Dong et al. “Insight into perovskite solar cells based on SnO<sub>2</sub> compact electron-selective layer”. In: *Journal of Physical Chemistry C* 119.19 (2015), pp. 10212–10217. ISSN: 19327455. DOI: 10.1021/acs.jpcc.5b00541.
- [41] Hua Shang Rao et al. “Improving the Extraction of Photogenerated Electrons with SnO<sub>2</sub> Nanocolloids for Efficient Planar Perovskite Solar Cells”. In: *Advanced Functional Materials* 25.46 (2015), pp. 7200–7207. ISSN: 16163028. DOI: 10.1002/adfm.201501264.
- [42] Lijian Zuo et al. “Polymer-modified halide perovskite films for efficient and stable planar heterojunction solar cells”. In: *Science Advances* 3.8 (2017), pp. 1–12. ISSN: 23752548. DOI: 10.1126/sciadv.1700106.

- [43] Qi Jiang et al. “Enhanced electron extraction using SnO<sub>2</sub> for high-efficiency planar-structure HC(NH<sub>2</sub>)<sub>2</sub> PbI<sub>3</sub>-based perovskite solar cells”. In: *Nature Energy* 2.1 (2017). ISSN: 20587546. DOI: 10.1038/nenergy.2016.177.
- [44] Valentina Rohnacher et al. “Analytical Study of Solution-Processed Tin Oxide as Electron Transport Layer in Printed Perovskite Solar Cells”. In: *Advanced Materials Technologies* (2020). ISSN: 2365709X. DOI: 10.1002/admt.202000282.
- [45] Haibing Wang et al. “Hydrogen peroxide-modified SnO<sub>2</sub> as electron transport layer for perovskite solar cells with efficiency exceeding 22%”. In: *Journal of Power Sources* 481.November 2020 (2021), p. 229160. ISSN: 03787753. DOI: 10.1016/j.jpowsour.2020.229160. URL: <https://doi.org/10.1016/j.jpowsour.2020.229160>.
- [46] Jianying Pei et al. “EMIMBF<sub>4</sub>-Assisted SnO<sub>2</sub>-Based Planar Perovskite Films for Label-Free Photoelectrochemical Sensing”. In: *ACS Omega* 2.8 (2017), pp. 4341–4346. ISSN: 24701343. DOI: 10.1021/acsomega.7b00496.
- [47] Dong Yang et al. “High efficiency planar-type perovskite solar cells with negligible hysteresis using EDTA-complexed SnO<sub>2</sub>”. In: *Nature Communications* 9.1 (2018). ISSN: 20411723. DOI: 10.1038/s41467-018-05760-x.
- [48] Yohan Ko et al. “Improved performance of sol–gel ZnO-based perovskite solar cells via TiCl<sub>4</sub> interfacial modification”. In: *Solar Energy Materials and Solar Cells* 183.December 2017 (2018), pp. 157–163. ISSN: 09270248. DOI: 10.1016/j.solmat.2018.04.021.
- [49] M. Dehghan and A. Behjat. “Deposition of zinc oxide as an electron transport layer in planar perovskite solar cells by spray and SILAR methods comparable with spin coating”. In: *RSC Advances* 9.36 (2019), pp. 20917–20924. ISSN: 20462069. DOI: 10.1039/c9ra01839e.
- [50] Jinli Yang et al. “Origin of the Thermal Instability in CH<sub>3</sub>NH<sub>3</sub>PbI<sub>3</sub> Thin Films Deposited on ZnO”. In: *Chemistry of Materials* 27.12 (2015), pp. 4229–4236. ISSN: 15205002. DOI: 10.1021/acs.chemmater.5b01598.
- [51] Dong Yang et al. “Stable Efficiency Exceeding 20.6% for Inverted Perovskite Solar Cells through Polymer-Optimized PCBM Electron-Transport Layers”. In: *Nano Letters* 19.5 (2019), pp. 3313–3320. ISSN: 15306992. DOI: 10.1021/acs.nanolett.9b00936.



- [52] Long Zhou et al. “Enhanced planar perovskite solar cell efficiency and stability using a perovskite/PCBM heterojunction formed in one step”. In: *Nanoscale* 10.6 (2018), pp. 3053–3059. ISSN: 20403372. DOI: 10.1039/c7nr07753j.
- [53] Jiangsheng Li et al. “Inverted MAPbI<sub>3</sub> Perovskite Solar Cells with Graphdiyne Derivative-Incorporated Electron Transport Layers Exceeding 20% Efficiency”. In: *Solar RRL* 3.10 (2019), p. 1900241. ISSN: 2367-198X. DOI: 10.1002/solr.201900241.
- [54] Giles E. Eperon et al. “Formamidinium lead trihalide: A broadly tunable perovskite for efficient planar heterojunction solar cells”. In: *Energy and Environmental Science* 7.3 (2014), pp. 982–988. ISSN: 17545692. DOI: 10.1039/c3ee43822h.
- [55] Wen Guang Li et al. “A formamidinium-methylammonium lead iodide perovskite single crystal exhibiting exceptional optoelectronic properties and long-term stability”. In: *Journal of Materials Chemistry A* 5.36 (2017), pp. 19431–19438. ISSN: 20507496. DOI: 10.1039/c7ta04608a.
- [56] Amalie Dualeh et al. “Effect of annealing temperature on film morphology of organic-inorganic hybrid perovskite solid-state solar cells”. In: *Advanced Functional Materials* 24.21 (2014), pp. 3250–3258. ISSN: 16163028. DOI: 10.1002/adfm.201304022.
- [57] Jin Wook Lee and Nam Gyu Park. “Two-step deposition method for high-efficiency perovskite solar cells”. In: *MRS Bulletin* 40.8 (2015), pp. 654–659. ISSN: 08837694. DOI: 10.1557/mrs.2015.166.
- [58] Jeong Hyeok Im et al. “Growth of CH<sub>3</sub>NH<sub>3</sub>PbI<sub>3</sub> cuboids with controlled size for high-efficiency perovskite solar cells”. In: *Nature Nanotechnology* 9.11 (2014), pp. 927–932. ISSN: 17483395. DOI: 10.1038/nnano.2014.181.
- [59] Yongzhen Wu et al. “Retarding the crystallization of PbI<sub>2</sub> for highly reproducible planar-structured perovskite solar cells via sequential deposition”. In: *Energy and Environmental Science* 7.9 (2014), pp. 2934–2938. ISSN: 17545706. DOI: 10.1039/c4ee01624f.
- [60] Nam Joong Jeon et al. “Solvent engineering for high-performance inorganic-organic hybrid perovskite solar cells”. In: *Nature Materials* 13.9 (2014), pp. 897–903. ISSN: 14764660. DOI: 10.1038/nmat4014.

- [61] Kun Mu Lee et al. "Selection of anti-solvent and optimization of dropping volume for the preparation of large area sub-module perovskite solar cells". In: *Solar Energy Materials and Solar Cells* 172 (2017), pp. 368–375. ISSN: 09270248. DOI: 10.1016/j.solmat.2017.08.010. URL: <http://dx.doi.org/10.1016/j.solmat.2017.08.010>.
- [62] Kun Mu Lee et al. "Effect of anti-solvent mixture on the performance of perovskite solar cells and suppression hysteresis behavior". In: *Organic Electronics* 65 (2019), pp. 266–274. ISSN: 15661199. DOI: 10.1016/j.orgel.2018.08.048.
- [63] Mohammad Mahdi Tavakoli et al. "Controllable Perovskite Crystallization via Antisolvent Technique Using Chloride Additives for Highly Efficient Planar Perovskite Solar Cells". In: *Advanced Energy Materials* 9.17 (2019), pp. 1–10. ISSN: 16146840. DOI: 10.1002/aenm.201803587.
- [64] Michael Saliba et al. "How to Make over 20% Efficient Perovskite Solar Cells in Regular (n-i-p) and Inverted (p-i-n) Architectures". In: *Chemistry of Materials* 30.13 (2018), pp. 4193–4201. ISSN: 15205002. DOI: 10.1021/acs.chemmater.8b00136.
- [65] Eui Hyuk Jung et al. "Efficient, stable and scalable perovskite solar cells using poly(3-hexylthiophene)". In: *Nature* 567.7749 (2019), pp. 511–515. ISSN: 14764687. DOI: 10.1038/s41586-019-1036-3. URL: <http://dx.doi.org/10.1038/s41586-019-1036-3>.
- [66] Narges Yaghoobi Nia et al. "High-Efficiency Perovskite Solar Cell Based on Poly(3-Hexylthiophene): Influence of Molecular Weight and Mesoscopic Scaffold Layer". In: *ChemSusChem* 10.19 (2017), pp. 3854–3860. ISSN: 1864564X. DOI: 10.1002/cssc.201700635.
- [67] Tae Youl Yang et al. "Achieving Long-Term Operational Stability of Perovskite Solar Cells with a Stabilized Efficiency Exceeding 20% after 1000 h". In: *Advanced Science* 6.14 (2019), pp. 1–7. ISSN: 21983844. DOI: 10.1002/advs.201900528.
- [68] Xixia Liu et al. "20.7% Highly Reproducible Inverted Planar Perovskite Solar Cells With Enhanced Fill Factor and Eliminated Hysteresis". In: *Energy and Environmental Science* 12.5 (2019), pp. 1622–1633. ISSN: 17545706. DOI: 10.1039/c9ee00872a.

- [69] Wenbin Han et al. “Recent Progress of Inverted Perovskite Solar Cells with a Modified PEDOT:PSS Hole Transport Layer”. In: *ACS Applied Materials and Interfaces* 12.44 (2020), pp. 49297–49322. ISSN: 19448252. DOI: 10.1021/acsami.0c13576.
- [70] Jianyong Ouyang et al. “High-conductivity poly(3,4-ethylenedioxythiophene):poly(styrene sulfonate) film and its application in polymer optoelectronic devices”. In: *Advanced Functional Materials* 15.2 (2005), pp. 203–208. ISSN: 1616301X. DOI: 10.1002/adfm.200400016.
- [71] Jun Yuan Jeng et al. “CH<sub>3</sub>NH<sub>3</sub>PbI<sub>3</sub> perovskite/fullerene planar-heterojunction hybrid solar cells”. In: *Advanced Materials* 25.27 (2013), pp. 3727–3732. ISSN: 09359648. DOI: 10.1002/adma.201301327.
- [72] Kui Jiang et al. “Inverted planar perovskite solar cells based on CsI-doped PEDOT:PSS with efficiency beyond 20% and small energy loss”. In: *Journal of Materials Chemistry A* 7.38 (2019), pp. 21662–21667. ISSN: 20507496. DOI: 10.1039/c9ta08995k.
- [73] Chuantian Zuo and Liming Ding. “Modified PEDOT Layer Makes a 1.52 V Voc for Perovskite/PCBM Solar Cells”. In: *Advanced Energy Materials* 7.2 (2017), pp. 4–9. ISSN: 16146840. DOI: 10.1002/aenm.201601193.
- [74] Qin Wang et al. “Modulation of PEDOT:PSS pH for efficient inverted perovskite solar cells with reduced potential loss and enhanced stability”. In: *ACS Applied Materials and Interfaces* 8.46 (2016), pp. 32068–32076. ISSN: 19448252. DOI: 10.1021/acsami.6b11757.
- [75] Wei Hu et al. “High Open-Circuit Voltage of 1.134 v for Inverted Planar Perovskite Solar Cells with Sodium Citrate-Doped PEDOT:PSS as a Hole Transport Layer”. In: *ACS Applied Materials and Interfaces* 11.24 (2019), pp. 22021–22027. ISSN: 19448252. DOI: 10.1021/acsami.9b06526.
- [76] Antonella Giuri et al. “Cooperative Effect of GO and Glucose on PEDOT:PSS for High VOC and Hysteresis-Free Solution-Processed Perovskite Solar Cells”. In: *Advanced Functional Materials* 26.38 (2016), pp. 6985–6994. ISSN: 16163028. DOI: 10.1002/adfm.201603023.
- [77] Ju Huang et al. “Improving the efficiency and stability of inverted perovskite solar cells with dopamine-copolymerized PEDOT:PSS as a hole extraction layer”. In: *Journal*

- of Materials Chemistry A* 5.26 (2017), pp. 13817–13822. ISSN: 20507496. DOI: 10.1039/c7ta02670f.
- [78] C. Redondo-Obispo et al. “Enhanced stability and efficiency in inverted perovskite solar cells through graphene doping of PEDOT:PSS hole transport layer”. In: *Materials and Design* 191 (2020). ISSN: 18734197. DOI: 10.1016/j.matdes.2020.108587.
- [79] Xingtian Yin et al. “Nickel Oxide as Efficient Hole Transport Materials for Perovskite Solar Cells”. In: *Solar RRL* 3.5 (2019), p. 1900001. ISSN: 2367-198X. DOI: 10.1002/solr.201900001.
- [80] Zonghao Liu et al. “Nickel oxide nanoparticles for efficient hole transport in p-i-n and n-i-p perovskite solar cells”. In: *Journal of Materials Chemistry A* 5.14 (2017), pp. 6597–6605. ISSN: 20507496. DOI: 10.1039/c7ta01593c.
- [81] Neha Arora et al. “Perovskite solar cells with CuSCN hole extraction layers yield stabilized efficiencies greater than 20%”. In: *Science* 358.6364 (2017), pp. 768–771. ISSN: 10959203. DOI: 10.1126/science.aam5655.
- [82] Mei Lyu, Jiangzhao Chen, and Nam Gyu Park. “Improvement of efficiency and stability of CuSCN-based inverted perovskite solar cells by post-treatment with potassium thiocyanate”. In: *Journal of Solid State Chemistry* 269 (2019), pp. 367–374. ISSN: 1095726X. DOI: 10.1016/j.jssc.2018.10.014. URL: <https://doi.org/10.1016/j.jssc.2018.10.014>.
- [83] Kaijie Wang et al. “Surface Treatment on Nickel Oxide to Enhance the Efficiency of Inverted Perovskite Solar Cells”. In: *International Journal of Photoenergy* 2019 (2019). ISSN: 1687529X. DOI: 10.1155/2019/4360816.
- [84] Mei Feng Xu et al. “The effect of solution processed nickel oxide and nickel oxide by-products on planar MAPbI<sub>3</sub>perovskite solar cells”. In: *Applied Physics Letters* 117.4 (2020), pp. 0–6. ISSN: 00036951. DOI: 10.1063/5.0016511.
- [85] Wanyi Nie et al. “Critical Role of Interface and Crystallinity on the Performance and Photostability of Perovskite Solar Cell on Nickel Oxide”. In: *Advanced Materials* 30.5 (2018), pp. 1–9. ISSN: 15214095. DOI: 10.1002/adma.201703879.

- [86] Shuyi Liu et al. “Nickel oxide hole injection/transport layers for efficient solution-processed organic light-emitting diodes”. In: *Chemistry of Materials* 26.15 (2014), pp. 4528–4534. ISSN: 15205002. DOI: 10.1021/cm501898y.
- [87] Uisik Kwon et al. “Solution-Processible Crystalline NiO Nanoparticles for High-Performance Planar Perovskite Photovoltaic Cells”. In: *Scientific Reports* 6.July (2016), pp. 1–10. ISSN: 20452322. DOI: 10.1038/srep30759. URL: <http://dx.doi.org/10.1038/srep30759>.
- [88] Yi Hou et al. “Overcoming the Interface Losses in Planar Heterojunction Perovskite-Based Solar Cells”. In: *Advanced Materials* 28.25 (2016), pp. 5112–5120. ISSN: 15214095. DOI: 10.1002/adma.201504168.
- [89] Menglin Li et al. “Improving the conductivity of sol-gel derived NiOx with a mixed oxide composite to realize over 80% fill factor in inverted planar perovskite solar cells”. In: *Journal of Materials Chemistry A* 7.16 (2019), pp. 9578–9586. ISSN: 20507496. DOI: 10.1039/c8ta10821h.
- [90] Raisul Islam et al. “Investigation of the changes in electronic properties of nickel oxide (NiO) due to UV/Ozone treatment”. In: (2017). DOI: 10.1021/acsami.7b01629.
- [91] Qinyuan Qiu et al. “Surface Modification of NiO Nanoparticles for Highly Stable Perovskite Solar Cells Based on All-Inorganic Charge Transfer Layers”. In: *Journal of Electronic Materials* 49.11 (2020), pp. 6300–6307. ISSN: 1543186X. DOI: 10.1007/s11664-020-08403-4. URL: <https://doi.org/10.1007/s11664-020-08403-4>.
- [92] Lixin Hou et al. “18.0% efficiency flexible perovskite solar cells based on double hole transport layers and CH<sub>3</sub>NH<sub>3</sub>PbI<sub>3</sub>-xCl<sub>x</sub> with dual additives”. In: *Journal of Materials Chemistry C* 6.32 (2018), pp. 8770–8777. ISSN: 20507526. DOI: 10.1039/c8tc02906g.
- [93] Jae Ho Kim et al. *Flexible ITO films with atomically flat surfaces for high performance flexible perovskite solar cells*. Vol. 10. 44. 2018, pp. 20587–20598. ISBN: 8231201246. DOI: 10.1039/c8nr06586a.
- [94] Juan Long et al. “Flexible perovskite solar cells: Design and perspective”. In: May (2009).

- [95] Yangjie Lan, Yang Wang, and Yanlin Song. “Efficient Flexible Perovskite Solar Cells Based on Polymer Additive”. In: December 2016 (2018), pp. 11–14.
- [96] Stefano Razza et al. “Research Update: Large-area deposition, coating, printing, and processing techniques for the upscaling of perovskite solar cell technology”. In: *APL Materials* 4.9 (2016). ISSN: 2166532X. DOI: 10.1063/1.4962478. URL: <http://dx.doi.org/10.1063/1.4962478>.
- [97] Jiangwei Li et al. “Direct Evidence of Ion Diffusion for the Silver-Electrode-Induced Thermal Degradation of Inverted Perovskite Solar Cells”. In: *Advanced Energy Materials* 7.14 (2017). ISSN: 16146840. DOI: 10.1002/aenm.201602922.
- [98] Joel Troughton et al. “Highly efficient, flexible, indium-free perovskite solar cells employing metallic substrates”. In: *J. Mater. Chem. A* 3.17 (2015), pp. 9141–9145. ISSN: 2050-7488. DOI: 10.1039/C5TA01755F. URL: <http://xlink.rsc.org/?DOI=C5TC02043C%20http://xlink.rsc.org/?DOI=C5TA01755F>.
- [99] Daniel Bryant et al. “A transparent conductive adhesive laminate electrode for high-efficiency organic-inorganic lead halide perovskite solar cells”. In: *Advanced Materials* 26.44 (2014), pp. 7499–7504. ISSN: 15214095. DOI: 10.1002/adma.201403939.
- [100] Fei Guo et al. “High-performance semitransparent perovskite solar cells with solution-processed silver nanowires as top electrodes”. In: *Nanoscale* 7.5 (2015), pp. 1642–1649. ISSN: 20403372. DOI: 10.1039/c4nr06033d.
- [101] Eunsong Lee et al. “All-Solution-Processed Silver Nanowire Window Electrode-Based Flexible Perovskite Solar Cells Enabled with Amorphous Metal Oxide Protection”. In: *Advanced Energy Materials* 8.9 (2018), pp. 1–11. ISSN: 16146840. DOI: 10.1002/aenm.201702182.
- [102] Areum Kim et al. “Fully solution-processed transparent electrodes based on silver nanowire composites for perovskite solar cells”. In: *Nanoscale* 8.12 (2016), pp. 6308–6316. ISSN: 20403372. DOI: 10.1039/c5nr04585a.
- [103] Luoyi Gao et al. “Fully slot-die-coated perovskite solar cells in ambient condition”. In: *Applied Physics A: Materials Science and Processing* 126.6 (2020), pp. 1–7. ISSN: 14320630. DOI: 10.1007/s00339-020-03628-w. URL: <https://doi.org/10.1007/s00339-020-03628-w>.

- [104] Anand Verma et al. “Towards industrialization of perovskite solar cells using slot die coating”. In: *Journal of Materials Chemistry C* 8.18 (2020), pp. 6124–6135. ISSN: 20507526. DOI: 10.1039/d0tc00327a.
- [105] James B. Whitaker et al. “Scalable slot-die coating of high performance perovskite solar cells”. In: *Sustainable Energy and Fuels* 2.11 (2018), pp. 2442–2449. ISSN: 23984902. DOI: 10.1039/c8se00368h.
- [106] Anuja Vijayan et al. “Simple Method for Efficient Slot-Die Coating of MAPbI<sub>3</sub> Perovskite Thin Films in Ambient Air Conditions”. In: *ACS Applied Energy Materials* 3.5 (2020), pp. 4331–4337. ISSN: 25740962. DOI: 10.1021/acsaem.0c00039.
- [107] Young Yun Kim et al. “Gravure-Printed Flexible Perovskite Solar Cells: Toward Roll-to-Roll Manufacturing”. In: *Advanced Science* 6.7 (2019). ISSN: 21983844. DOI: 10.1002/advs.201802094.
- [108] Zehua Li et al. “Ink Engineering of Inkjet Printing Perovskite”. In: *ACS Applied Materials and Interfaces* 12.35 (2020), pp. 39082–39091. ISSN: 19448252. DOI: 10.1021/acsaami.0c09485.
- [109] Anand Verma et al. “Inkjet printed mesoscopic perovskite solar cells with custom design capability”. In: *Materials Advances* 1.2 (2020), pp. 153–160. DOI: 10.1039/d0ma00077a.
- [110] Ming Chun Tang et al. “Ambient blade coating of mixed cation, mixed halide perovskites without dripping:: In situ investigation and highly efficient solar cells”. In: *Journal of Materials Chemistry A* 8.3 (2020), pp. 1095–1104. ISSN: 20507496. DOI: 10.1039/c9ta12890e.
- [111] Junwen Zhang et al. “Two-step sequential blade-coating of high quality perovskite layers for efficient solar cells and modules”. In: *Journal of Materials Chemistry A* 8.17 (2020), pp. 8447–8454. ISSN: 20507496. DOI: 10.1039/d0ta02043e.
- [112] Kun Cao et al. “Efficient screen printed perovskite solar cells based on mesoscopic TiO<sub>2</sub>/Al<sub>2</sub>O<sub>3</sub>/NiO/carbon architecture”. In: *Nano Energy* 17 (2015), pp. 171–179. ISSN: 22112855. DOI: 10.1016/j.nanoen.2015.08.009. URL: <http://dx.doi.org/10.1016/j.nanoen.2015.08.009>.

- [113] Zhining Wan et al. “Screen printing process control for coating high throughput titanium dioxide films toward printable mesoscopic perovskite solar cells”. In: *Frontiers of Optoelectronics* 12.4 (2019), pp. 344–351. ISSN: 20952767. DOI: 10.1007/s12200-019-0904-7.
- [114] Brian G Higgins. “The Physics of the Viscocapillary Coating Bead”. In: *Converttech & e-Print* April (2011), pp. 2–7.
- [115] Daniel Burkitt et al. “Sequential slot-die deposition of perovskite solar cells using dimethylsulfoxide lead iodide ink”. In: *Materials* 11.11 (2018). ISSN: 19961944. DOI: 10.3390/ma11112106.
- [116] Tianshi Qin et al. “Amorphous hole-transporting layer in slot-die coated perovskite solar cells”. In: *Nano Energy* 31.August 2016 (2017), pp. 210–217. ISSN: 22112855. DOI: 10.1016/j.nanoen.2016.11.022. URL: <http://dx.doi.org/10.1016/j.nanoen.2016.11.022>.
- [117] Benjia Dou et al. “Roll-to-Roll Printing of Perovskite Solar Cells”. In: *ACS Energy Letters* 3.10 (2018), pp. 2558–2565. ISSN: 23808195. DOI: 10.1021/acsenenergylett.8b01556.
- [118] Tongle Bu et al. “Universal passivation strategy to slot-die printed SnO<sub>2</sub> for hysteresis-free efficient flexible perovskite solar module”. In: *Nature Communications* 9.1 (2018), pp. 1–10. ISSN: 20411723. DOI: 10.1038/s41467-018-07099-9.
- [119] Yulia Galagan et al. “Roll-to-Roll Slot Die Coated Perovskite for Efficient Flexible Solar Cells”. In: *Advanced Energy Materials* 8.32 (2018), pp. 1–7. ISSN: 16146840. DOI: 10.1002/aenm.201801935.
- [120] Roar R. Søndergaard, Markus Hösel, and Frederik C. Krebs. “Roll-to-Roll fabrication of large area functional organic materials”. In: *Journal of Polymer Science, Part B: Polymer Physics* 51.1 (2013), pp. 16–34. ISSN: 08876266. DOI: 10.1002/polb.23192.
- [121] Jin Hyuck Heo et al. “Recent advancements in and perspectives on flexible hybrid perovskite solar cells”. In: *Journal of Materials Chemistry A* 7.3 (2019), pp. 888–900. ISSN: 20507496. DOI: 10.1039/c8ta09452g.



- [122] Thomas M. Schmidt et al. “Upscaling of Perovskite Solar Cells: Fully Ambient Roll Processing of Flexible Perovskite Solar Cells with Printed Back Electrodes”. In: *Advanced Energy Materials* 5.15 (2015), pp. 1–9. ISSN: 16146840. DOI: 10.1002/aenm.201500569.
- [123] Peng Zhang et al. “Perovskite Solar Cells with ZnO Electron-Transporting Materials”. In: *Advanced Materials* 30.3 (2018), pp. 1–20. ISSN: 15214095. DOI: 10.1002/adma.201703737.
- [124] Yijie Xia, Kuan Sun, and Jianyong Ouyang. “Solution-processed metallic conducting polymer films as transparent electrode of optoelectronic devices”. In: *Advanced Materials* 24.18 (2012), pp. 2436–2440. ISSN: 09359648. DOI: 10.1002/adma.201104795.
- [125] Junyu Yang et al. “Roll-to-Roll Slot-Die-Printed Polymer Solar Cells by Self-Assembly”. In: *ACS Applied Materials and Interfaces* 10.26 (2018), pp. 22485–22494. ISSN: 19448252. DOI: 10.1021/acsami.8b05673.
- [126] John Ciro, Mario Alejandro Mejía-Escobar, and Franklin Jaramillo. “Slot-die processing of flexible perovskite solar cells in ambient conditions”. In: *Solar Energy* 150 (2017), pp. 570–576. ISSN: 0038092X. DOI: 10.1016/j.solener.2017.04.071.
- [127] Kallista K. Sears et al. “ITO-Free Flexible Perovskite Solar Cells Based on Roll-to-Roll, Slot-Die Coated Silver Nanowire Electrodes”. In: *Solar RRL* 1.8 (2017), pp. 1–9. ISSN: 2367198X. DOI: 10.1002/solr.201700059.
- [128] Daniel Burkitt et al. “Meniscus Guide Slot-Die Coating For Roll-to-Roll Perovskite Solar Cells”. In: *MRS Advances* 4.24 (Jan. 2019), pp. 1399–1407. ISSN: 2059-8521. DOI: 10.1557/adv.2019.79. URL: [https://www.cambridge.org/core/product/identifier/S2059852119000793/type/journal\\_article](https://www.cambridge.org/core/product/identifier/S2059852119000793/type/journal_article).
- [129] Daniel Burkitt et al. “Roll-to-roll slot-die coated P-I-N perovskite solar cells using acetonitrile based single step perovskite solvent system”. In: *Sustainable Energy and Fuels* 4.7 (2020), pp. 3340–3351. ISSN: 23984902. DOI: 10.1039/d0se00460j.
- [130] Francesco Di Giacomo et al. “Large area 140 cm<sup>2</sup> perovskite solar modules made by sheet to sheet and roll to roll fabrication with 14.5% efficiency”. In: *2018 IEEE 7th World Conference on Photovoltaic Energy Conversion, WCPEC 2018 - A Joint Conference of 45th IEEE PVSC, 28th PVSEC and 34th EU PVSEC* (2018), pp. 2795–2798. DOI: 10.1109/PVSC.2018.8548157.

- [131] Shih Han Huang et al. “Toward All Slot-Die Fabricated High Efficiency Large Area Perovskite Solar Cell Using Rapid Near Infrared Heating in Ambient Air”. In: *Advanced Energy Materials* 10.37 (2020), pp. 1–9. ISSN: 16146840. DOI: 10.1002/aenm.202001567.
- [132] Pengyun Liu et al. “Fundamental Understanding of Photocurrent Hysteresis in Perovskite Solar Cells”. In: *Advanced Energy Materials* 9.13 (2019), pp. 1–33. ISSN: 16146840. DOI: 10.1002/aenm.201803017.
- [133] Henry J. Snaith et al. “Anomalous hysteresis in perovskite solar cells”. In: *Journal of Physical Chemistry Letters* 5.9 (2014), pp. 1511–1515. ISSN: 19487185. DOI: 10.1021/jz500113x.
- [134] Joel Troughton, Katherine Hooper, and Trystan M. Watson. “Humidity resistant fabrication of CH<sub>3</sub>NH<sub>3</sub>PbI<sub>3</sub> perovskite solar cells and modules”. In: *Nano Energy* 39 (2017), pp. 60–68. ISSN: 22112855. DOI: 10.1016/j.nanoen.2017.06.039. URL: <http://dx.doi.org/10.1016/j.nanoen.2017.06.039>.

## Chapter 2

# Experimental methods

In this chapter, details will be given for all the experimental methods used throughout this research project, as well as information on the equipment used for analysis.

### 2.1 Spin Coating

Spin coating is the most simple method for depositing homogenous, reproducible thin films from a liquid based solution [1]. This process is a batch process with a significant bottleneck as to how large the substrates can be, up to 1 x 1m is possible, however, substrates of only a few cm are generally used. In addition to this, the process suffers from a significant amount of waste, as most of the solution deposited onto the substrate is lost during the spinning process. Spin-coating was used throughout this project to produce “control” devices with known reproducibility for comparison with slot-die coated layers.

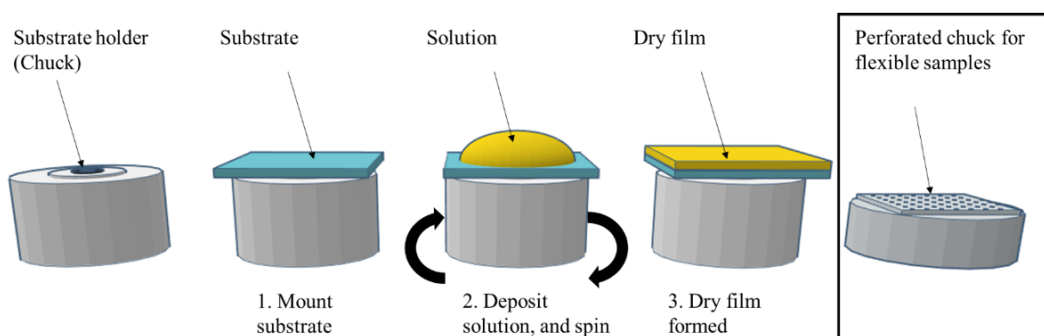


Figure 2.1: Diagram of spin coating procedure

Figure 2.1 shows a typical spin coating procedure, in which a substrate is held down onto the substrate holder (chuck) via vacuum, the nature of the chuck causes bowing of flexible sub-

strates, so a custom-made perforated chuck was purchased and included in the diagram. Once the solution has been deposited onto the substrate, the spin settings can be chosen, with the final film thickness being controlled by this setting, albeit with a dependence on the precursor solution properties. Dry film thicknesses ranging from several microns to a few nanometres can be achieved with spin-coating with excellent reproducibility. During spinning at high speeds, the solution is spread out evenly by centripetal forces and the surface tension of the solution. Removal of the solvent during this stage also contributes to the final film quality, therefore it is paramount the solution processing and spin settings are optimised otherwise film defects can occur.

In this work, spin coating was used mainly for the perovskite layer, and had already been optimised by various co-workers. The deposition of the perovskite layer used in this work was kept consistent throughout to ensure repeat ability. This method was the “anti-solvent” in which a perovskite compatible solvent is used to force crystallisation of the perovskite layer during spinning. This is a well-known method with several papers being published displaying its effectiveness [2] [3] [4], and is discussed in more detail in Chapter 1.4.5.3.

All spin coating in this work (apart from the dynamic spinning of the anti-solvent) was static, i.e. the solution was pipetted onto the substrate prior to spinning.

### **2.1.1 Glass cleaning**

Cleaning of the glass substrates prior to film deposition was necessary to remove any contaminants and was performed as follows:

- Submerge substrates in a 2% Hellmanex in DI water and place in an ultrasonic bath for 15 minutes
- Rinse with copious amounts of DI water
- Ultrasonic bath in DI water for 10 minutes
- Rinse again with DI water
- Ultrasonic bath in Acetone for 10 minutes
- Ultrasonic bath in isopropanol for 10 minutes
- Leave to dry in air for 1 hour

### 2.1.2 Plasma cleaning

Prior to deposition of the first layer in the device stack, plasma cleaning was employed to remove any surface contaminants which were not removed during the cleaning process, and also to increase the surface energy of the substrate allowing better wetting of the layer to be coated. A Diener electronic plasma system was used under a vacuum of 0.2 mbar with a feed of oxygen as the gas source.

### 2.1.3 Perovskite Deposition

As all of the work in this project was conducted in ambient conditions, the ethyl acetate anti-solvent system was used due to it being proven to produce excellent quality perovskite films in these conditions [3]. The perovskite precursor used was Methyl Ammonium Lead Iodide (MAPI), consisting of 602 mg lead iodide ( $\text{PbI}_2$ ) (Sigma Aldrich) and 199 mg Methyl Ammonium Iodide (MAI) (Dyesol) dissolved in 1 ml of a 4:1 solution of dimethyl formamide (DMF) (Sigma Aldrich) and dimethyl sulfoxide (DMSO) (Sigma Aldrich). This solution was left to dissolve on a hot plate at 60 °C for 24 hours, prior to deposition the solution was cooled and filtered through a 0.45  $\mu\text{m}$  PTFE filter. For formation of the perovskite layer, 100  $\mu\text{l}$  of the MAPI precursor was spread onto the substrate and spun at 4000 rpm for 30 seconds, with 200  $\mu\text{l}$  of the ethyl-acetate antisolvent dropped onto the spinning substrate approximately 15 seconds before the end. Finally, the films were annealed at 110 °C for 10 minutes.

### 2.1.4 Hole-transport Layers

Nickel oxide hole transport layers were deposited by spin coating a 0.2M sol-gel containing 50 mg of nickel acetate tetrahydrate (Sigma Aldrich), dissolved in 1 mL of 2-methoxyethanol (Sigma Aldrich), with 12  $\mu\text{L}$  of ethanolamine (Sigma Aldrich) added to stabilise the solution. This was left to stir on a hot plate at 60 °C for 24 hours and filtered through a 0.45  $\mu\text{m}$  PTFE filter after cooling. 100  $\mu\text{L}$  was then deposited onto an ITO/glass substrate and spun at 3000 rpm for 30 seconds and annealed at 300 °C for 30 minutes.

Spiro-OMeTAD (2,2',7,7'-Tetrakis[N,N-di(4-methoxyphenyl)amino]-9,9'-spirobifluorene) films were prepared by dissolving 90 mg spiro-MeOTAD (Sigma Aldrich), 34  $\mu\text{l}$  4-tert-butylpyridine (TBP) (Sigma Aldrich), 19  $\mu\text{l}$  of a stock solution of 520 mg/ml bis(trifluoromethane) sulfonimide lithium salt (sigma Aldrich) in acetonitrile (sigma Aldrich), and 10  $\mu\text{l}$  of a stock solution

of 300 mg/ml bis(trifluoromethane) sulfonimide cobalt (III) salt (sigma Aldrich) in acetonitrile in 1 ml chlorobenzene (Sigma Aldrich). Dissolving of the components at 60 °C for 24 hours was required before deposition, and upon cooling filtered through a 0.2  $\mu\text{m}$  PTFE filter. Films were spin-coated at 4000 rpm for 30 seconds and did not require drying. Prior to testing of devices employing a Spiro-MeOTAD hole transport layer, they were left for 24 hours for the Spiro to oxidise.

### **2.1.5 Electron-transport Layers**

Tin oxide electron transport layers were deposited from a 0.2M solution of tin chloride (II) dihydrate ( $\text{SnCl}_2 \cdot 2\text{H}_2\text{O}$ ) (Sigma Aldrich) dissolved in 1-propanol (sigma Aldrich). Stirring at 60 °C on a hot plate for 24 hours, cooling and filtering through a 0.2  $\mu\text{m}$  PTFE filter was required before spin coating 100  $\mu\text{L}$  onto an ITO coated glass substrate for 30 seconds at 3000 rpm. Films were then annealed at 180 °C for 1 hour. PCBM (Phenyl-C61-butyric acid methyl ester) electron transport layers were manufactured by dissolving 40 mg of 99.95% purity PCBM (Solenne BV) in chlorobenzene for 24 hours on a hot plate at 60 °C. Prior to deposition solutions were cooled and filtered through a 0.2  $\mu\text{m}$  PTFE filter and 100  $\mu\text{L}$  spun on top of a perovskite layer at 3000 rpm for 20 seconds. Films required no further drying steps.

Although not an electron transport layer, bathocuprine (BCP) was used in the n-i-p device stacks as a buffer layer. This was made up of 0.5 mg BCP (Ossila) dissolved in 1 mL of ethanol (Sigma Aldrich), and 200  $\mu\text{L}$  spun on top of the PCBM layer at 7000 rpm with no further drying step required. The approximate thickness of this layer was 10 nm.

### **2.1.6 Glass based device layout**

Glass based perovskite devices were manufactured on 28 x 28 mm ITO coated glass substrates from Kintec with a sheet resistance of 15 Ohms/sq. The ITO layer covers the majority of the glass but with 4 mm removed at two edges as shown in Figure 2.2 to prevent direct contact with the counter electrodes. After perovskite devices are made a center strip is either removed with a razor blade to expose the ITO surface for the working electrode to contact, or solder is used to expose the ITO. To deposit the counter and working electrodes, cells are loaded into a thermal evaporator against a shadow mask to define the areas for gold or silver evaporation as shown in Figure 2.2.

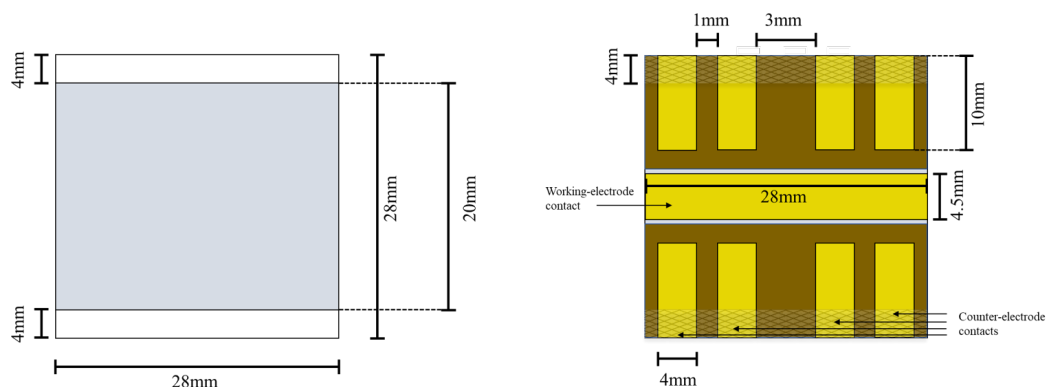


Figure 2.2: Schematic of the ITO coated glass substrates used in this work as well as a schematic of an individual perovskite solar cell showing the working electrode and 8 counter-electrode "pixels".

### 2.1.7 Manufacturing of flexible devices

For slot-die coated ETLs or HTLs, devices were manufactured by spin-coating the remainder of the device stack as outlined in section 2.1. Prior to spin-coating, slot-die coated films were cut into smaller 28 x 28 mm squares so that they would fit in the spin-coater. Flexible substrates (ITO coated PET) were provided by Meko print with a sheet resistance of 50 Ohms/square and pre-patterned as desired. Device layout was then identical as described in Section 2.1.6. A schematic illustration of the PET/ITO pattern and subsequent dissection can be found in Figure 2.3

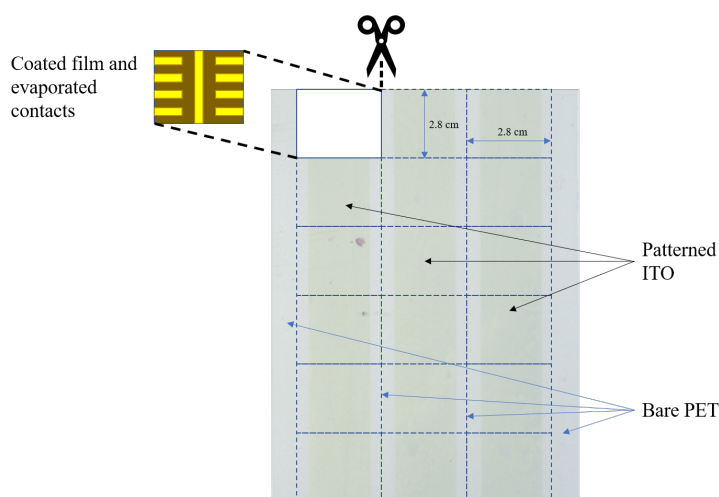


Figure 2.3: Schematic illustration of the pre-patterned PET/ITO provided by Meko print and the method used to cut into smaller samples.

## 2.2 Slot-Die Meniscus Coating

Slot-die coating is one of the many methods for large scale deposition of thin films onto rigid or flexible substrates, with the main advantage of it being easily integrated into roll-to-roll coating units. In addition to this, solutions with a wide range of rheological properties can be coated with excellent uniformity and thin films from many microns down to a few nanometres thick. Pre-metering of the coating solution leads to very little wastage unlike deposition methods such as spin-coating or bar-coating. In this work, meniscus guide slot-die coating was used, with the meniscus guide aiding the formation of a meniscus between the slot-die head and the substrate. A FOM technologies bench-top slot-die coater was used throughout this work and positioned in a fume hood inside a humidity controlled clean room environment (relative humidity approximately 30%), with a diagram of the coating set up given in Figure 2.4.

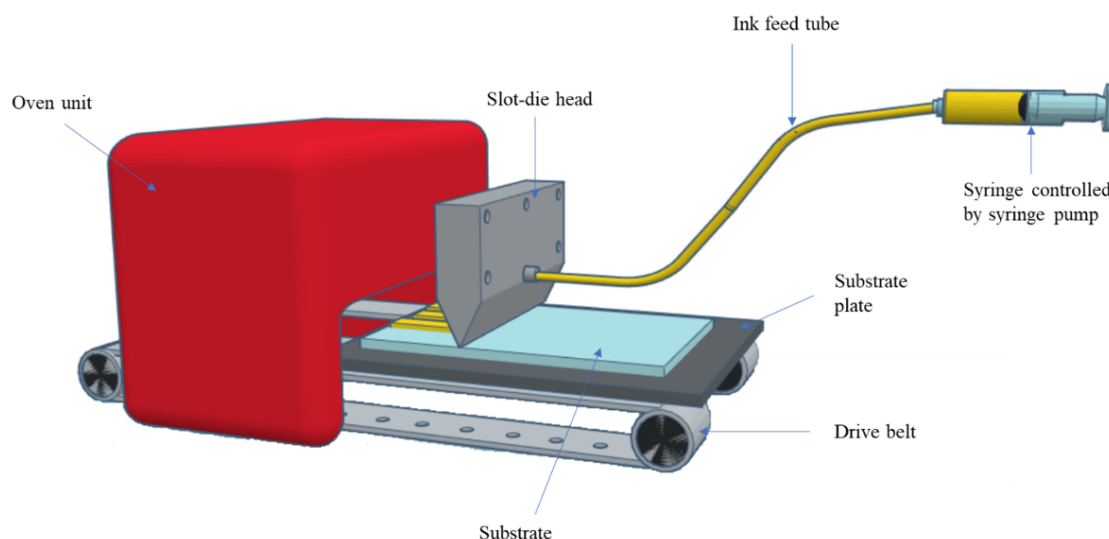


Figure 2.4: Schematic diagram of the bench-top FOM slot-die coater used in this work with the key parts labelled.

The coating unit consists of substrate plate which is moved via machine driven belts to take the substrate under the slot-die coating head and through the in-line oven. The belt can be driven at various speeds and as well as stopping at certain intervals and is controlled by a main computer. The slot-die head is mounted near the start of the belt, with the in-line oven situated approximately 30 cm after this and being 30 cm long itself. Mounting in which the slot-die head is situated on is controlled via micrometre adjustment screws to allow fine tuning of the heads position in the horizontal and vertical planes. Ink flow from the syringe to the



coating head is controlled by a syringe pump which is connected to the main computer, with the flow rate determining the overall wet film thickness deposited. With regards to the slot-die coating head itself, a FOM technologies head with interchangeable shims and meniscus guides were used throughout this work. The coating head has a maximum coating width of 10 cm, however the maximum used in this work was 9 cm. Shims were changed to control the area of the substrate, which was coated, however, full width coating was used most of the time. Shim thicknesses of  $50\ \mu\text{m}$  were used throughout, and a meniscus guide tab length of  $1000\ \mu\text{m}$  was kept constant as well. Schematic diagrams showing the slot-die coating head, and how it is assembled is shown in Figure 2.5 and Figure 2.6.

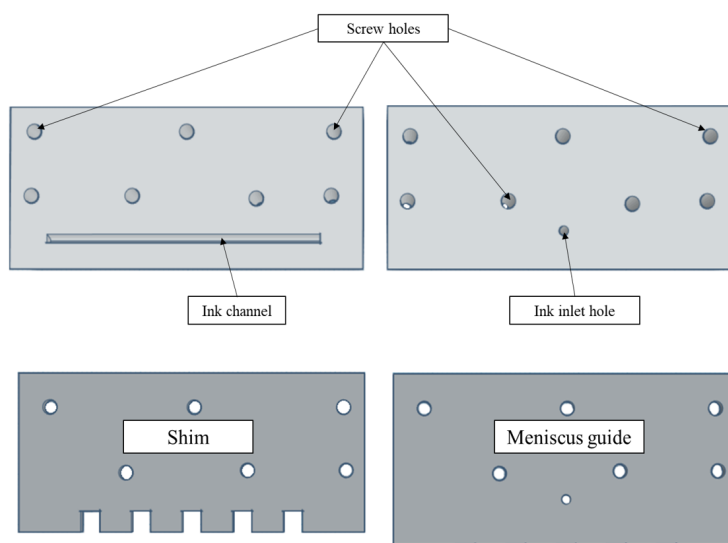


Figure 2.5: Schematic diagram of the slot-die head used in this work with the key components labelled.

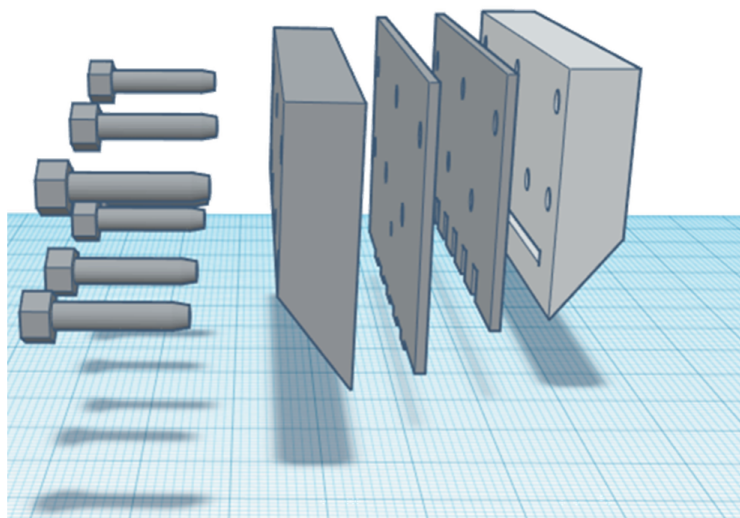


Figure 2.6: Schematic diagram showing how the slot-die head is assembled.

### 2.2.1 Slot-Die Coating and Visco-Capillary Model Calculations

Calculations used for the capillary number (Ca) and dimensionless gap (DG) for integration into the visco-capillary model were as follows:

$$Ca = \frac{\mu V}{\sigma} \quad (2.1)$$

Where:

$\mu$  = Viscosity

V = Velocity (of substrate)

$\sigma$  = Surface tension

$$DG = \frac{H_o}{t_{min}} \quad (2.2)$$

Where:

$H_o$  = Head-substrate gap

$t_{min}$  = Wet-film thickness

## 2.3 Thermal Evaporation

Thermal evaporation was used in this work for the deposition of the top electrode in the perovskite solar cells of either silver or gold. As these materials require high temperatures to evaporate, and to prevent damage to the film they are evaporated onto, a vacuum system must be used in order to lower this temperature. Also, this vacuum environment removes the chance of any reactions occurring such as oxidation of the evaporated material. Either silver or gold is placed into a tungsten crucible and secured inside a concealed bell jar, with the target substrates suspended approximately 30 cm above this. Vacuum is then applied to the closed system via a vacuum pump, typically to pressures of around  $1 \times 10^{-5}$  mbar. Electrical current is then passed through the tungsten crucible, and evaporation rates, thus thickness of the final layer is controlled by the temperature applied and residence evaporation time. Several microns of metal can be evaporated, down to a few nm very accurately and reproducibly.

## 2.4 Rheological Measurements

### 2.4.1 Viscosity Measurements

Viscosity measurements were made using a Rheosense *micro*VISC which uses a Micro-Electrical Mechanical System (MEMS) which results in a viscometer which can measure over a wide range of viscosities and use very small volumes of sample. The viscometer uses a “chip” consisting of a rectangular slit flow channel made from borosilicate glass, where the sample is injected at a constant rate through the flow channel. Multiple pressure sensors mounted within the base monitor the pressure drop from the inlet to the outlet. This pressure drop is correlated with the shear-stress at the boundary wall. The shear stress and rate are directly related to the geometry of the rectangular slit flow channel which allows for viscosity measurements. Prior to measurements it was ensured the flow channel was thoroughly cleaned, and a reference material such as ethanol with a known viscosity was measured for calibration.

### 2.4.2 Surface Tension Measurements

Surface tension measurements were made using pendant drop shape fitting in an in-house built rig consisting of a box with a DSLR camera for high quality imaging. First Ten Angstroms (FTA32) software was used to measure the surface tension of a liquid, using a needle with known width to calibrate images via measurements in the images taken by the camera. An example of an image taken for surface tension measurements is shown in Figure 2.7.

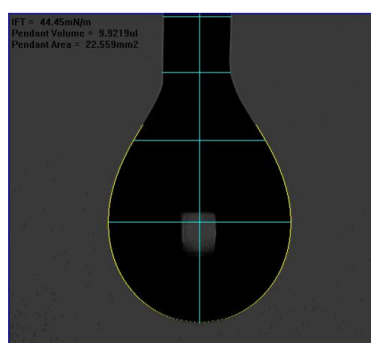


Figure 2.7: Example of an image taken for surface tension calculation.

### 2.4.3 Contact Angle Measurements

Contact angles were measured between liquids (coating formulations) and different substrates in an air environment. The measurements were made using the same setup and software as

the surface tension measurements in Chapter 2.4.2. As illustrated in Figure 2.8 contact angles are measured where a liquid-vapor interface meets a solid surface and is a good measurement of how well a liquid will wet on a substrate, with the smaller the contact angle, the better the wetting, thus coating. Measurements were made by dropping a small amount of the liquid to be measured onto a substrate with a micro-pipette. Contact angles were then measured using the Sessile Drop Profile included in the FTA32 software.

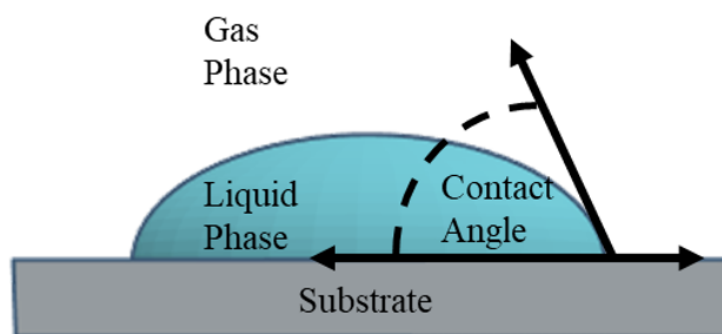


Figure 2.8: Schematic representation of the contact angle formed between a liquid and a substrate.

## 2.5 Optical Measurements

### 2.5.1 Ultraviolet-Visible-Near Infrared Spectroscopy (UV-Vis-NIR)

Optical measurements of films were made using a UV-Vis-NIR spectrophotometer (Perkin Elmer Lambda 750S). This equipment illuminates the sample with light of a known wavelength, and the transmitted light is measured by various photo-detecting diodes. The transmitted light is then compared to the intensity of the original light beam and repeated for each of the wavelengths set by the user. A transmission spectrum is then produced at the set wavelengths in small increments also set by the user. Transmission is given as a percentage and can be converted to an absorbance value with arbitrary units using Equation 2.3

$$A = 2 - \text{Log}(\%T) \quad (2.3)$$

### 2.5.2 Fourier Transform Infrared Spectroscopy (FTIR)

Fourier Transform Infrared Spectroscopy (FTIR) is used to measure the transmission of infrared light through a sample typically between  $400 - 4000 \text{ cm}^{-1}$ . Unlike a typical monochromator in which light of a known wavelength is illuminated through the sample, measured and

repeated for each wavelength, FTIR spectroscopy illuminates the sample with a beam containing many frequencies at once and measures the absorbance. This process is repeated with a different combination of frequencies until the full spectrum has been covered. This data is then mathematically converted into a transmittance spectrum by a computer using a Fourier Transform method. Molecules in the sample are then found as each molecule has a characteristic absorption at certain wavelengths and can be compared to reference spectra for identification.

FTIR measurements were taken using a Perkin Elmer Frontier FTIR spectrometer with an Attenuated Total Reflectance crystal (ATR). Samples were placed directly onto the crystal for measurements, and in the case of a solid sample, the films to be measured were placed face down on the ATR crystal and force applied by the machines calibrated arm.

### **2.5.3 Optical Imaging**

High resolution images of slot-die coated films were taken using a V700 flatbed scanner with image resolutions of 1200 dots per square inch. As the imaged films were highly transparent they were edited in Microsoft PowerPoint by increasing the colour and saturation until the film quality could be seen.

## **2.6 Other Characterisation Methods**

### **2.6.1 Scanning Electron Microscopy (SEM)**

Scanning Electron Microscopy (SEM) images were taken using a JEOL JSM-7800F field emission gun electron microscope. Accelerating voltages, probe currents and working distances were adjusted depending on the nature of the film to achieve high quality images.

### **2.6.2 Transmission Electron Microscopy**

TEM measurements were made on a Talos system using an accelerating voltage of 200 kV. Samples were prepared and then transferred to a copper grid for analysis.

### **2.6.3 Cyclic Voltammetry**

Cyclic Voltammetry (CV) is an electrochemical technique employed to investigate the oxidation and reduction reactions of molecular species. In this work, CV was used to determine the quality of an electron blocking layer on ITO coated glass substrates. A typical CV set up is

shown in Figure 2.9 which consists of the sample (working electrode) with an exposed area of 1 cm<sup>2</sup> (the rest covered by an applied lacquer), a reference electrode (A calomel electrode in this work) and a platinum counter electrode. All three electrodes are submerged in an electrolyte of 0.5M potassium ferri/ferrocyanide. CV profiles were measured using Gamry Reference 600 potentiostat.

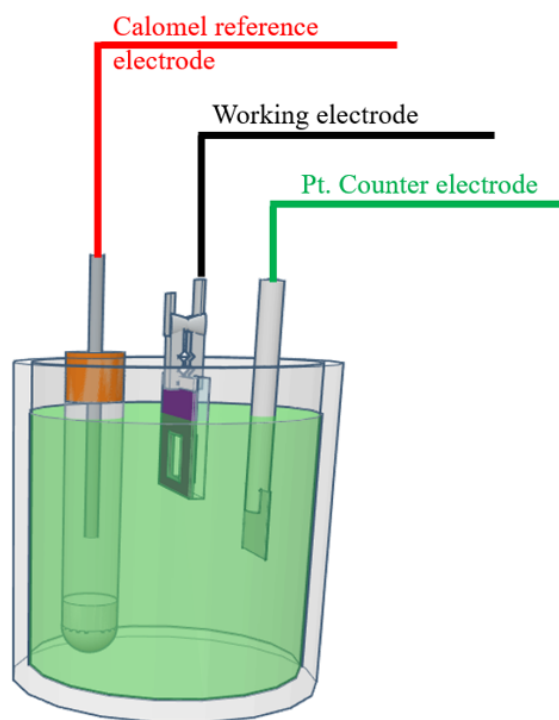
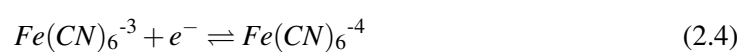


Figure 2.9: Schematic diagram of the CV setup used in this work.

During CV measurements a cyclic sweep of potential on the working electrode is compared to a reference electrode and the current at the working electrode measured. If no reaction with the electrolyte occurs during the sweep, then no current will flow and confirm whether an ETL is of good quality. If current is observed, then a reaction is happening at the working electrode suggesting poor electron blocking behaviour. Regarding the reaction occurring at the working electrode, oxidation and reduction are summarised by the single electron reaction as shown in Equation 2.4



A typical Cyclic Voltammogram of an ITO working electrode is shown in Figure 2.10 in which the voltage is swept from -0.8 V to 0.8 V at a scan rate of 100 mVs<sup>-1</sup>. As the potential

is scanned cathodically (negatively)  $\text{Fe}(\text{CN})_6^{-3}$  is steadily depleted near the electrode as it is reduced to  $\text{Fe}(\text{CN})_6^{-4}$ . As the peak cathodic current ( $I_p^a$ ) is reached, the current density is dictated by the diffusion of  $\text{Fe}(\text{CN})_6^{-3}$  from the electrolyte. The volume of solution which contains the reduced  $\text{Fe}(\text{CN})_6^{-4}$  at the electrode continues to grow throughout the scan and slows down the mass transport of  $\text{Fe}(\text{CN})_6^{-3}$ . Therefore, as the potential increases negatively, the rate of  $\text{Fe}(\text{CN})_6^{-3}$  diffusion decreases resulting in a decrease in current. When the maximum potential of 0.8 V is reached the scan direction is reversed in the positive (anodic) direction the  $\text{Fe}(\text{CN})_6^{-4}$  at the electrode surface is oxidised back to  $\text{Fe}(\text{CN})_6^{-3}$  as the potential becomes more positive. The peak-to-peak separation ( $\Delta E$ ) observed between the anodic and cathodic peaks occurs if the reduction process is chemically and electrochemically reversible.

The equilibrium between  $\text{Fe}(\text{CN})_6^{-3}$  and  $\text{Fe}(\text{CN})_6^{-4}$  is described by the Nernst equation (Equation 2.5) and relates the potential of an electrochemical cell ( $E$ ) to the standard potential of a species ( $E^0$ ) and the relative activities of the oxidised (Ox) and reduced (Red) analyte in the system at equilibrium [5].

$$E = E^0 + \frac{RT}{nF} \ln \frac{\text{Ox}}{\text{Red}} \quad (2.5)$$

Where  $F$  is Faraday's constant,  $R$  is the universal gas constant,  $n$  the number of electrons and  $T$  is the temperature.

In this work, CV was used to determine the effectiveness of ETL's and confirmed by the peak current observed in the voltammograms. Also, the peak current ( $I_p^a$ ) is related to the exposed electrode area, thus knowing the peak current when using bare ITO as the electrode the effective surface area of the ETL can be estimated by its peak current values.

#### **2.6.4 ThermoGravimetric Analysis (TGA) and Differential Scanning Calorimetry (DSC)**

Thermogravimetric Analysis (TGA) and Differential Scanning Calorimetry (DSC) were performed using a Simultaneous Thermal Analysis (STA) 6000 from Perkin Elmer. This instrument enables real time measurement of the weight change of a sample and heat flow. TGA measures the weight loss as a function of temperature, or time at very high precisions. It can provide insight into any physical phenomena, such as phase transitions like vaporisation or sublimation. DSC, on the other hand, measures the difference in amount of heat required to

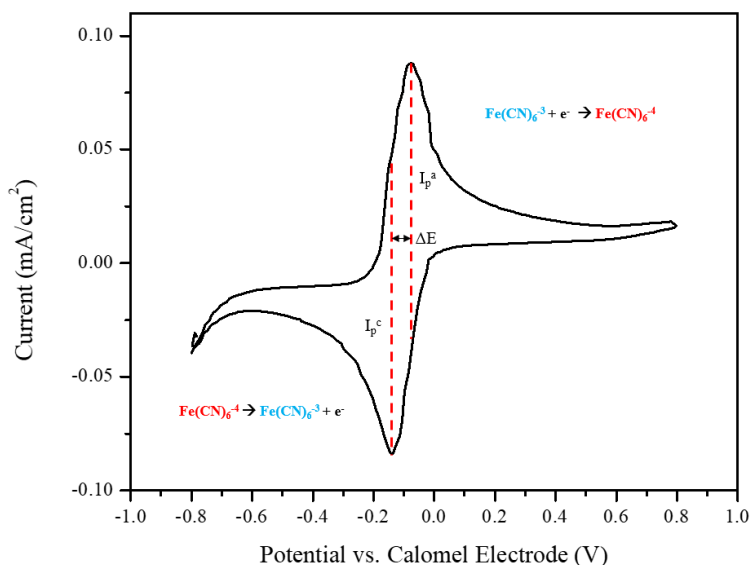


Figure 2.10: A typical cyclic voltammogram produced from an ITO coated glass working electrode with a potassium ferri/ferrocyanide redox couple and Calomel reference electrode.  $I_p^a$  is the peak anodic current,  $I_p^c$  is the peak cathodic current and  $\Delta E$  is the peak-to-peak separation. Also included are the respective single electron reduction and oxidation reactions.

increase the temperature of a sample and reference. Phase transitions can then be detected, by an endothermic or exothermic peak on the DSC curve. Combining the TGA and DSC in one single instrument provides greater insight into the characterisation of the material being analysed. The STA consists of a small furnace, in which a small ceramic alumina crucible sits on a corrosion resistant, pure platinum pan holder. The furnace can be purged with different gases, with flow control. For the experiments performed in this project, Nitrogen or air was the purge gas used at a rate of 20 ml/min.

### 2.6.5 Atomic Force Microscopy

Atomic Force Microscopy was performed by Dr Vasil Stoichkov at the Wexford Institute of Technology in Ireland.

### 2.6.6 X-ray Photoelectron Spectroscopy

XPS was carried out on a Kratos Axis Supra instrument using a monochromated Al  $K\alpha$  source operating at 225W (15mA, 20kV). Wide scans were performed with a pass energy of 160 eV to identify the elements present on the surface, with the exception of hydrogen and helium, with an x-ray footprint of 300 x 700  $\mu\text{m}$ . High resolution spectra were run with a pass energy of 40 eV. Typical detection limits are around 0.1 atom% and the technique samples a depth of



<10 nm. The samples are semiconducting materials coated on glass, which were mounted in electrical connection with the sample stage so that charge neutralisation was not used. Data was analysed using CasaXPS 2.3.23rev1.1K using the Kratos RSF library, and Shirley backgrounds were used. Peak positions were calibrated to the adventitious carbon line at 284.8 eV.

## **2.7 Device Characterisation**

This section details the methods used to characterise the opto-electric properties of the perovskite solar cells made throughout this work.

### **2.7.1 Current-Voltage Measurements**

Current-voltage measurements were made using a Keithley 2400 source measure unit, which provides electrical biasing of the device and measures the current produced. A class AAA Newport Oriel Sol3A was used as the light source and calibrated to AM1.5 sun equivalent using a silicon reference cell fitted with a KG5 filter (Newport Oriel 91150-KG5). Throughout this work the same measurement routine was adhered to which was as follows: expose the device to illumination and immediately sweep the voltage from 1.2 V to -0.1 V with a voltage sweep rate of  $0.15 \text{ Vs}^{-1}$ , followed by a scan in the opposite direction from -0.1 V to 1.2 V. Data was collated using in-house software made by Dr Justin Searle. Each measurement was made on a  $1 \text{ cm}^2$  pixel, defined by a shadow mask.

### **2.7.2 External Quantum Efficiency Measurements (EQE)**

External quantum efficiency measurements were made using a QEX10 unit from PV Measurements over a wavelength between 300 - 900 nm. Calibration was conducted using a silicon based reference device prior to each measurement.

## **2.8 Alternative Processing Methods**

### **2.8.1 Near Infra-Red Annealing (NIR)**

NIR annealing was conducted using a system provided by Heraeus with a supply voltage of 415 V. This unit consisted of enclosed NIR emitters and a moving substrate bed to control the residence time of samples passing underneath. The emitters installed in this unit are high power

short wave, with a total load of 6.6 kW. The emitters were coated with a QRC (quartz reflective coating) which helps with more targeted infrared radiation giving a peak output of 1200 nm. figure 2.11 is an image of the NIR system used in this work.



Figure 2.11: Heraeus NIR system

## 2.8.2 UltraViolet-Ozone (UVO)

UVO was performed using a unit provided by Jelight with model number: 144AX-220. The lamp was a low pressure mercury vapor with an intensity of 28 - 32 mW/cm<sup>2</sup> at 253.7 nm. The distance between the sample and the lamp was approximately 3 mm.

## 2.8.3 Photonic Curing

Photonic curing was conducted using a Novacentrix PulseForge 1300 system with a spectral output from 200 - 1000 nm. Further information on the equipment can be found in Chapter 5.3.2

## 2.9 References

- [1] Nam-Trung Nguyen. *Fabrication technologies*. 2012, pp. 113–161. ISBN: 9781437735208. DOI: 10.1016/b978-1-4377-3520-8.00004-8.
- [2] Karsten Bruening and Christopher J. Tassone. “Antisolvent processing of lead halide perovskite thin films studied by: In situ X-ray diffraction”. In: *Journal of Materials Chemistry A* 6.39 (2018), pp. 18865–18870. ISSN: 20507496. DOI: 10.1039/c8ta06025h.
- [3] Joel Troughton, Katherine Hooper, and Trystan M. Watson. “Humidity resistant fabrication of CH<sub>3</sub>NH<sub>3</sub>PbI<sub>3</sub> perovskite solar cells and modules”. In: *Nano Energy* 39 (2017), pp. 60–68. ISSN: 22112855. DOI: 10.1016/j.nanoen.2017.06.039. URL: <http://dx.doi.org/10.1016/j.nanoen.2017.06.039>.
- [4] Kun Mu Lee et al. “Selection of anti-solvent and optimization of dropping volume for the preparation of large area sub-module perovskite solar cells”. In: *Solar Energy Materials and Solar Cells* 172. August (2017), pp. 368–375. ISSN: 09270248. DOI: 10.1016/j.solmat.2017.08.010. URL: <http://dx.doi.org/10.1016/j.solmat.2017.08.010>.
- [5] Noémie Elgrishi et al. “A Practical Beginner’s Guide to Cyclic Voltammetry”. In: *Journal of Chemical Education* 95.2 (2018), pp. 197–206. ISSN: 19381328. DOI: 10.1021/acs.jchemed.7b00361.

## Chapter 3

# Tin Oxide Electron Transport Layer, Optimisation, Coating and Device Characterisation

### 3.1 Introduction

The overall aim of this thesis is to develop methods for depositing electron and hole transport layers for use in large scale manufacture of perovskite solar cells, focusing on low-temperature, high throughput compatibility.

In this chapter the experimental work begins with the optimisation of a low-temperature tin oxide ( $\text{SnO}_2$ ) electron transport layer, initially via spin coating, and then scaled up to a sheet-to-sheet slot-die coating process. As discussed in Chapter 1.4.4 the electron transport layer serves as an intermediate between the perovskite layer and the bottom electrode, helping to improve the collection of electrons, as well as preventing recombination reactions via the blocking of holes.

Tin oxide was chosen as the ETL due to its suitable electronic and optical properties for use in a perovskite device. Perhaps the most common ETL in the literature is titanium dioxide ( $\text{TiO}_2$ ), which requires a significantly high annealing temperature ( $>450\text{ }^\circ\text{C}$ ) [1] and was thus not suitable for roll-to-roll deposition. In addition to this it has been reported that tin oxide is a more stable alternative with better energy alignment with the perovskite layer [2]. For a roll-to-roll compatible tin oxide layer to be realised, low temperatures are required ( $<150\text{ }^\circ\text{C}$ ) as well as a suitably quick processing time. For example; a well-known precursor solution for the

deposition of tin oxide has already been well established, which involves depositing a layer of tin chloride ( $\text{SnCl}_2$ ) in ethanol and annealing at  $180\text{ }^\circ\text{C}$  for 1 hour [2, 3]. This may appear to be a “low-temperature” method, however, the conversion of the tin chloride into tin oxide requires a higher temperature than desirable as well as a significantly long annealing time, which would hinder the use of this precursor in a roll-to-roll setting. Reduction of the temperature and annealing time is crucial for a roll-to-roll compatible tin oxide electron transport layer to be realised.

A more obvious candidate for this would be to negate the requirement of a precursor conversion and use a nanoparticle suspension, which should reduce the processing temperature; as only solvent removal would be necessary. In addition to this, processing time should also be significantly reduced as no conversion is required.

It must be noted that during the optimisation of the tin oxide nanoparticle layer in this work two publications were made using the same nanoparticle suspension for slot-die coating. Firstly, Galagan et al used the nanoparticles as part of their roll-to-roll slot-die coated perovskite devices, however, the emphasis in this paper was on the coating of the perovskite layer itself and not the tin oxide [4]. Little information on the tin oxide layer was included, only the formulation used described in the experimental section. A 10 volume% addition of 1-butanol was added to their nanoparticle suspension to aid in the wetting of the solution as it is provided as a water-based suspension. Bu et al also employed this nanoparticle suspension in their perovskite device stack, with a particular focus on the tin oxide layer itself, however, the majority of this was based on spin coated devices. Slot-die coating of the tin oxide layer was discussed, with the formulation including IPA to aid in the wetting of the solution [5]. This group also stated that they slot-die coated the tin oxide layer 3 times to alleviate issues with pinhole formation, which is not a desirable factor for large scale production. Although these two groups have successfully incorporated these nanoparticles in a roll-to-roll setting, the novelty in this chapter arises from the solvent engineering, and more in-depth optimisation and characterisation of the slot-die coated layer itself.

The work in this chapter involves the optimisation and characterisation of two nanoparticle suspensions from two different suppliers. We found that one suspension was unsuitable for perovskite devices due to the formation of pinholes in the layer leading to poor device performances, with different deposition methods unable to alleviate the issue. The second nanoparticle suspension led to excellent spin coated device efficiencies of up to 18% PCE and very

homogenous layers. As the nanoparticles were suspended in water, high surface tension and thus large contact angles prevented the slot-die coating of the solution. Therefore, the rheology was manipulated via solvent engineering to aid in the wetting of the solution on PET/ITO substrates. Finally, a low-temperature (140 °C) slot-die coated tin oxide layer was achieved with comparable characteristics and device efficiencies to a spin-coated equivalent.

## **3.2 Experimental Methods**

Spin coating of perovskite devices was conducted as described in Chapter 2.1. Subsequent characterisation of the device performance parameters were carried out as described in Chapter 2.7. Characterisation of the tin oxide layers themselves were conducted via various methods including; Scanning Electron Microscopy (Chapter 2.6.1), Cyclic voltammetry (Chapter 2.6.3) and Thermogravimetric Analysis (Chapter 2.6.4). Optimisation of the slot-die coated tin oxide layers was carried out by rheological manipulation, using viscosity, surface tension and contact angle measurements as described in Chapter 2.4. Finally, meniscus slot-die coating was carried out using a bench top slot-die coater, fully described in Chapter 2.2.

## **3.3 Results and Discussion**

### **3.3.1 Low-temperature spin coated tin oxide optimisation**

A tin oxide nanoparticle suspension was purchased from Avantama® and was chosen due to it being a suspension in a mixture of butanols, which is an excellent solvent choice for slot-die coating as it coats well on glass and PET substrates as well as having a low-toxicity. The nanoparticles were provided as a 2.5 weight% suspension, with particle sizes of 7 nm and a work function of 4.13 eV which is similar to the work function of a tin oxide layer formed from a tin chloride precursor. Processing conditions were provided by the supplier and a drying temperature of >100 °C for 10 minutes was recommended. Prior to slot-die coating, optimisation of the layer was required and was carried out via spin coating.

To determine the optimal thickness of a layer of these nanoparticles, they were spin coated onto ITO coated glass substrates at varying spin speeds, with perovskite devices then being built on top. Testing of these devices under a solar simulator would then show the best performing devices and thus the optimal thickness. For comparison, these devices were compared against

a control device employing a tin oxide layer formed from a tin chloride precursor. In addition to this, devices with no electron transport layer were produced to determine how effective the tin oxide nanoparticles were. As detailed in Chapter 2.1 The full device stack was finished using the standard fabrication method via spin coating and was made up of the following: Glass/ITO/SnO<sub>2</sub>/Perovskite/Spiro-OMeTAD/Gold (Figure 3.1).

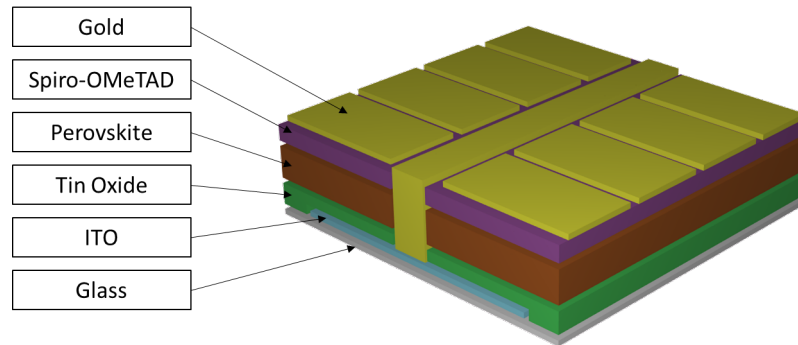


Figure 3.1: Tin oxide perovskite device structure

100  $\mu\text{L}$  of the nanoparticle was deposited onto the glass substrate and three spin speeds were used initially; 2000, 4000 and 6000 rpm, with their thicknesses measured by profilometry and were approximately 60, 50 and 35 nm respectively. A summary of the JV characteristics of the devices are shown in Figure 3.2, which showed the devices prepared with the nanoparticle films to have reduced, very poor and sporadic efficiencies, showing no improvement compared to devices made with no ETL at all. It could be argued that 4000 rpm gave the best performance of the three spin speeds, with a champion efficiency of 10.45% in the reverse scan direction, however, the efficiency of the tin chloride based ETL gave much better, and consistent efficiencies with a maximum PCE of 13.53%. More noticeably, the devices made with no ETL showed similar performances to the nanoparticle-based devices, suggesting that they were not enhancing electron transport, nor blocking holes. Fill factor values for each of the nanoparticle films were very poor, averaging approximately 40%, suggesting high series resistances as well as low shunt resistances, and hypothesised to be due to poor film coverage and a bad interface between the ETL and perovskite layers.

Investigation of the JV curves in Figure 3.3 for the best performing devices from each spin setting, revealed that a severe amount of hysteresis was present between the forward and reverse scans in the nanoparticle films. This suggested that recombination reactions were occurring, most likely down to a poor interface between the ETL and perovskite layer, or incomplete coverage of the ITO by the ETL.

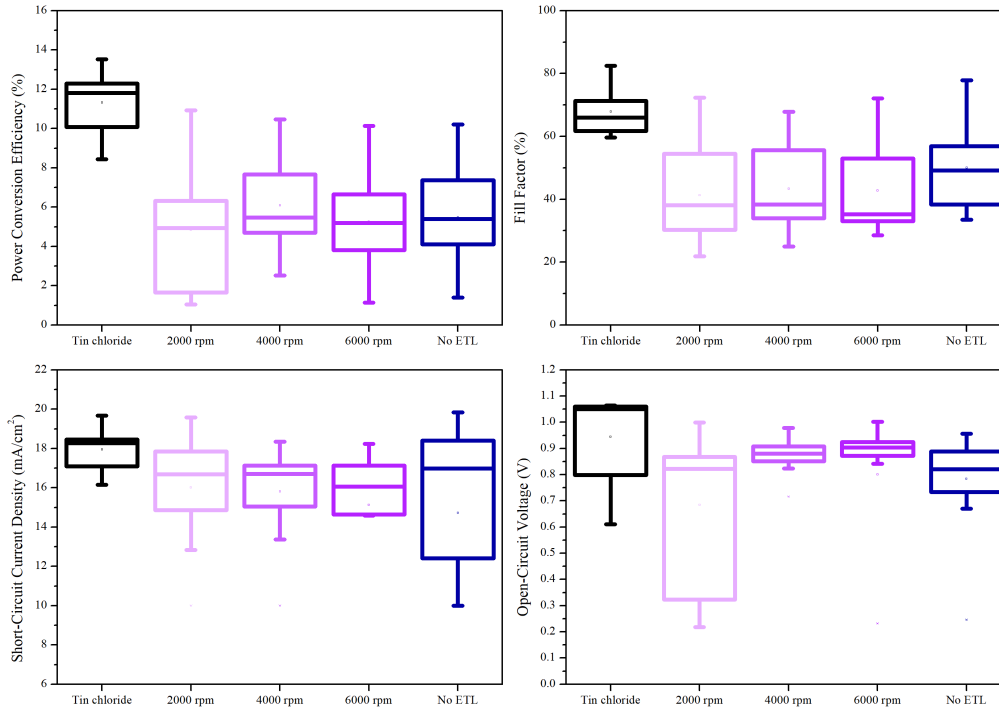


Figure 3.2: Statistical analysis of J-V data from perovskite solar cells prepared from spin coating of Avantama tin oxide nanoparticle ETLs at different spin speeds (Reverse scans). Data presented from 15 devices.

It also appears that the J-V curves for each spin speed were very similar and exhibit the same hysteresis issues, meaning there was a problem with the nanoparticle film morphology, hypothesised to be due to pinholes. To investigate the quality of the nanoparticle films, cyclic voltammetry was used to assess the hole blocking capability and compared to a bare ITO substrate. Tin oxide films were prepared at spin speeds of 4000 and 6000 rpm and cyclic voltammetry was performed on them using the method described in Chapter 2.6.3, employing a ferri/ferro-cyanide electrolyte solution, Calomel electrode and platinum counter electrode. The redox couple made in the ferri/ferro-cyanide electrolyte is made up of small molecules which can easily move into any pores present in the tin oxide film, thus reaching the ITO electrode, making it useful for determining the films hole-blocking ability as well as giving an estimate for surface coverage.

As shown in Figure 3.4 the bare ITO substrate produces a typical cyclic voltammogram exhibiting obvious cathodic reduction peaks as well as anodic oxidation current peaks. An anodic current density of approximately 0.076 mA and peak to peak separation between anodic and cathodic currents of around 50 mV. This shows that a reaction is occurring at the working electrode (ITO substrate), and the peak to peak separation showing a reversible reaction within



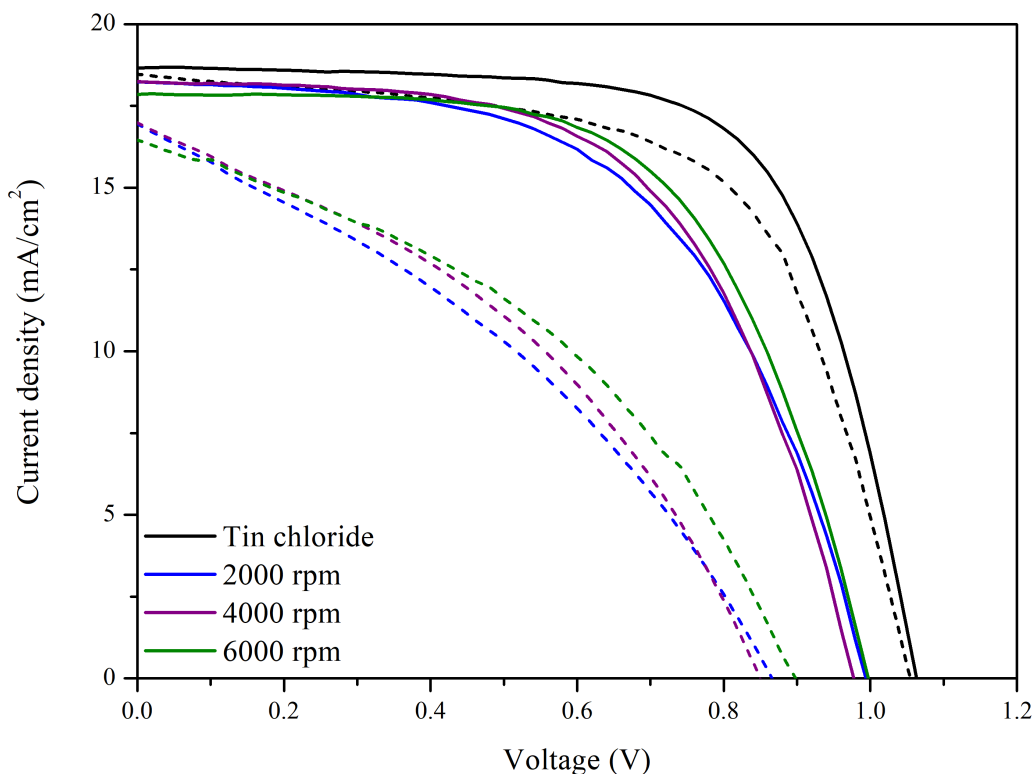


Figure 3.3: J-V curves showing the forward (dashed lines) and reverse (solid lines) scans for best performing devices prepared from spin coating of the Avantama tin oxide nanoparticles.

the electrolyte. For a good performing ETL, the anodic current should reduce, and the peak to peak separation increase. Regarding the nanoparticle films, very similar traces to the ITO substrate were observed, which clearly shows that the films contained a significant number of pinholes allowing the ferri/ferro-cyanide redox couple to reach the ITO surface. In order to determine what a voltammogram for a blocking layer should look like, a tin chloride based control  $\text{SnO}_2$  film was also analysed and included in the voltammogram. The trace for the control film exhibited typical blocking layer behaviour with almost no anodic current.

Table 3.1 summarises the values obtained from the cyclic voltammetry experiments and coincides with the device performances, confirming the cause of the hysteresis observed. Surface coverage of both nanoparticle films was calculated using equation 3.1 as a percentage. This value is qualitative and used as a way to compare different samples' surface coverage numerically.

$$\text{Surface area}(\%) = 100 - \left( \frac{\text{Anodic current}_{\text{sample}}}{\text{Anodic current}_{\text{ITO reference}}} \times 100 \right) \quad (3.1)$$

surface coverage of the nanoparticle films was extremely poor compared to the tin chloride

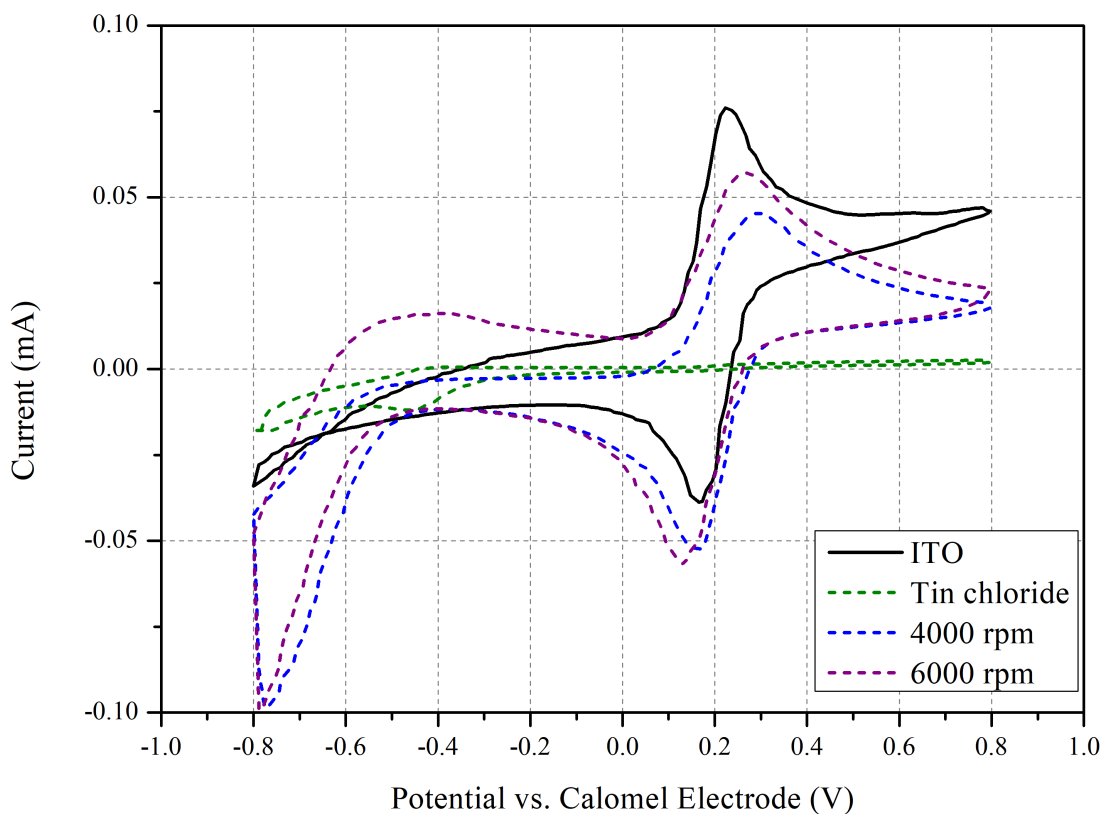


Figure 3.4: Cyclic voltammograms of spin coated Avantama tin oxide nanoparticles vs. bare ITO substrate vs. tin chloride-based control film.

based tin oxide film, which had an approximate surface coverage of 96.58%. With regards to the spin speed used for the nanoparticle films, the surface coverage almost halved from 41% to 25% when increasing the speed from 4000 rpm to 6000 rpm, which was expected as the layer is thinner, revealing more pinholes. Both films did show an increase in peak to peak separation compared to the bare ITO sample, suggesting a change in charge transfer kinetics of the electrolyte redox molecule and the ITO surface signifying slight blocking behaviour. However, the surface coverage was still inadequate for use as an electron transport layer and needed improvement.

In an attempt to fill the pinholes in the film, devices were made again using the same spin speed settings, however, after the film had dried another film was spun on top at the same speed and dried again. A summary of the J-V characteristics in Figure 3.5 shows a definite trend that adding a second layer of nanoparticles can improve the PCE of the devices, with a hero PCE of 15.48% for the device with two layers spun at 4000 rpm. However, a huge variation in data meant that the film quality had not been improved sufficiently, the hero device showed

Table 3.1: Table of cyclic voltammetry parameters calculated for Avantama tin oxide nanoparticles deposited via spin coating, compared to a control film deposited by thermal decomposition of tin chloride

Sample	Anodic Current (mA)	Peak to Peak Separation (mV)	Approximate Surface Coverage (%)
Bare ITO	0.076	50.98	0
SnCl <sub>2</sub> based SnO <sub>2</sub> (4000 rpm)	0.003	1220.56	97
Nanoparticles (4000 rpm)	0.045	122.62	41
Nanoparticles (6000 rpm)	0.057	120.37	25

the largest spread in data with the poorest performing pixel producing a PCE of just 1.62%. Thicknesses of the SnO<sub>2</sub> layers with a single and double coating for 2000, 4000 and 6000 rpm were approximately 60 & 100 nm, 40 & 60 nm, and 30 & 45 nm respectively.

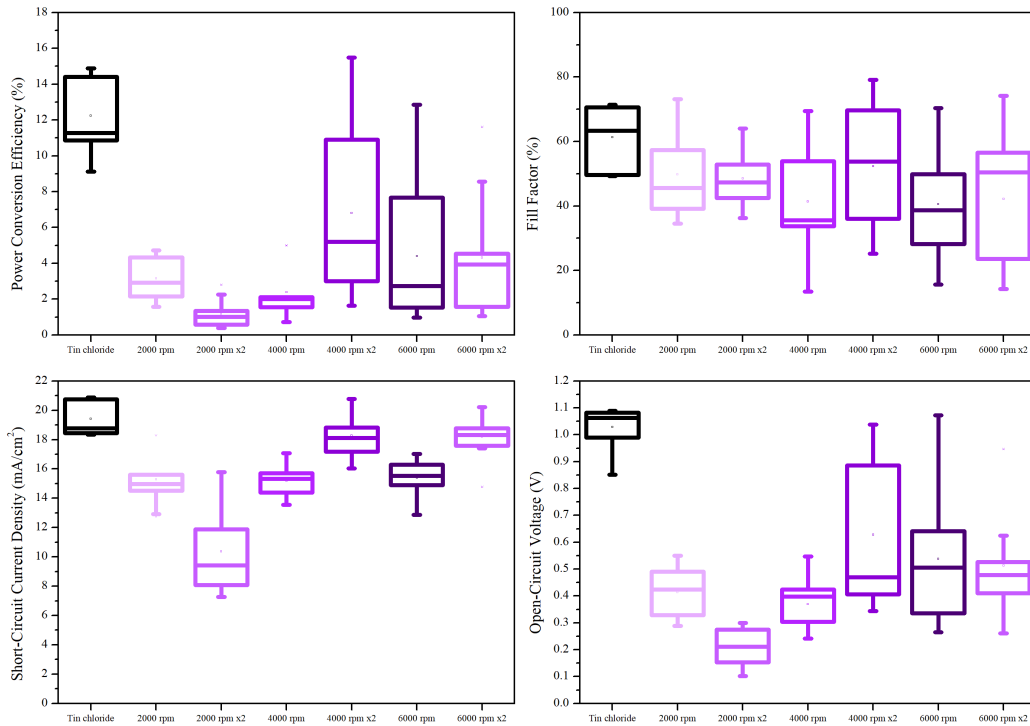


Figure 3.5: Statistical analysis of J-V data from spin coated perovskite solar cells prepared using spin coated Avantama tin oxide nanoparticle ETLs at different spin speeds, including double layers at each spin speed (Reverse scans). Data presented from 21 devices.

Data from one of the devices made with two layers of tin oxide spun at 4000 rpm is summarised in Table 3.2 to show the large deviations. It was clear throughout the samples how unreliable and irreproducible the films were due to the sporadic results shown in the box plots. This was hypothesised to be directly related to the morphology as the films were processed in

the same conditions (annealing time and deposition method) and was in agreement with the poor surface coverages measured with cyclic voltammetry. Firstly, the results for the single layers of tin oxide vastly differed to the results in the first batch of devices, which had reduced from an average PCE of around 9% to approximately 3%. Data did show however that spinning two layers at 2000 and 4000 rpm lead to an increase in current density, suggesting an improvement in surface coverage, and the double layer of 2000 rpm causing a loss in current density, most likely due to the layer being too thick for effective charge transfer to the ITO electrode.

Table 3.2: Table showing the JV characteristics from the hero device fabricated from spinning two layers of Avantama SnO<sub>2</sub> nanoparticles at 4000 rpm

Pixel	Scan Direction	$J_{SC}(mA/cm^2)$	$V_{OC}(V)$	FF (%)	PCE (%)
1	Forward	18.82	0.46	42.19	3.65
1	Reverse	18.46	0.45	36.04	2.99
2	Forward	20.44	0.89	60.2	10.98
2	Reverse	20.78	1.03	71.78	15.48
3	Forward	17.03	0.35	32.01	1.87
3	Reverse	16.04	0.4	25.2	1.62
4	Forward	18.07	0.83	57.9	8.69
4	Reverse	18.13	0.99	69.72	12.56

To determine what the performance issues were down SEM imaging was used to look in detail at the film with two layers of tin oxide nanoparticles spun at 4000 rpm as this had the best performance. Scratches were made in the film prior to imaging for differentiation between the ITO and tin oxide layers which are annotated in Figure 3.6. SEM images clearly show the number of pinholes present in the tin oxide film, and concludes that the poor device performances were due to these pores allowing direct contact between the ITO surface and the perovskite layer, preventing suppression of recombination reactions and inevitably leading to large variations in device performance.

Due to these results, it was safe to assume that the use of cyclic voltammetry was an effective way to determine whether a tin oxide layer would perform well or not and was thus used in further developments rather than relying on JV measurements.

It was thought that the poor film coverage could have been caused by the nanoparticles agglomerating, and thus sonication prior to deposition was attempted. Tin oxide nanoparticles were sonicated for 10 seconds at room temperature and a frequency of 40 KHz. Spin speeds of 4000 and 6000 rpm were used again, with cyclic voltammetry being employed to determine

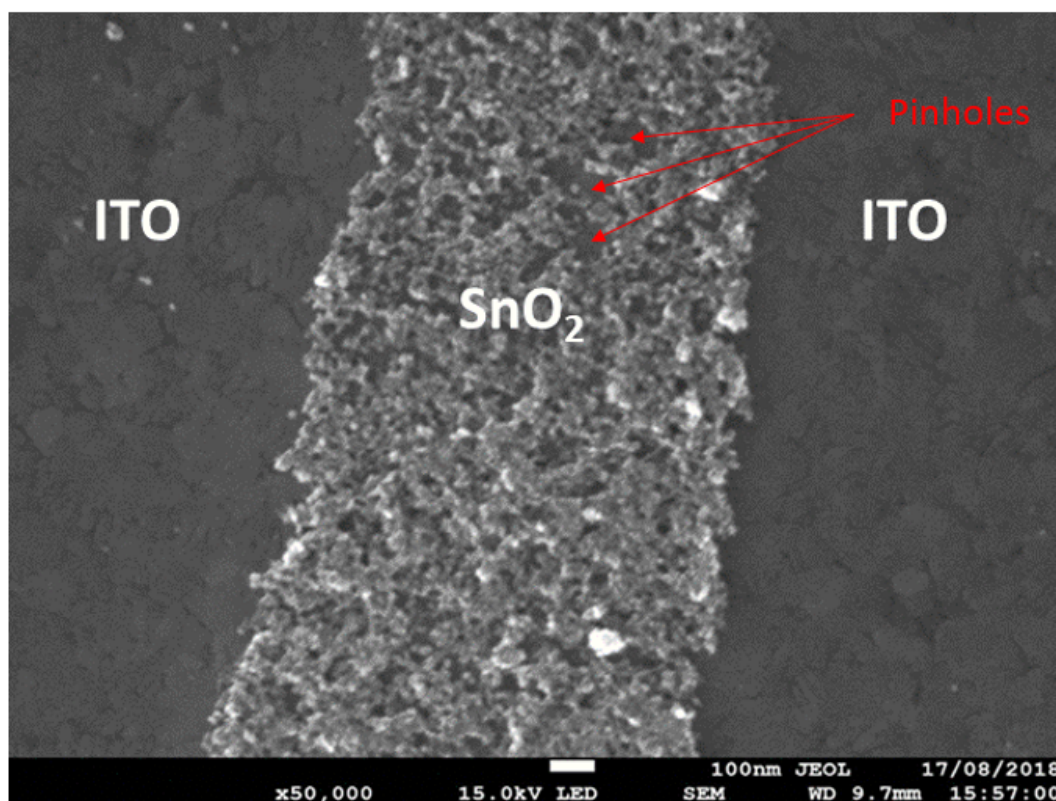


Figure 3.6: SEM image of a spin coated double layer of Avantama tin oxide nanoparticles showing a large amount of pinholes

the surface coverage and hole-blocking capability.

As shown in Figure 3.7, sonicating the nanoparticles did not improve the surface coverage. As seen in the previously spin coated films, peak to peak separation differed compared to the ITO film, showing some charge transfer kinetics changes, however, the surface coverage had gotten worse after sonicating. As expected, the film spun at 6000 rpm had less surface coverage than the 4000 rpm equivalent, which was 9.98% compared to 16.90%. Nevertheless, the films were of very poor quality and not suitable for device fabrication. One final attempt was made to improve the surface coverage of the nanoparticles, and was carried out by spray coating, as this is a proven method for deposition of homogenous compact nanoparticle films such as a Titanium dioxide blocking layer [3][4]. It was thought that spraying several layers of the tin oxide nanoparticles would encourage filling of the pinholes and increase surface coverage. Substrates were placed on a hot plate at 100 °C so the solvent would evaporate rapidly, ensuring the next layer would be sprayed onto a dry film. 3 samples were made and consisted of 10, 15 and 20 spray passes. Cyclic voltammetry was used to determine surface coverage and shown in Figure 3.8.

Surprisingly, surface coverage was worse than spin coating, which is most likely explained

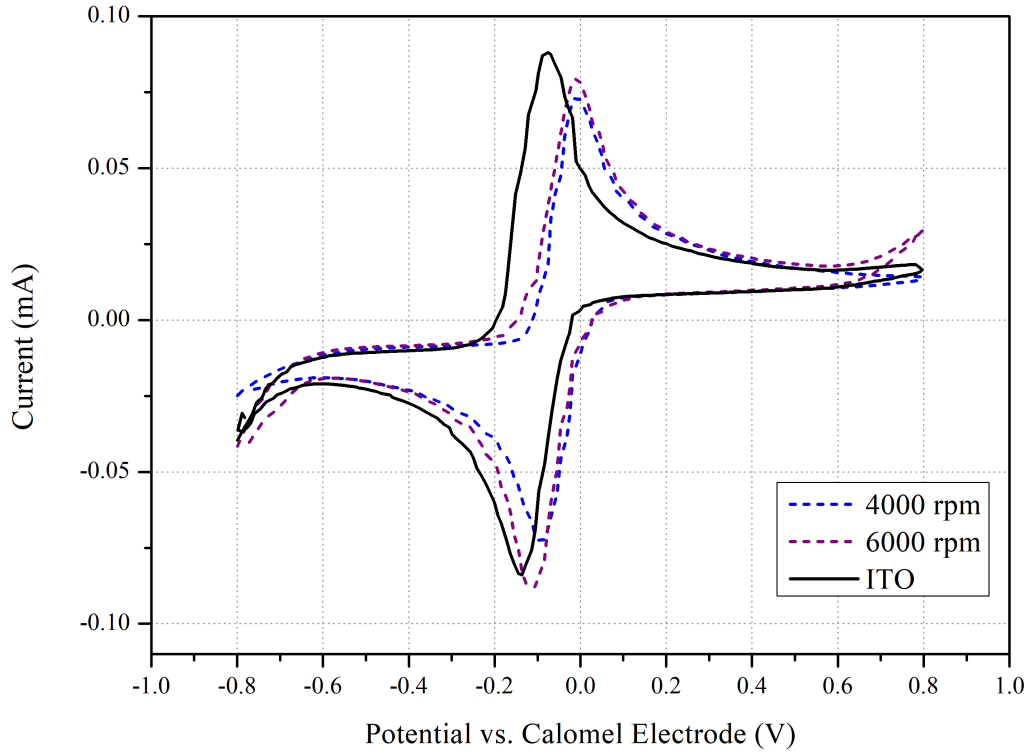


Figure 3.7: Cyclic voltammograms of spin coated Avantama tin oxide nanoparticles after sonication.

by the particles being either too large for the spray coating nozzle, or agglomeration of the particles in suspension preventing even coatings. Nevertheless, using the methods attempted it was not possible to deposit a homogenous layer of these tin oxide nanoparticles capable of providing the necessary electron transport and hole blocking capabilities for use in a perovskite device. A full summary of the surface coverage data from all tin oxide films is shown in Table 3.3 for ease of comparison.

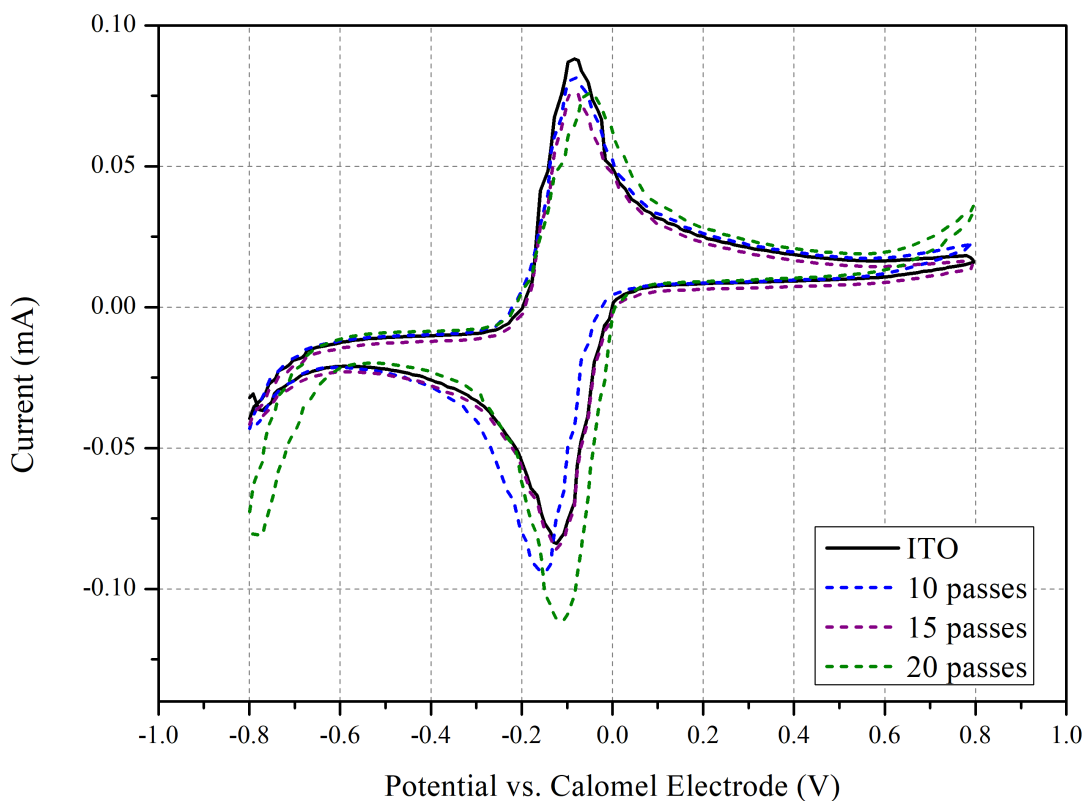


Figure 3.8: Cyclic voltammograms of spray coated Avantama tin oxide films.

Table 3.3: Table showing the approximate surface coverage calculated from CV data for each of the Avantama tin oxide nanoparticle films discussed in Chapter 4.1.

Tin Oxide Film	Approximate Surface Coverage (%)
Tin chloride-based tin oxide (Control)	97
4000 rpm (spin)	40
6000 rpm (spin)	25
4000 rpm (sonicated and spin)	17
6000 rpm (sonicated and spin)	10
10 passes (spray)	7
15 passes (spray)	8
20 passes (spray)	14

As expected, the thicker the tin oxide layer, the better the surface coverage, due to the higher chance of a pin hole being filled with a higher volume of material, shown for either

the lower spin speeds or the higher number of passes for spray coating. The highest surface coverage for a nanoparticle based film was reduced significantly when compared to the tin-chloride based tin oxide film by more than 50%. This appeared to be wholly down to the precursor material causing poor surface coverage, most likely down to particle agglomeration and it was concluded that the nanoparticle film was not suitable for any further optimisation for roll-to-roll processing. A conclusion as to why the nanoparticle films performed so poorly was not found, but was suspected to be caused by poor suspension of the particles in solution leading to inconsistencies in deposition.

During the Avantama nanoparticle optimisation, several publications were made using a colloidal suspension of tin oxide nanoparticles from Alfa Aesar with good performances reported [6, 5, 7]. Avantama did not reveal how the nanoparticles were suspended in the solution, or if they were even suspended at all. However, Alfa Aesar declared that a potassium hydroxide stabilising agent is used to prevent agglomeration of their nanoparticles. This suggested that the Alfa Aesar nanoparticles may provide better coverage due to their stability in solution. Again, these nanoparticles only required removal of the solvent and were therefore roll-to-roll compatible.

Firstly, cyclic voltammetry was used to determine surface coverage as this was a reliable method for confirming the quality of the film from a hole-blocking perspective and would give a good insight into subsequent device performances. As the suspension was provided as 15 weight%, which at the time appeared to be relatively concentrated for a nanoparticle suspension, it was diluted with DI water to the following weight percentages: 2.2, 2.7, 3.2, 3.7 and 4.2%. This time, rather than changing the spin speed to vary the film composition, weight percentages were varied and the spin speed kept the same. This prevented over complication in the optimisation process as changing weight % and spin speed simultaneously would lead to an excessive number of iterations. Due to the nanoparticles being suspended in water, which is less volatile than an alcohol solvent, drying temperature was increased to 140 °C and dried for 10 minutes to ensure full removal of the water. This time was expected to be reduced further as optimisation was undertaken. 100  $\mu\text{L}$  of each dilution of nanoparticles was spun onto ITO coated glass at 4000 rpm with the cyclic voltammograms for each of the films provided in Figure 3.9 and compared to a bare ITO surface

It was immediately clear that these films provided almost perfect blocking layers with little anodic current, and estimated surface coverages of 98, 98, 97, 99 and 99% respectively. When



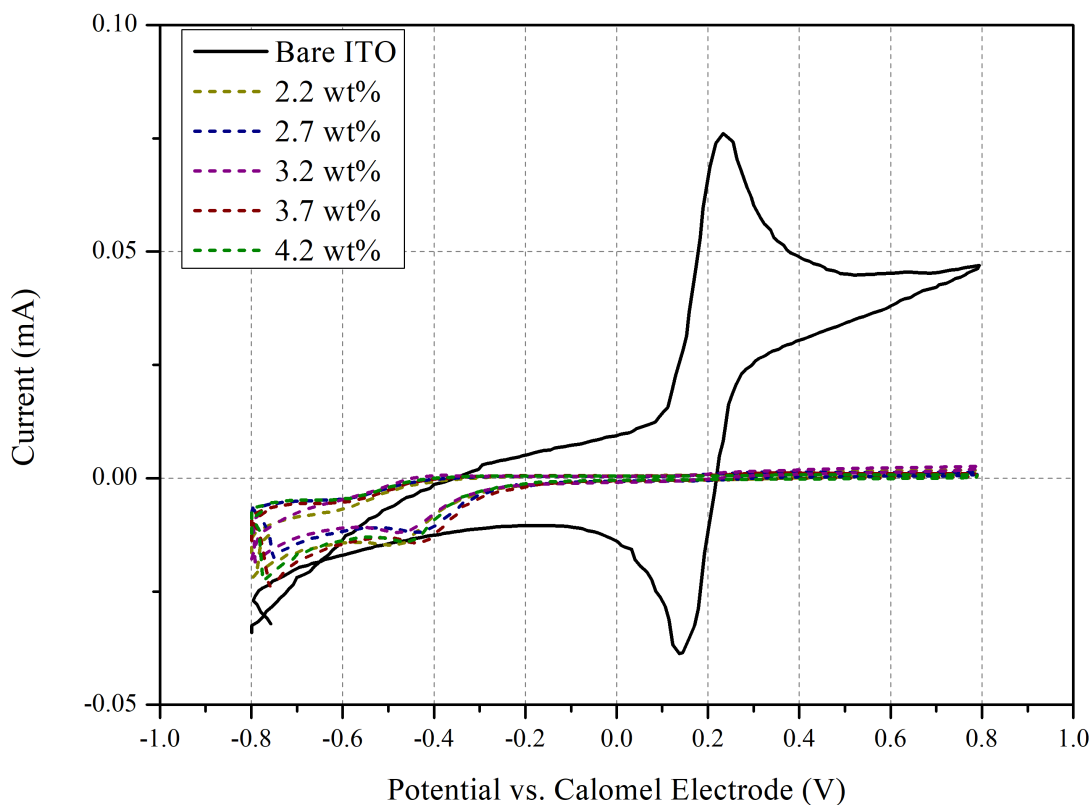


Figure 3.9: Cyclic voltammograms for spin coated Alfa Aesar tin oxide nanoparticles at different weight% suspensions.

compared to the previous batch of nanoparticles from Avantama, the Alfa Aesar suspension clearly showed superior blocking abilities and should theoretically contribute to much more consistent and higher performing devices.

Next the optimal thickness of the tin oxide film was required and found by building perovskite devices on each of the films produced from spin coating of each dilution of nanoparticles. Devices were made as explained in chapter 2.1 And their subsequent JV characteristics summarised in Figure 3.10

Overall, the Alfa Aesar nanoparticle films show greater device performance compared to the previous batch from Avantama and exceeds them in all parameters. In addition to this the performance of all weight percentages of the nanoparticles are either comparable, or better than the tin chloride-based control devices. With respect to the optimal weight% film, 3.7 weight% gave the highest performing pixel with a PCE of 17.46%, however, the film made from the 4.2 weight% suspension gave the highest average performance of 15.02%. Open-circuit voltage measurements were very similar for all the nanoparticle films, although less than the control device, perhaps due to differences in the perovskite/tin oxide interface. Fill

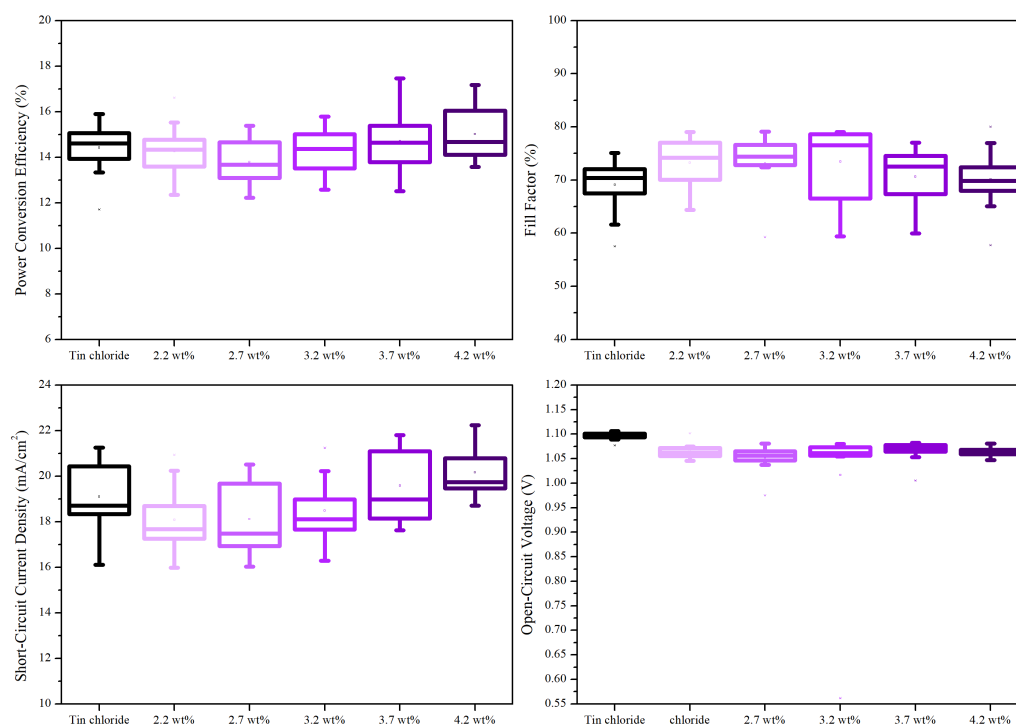


Figure 3.10: Statistical analysis of J-V data from spin coated perovskite solar cells employing increasing weight percentages of Alfa Aesar tin oxide nanoparticles as the ETL (Reverse scans). Data presented from 18 devices.

factors appear to be consistent across all nanoparticle films, and slightly better than the control device, signifying that the nanoparticles are preventing recombination reactions, agreeing with the cyclic voltammetry results. Short-circuit current density shows a general trend upwards as the weight% of the nanoparticle suspension is increased. Although results from this batch of devices gave excellent device performances, a clear optimal weight% suspension was not found, so the experiment was repeated with further increases in weight% in 0.5% increments (Figure 3.11).

After an increase in the amount of film thicknesses tested, two weight% formulations stood out, 3.7 and 4.2%, with the 4.2 weight% film giving a slightly higher average PCE of 16.83% compared to a PCE of 16.52% for the 3.7 weight% based devices. Open-circuit voltages start to drop off as the weight% increases past 4.2 weight% likely due to the films thickness increasing as the weight percentage increases. Song et al analysed the quality of a MAPbI<sub>3</sub> layer on differing weight percentages of SnO<sub>2</sub> nanoparticles and found that higher concentrations led to poor perovskite quality as seen by the holes in Figure 3.12. They also found that when reducing the concentration, the number of holes were reduced and the perovskite quality increased [8]. This would explain the drop in performance in this experiment when the tin oxide layer

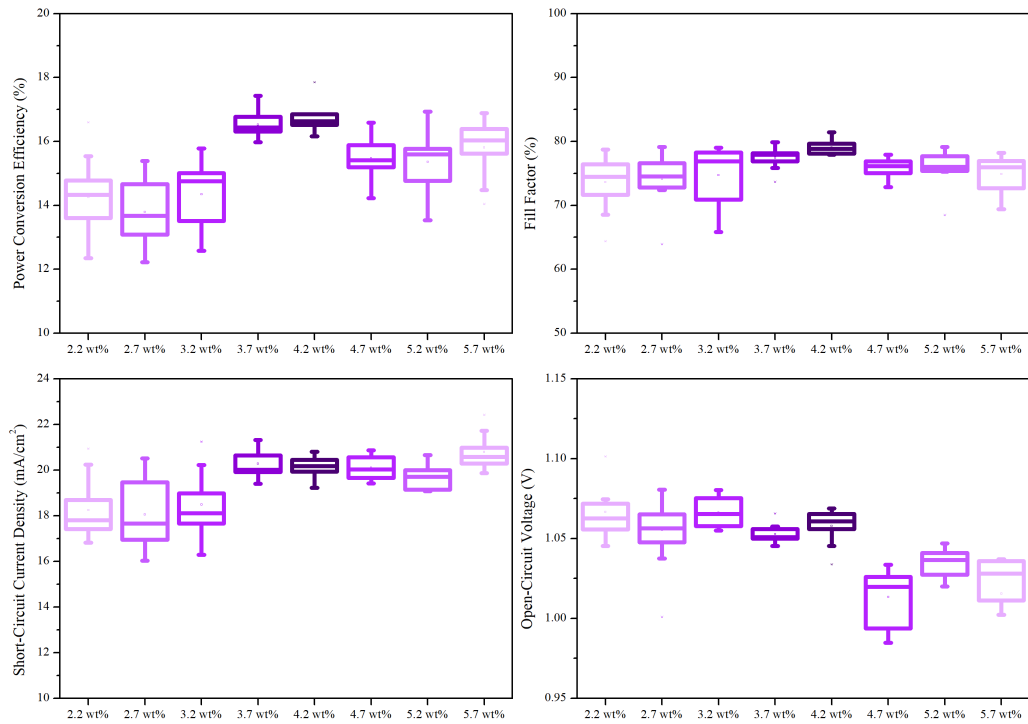


Figure 3.11: Statistical analysis of J-V data from the second optimisation of spin coated perovskite solar cells employing increasing weight percentages of Alfa Aesar tin oxide nanoparticles as the ETL (Reverse scans). Data presented from 24 devices.

increases in thickness.

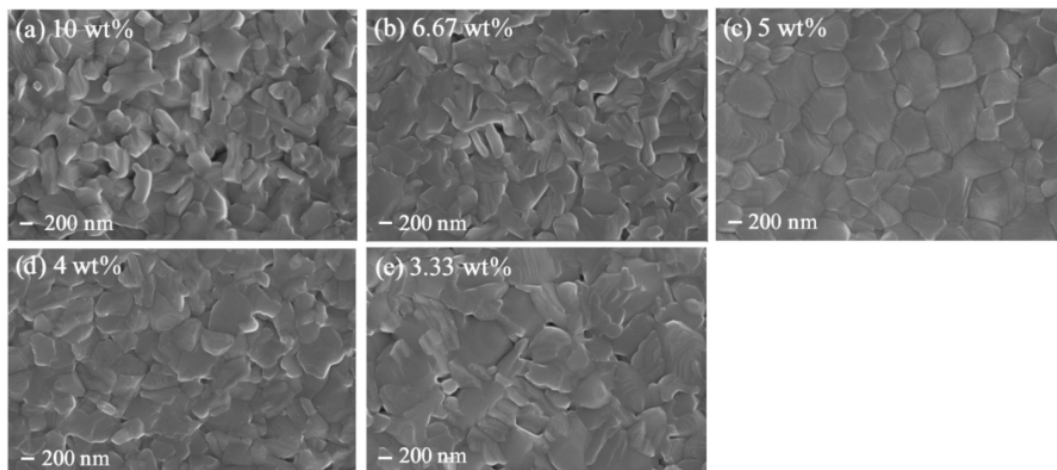


Figure 3.12: SEM images for the perovskite layers formed on different SnO<sub>2</sub> layers. SnO<sub>2</sub> colloid solutions of different concentrations: (a) 10 wt.%, (b) 6.67 wt.%, (c) 5 wt.%, (d) 4 wt.%, and (e) 3.33 wt%. [8]

A summary of the data for each film is given in Table 3.4 as averages across 16 pixels in the reverse scan direction. With regards to the best performing nanoparticle film, the 4.2 weight% suspension gave the highest averages for PCE and FF, with high  $J_{SC}$  and  $V_{OC}$  values as well, and was therefore chosen as the optimal method for a high performance low-temperature tin

oxide ETL. Profilometry was performed on this layer and confirmed it to be approximately 50 nm thick.

Table 3.4: Averages of cell data for spin coated perovskite solar cells with increasing weight % suspensions of Alfa Aesar tin oxide nanoparticles as the ETL (Reverse scans).

SnO <sub>2</sub> Weight%	J <sub>SC</sub> (mA/cm <sup>2</sup> )	V <sub>OC</sub> (V)	FF(%)	PCE(%)
2.2	18.25	1.07	73.63	14.26
2.7	18.05	1.06	74.16	13.80
3.2	18.49	1.07	74.70	14.35
3.7	20.28	1.05	77.42	16.52
4.2	20.13	1.06	79.04	16.83
4.7	20.10	1.01	75.93	15.47
5.2	19.69	1.03	75.94	15.36
5.7	20.79	1.02	74.92	15.81

Figure 3.13 displays the J-V curves for the highest performing nanoparticle-based perovskite solar cell and compared to the tin chloride-based control device. The corresponding key device measurements are shown in Table 3.5.

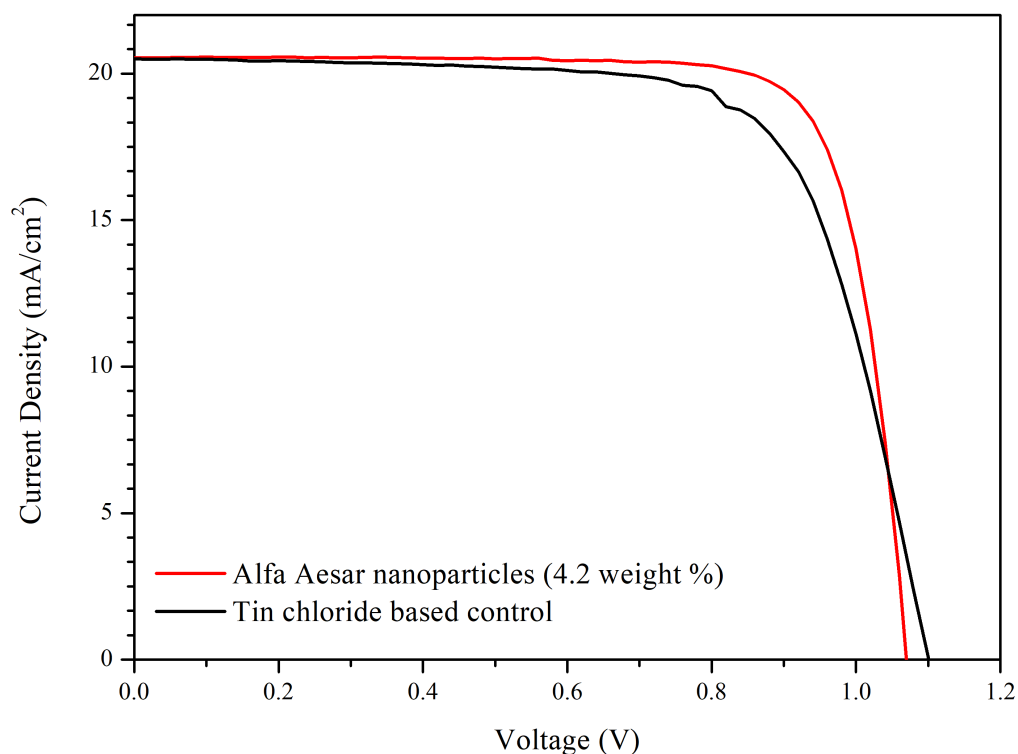


Figure 3.13: Hero device J-V curves for perovskite solar cells employing a tin chloride based tin oxide ETL and a 50nm thick tin oxide nanoparticle ETL (Alfa Aesar). Corresponding device performances are shown in Table 3.5

Device performance was greater than the control device in all aspects apart from a slightly lower V<sub>OC</sub> which was most likely due to the nature of the two precursors, a nanoparticle

Table 3.5: Cell data for hero perovskite solar cells comparing tin chloride based tin oxide ETL to an Alfa Aesar based tin oxide nanoparticle layer (Reverse scans).

ETL	$J_{SC}(mA/cm^2)$	$V_{OC}(V)$	FF(%)	PCE(%)
Spin coated $SnCl_2$	20.5	1.10	70.42	15.89
4.2 wt% nanoparticles	20.56	1.07	81.41	17.86

film would be more rough than a thermally annealed sample thus, the interface between the nanoparticles and perovskite would not be as homogenous. However, based on the JV results, the nanoparticle film was superior in all other aspects and therefore chosen as the method for further work on flexible substrates. Figure 3.14 shows an SEM micrograph of the Alfa Aesar and Avantama nanoparticle films. Unfortunately, higher magnifications on the Alfa Aesar films were unsuccessful due to the nature of the film. Therefore, comparison was only possible at low magnifications in which no discernible difference between the two was noticed. However, the JV and CV results proved the Alfa Aesar nanoparticles were the preferred option.

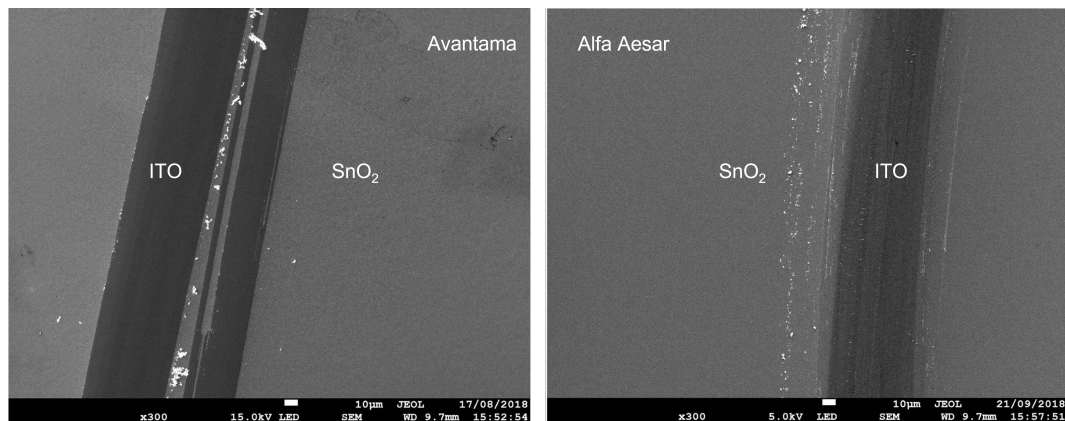


Figure 3.14: SEM micrographs comparing Alfa Aesar and Avantama  $SnO_2$  nanoparticle films on top of ITO coated glass. Scratches were made on the films to differentiate the ITO from the  $SnO_2$ .

In conclusion, a method for depositing a high performance, low-temperature tin oxide layer had been achieved. Perovskite device performance exceeded that of a thermally annealed tin chloride based tin oxide layer which requires annealing for 1 hour at 180 °C, whereas the nanoparticle layer only requires drying at 140 °C for 10 minutes. A difference in 40 °C may not sound substantial, but it is important to note that this film was being optimised for deposition onto a PET substrate, and subjecting a PET film to 180 °C, especially in a roll to roll setting would lead to stretching, or even full breakage. In addition to this, the Alfa Aesar nanoparticles outperformed the Avantama nanoparticles significantly, most likely due to the

way in which the nanoparticles were suspended in their solutions. This was not investigated any further, however, to conclude this hypothesis Dynamic Light Scattering (DLS) could be used to determine the effective particle sizes in the suspension. As discussed previously, the Alfa Aesar nanoparticle solution used KOH as a stabilising agent meaning that agglomeration of the particles are prevented, thus providing improved coating quality. A noteworthy mention is that the Alfa Aesar nanoparticles were vastly cheaper than the Avantama equivalent; £10.50/100 mL, compared to £385/100 mL, solidifying the decision to continue with the Alfa Aesar product.

It must be noted that there was a degree of hysteresis present in the JV curves which is shown in Figure 3.15. Hysteresis in SnO<sub>2</sub> devices, and n-i-p structures in general is a common occurrence and can be alleviated via various methods. The reason for the hysteresis has been attributed to low electron mobility of the SnO<sub>2</sub> and high trap-state density in the perovskite film [9, 10, 11]. Many groups have used self assembled monolayers (SAMs) to passivate interfacial trap sites, thus reducing hysteresis [6, 12]. Clearly, the main method for reducing the hysteresis is by surface passivation of the SnO<sub>2</sub> film and should be relatively simple to incorporate into a roll-to-roll coated device stack. Bu et al successfully removed the hysteresis present in a slot-die coated device incorporating the Alfa Aesar SnO<sub>2</sub> nanoparticles by surface passivation using potassium hydroxide (KOH) [5]. They stated that potassium ions have been used previously to reduce hysteresis and that KOH was able to reproduce this effect. In addition, SEM images of perovskite deposited on top of SnO<sub>2</sub> with and without a KOH treatment revealed much larger grain sizes on the KOH treated films, improving the overall device performance and reducing the hysteresis [5]. Although it is important to acknowledge the hysteresis, reduction of it was beyond the scope of this research. To determine a true efficiency in future, stabilised PCE measurements were also taken.

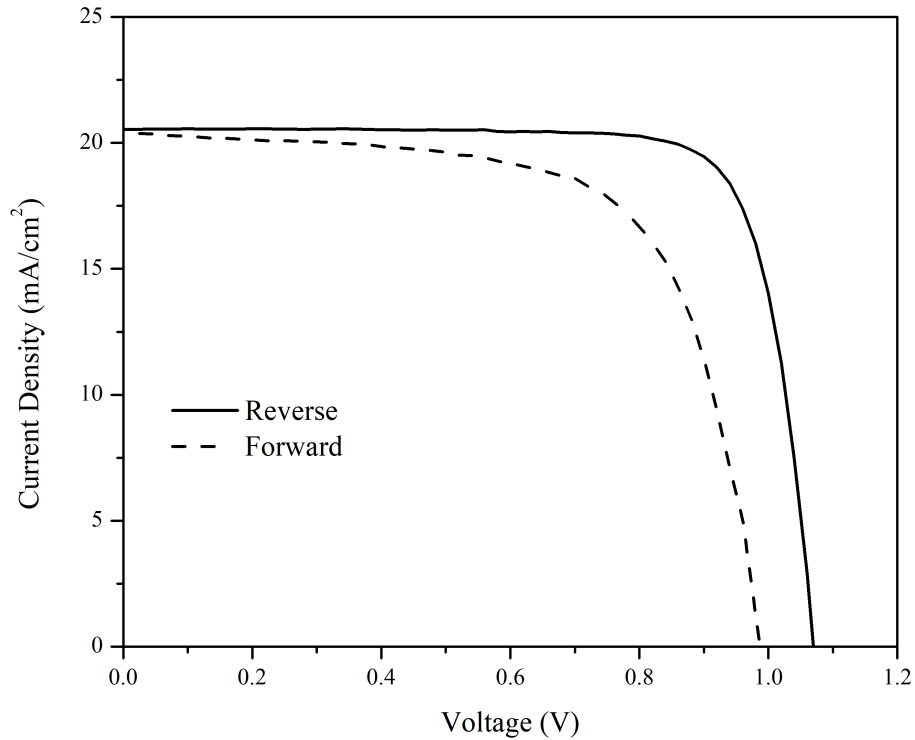


Figure 3.15: Forward and reverse scans for SnO<sub>2</sub> nanoparticle ETL showing hysteresis.

### 3.3.2 Slot-die coating of tin oxide

Research then moved onto slot-die coating of the Alfa Aesar nanoparticles, with the focus aimed at deposition onto pre-patterned 30 x 10 cm flexible ITO coated PET substrates using a 90 mm wide slot-die coating head. As the optimal thickness of the nanoparticle film was found to be 50 nm, calculations were required to determine the weight percentage required for slot-die coating. Using Equation 1.3 and setting a wet film thickness of 5  $\mu\text{m}$ , the weight% of tin oxide nanoparticles needed to be 1.2%, and was therefore diluted from the stock solution using DI water. Initial coating was performed on a plain piece of soda glass to determine how well the solution would coat due to its high surface tension (72 dynes/cm), however, plasma treatment of the glass reduces the contact angle from 90° to >5°, ensuring good wetting. A 5  $\mu\text{m}$  layer was slot die coated with a gap height of approximately 50  $\mu\text{m}$  at 0.25 m/min and dried in the slot-die coaters inline ovens for 10 minutes at 140 °C and 100% air flow. Wetting was not an issue due to the plasma treatment reducing the contact angle of the water based solution, however, a large amount of defects were present in the dry film and shown in Figure

3.16. These defects were due to the low volatility of the water, and therefore producing a non-homogenous layer unsuitable for perovskite solar cell manufacturing.

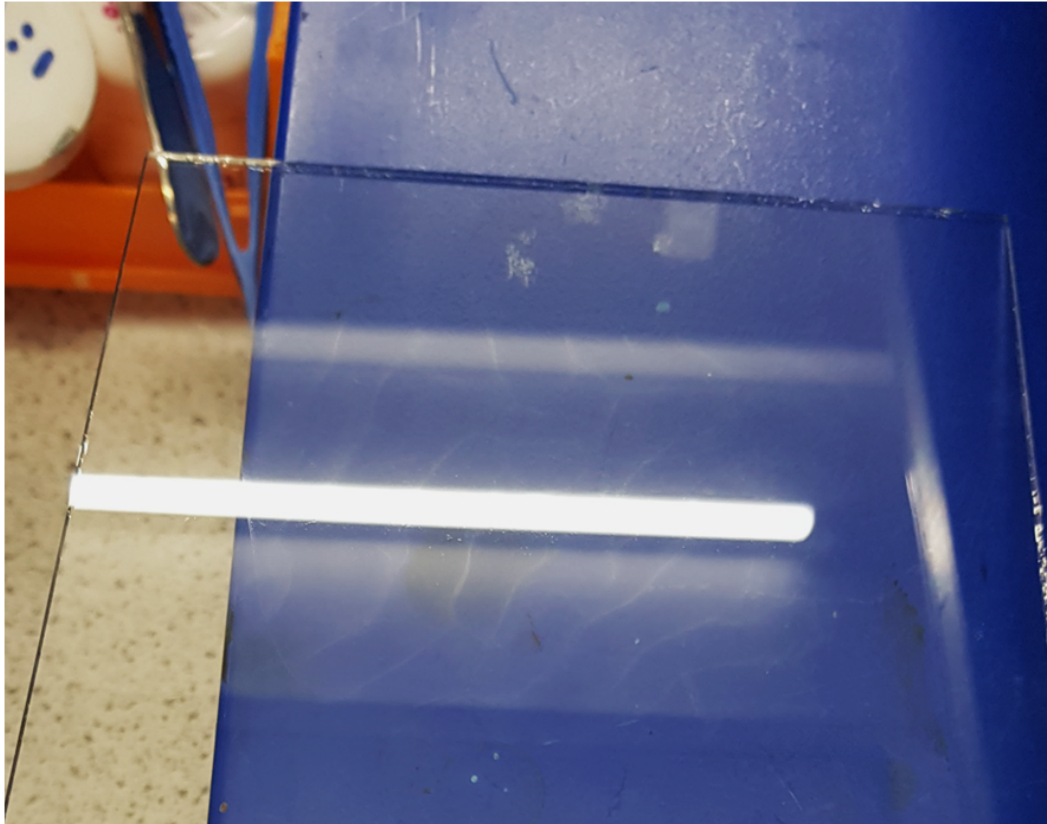


Figure 3.16: Photograph of dry slot-die coated tin oxide nanoparticle film on plasma cleaned soda glass.

Due to the drying issues present using the water-based nanoparticle solution, optimisation of the rheology was necessary for a homogenous deposition. In addition to this, although the water-based solution coated well onto plasma cleaned glass, the removal of a plasma cleaning process would be beneficial for roll-to-roll coating, and addition of solvents may allow good coating without the need for a substrate pre-treatment. Faster drying of the film would also have the potential to prevent reticulation of the dry film, however, this would require elevated temperatures and would remove the low-temperature aspect of the deposition, as well as exceeding the maximum compatible substrate temperature. Solvents had to be chosen with two constraints; water miscibility, and more importantly, toxicity, as this method must be scaled up to large scale coating lines. Two solvents were chosen initially; isopropyl alcohol (IPA) and ethanol (EtOH) as they both have low toxicity and are suitable for large scale deposition, as well as being well-established solvents used in industrial coating processes. Each solvent was used to dilute the initial 15 weight% nanoparticle solution to 1.2 weight%, however, this caused the



nanoparticles to agglomerate and precipitate out of suspension.

Figure 3.17 shows images of the nanoparticles precipitating, which was later discovered to be due to a change of pH in the solution from basic to neutral. Controlling the pH of a nanoparticle suspension is crucial to prevent the agglomeration of the particles. Nanoparticles are stabilised by electrostatic repulsive forces, and the pH of a solution has a significant effect on these forces [13]. Particle agglomeration is observed in nanoparticle suspensions at differing pH values based on the isoelectric point of the metal oxide, and adjusting the pH value far from the  $pH_{iso}$  leads to changes in the effective particle sizes. The addition of a large amount of solvent was enough to shift the pH to neutral, thus far from its  $pH_{iso}$ , confirmed using pH papers comparing the water based solution to the solution diluted with IPA.

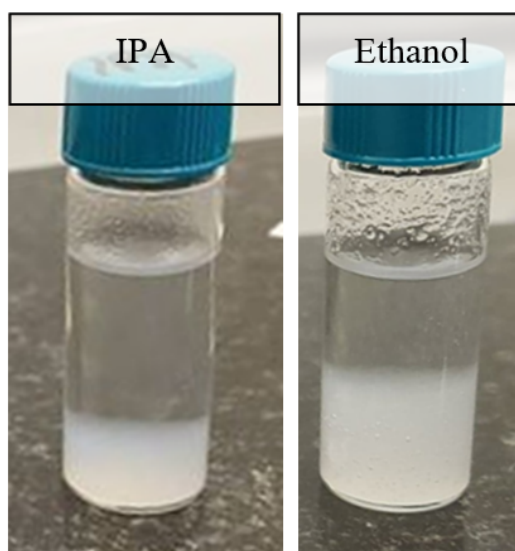


Figure 3.17: Photographs of tin oxide nanoparticles diluted to 1.2wt% using IPA, and ethanol.

Figure 3.18 illustrates how the pH changes upon dilution with IPA, represented by a colour change on pH test strips. To prevent the pH from changing and the nanoparticles from precipitating, smaller additions of each solvent were added by volume% ensuring enough DI water was also used to reach the desired nanoparticle weight of 1.2%. Precipitation of the nanoparticles was confirmed by a “milky” appearance, which occurred at 60 volume% for IPA and 70 volume% for ethanol. Images of these dilutions as the volume percentage of each solvent is increased in 10% increments are shown in Figure 3.19.

Rheology measurements were then made on each of the solutions to find the ideal solvent system for slot-die coating, which would be determined using the visco-capillary model discussed in Chapter 1.5.1.1. Viscosity and surface tension measurements are summarised in

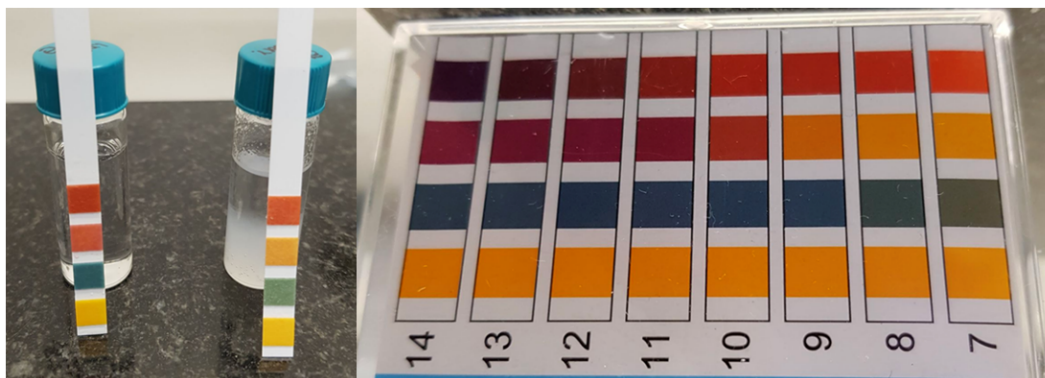


Figure 3.18: Photographs showing the change in PH of the nanoparticle suspension before and after dilution with IPA.

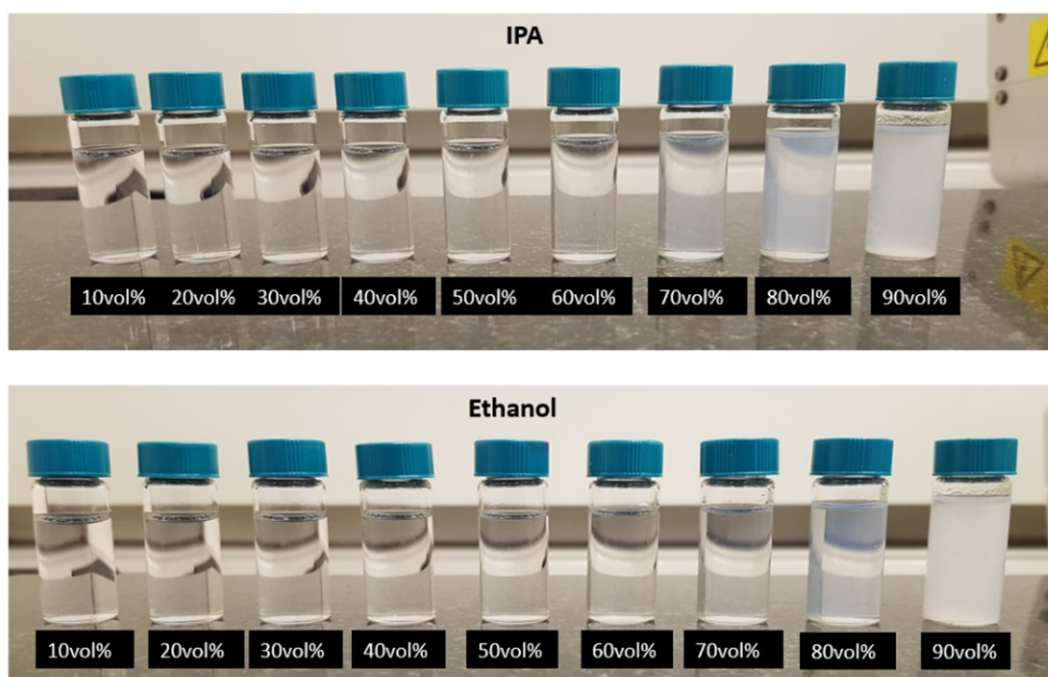


Figure 3.19: Photographs of tin oxide nanoparticles diluted to 1.2 wt% using increasing volume percentages of IPA and ethanol.

Table 3.6 and the contact angles of each solvent system on an ITO surface shown in Figure 3.20. Measurements were not made on the solutions in which the nanoparticles had precipitated.

A variety of formulation contact angles, viscosities and surface tensions were therefore available through choice of solvent and the subsequent volume% additions. Using the visco-capillary model to predict whether each solvent system would produce a stable coating would prevent unnecessary “trial and error” experiments. Using the model as discussed in Chapter 1.5.1.1, each solvent system required plotting to give a good estimate as to how stable the coating would be.

However, prior to calculating the capillary numbers, two set parameters were required for

Table 3.6: Rheological properties of tin oxide nanoparticle solvent systems using increasing volume % additions of ethanol and IPA. Viscosity and surface tensions measured at 25 °C.

Volume%	Viscosity (mPa.s)		Surface tension (Nm <sup>-1</sup> )	
	Ethanol	IPA	Ethanol	IPA
0	1.07	1.07	71.92	71.92
10	1.25	1.54	59.0	41.0
20	1.80	2.49	50.0	32.1
30	2.08	2.54	44.5	27.5
40	2.32	2.58	38.5	26.0
50	2.43	3.25	36.0	24.0
60	2.36	3.56	32.3	23.5
70	2.17	N/A	28.8	N/A

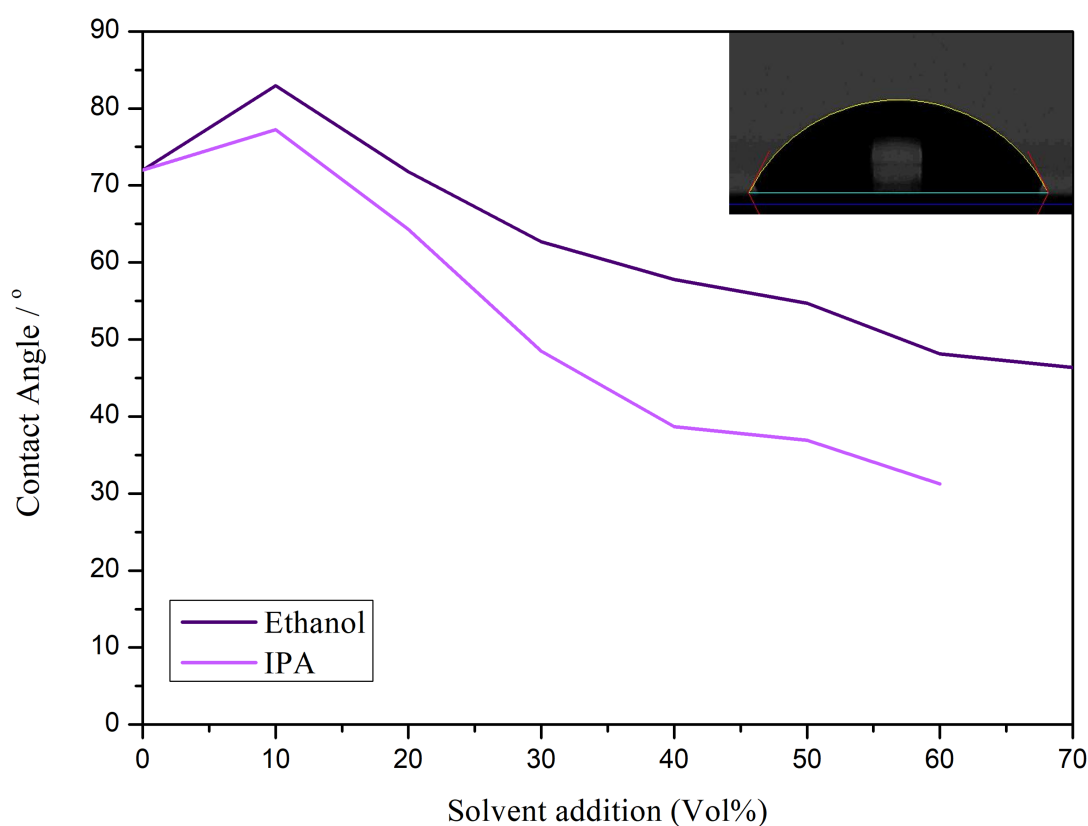


Figure 3.20: Contact angles of both tin oxide nanoparticle solvent system as a function of increasing volume% additions of IPA and ethanol. Inset is an image taken during the measurement of a 5 volume% IPA solution

the slot-die coater; coating speed and head-substrate gap. Use of a meniscus guide in the slot-die set up was employed to aid the formation of the meniscus between the slot-die head and the substrate, which protruded 1000  $\mu\text{m}$  below the lips of the slot-die head. Gap-height between the meniscus guide and substrate was then determined by personal choice and was selected at 200  $\mu\text{m}$  giving a total head-substrate gap height of 1200  $\mu\text{m}$ . This was a good compromise

as smaller gaps become more difficult to measure accurately. This gap height was set prior to each coating as accurately as possible using feeler gauges. Secondly, the coating speed was required as it is directly related to the residence drying time in the coater's ovens. As the film only requires drying it was relatively simple to determine an approximate drying time using ThermoGravimetric Analysis (TGA). To be safe, the sample tested was a 40 volume% IPA solvent system as further increments of volume% additions will only decrease the drying times due to the increased amount of the more volatile solvent. 100  $\mu$ l of the nanoparticle solution was placed into an alumina crucible in the TGA furnace and subjected to a heat ramp from 30 °C to 140 °C at its maximum speed with the weight% of the solution being recorded throughout.

Figure 3.21 shows the weight% of the solution as a function of time and temperature

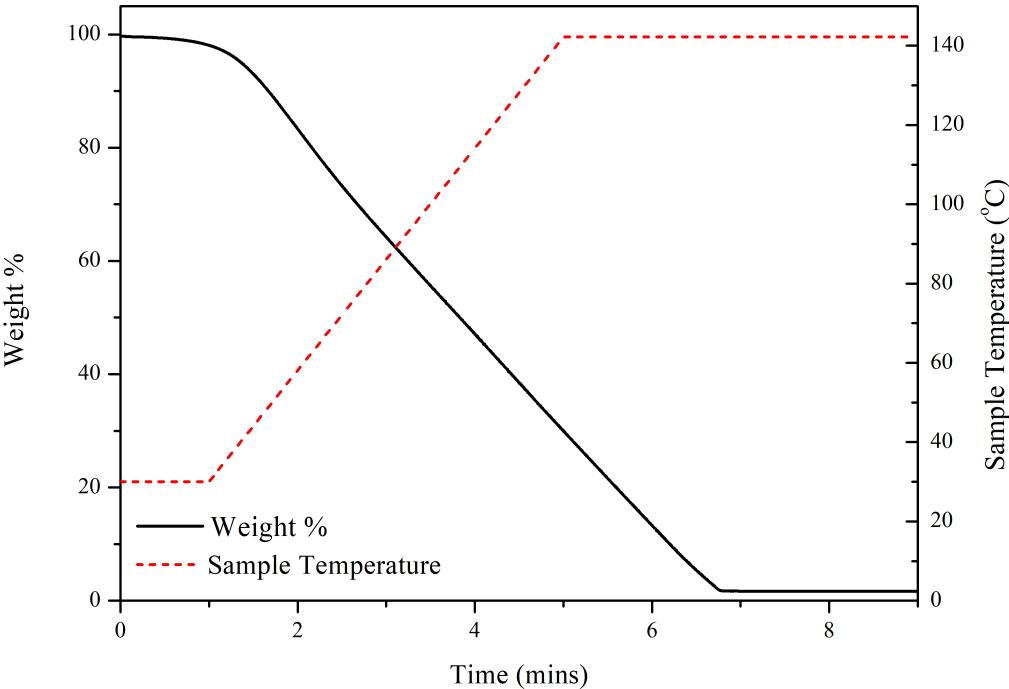


Figure 3.21: TGA of a 1.2 weight% tin oxide nanoparticle solvent system with a 10 volume% addition of IPA.

By the time the sample temperature had reached 140 °C, approximately 70 weight% of the solution had already evaporated. In addition to this, the coated wet film would be significantly thinner than the sample in the crucible, leading to even faster evaporation. This showed that a very short drying time was required, and that a coating speed could be chosen with relative leniency. Since the main objective for the tin oxide electron transport layer was roll-to-roll deposition within a smart coater coating line, parameters were chosen to suit this. The smart coater has a 1 metre long oven, and therefore a coating speed of 0.25 m/min was chosen which

would give a 4-minute residence drying time, more than long enough for drying of the wet film. Initial trials would, however, be conducted on a FOM benchtop coater with a 30 cm long oven, so the substrate speed was changed after the film had been coated to 0.125 m/min as to keep the residence drying time at 4 minutes. As the coating parameters had been chosen, visco-capillary models could be plotted for each solvent system and theoretical coating stability determined. As shown in Figure 3.22, the capillary number for each nanoparticle solution is displayed on the two visco-capillary models, with the stable and unstable boundaries clearly identified. Most of the solvent systems were predicted to be stable, apart from two IPA additions; 50 and 60 volume%.

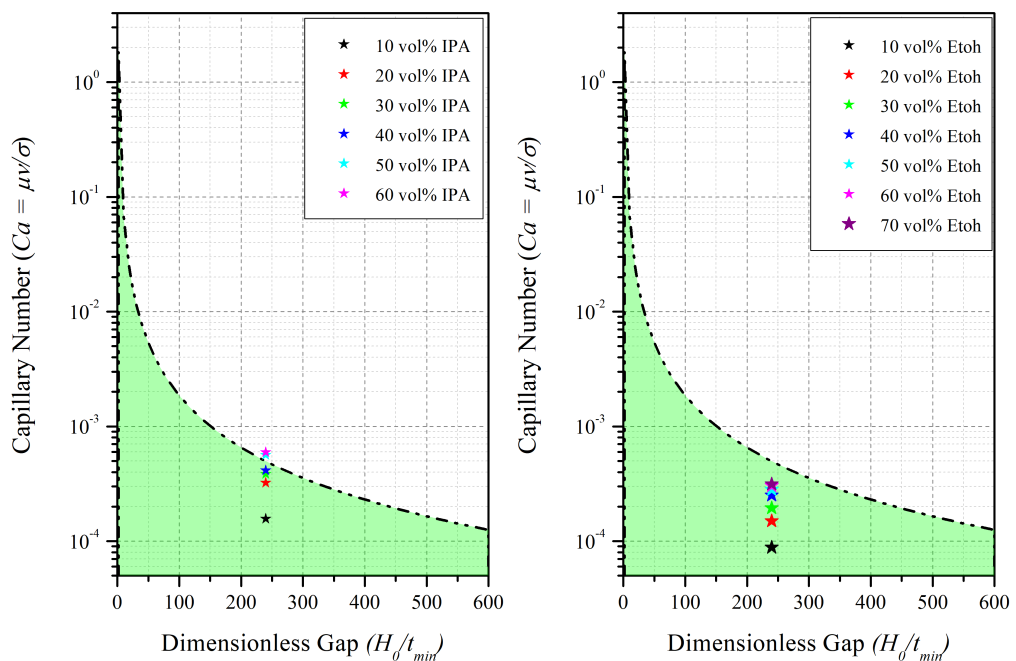


Figure 3.22: Visco-capillary model of Alfa Aesar tin oxide nanoparticle IPA and ethanol solvent systems.

Prior to slot-die coating of the chosen solvent systems, it was decided that a validation of the visco-capillary model was required, more for peace of mind that the model could be used with confidence in future slot-die coating solution optimisation. Due to the solution containing 60 volume% of IPA predicted to produce unstable coatings, it was a good example to see if it could be made stable either by manipulating the capillary number (change the speed) or altering the dimensionless gap by reducing the head-substrate gap, or increasing the wet film thickness. Increasing the wet film thickness was the safest option as this would remove any human error,

whereas reducing the gap height to a value low enough to reduce the dimensionless gap would not be as accurate. By increasing the wet film thickness from 5  $\mu\text{m}$  to 10  $\mu\text{m}$  the dimensionless gap is reduced from 240 to 120, thus moving the 60 volume% IPA solution into the stable range. In order to validate the visco-capillary model, films coated in the stable, and unstable region would need to be analysed for visualisation of the coating quality. As the nanoparticle solution was transparent, a small amount of pararosaniline acetate dye was added, ensuring that the viscosity of the solution was unchanged (1 mg/ml).

Figure 3.23 shows the change in dimensionless number when the wet film thickness is increased from 5  $\mu\text{m}$  to 10  $\mu\text{m}$  for 60 volume% IPA solvent systems, which in turn moves the solution into the stable coating region. Films were coated onto ITO coated PET at 0.25 m/min with both 5 and 10  $\mu\text{m}$  wet films, dried in an inline oven at 140 °C for 4 minutes and images scanned of each. In addition to this a 40 volume% solution was also coated with a wet film of 5  $\mu\text{m}$  for comparison as it was predicted to provide stable coatings. Images for each of the coated films in Figure 3.23 clearly show that printing a 5  $\mu\text{m}$ , 60 volume% IPA solution leads to unstable coatings, with significant defects, whereas increasing the wet film to 10  $\mu\text{m}$  appears to stabilise the coating. Due to these results it was concluded that the visco-capillary model could be relied upon for any further coating trials using similar solvent systems, it did not however, confirm the reliability when using high viscosity fluids, which was beyond the scope of this research.

Two solvent systems were then chosen for further coating trials, 40 volume% IPA, and 70 volume% ethanol. For experimental consistency it was decided that using the same wet film thickness for the IPA and ethanol solutions would be preferred, and therefore was kept at 5  $\mu\text{m}$ , meaning that the 50 and 60 volume% IPA solutions were invalid due to them being in the unstable coating region of the visco-capillary model. Each solvent system was chosen for its maximum volume% of solvent due to them having the lowest contact angles, which theoretically would coat better than their lower volume% equivalents. Sheet-to-sheet slot-die coating was performed for optimisation prior to deposition in a roll-to-roll coater, mainly due to cost savings on the amount of substrate required to run a roll-to-roll trial. Scaling up from a benchtop coater to a roll-to-roll coater is simple, if the same parameters are used, the coatings should be identical. Sheet-to-sheet coating was performed using 10 x 20 cm ITO coated glass (15  $\Omega/\text{cm}$ ) and 10 x 30 cm pre-patterned ITO coated PET (50  $\Omega/\text{cm}$ ), with the experimental methods described in Chapter 2.2. Glass substrates were cleaned prior to coating using the

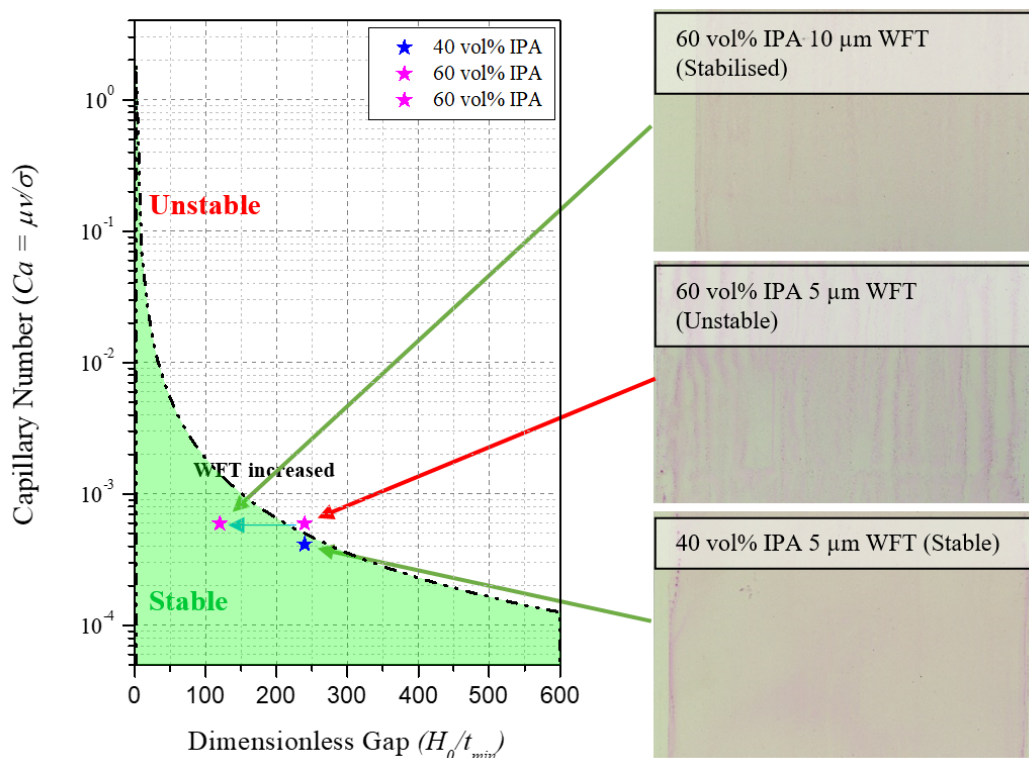


Figure 3.23: Visco-capillary verification. Inserted images are dried films taken with a flat-bed scanner.

same cleaning method for spin coated devices, and PET films did not require cleaning as they are supplied clean on a roll. Each solvent system was then slot-die coated onto each of the substrates and dried for 4 minutes at 140 °C in the slot-die coater ovens, and subsequently cut up into 2.8 x 2.8 cm squares for the remainder of the perovskite solar cell to be spun on top. Four sections of each substrate were chosen at random for device fabrication to ensure an unbiased selection. Cyclic voltammetry was also performed on each of the substrates, and Figure 3.24 suggests that the IPA solvent system leads to better hole-blocking compared to the ethanol system, on both glass and PET. Higher anodic currents for the ethanol-based films are due to having lower surface coverage than the IPA equivalents, with a full summary of these parameters in Table 3.7.

Statistical JV analysis in Figure 3.26 confirms the trend presented in the cyclic voltammetry graphs, with higher performing devices coming from the IPA based solvent system. For both substrate types, the IPA solvent system outperformed the ethanol system, possibly due to the lower contact angle allowing better wetting of the substrate. Efficiencies for the slot-die coated IPA based solvent system on glass substrates reached similar efficiencies to the spin coated control devices, albeit with a larger spread in data points. Further optimisation would

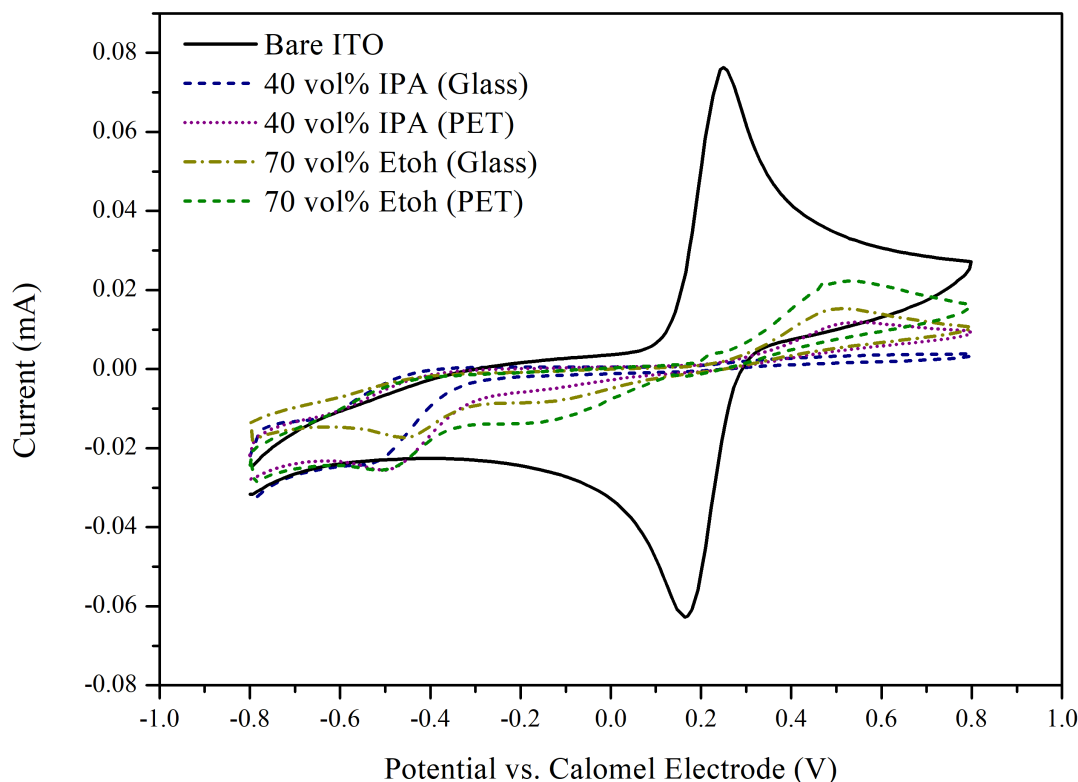


Figure 3.24: Cyclic voltammograms comparing slot-die coated IPA and ethanol tin oxide nanoparticle solvent systems on glass and PET substrates.

Table 3.7: Calculated estimate for surface coverage of slot-die coated tin oxide ETLs from IPA and ethanol solvent systems on glass and PET.

Solvent system and substrate	Anodic Current (mA)	Estimated Surface Coverage(%)
Bare ITO glass substrate	0.076	0
40 volume% IPA (Glass)	0.004	95.00
40 volume% IPA (PET)	0.012	84.48
70 volume% ethanol (Glass)	0.015	79.91
70 volume% ethanol (PET)	0.022	70.87

certainly lead to better consistency. With respect to the IPA based solvent system coated on PET, average efficiencies were lower than the glass equivalent, however, a champion PCE of 15.65% was achieved, proving that it was possible to slot-die coat high performance tin oxide layers. Loss in  $V_{OC}$  for the PET based films was most likely due to poor homogeneity, perhaps due to drying defects. In this section, glass based devices were used to determine whether comparable efficiencies could be achieved between slot-die and spin-coating. It was confirmed that performances were close to spin coating and therefore for the remainder of the optimisation, slot-die coating was only performed on PET substrates. It was clear from the J-V characteris-



tics that the IPA based solvent system lead to better efficiencies than the ethanol based system, thus better surface coverage, coinciding with the CV results in 3.24. This appeared to be due to the ethanol based system having a larger contact angle and higher surface tension than the IPA system.

Images of the slot-die coated films of the IPA and Ethanol based suspensions were taken using a flatbed scanner to see if any differences could be seen. Images were supersaturated to improve the visibility and shown in 3.25. The images show a clear difference between the two films, with the IPA film looking much more homogenous, coinciding with the JV and CV results.

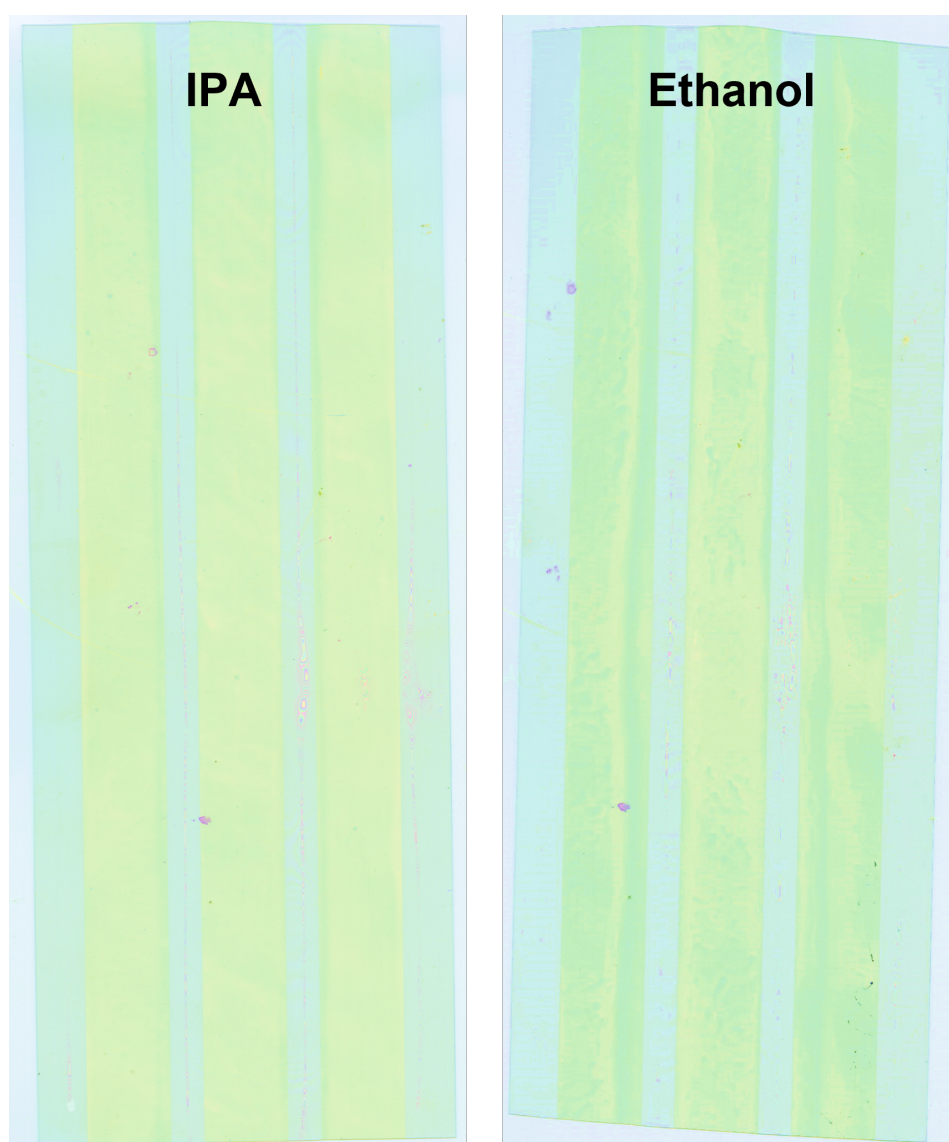


Figure 3.25: Scanned images of the slot-die coated tin oxide films deposited from IPA and Ethanol solvents.

Hero device efficiencies are summarised in Table 3.8 As well as the subsequent J-V curves

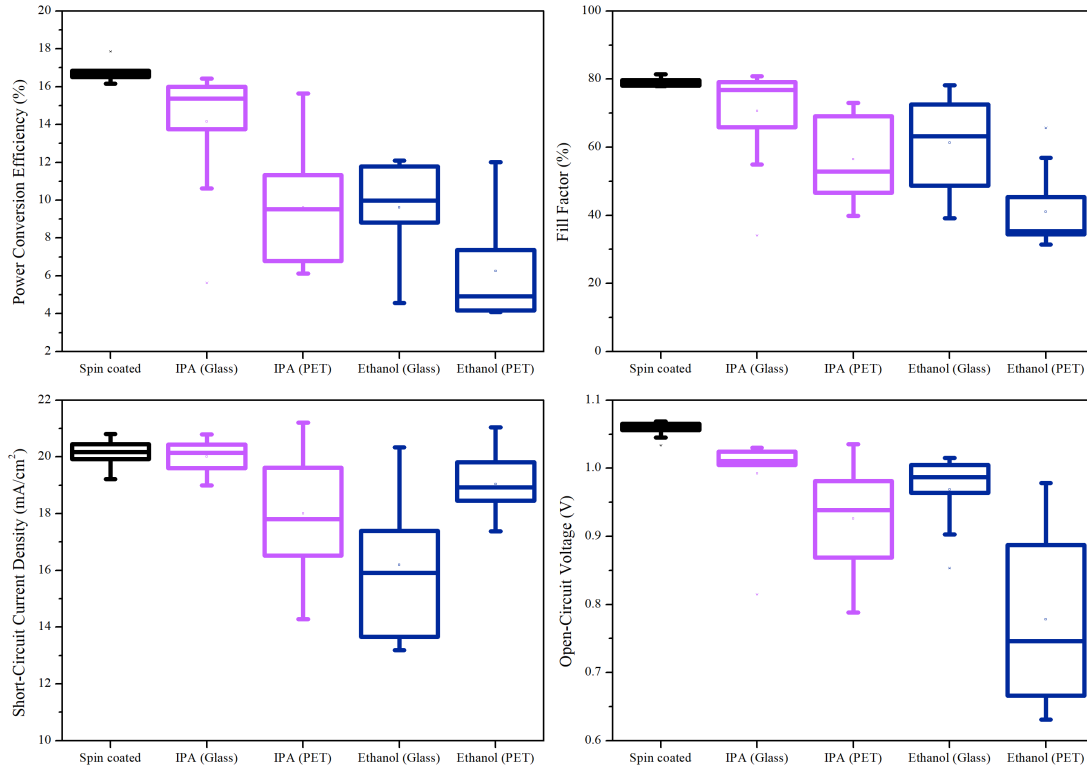


Figure 3.26: Statistical analysis of J-V data from slot-die coating of two different tin oxide nanoparticle solvent systems coated onto ITO coated glass, and PET substrates. Data presented from 20 devices.

plotted in Figure 3.27. As the ethanol based solvent system led to worse performance compared to the IPA system, it was omitted from any further optimisation.

Table 3.8: Cell data for hero perovskite solar cells made with slot-die coated tin oxide nanoparticle ETLs in IPA and ethanol solvent systems (Reverse scans).

Solvent system and substrate	$J_{SC}(mA/cm^2)$	$V_{OC}(V)$	FF(%)	PCE(%)
Spin coat (Control)	20.56	1.06	81.41	17.85
40 volume% IPA (Glass)	20.75	1.01	77.99	16.42
40 volume% IPA (PET)	20.71	1.04	72.97	15.65
70 volume% ethanol (Glass)	15.25	1.02	78.16	12.10
70 volume% ethanol (PET)	18.72	0.98	65.61	12.02

Hero device J-V curves for the IPA based solvent system on a glass substrate were very similar to the spin-coated control device, apart from having a slightly lower  $V_{OC}$ . However, as

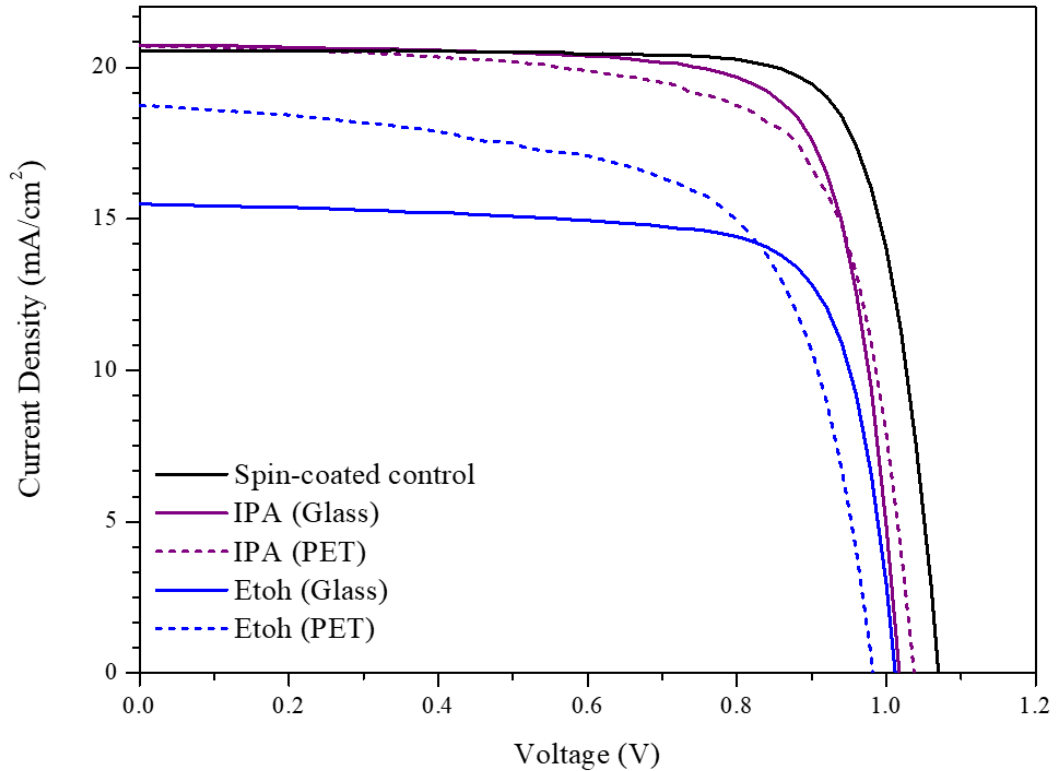


Figure 3.27: Hero device J-V curves for perovskite solar cells using slot-die coated tin oxide nanoparticle ETLs in IPA and ethanol solvent systems. Corresponding device performances are shown in Table 3.8

the focus of the slot-die coated tin oxide ETL was towards roll-to-roll processing, only the PET films were optimised further. Comparing the slot-die coated film on PET to the spin coated control device, a loss in PCE was due to a drop-in fill factor and  $V_{OC}$ , suggesting a difference in morphology leading to a poorer ETL/perovskite interface. In addition to this, the larger spread in data points throughout the pixels in each device had to be addressed, although this was expected from the first trial with a new solvent system. Upon visual inspection of the slot-die coated layers on PET it became apparent that there were several defects which appeared to be induced by drying and not coating defects. “Rippling” was observed, much like the film in Figure 3.16 which was slot-die coated from a water-based solution. Figure 3.29 shows an image taken of the coated film using a flatbed scanner which had been super saturated for increased visibility of the defects, clearly showing the drying defects present, explaining the poor averages of the perovskite device data.

It was first thought that these defects could have been due to the air flow in the coater ovens causing movement of the wet film, thus leading to defects, so films were coated again and dried with the oven fans off, and also dried on a hot plate for comparison.

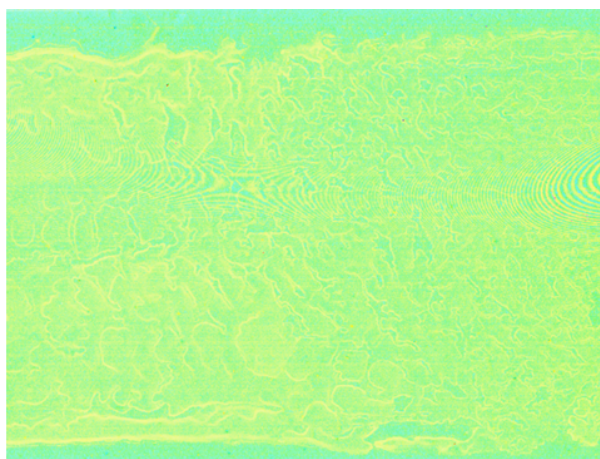


Figure 3.28: Flat-bed scanner image of a slot-die coated tin oxide nanoparticle layer from an IPA based solvent system.

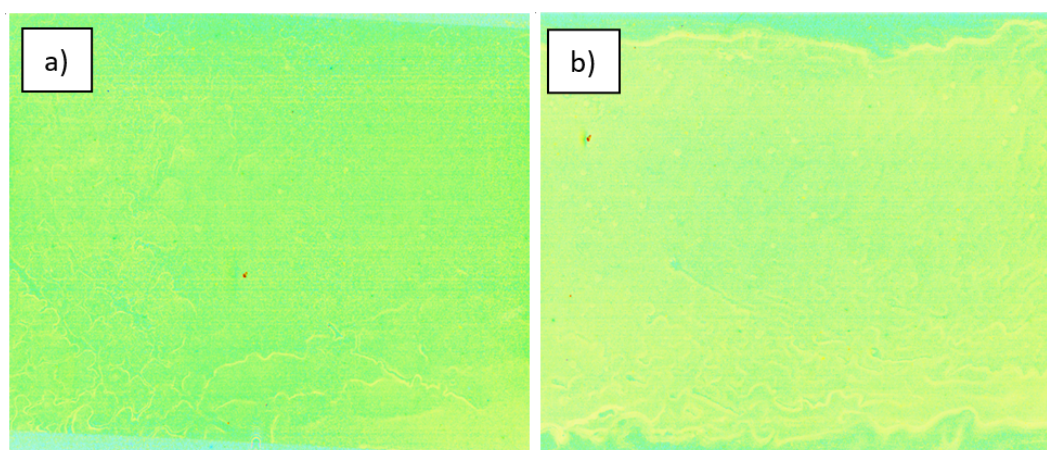


Figure 3.29: Flat-bed scanner images of a slot-die coated tin oxide nanoparticle layer from an IPA based solvent system, dried via: a) a hot plate at 140 °C, and b) in coater ovens with fans off at 140 °C.

Figure 3.29 shows a slight improvement in the film dried on a hot plate, however, significant defects were still present, and recreating this drying process on a roll-to-roll line would be difficult. On the other hand, the sample dried in the coater ovens with the fans off looked no different to the film dried with the fans on (Figure 3.28), concluding that the defects were due to the solvent system itself rather than the drying conditions. As the boiling point of IPA (82.5 °C) is lower than that of water (100 °C), it was assumed that the IPA was evaporating first, leaving the remaining water to reticulate due to its high surface tension. Thermogravimetric analysis of the tin oxide solvent system in Figure 3.30 revealed two separate mass losses illustrated by two different gradients on the weight loss curve confirming that the IPA was evaporating first, and concluding the hypothesis that drying defects were most likely due to this.

Results from the slot-die coating trial and subsequent images showed that IPA was not

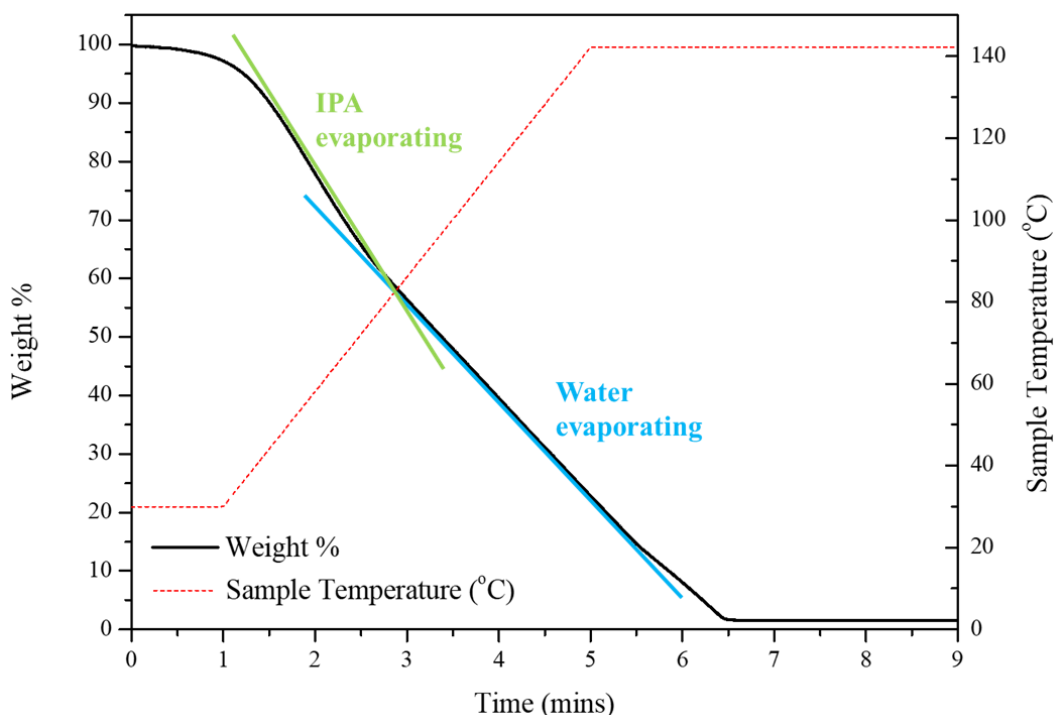


Figure 3.30: TGA graph showing weight loss as a percentage of a tin oxide nanoparticle solvent system with a 40 volume % addition of IPA.

a suitable solvent for depositing homogenous films of tin oxide nanoparticles due to its low boiling point and volatility. In order to improve the quality of the films a new solvent system was required, and two new solvents, 1-butanol and 1-propanol were chosen as their boiling points of 117.7 °C and 97 °C respectively, were higher than that of IPA. These solvent systems were then compared to IPA and ethanol using cyclic voltammetry, J-V measurements and scanned images. The two new solvent systems had to be tested for solution stability like the IPA and ethanol systems were in Figure 3.19, so solutions were made up with increasing volume percentages and the appearance monitored. Due to the low miscibility of 1-butanol of around 10 volume%, smaller increments were used for this solution and annotated in Figure 3.31. 1-propanol had a similar reaction with the nanoparticles to IPA with 60 volume% being the maximum addition before the nanoparticles precipitated out of solution. As expected, the maximum volume percent of 1-butanol was 10% due to miscibility issues, not precipitation of the nanoparticles. It was also noticed after leaving the solutions overnight, all of the solvent systems apart from 1-butanol had precipitated from 50 volume% upwards, this would not be an issue if the inks were to be used in a short time frame, but often in scaled up roll-to-roll processes solutions would be prepared days before coating, and also re-used to prevent unnecessary waste. No further stability issues were observed after a week, so the remainder of the

solutions were deemed to be stable. Therefore, the four solutions which were unstable after 24 hours were omitted from being potential solvent systems.

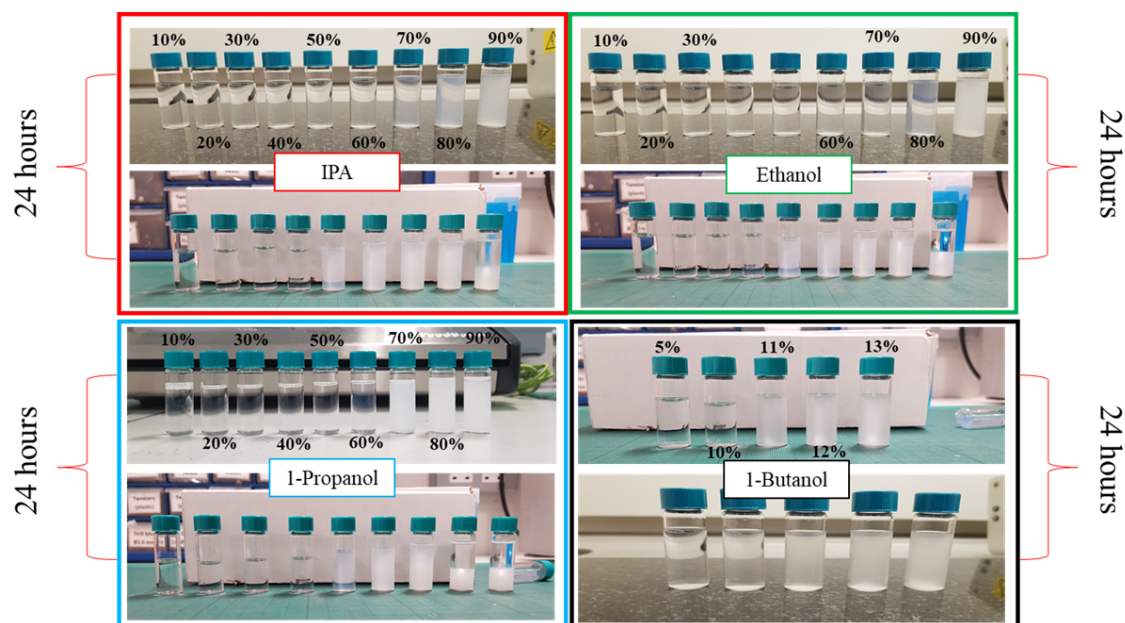


Figure 3.31: Images of each tin oxide solvent system with increasing volume percentage addition of solvent labelled for each vial. Also included are the same solvent systems after 24 hours storage. Images on the bottom row of each solvent system are after 24 hours

Prior to more coating trials being conducted, the rheological properties of each solvent system were measured for incorporation into the visco-capillary model, with surface tension measurements shown in Figure 3.32 and viscosity measurements in Table 3.9. Surface tensions reduced with increasing amounts of solvent in all cases, with 40 volume% of 1-propanol reaching the lowest value of  $25 \text{ Nm}^{-1}$ , and interestingly a 10 volume% addition of 1-butanol reached a similar surface tension of  $28 \text{ Nm}^{-1}$ .

Table 3.9: Viscosity measurements for each of the volume% additions of IPA, ethanol, 1-propanol and 1-butanol to the water based tin oxide nanoparticles. Measurements were made at  $25 \text{ }^\circ\text{C}$

Volume% solvent	Viscosity (mPa.s)			
	IPA	Ethanol	1-propanol	1-butanol
0	1.36	1.36	1.36	1.36
5	N/A	N/A	N/A	1.20
10	1.46	1.46	1.45	1.44
20	2.05	1.99	1.99	N/A
30	2.51	2.43	2.45	N/A
40	2.74	2.85	2.88	N/A

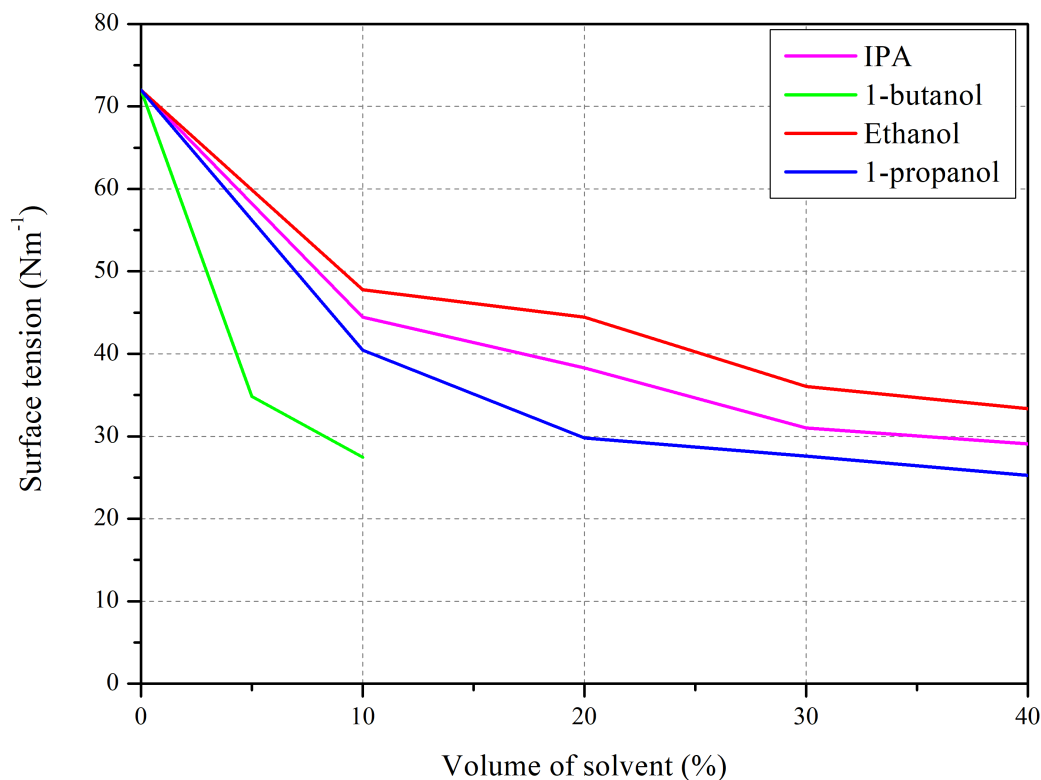


Figure 3.32: Surface tension measurements for each of the volume% additions of IPA, ethanol, 1-propanol and 1-butanol to the water based tin oxide nanoparticles. Measurements were made at 25 °C.

Visco-capillary models were plotted for each solvent system as shown in Figure 3.33, keeping the same coating parameters as the previous trial. Each of the solvent systems were predicted to give stable coatings, and thus the highest volume percent addition of each was chosen for further trials. This was due to the lower surface tensions with the higher volume of solvent, suggesting better coating of the substrate. Therefore, the four solvent systems consisted of; 40 volume% IPA, 40 volume% ethanol, 40 volume% 1-propanol and 10 volume% 1-butanol.

Coating trials for each solvent system was then required, and it was also decided to see if a difference in the coatings was observed after plasma cleaning the PET substrates in air. This was incorporated as a cleaning step, which would also assist in the wetting of the solution, perhaps improving the quality of the films. Although plasma cleaning would be difficult and expensive to integrate into a roll-to-roll coating line, a similar process called corona treatment is a more common cleaning step in roll-to-roll coating lines, which is also present on the roll-to-roll coater used later on in this work. Thus, the plasma cleaning may be able to be replicated on the smart coater using corona. Plasma cleaning in air was performed for one minute on the PET substrates for each solvent system and compared to films coated with no plasma treatment.

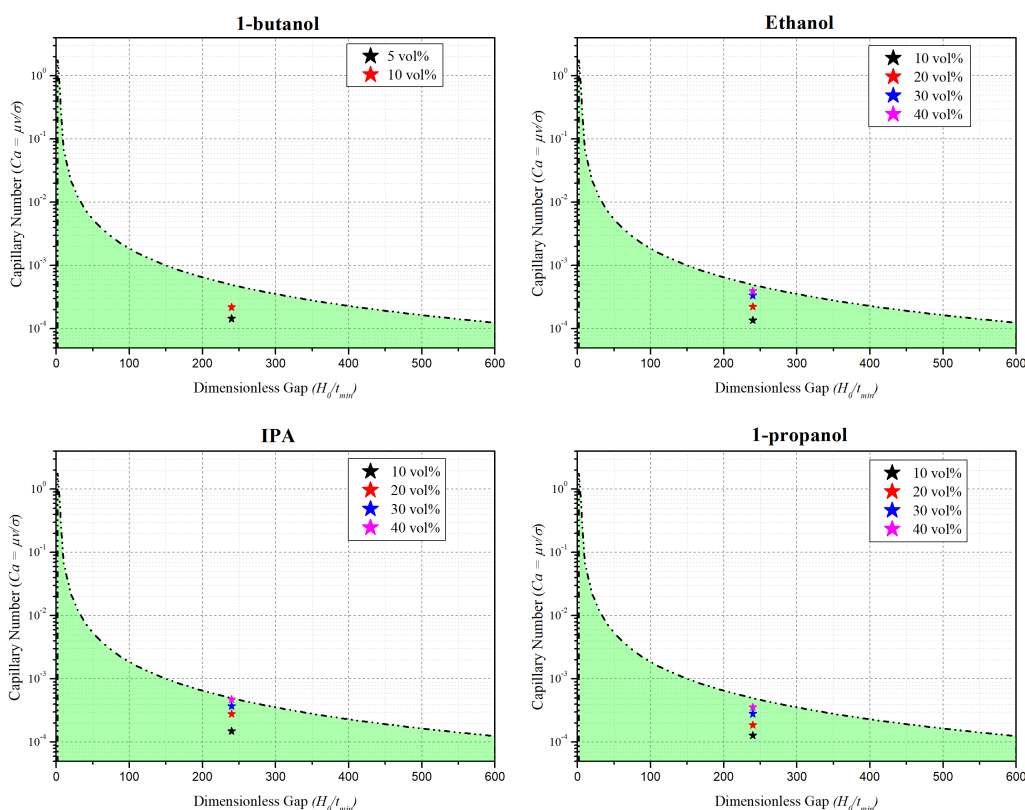


Figure 3.33: Visco-capillary models for all four solvent systems of tin oxide nanoparticle suspensions.

Prior to making devices on the slot-die coated films of each nanoparticle solvent system, images were taken of the films. Figures 3.34 and 3.35 shows images taken of random sections of the slot-die coated films, with the images being super saturated to enhance any defects.

Comparing the films deposited onto PET with and without plasma treatment, there is an obvious improvement for each of the solvent systems, more so with the IPA and ethanol solutions. 1-propanol and 1-butanol appear to provide better coatings without plasma treatment compared to ethanol and IPA, confirming the hypothesis that when the solvent evaporates first, left over water reticulates. Plasma treatment seems to suppress this reticulation, most likely due to the change in surface energy of the ITO/PET, thus preventing the water from reticulating due to better wetting of the substrate during drying. Images give the impression that the 1-propanol and 1-butanol films are more homogenous than the IPA and ethanol films, which was confirmed by cyclic voltammetry.

Table 3.10 summarises the estimated surface coverage calculated from each of the voltammograms in Figure 3.36. Interestingly, the surface coverage does not change with plasma treatment for the 1-butanol based solution, most likely due to the 1-butanol having a higher



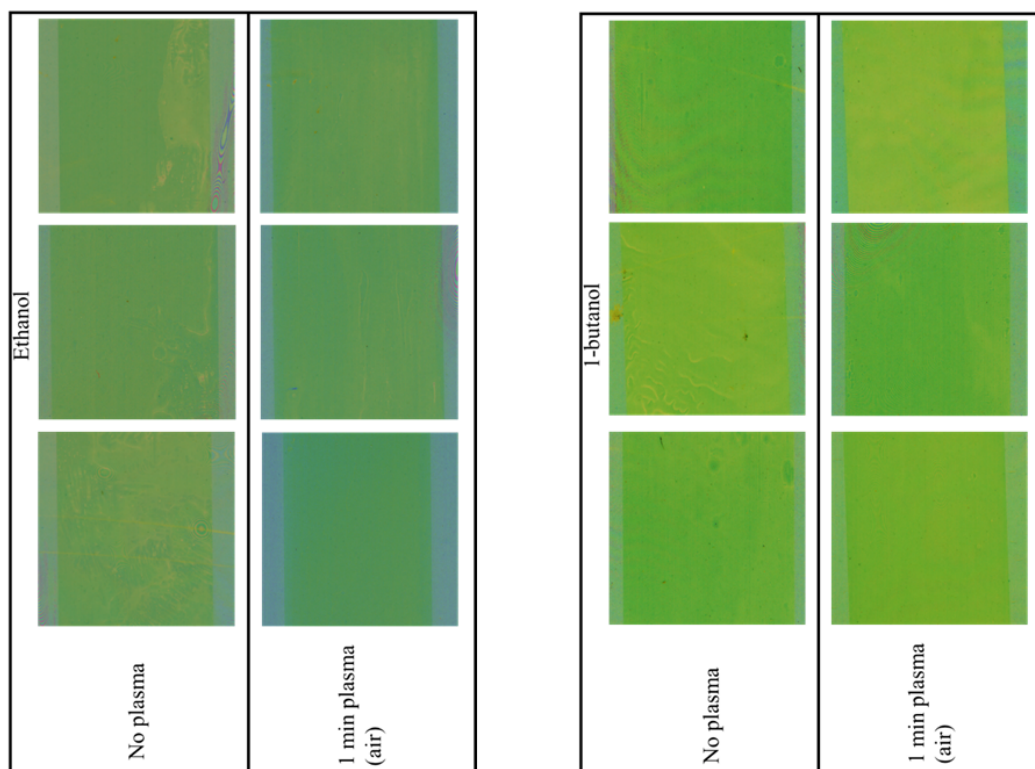


Figure 3.34: Images of ethanol and 1-butanol tin oxide nanoparticle solvent system slot-die coated onto either: non-treated ITO coated PET, or plasma treated ITO coated PET substrates.

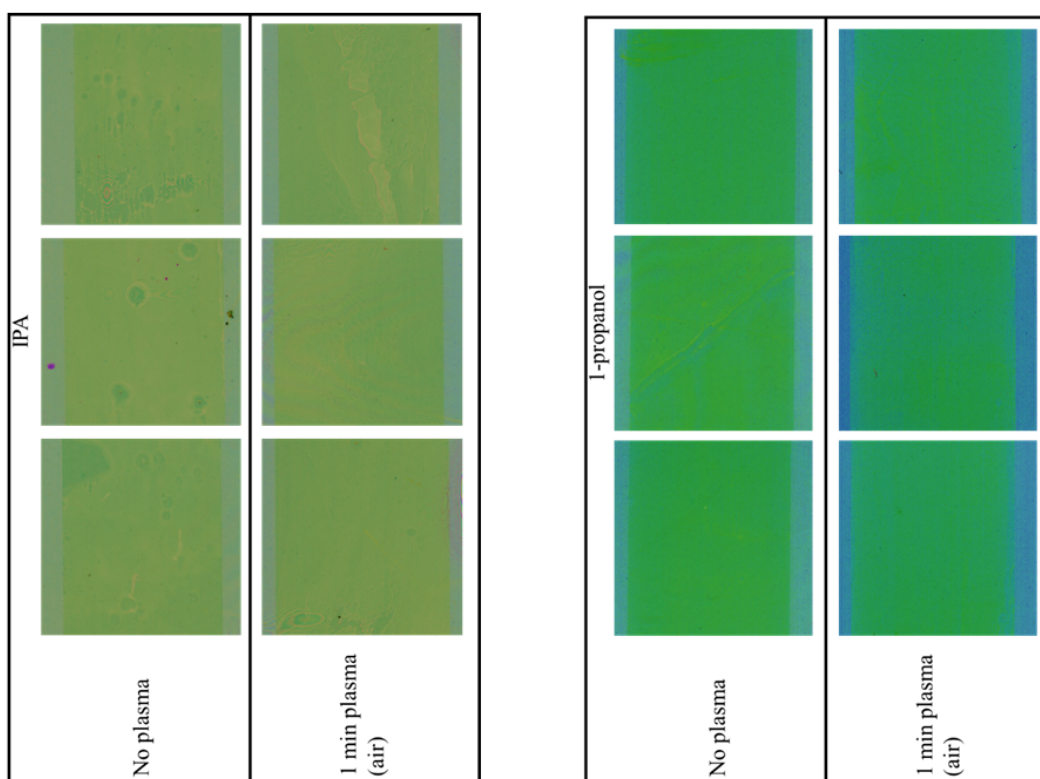


Figure 3.35: Images of IPA and 1-propanol tin oxide nanoparticle solvent system slot-die coated onto either: non-treated ITO coated PET, or plasma treated ITO coated PET substrates.

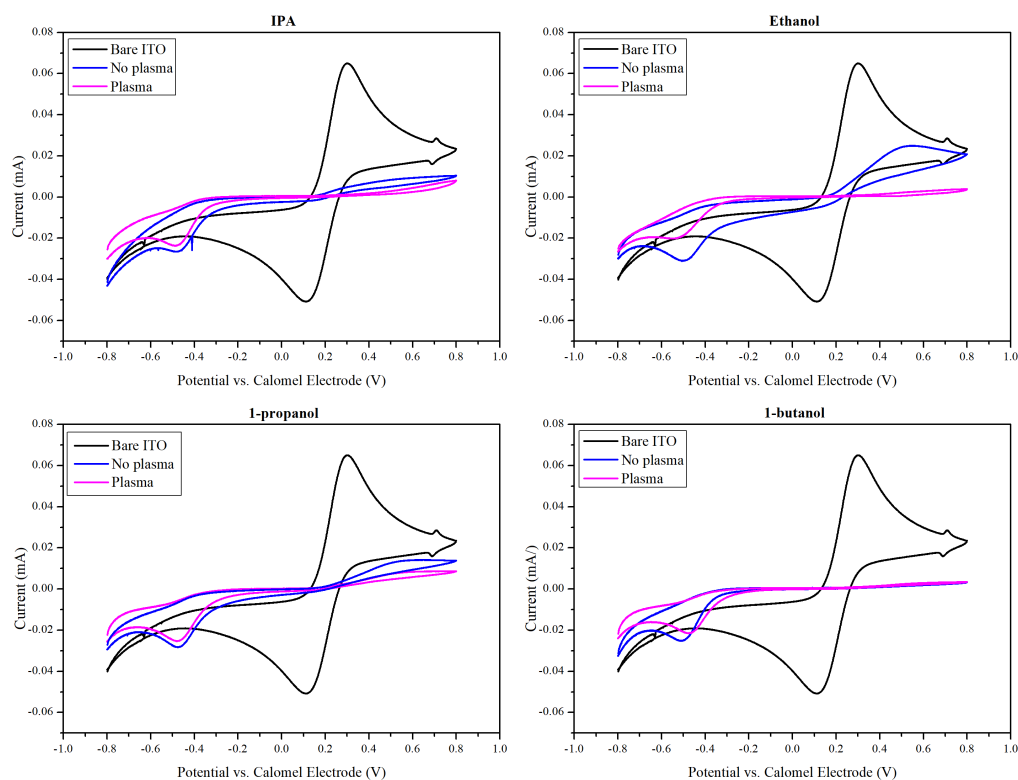


Figure 3.36: Cyclic voltammograms of each tin oxide nanoparticle solvent system slot-die coated onto either: non-treated ITO coated PET, or plasma treated ITO coated PET substrates.

boiling point than water, meaning it doesn't evaporate before the water, maintaining a lower contact angle throughout the drying process. With respect to the other three solvent systems, the plasma treatment appears to have a significant effect on the surface coverage, especially for the ethanol-based solution. This fits in with the theory that the change in surface energy from the plasma treatment reduces the contact angle of the left-over water during drying, reducing the reticulation, in turn improving the film quality. Plasma treated films were expected to improve the efficiency and averages for perovskite devices built on top of the slot-die coated ETLs.

TGA was performed on each of the solvent systems for analysis on the weight loss profiles to investigate the difference in the evaporation of the solvents. Visually all four of the weight loss profiles in Figure 3.37 look similar, however, plotting of the derivatives shows an obvious difference between the curve for 1-butanol and the other three solvent systems. A very linear mass loss curve is seen for the 1-butanol solvent system up until around 8 minutes due to the water evaporating, then a small peak around the 8-minute mark shows the evaporation of the 1-butanol, proving the 1-butanol evaporates after the water and contributes to improving the film quality.

Table 3.10: Estimated surface coverage values for each tin oxide nanoparticle solvent system slot-die coated onto either: non-treated ITO coated PET, or plasma treated ITO coated PET substrates.

Film	Anodic Current (mA)	Estimated Surface Coverage(%)
Bare ITO	0.065	0
IPA	0.010	83.94
IPA (plasma)	0.008	87.62
Ethanol	0.025	61.59
Ethanol (plasma)	0.004	94.02
1-propanol	0.014	78.19
1-propanol (plasma)	0.009	86.62
1-butanol	0.003	94.94
1-butanol (plasma)	0.004	94.58

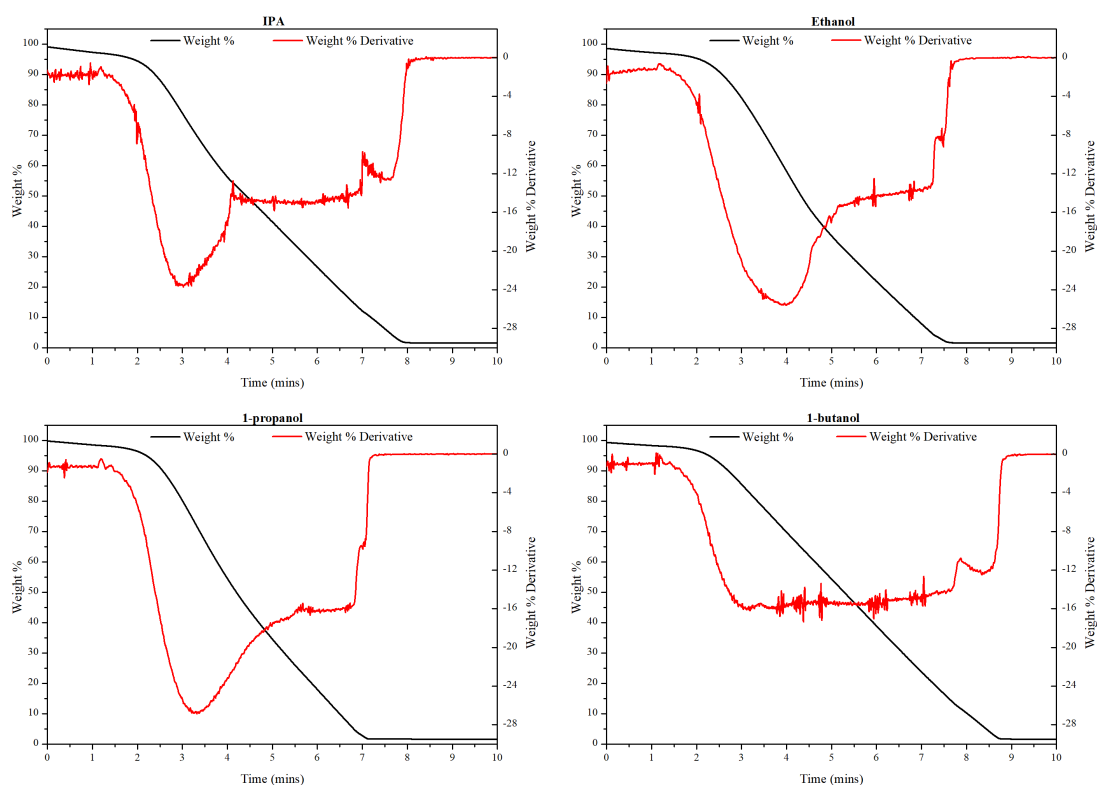


Figure 3.37: TGA graphs for each tin oxide nanoparticle solvent system with the weight % derivative plotted.

For the other three solvent systems, they all show very similar attributes, two large separate mass losses, with the first being due to the solvent, and the second from the remaining water. This concluded the hypothesis of why the non-plasma treated films lead to poor surface coverage and differed from the 1-butanol system. Therefore, it was assumed that the 1-butanol system would provide the most homogenous and high-performance, slot-die coated tin oxide

ETL.

To conclude which solvent system was the most compatible for slot-die coating of the tin oxide ETL, perovskite devices were built on top of each of the coated films and tested for their J-V characteristics. Substrates were cut up into 2.8 x 2.8 cm squares, and the rest of the perovskite device stack spin coated on top. 4 squares from each slot-die coated film were chosen at random to ensure an unbiased result, and to avoid any unfair precedence on film sections that appeared better than others. JV characteristics are summarised in Figure 3.38, and replicate the results from the cyclic voltammetry and images of the films. It is evident that the plasma cleaning has a profound positive effect on the averages of the data for each solvent system, linking the results to the estimated surface areas calculated through the cyclic voltammetry measurements. It must be noted that the control device (spin coated nanoparticles on glass) efficiency was lower than usual. It was discovered to be caused by a lower than usual purity lead iodide from Sigma Aldrich and confirmed by colleagues after XPS characterisation and device making. However, the results were still relevant as the same lead iodide was used for all the devices and therefore comparable between all iterations and control device results. Interestingly, although the cyclic voltammetry results suggested that the 1-butanol solvent system coated onto a PET film with no plasma treatment had excellent surface coverage, the device data averages were much more consistent after plasma cleaning. This could have either been due to the plasma cleaned substrate being inherently cleaner than the non-treated substrate, or that the coating quality on the particular sections chosen for CV were better. With regards to the devices built on top of the films with no plasma treatment, they all reached efficiencies within 2% of the control device but had very poor consistency throughout each pixel. A champion efficiency of 12.32% came from the 1-propanol solvent system on a plasma cleaned substrate, which was comparable to the control device of 12.53%.

As the cyclic voltammetry data suggested, the ethanol based solvent system had the worst results on the non-treated substrate followed closely by the IPA based solution, however, their efficiencies became much more consistent after plasma treatment. Fill factors for the devices on the non-treated substrates were lower due to the poor morphology of the SnO<sub>2</sub> films, thus leading to poor perovskite film qualities. Fill factors increased after plasma treatment, due to the increased quality of the SnO<sub>2</sub> and therefore the quality of the perovskite deposited on top, concluding that plasma treatment prevents the water from reticulating during drying. It appeared that the 1-butanol based solvent system was the most compatible for slot-die coating

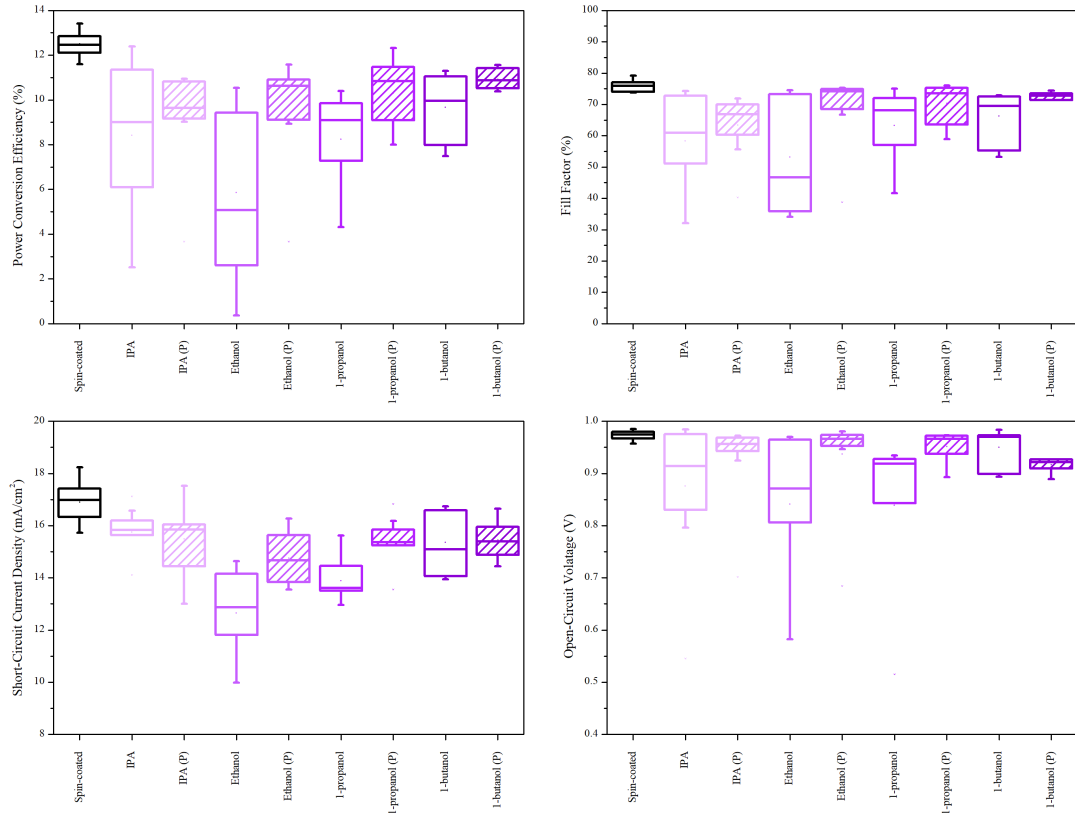


Figure 3.38: Statistical analysis of J-V data from slot-die coating of four tin oxide nanoparticle solvent systems coated onto ITO coated PET substrates with and without plasma treatment prior to deposition. Plasma treated films are denoted via the lined boxes. (Reverse scans). Data presented from 36 devices.

onto PET due to its data consistency being better than the other three solvent systems, with and without plasma treatment. Table 3.11 Summarises the averages for the J-V data in Figure 3.38, showing that the 1-butanol solvent system gave the highest average efficiency of 10.95% compared to 12.33% for the control all spin-coated device. 1-butanol also gave the best averages for layers coated on untreated substrates and was therefore, chosen as the solvent system to be used for final slot-die optimisations.

To improve the slot-die coated tin oxide layer to comparable performance to a spin-coated layer, thickness optimisation was required. Measuring the thickness of the slot-die coated layer on PET proved to be difficult due to its flexible nature and measurements made were not reliable, so thickness optimisation was conducted by changing the wet film thickness and basing the optimal thickness off the subsequent device results. Plasma treated PET substrates were used for this optimisation with the view that a corona treatment could be optimised to accommodate the surface energy change required for homogenous deposition. Wet film thicknesses

Table 3.11: Averages of J-V data from slot-die coating of four tin oxide nanoparticle solvent systems coated onto ITO coated PET substrates with and without plasma treatment prior to deposition.

Film	$J_{SC}(mA/cm^2)$	$V_{OC}(V)$	FF(%)	PCE(%)
Spin coat (Control)	16.90	0.97	76.03	12.33
IPA	15.75	0.88	58.39	8.88
IPA (plasma)	15.49	0.93	63.36	9.89
Ethanol	12.65	0.77	53.24	5.77
Ethanol (plasma)	14.75	0.94	69.13	9.58
1-propanol	13.88	0.84	63.27	7.65
1-propanol (plasma)	15.35	0.95	70.33	10.43
1-butanol	15.35	0.95	66.30	9.46
1-butanol (plasma)	15.45	0.92	72.73	10.95

from 3 to 11  $\mu m$  in 2  $\mu m$  increments were slot die coated onto the plasma treated PET substrates, then cut into squares and perovskite devices built on top. Figure 3.39 shows the statistical analysis of the devices built on each wet film thickness against a control device. An optimal wet film thickness of 7  $\mu m$  was found with a champion efficiency of 14.38%, compared to a 15.99% champion efficiency for a spin-coated control device. Although the champion efficiency of the slot-die coated layer was not as high, an average of 13.6% compared to 14.44% for the spin-coated device made it clear that the films were certainly comparable. The main reason for the small difference in efficiencies was down to lower short circuit current densities, and open circuit voltages which was thought to be down to the PET/ITO having a higher resistance than the glass ITO (50 Ohms/sq compared to 15 Ohms/sq). Hero device J-V characteristics are summarised in Table 3.12, with the corresponding current-voltage curves in Figure 3.40.

Table 3.12: Hero device J-V characteristics comparing a slot-die coated tin oxide ETL to a spin-coated equivalent (Reverse scans). Corresponding J-V curves plotted in Figure 3.40

Deposition Method %	$J_{SC}(mA/cm^2)$	$V_{OC}(V)$	FF(%)	PCE(%)
Spin-coated	21.99	0.95	76.69	15.99
Slot-die coated	20.71	0.95	73.36	14.38

It is evident from the hero device J-V curves in Figure 3.40 that the slot-die coated tin oxide ETL is very similar to the spin-coated device, with the small loss in efficiency down to a lower  $J_{SC}$  and higher series resistance, thus fill factor. Again, the slightly lower efficiency was down to the higher resistance of the PET/ITO substrate and not the ETL itself. Improvements of the efficiency could be achieved by using a more conductive ITO coated PET substrate, however

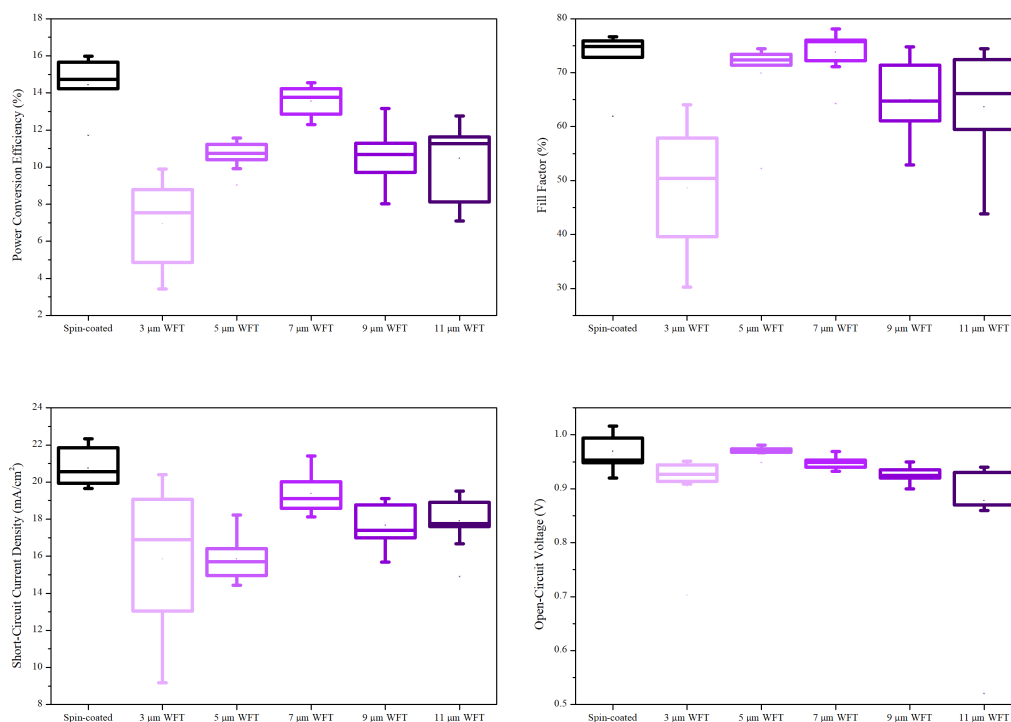


Figure 3.39: Statistical analysis of J-V data from the thickness optimisation of a slot-die coated tin oxide ETL using a 10 volume% 1-butanol solvent system (Reverse scans). Data presented from 24 devices.

this would prove more costly.

Stabilised current measurements were also made to give a more accurate comparison of the efficiencies. Hero devices from the spin-coated and slot-die coated films were held at their maximum power point voltage of the JV scan with the power output recorded over time. Figure 3.41 shows the forward and reverse scans for the stabilised PCE's of both the spin-coated and slot-die coated hero devices. A true PCE for each device was taken by the average of the reverse and forward scans which was 13.24% for the spin-coated device and 11.6% for the slot-die coated device. Nonetheless, there was only a 1.64% difference in efficiency between the spin-coated and slot-die coated devices concluding the optimisation of a roll-to-roll compatible coating of a SnO<sub>2</sub> ETL.

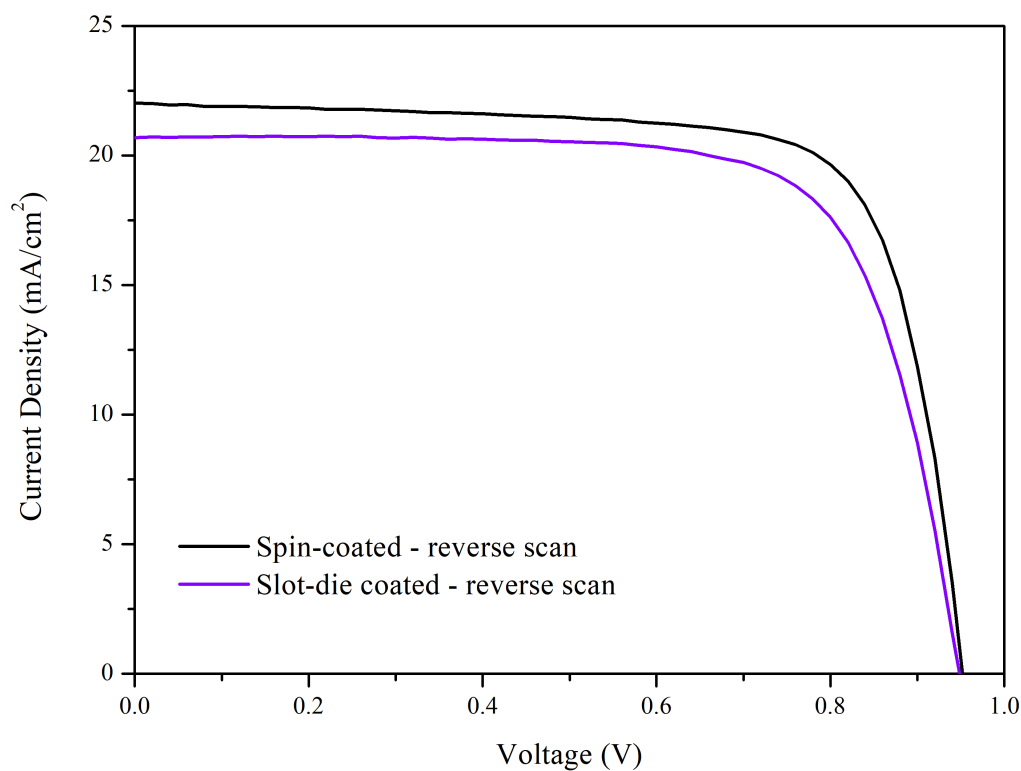


Figure 3.40: Hero device J-V curves for hero perovskite solar cells comparing slot-die coated and spin-coated tin oxide ETLs. Corresponding device performances are shown in Table 3.12.

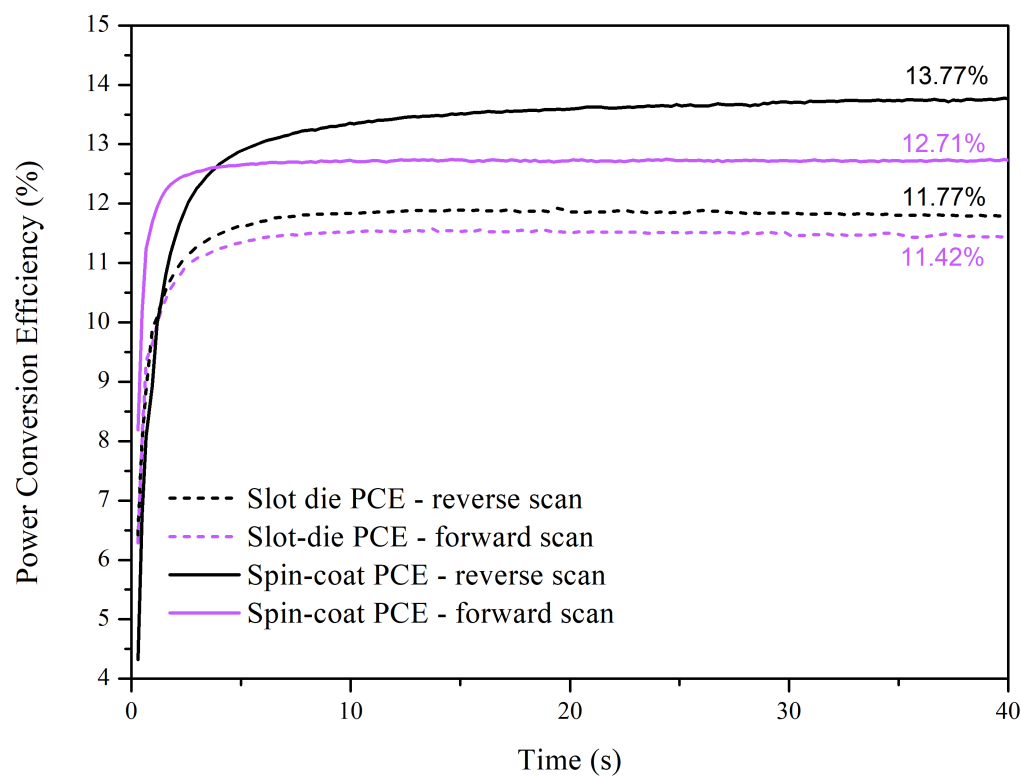


Figure 3.41: Stabilised power conversion efficiencies of hero spin-coated and slot-die coated  $\text{SnO}_2$  films.



### 3.4 Conclusions

A method for depositing high efficiency, low-temperature and roll-to-roll compatible tin oxide ETLs was achieved, both for spin-coating and slot-die coating. In addition to this, all films were deposited in ambient conditions removing the need for high cost enclosed coating lines. Solvent incompatibility of the neat tin oxide nanoparticle suspension caused defects in slot-die coated layers, showing cracks and pinholes, both on glass and PET substrates. Various solvent systems were tested for coating quality, and it was discovered that a 10 volume% addition of 1-butanol lead to the best film morphologies and subsequent perovskite device efficiencies. It was found that the lower boiling point solvent systems such as IPA caused significant defects in the dry film due to the solvent evaporating prior to the water, leaving the water to reticulate owing to its high surface tension. Plasma cleaning of the PET substrates before coating lead to improvements in film qualities for all solvent systems trialled as the contact angle of the water was reduced, preventing reticulation. Nonetheless, the 1-butanol based solvent system provided the best average efficiencies of perovskite solar cells built on top and was chosen as the most compatible solvent system. A 7  $\mu\text{m}$  wet film slot-die coated from a 1.2 weight% solution of tin oxide nanoparticles was found to be optimal, leading to a champion perovskite device efficiency of 14.38% (11.6% stabilised), and averaged 13.6% PCE over 16 pixels, compared to a spin-coated equivalent averaging 14.44% (13.24% stabilised) PCE.

### 3.5 References

- [1] Peng Zhou et al. “Ultrasonic spray-coating of large-scale TiO<sub>2</sub> compact layer for efficient flexible perovskite solar cells”. In: *Micromachines* 8.2 (2017), pp. 1–12. ISSN: 2072666X. DOI: 10.3390/mi8020055.
- [2] Qamar Wali et al. “Tin oxide as an emerging electron transport medium in perovskite solar cells”. In: *Solar Energy Materials and Solar Cells* 179.October 2017 (2018), pp. 102–117. ISSN: 09270248. DOI: 10.1016/j.solmat.2018.02.007. URL: <https://doi.org/10.1016/j.solmat.2018.02.007>.
- [3] Qi Jiang, Xingwang Zhang, and Jingbi You. “SnO<sub>2</sub>: A Wonderful Electron Transport Layer for Perovskite Solar Cells”. In: *Small* 14.31 (2018), pp. 1–14. ISSN: 16136829. DOI: 10.1002/smll.201801154.

- [4] Yulia Galagan et al. “Roll-to-Roll Slot Die Coated Perovskite for Efficient Flexible Solar Cells”. In: *Advanced Energy Materials* 8.32 (2018), pp. 1–7. ISSN: 16146840. DOI: 10.1002/aenm.201801935.
- [5] Tongle Bu et al. “Universal passivation strategy to slot-die printed SnO<sub>2</sub> for hysteresis-free efficient flexible perovskite solar module”. In: *Nature Communications* 9.1 (2018), pp. 1–10. ISSN: 20411723. DOI: 10.1038/s41467-018-07099-9.
- [6] Dong Yang et al. “High efficiency planar-type perovskite solar cells with negligible hysteresis using EDTA-complexed SnO<sub>2</sub>”. In: *Nature Communications* 9.1 (2018). ISSN: 20411723. DOI: 10.1038/s41467-018-05760-x.
- [7] Yonghui Lee et al. “Efficient Planar Perovskite Solar Cells Using Passivated Tin Oxide as an Electron Transport Layer”. In: *Advanced Science* 5.6 (2018), pp. 1–6. ISSN: 21983844. DOI: 10.1002/advs.201800130.
- [8] Keke Song et al. “Effect of SnO<sub>2</sub> colloidal dispersion solution concentration on the quality of perovskite layer of solar cells”. In: *Coatings* 11.5 (2021), pp. 1–10. ISSN: 20796412. DOI: 10.3390/coatings11050591.
- [9] Philip Schulz, David Cahen, and Antoine Kahn. “Halide Perovskites: Is It All about the Interfaces?” In: *Chemical Reviews* 119.5 (2019), pp. 3349–3417. ISSN: 15206890. DOI: 10.1021/acs.chemrev.8b00558.
- [10] Yang Bai, Xiangyue Meng, and Shihe Yang. “Interface Engineering for Highly Efficient and Stable Planar p-i-n Perovskite Solar Cells”. In: *Advanced Energy Materials* 8.5 (2018), pp. 1–14. ISSN: 16146840. DOI: 10.1002/aenm.201701883.
- [11] Liangbin Xiong et al. “Review on the Application of SnO<sub>2</sub> in Perovskite Solar Cells”. In: *Advanced Functional Materials* 28.35 (2018), pp. 1–18. ISSN: 16163028. DOI: 10.1002/adfm.201802757.
- [12] Lijian Zuo et al. “Tailoring the interfacial chemical interaction for high-efficiency perovskite solar cells”. In: *Nano Letters* 17.1 (2017), pp. 269–275. ISSN: 15306992. DOI: 10.1021/acs.nanolett.6b04015.
- [13] Layth Al-Gebory and M. Pinar Mengüç. “The effect of pH on particle agglomeration and optical properties of nanoparticle suspensions”. In: *Journal of Quantitative*

*Spectroscopy and Radiative Transfer* 219 (2018), pp. 46–60. ISSN: 00224073. DOI:  
10.1016/j.jqsrt.2018.07.020.

## Chapter 4

# Roll-to-Roll Coating Of Tin Oxide

### 4.1 Introduction

In chapter 3 it was demonstrated that comparable efficiencies to a spin coated layer of tin oxide could be achieved via slot-die coating on large area PET substrates by manipulation of the precursor solution to more desirable rheological properties, mainly to aid in the wetting of the solution to produce homogenous dry films. This was achieved by the addition of 10 volume% 1-butanol to the precursor solution. It was also discovered that a short plasma treatment of the PET films prior to tin oxide deposition led to a slight improvement in device performances due to a further improvement in the wetting, and preventing reticulation of the large portion of water in the solution during the drying process. In this chapter, roll-to-roll slot-die coating of a tin oxide electron transport layer is demonstrated. This was an important step towards mass manufacture of an ETL, and roll-to-roll coating trials such as this are an essential stepping stone towards achieving true mass manufacture. Although moving from sheet-to-sheet coating to roll-to-roll coating may sound relatively simple, there are many complex challenges to overcome. Firstly, the coated area is much larger, and achieving reliable and reproducible coatings is paramount. Coating speeds were also increased to be compatible with large scale deposition which present further challenges with regards to coating stability. Substrates are also wound onto a coil after deposition, so it was crucial to confirm whether this had a negative effect on the performance of the deposited layer. Finally, due to the more complex nature of a roll-to-roll setting, the substrate required alignment to ensure coatings were applied evenly over the whole substrate, and optimal winding parameters such as tension to prevent damage to the substrate.

Several coating parameters were investigated in order to optimise the coating process, with

characterisation of the layer to confirm this. Finally, perovskite devices built on top of the coated tin oxide were characterised electronically and compared to a spin coated equivalent.

## 4.2 Experimental Methods

Slot-die coating was performed in a “Smart Coater” made by Coatema, which allows full roll-to-roll coatings onto a variety of flexible substrates via several deposition methods, including slot-die as used in this thesis. An image of the smart coater is shown in figure 4.1 with the main components labelled. The smart coater consists of several rollers which turn under tension to keep the substrate flat, and to pull it through the coating unit to be rewound at the end. In figure 4.1, the three main components of the smart coater are shown. Firstly, the coating station where a variety of deposition apparatus can be installed. Secondly, there are two 30 cm long ovens in series which can be controlled separately (temperature and air flow). Finally, a corona unit for substrate cleaning or surface energy manipulation which is explained in further detail in Chapter 4.3.1.

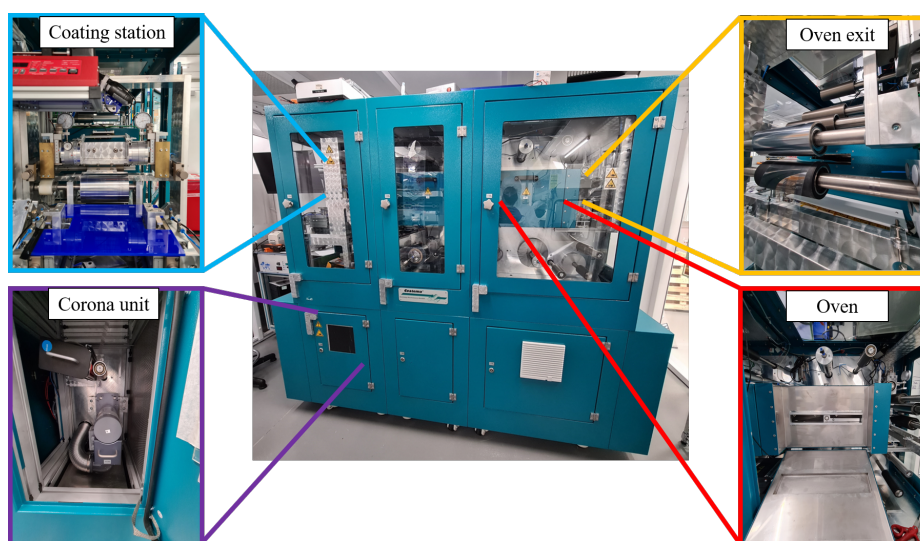


Figure 4.1: Images of the Coatema smart coater used for roll-to-roll coating trials in this chapter

Figure 4.2 is a schematic illustration of the roller set up inside the smart coater. Each section has been numbered in order from start to finish:

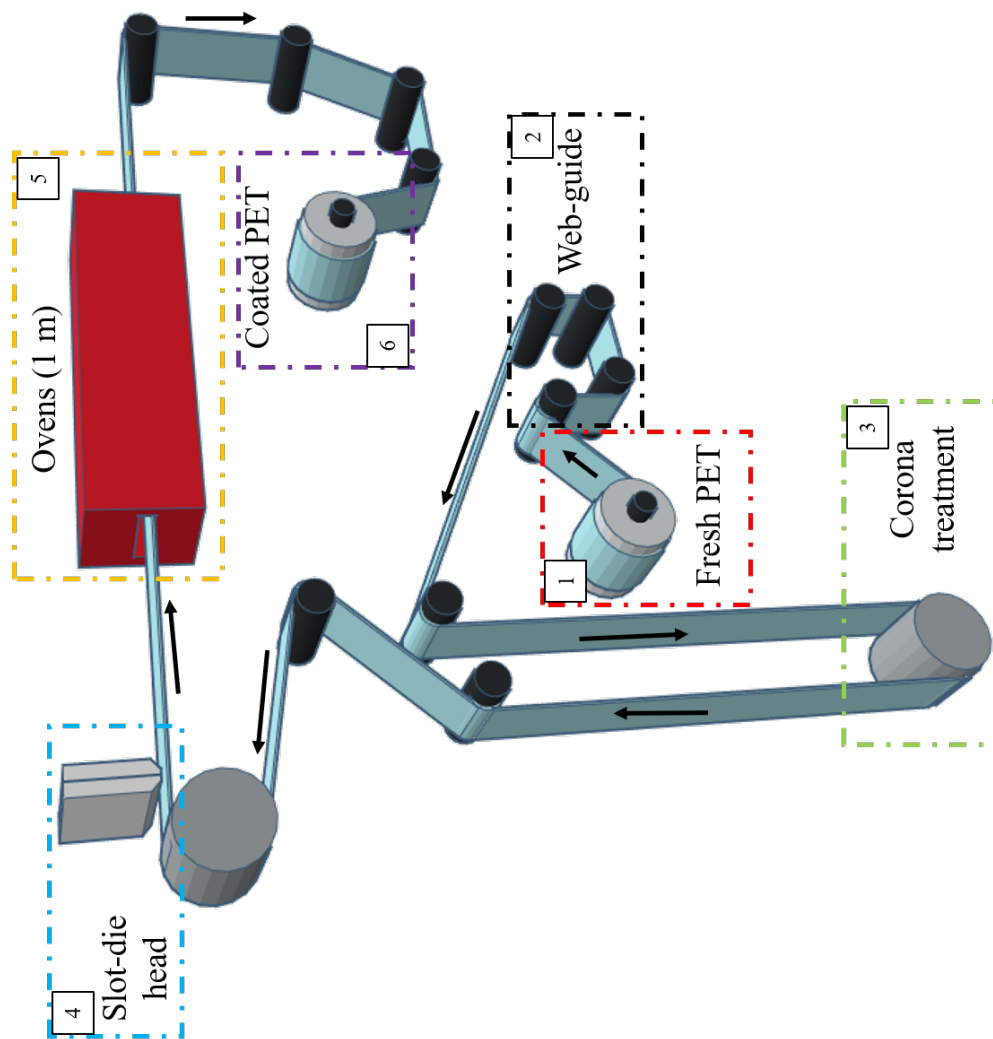


Figure 4.2: Schematic diagram of the layout of the Coatema smart coater

1. This is where the substrate is loaded into the coater, and can consist of any flexible material up to a maximum of 100 mm in width.
2. A web guide is used to keep the substrate centred throughout and adjusts the web position by twisting, with the position monitored by a camera.
3. A corona treatment which can clean the substrate and increase the surface energy for improvement in coatings. More detail on the corona unit is given in section 4.3.1
4. A mount for several different coating heads is included here, however, this work only uses a slot-die head. Included here are micrometre screws and nitrogen assisted pneumatics to adjust the position of the coating head.

5. Two 30 cm long ovens with separately controlled air flows and temperature.
6. Coated substrate is finally wound onto a core which can be removed from the coater at the end of a coating trial. It can also be rewound for a second coating.

Full width coatings of 100 mm were made using a purpose-built slot-die head with a shim and corresponding meniscus guide used to define the coating area. The slot-die head was positioned vertically above the coating roller as shown in Figure 4.3, with the coating gap height set using thickness “feeler” gauges and micrometre adjustment screws. Ink was delivered to the slot-die head using a syringe pump and the flow rate changed to control the wet film thickness.

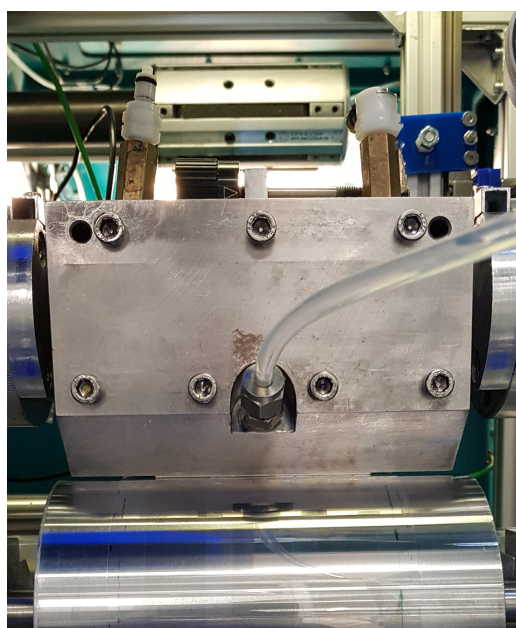


Figure 4.3: Image of the slot die head during coating of the tin oxide ETL in the smart coater.

A pre-patterned ITO coated PET substrate (Mekoprint) was used, with a web width of 100 mm and sheet resistance of 50 Ohms/sq. Web speed was controlled by an in built computer and the position of the web kept constant throughout the coater controlled via an in-built web-guide. Drying of the layer was achieved by two in-line ovens directly after the slot-die head, controlled by the in built computer and also monitored by two thermocouples situated within the ovens. Air flow within the ovens can also be controlled but were kept constant at 100% throughout the trials. Air flow was approximately 90 m<sup>3</sup>/hour per unit. The tin oxide ink was the same as the optimised ink in Chapter 1 at 1.2 weight% in DI water with an addition of 10 vol% 1-butanol.

### 4.3 Results and Discussion

Although during sheet-to-sheet optimisation a coating speed of 0.25 m/min was used, this speed would hinder the high throughput required for an industrial coating line. Work previously completed at SPECIFIC on roll-to-roll coating of perovskite layers employed a coating speed of 1 m/min which is a good compromise for the short ovens in the smart coater and a proof of concept for scalability. It is also important to match the speed of deposition for each layer to ensure that no bottlenecks are created, also allowing for all of the layers to be deposited in sequence. Clearly the speed could be increased in a larger roll-to-roll coater in which the ovens would be significantly longer to achieve the desirable annealing time. In addition to this, previous sheet-to-sheet trials saw an oven residence time of 4 minutes, whereas coating at 1 m/min would only subject the tin oxide film to 1 minute of annealing. This was not thought to be an issue as the layer only requires drying and no phase conversion. Layers are extremely thin and should easily dry within 1 minute. Tests to determine whether the layer had dried or not were conducted to confirm this.

In chapter 3, the optimised wet film thickness of the tin oxide layer was 7  $\mu\text{m}$ , and thus formed the basis of the roll-to-roll optimisation. Although it would be reasonable to assume that a 7  $\mu\text{m}$  wet film in the smart coater would provide the same results as the sheet-to-sheet trials, stabilisation of the coating over a 30 cm long sheet-to-sheet coated film cannot be guaranteed and could lead to thicker/thinner films than calculated. Therefore, three wet film thicknesses were coated in the smart coater; 5, 7 and 9  $\mu\text{m}$ . Also, plasma treatment was found to improve the consistency of the sheet to sheet tin oxide based perovskite devices, but plasma treatment was not available in-line on the smart coater. However, an in-line corona treatment unit was installed which has the potential to replicate the effects plasma had on the PET/ITO substrate.

Prior to any coating trials, the viscocapillary model required updating as the coating speed had now increased. Keeping the same overall gap height of 1200  $\mu\text{m}$ , the model was updated for a 1 m/min coating speed. Previously, at 0.25 m/min and 5  $\mu\text{m}$  WFT, the tin oxide ink was in the stable region according to the model, however now that the coating speed had increased, so had the capillary number, moving it into the unstable region. For the 7  $\mu\text{m}$  WFT it was on the edge of the boundary between the stable and unstable region, however reducing the gap height by 150  $\mu\text{m}$  moved it into the stable region. A 9  $\mu\text{m}$  WFT was predicted as stable with both gap heights. Reducing the gap height to 1050  $\mu\text{m}$  still did not move the 5  $\mu\text{m}$  WFT into



the stable region. A smaller gap than 1050  $\mu\text{m}$  was not chosen as this would be difficult to measure with any true accuracy. A 5  $\mu\text{m}$  wet film was still coated to confirm the accuracy of the viscocapillary model.

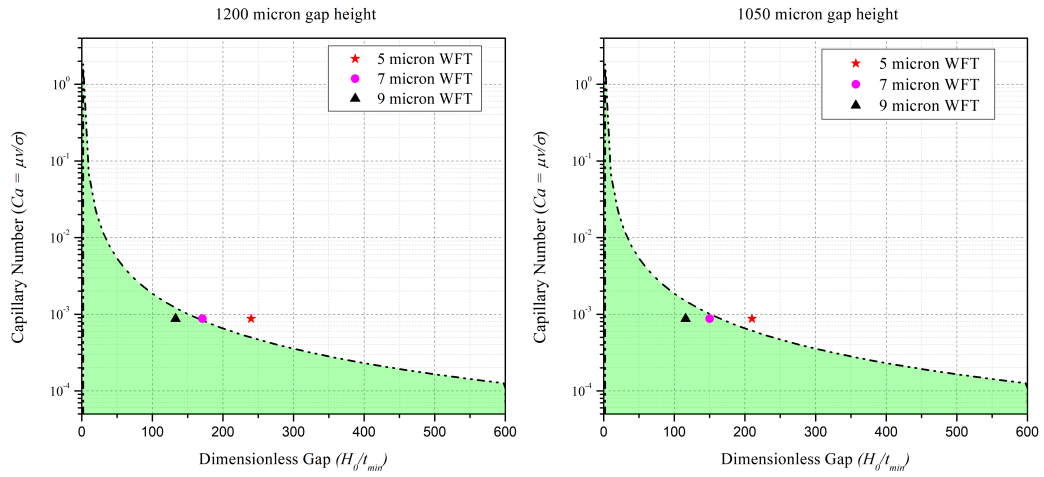


Figure 4.4: Visco capillary models for roll-to-roll coating of SnO<sub>2</sub> at 1 m/min

Experiments were also carried out to determine whether the oven set point controlled by the smart coater gave accurate temperature readings within the oven. One thermocouple was installed in the middle of the ovens and another taped to the substrate, therefore temperature could be continuously recorded whilst the substrate was moving through the ovens and compared to the set point. Initially the oven set-point was 140 °C and left to stabilise for at least 30 minutes prior to sampling. The substrate was wound through at 1 m/min, and data from the thermocouples recorded and plotted in Figure 4.5. With a set-point of 140 °C the actual temperature reached in the ovens was 120 °C, with the web being roughly 120 °C as well, and therefore the experiment was repeated with a set point of 160 °C in an attempt to get the substrate to 140 °C. With the set-point at 160 °C, the temperature in the oven was 150 °C and the web temperature between 135 - 140 °C. A set-point of 160 °C was thus used for the roll-to-roll trials going forward.

### 4.3.1 Corona treatment

Corona treatment is an established method in industry for increasing the surface energy of substrate/coating surfaces. Corona treatment is achieved by creating an electrical discharge with high voltage and high frequency, which causes an ionisation by collision reaction with the surrounding air forming ions, radicals and ozone. The difference being that plasma treatment

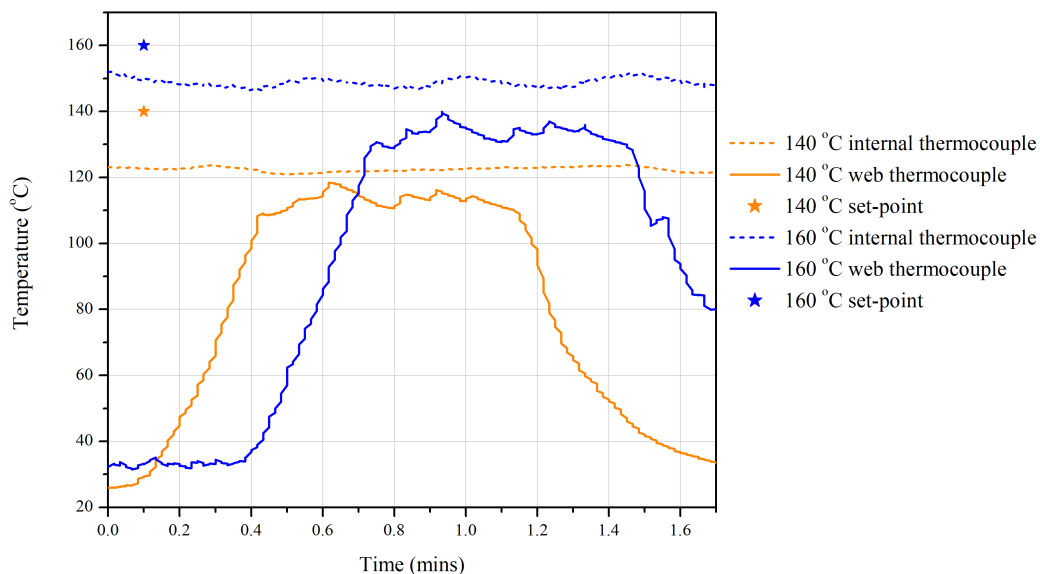


Figure 4.5: Temperature measured within the smart coater ovens compared to the set-point.

does not produce ozone. Therefore, the corona treatment causes reactions with the PET surface primarily by the breakage of H-C bonds, thus allowing the formation of polar groups on non-polar polymer surfaces. This in turn increases the overall surface energy of the substrate. More importantly, corona treatment can remove particles from film surfaces and cause an increase in roughness in that area. Control of the corona treatment is achieved via the change in power provided to the corona unit and changes in this power were made to investigate the quality of the subsequent coated tin oxide layer.

Figure 4.6 shows an image of the corona unit used in this work as well as a diagram showing the basic configuration

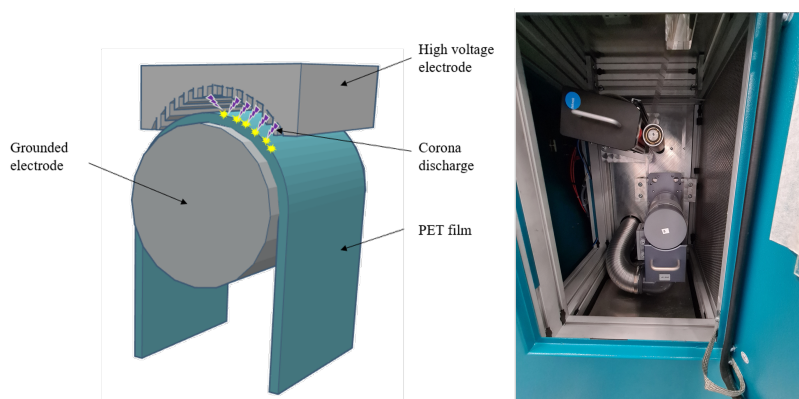


Figure 4.6: Diagram of the corona treatment unit used in this experiment and an image of the unit itself.

Firstly, it was necessary to characterise the PET/ITO film before and after various corona

treatments. Treating the PET/ITO film at 4 different power settings; 0.33, 0.5, 0.75 and 1.0 kW at a set speed of 1 m/min without any coating allowed for measurement of the conductivity and contact angle of the tin oxide solution in order to see any changes. It must be noted that initially the corona power settings were to be 0.25, 0.5, 0.75 and 1 kW, however, 0.33 kW was the lowest available power setting on the unit.

Measuring the conductivity at each corona power setting revealed a large increase in resistivity from 50 to 500 Ohms/sq. Surprisingly, this was also observed with the film unexposed to corona. CV results also showed a reduction in anodic current and increased peak-to-peak separation when compared to a film which had not been put through the smart coater (Figure 4.7)

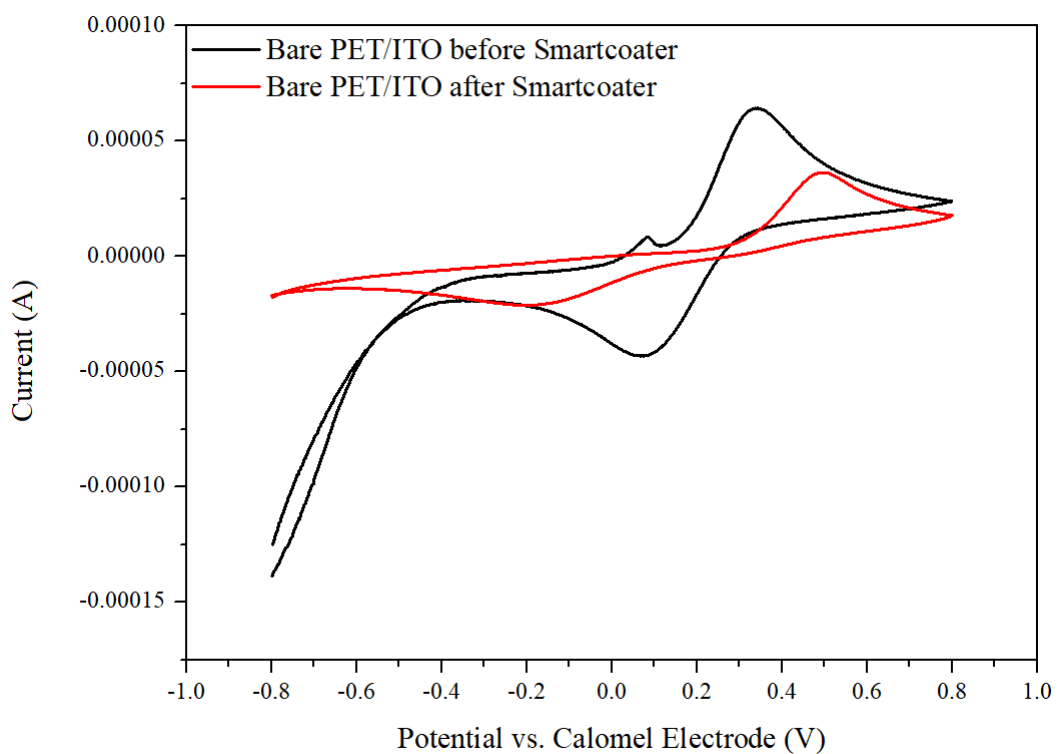


Figure 4.7: Cyclic voltammetry on bare PET/ITO substrates before and after running through the smartcoater

To investigate the reason behind this, SEM images were taken of the film before and after being pulled through the smart coater, from these images the cause became obvious. Figure 4.8 shows the SEM images taken, with the before film defect free. After being pulled through the smart coater cracks had appeared horizontal to the winding direction. This was found to be caused by the tension used on the rollers causing the ITO to stretch and crack. Reducing the tension from 90 nM to 40 nM prevented the cracks without being detrimental to the winding

process. To confirm this, conductivity measurements were made again and the resistance was unchanged both with and without corona treatment.

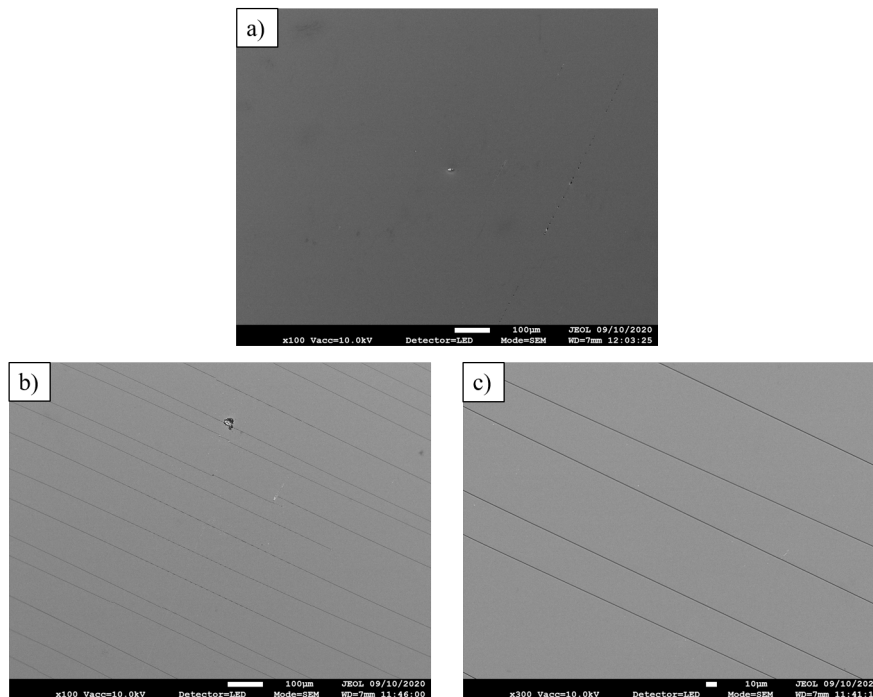


Figure 4.8: SEM images of PET/ITO substrate before (a) and after running through the smart coater (b&c). Images taken by Rahul Patidar.

Contact angle measurements of the tin oxide ink were then made on each of the corona power settings and summarised in figure 4.9. Corona treatment clearly had a significant effect on the surface energy of the PET/ITO films, thus reducing the contact angle of the tin oxide ink.

To determine the effect that the corona treatment had on the quality of the tin oxide films, it was decided that adding a dye to the ink would allow for better visualisation of the coatings. A small amount (1 mg/ml) of pararosoniline acetate dye was added to the tin oxide ink and coated onto the PET/ITO substrate with a 7 micron WFT at each corona power setting. Images of each film were taken by scanning in an Epson scanner then super saturated to enhance the colour, thus revealing the quality of each layer. Figure 4.10 Shows the images of each film at each power setting and labelled as such.

It is clearly visible that the corona treatment has a detrimental effect on the coating quality, with several defects on all corona treated substrates, appearing to worsen as the corona power increases. The three stripes in each image are the pre-patterned ITO and it is evident that the majority of the defects are on the ITO itself. This suggested that the corona treatment is causing

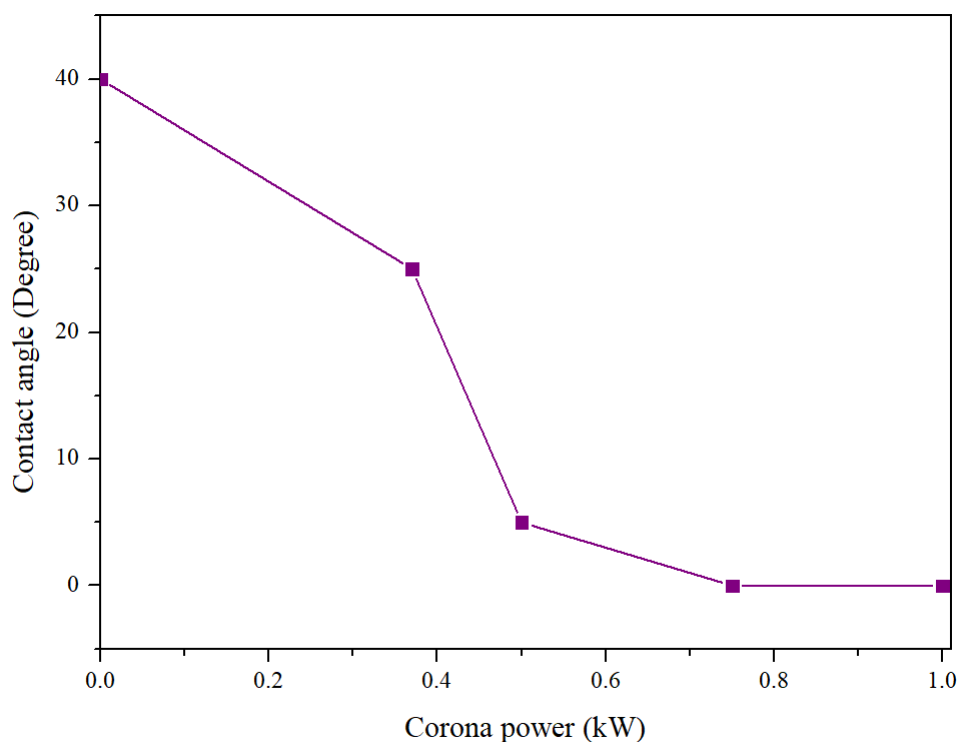


Figure 4.9: Contact angle measurements of tin oxide slot-die coating ink on PET/ITO substrates after different corona treatments

a surface energy difference between the ITO and bare PET sections of the substrate, leading to a difference in coating between the two surfaces. Although it was clear that the film deposited on an untreated substrate appeared far superior to the treated films, it was necessary to confirm this, with CV being the method chosen as this gives an estimation of surface coverage. Corona treatment was repeated but on films without a dye addition with figure 4.11 showing the CV traces for 7  $\mu\text{m}$  wet film coatings of  $\text{SnO}_2$  with and without corona treatments. Results from the CV show that the film without any corona treatment leads to excellent blocking behaviour with an estimated surface coverage of 94.69 %. With respect to the corona treatment, anodic current from the CV traces increases and the related surface coverage decreases. Using a corona power of 1.0 kW leads to an estimated surface coverage of 88.34 % and concludes that corona treatment is detrimental to the coating quality and therefore, further R2R trials were conducted without the use of a corona treatment.

In order to understand why the corona treatment led to a decrease in surface coverage despite it improving the wetting of the tin oxide, videos were taken of drop tests of the test ink onto the treated and untreated substrates and snapshots taken. Although contact angle measurements have been presented previously, this was only on the ITO coated section of the

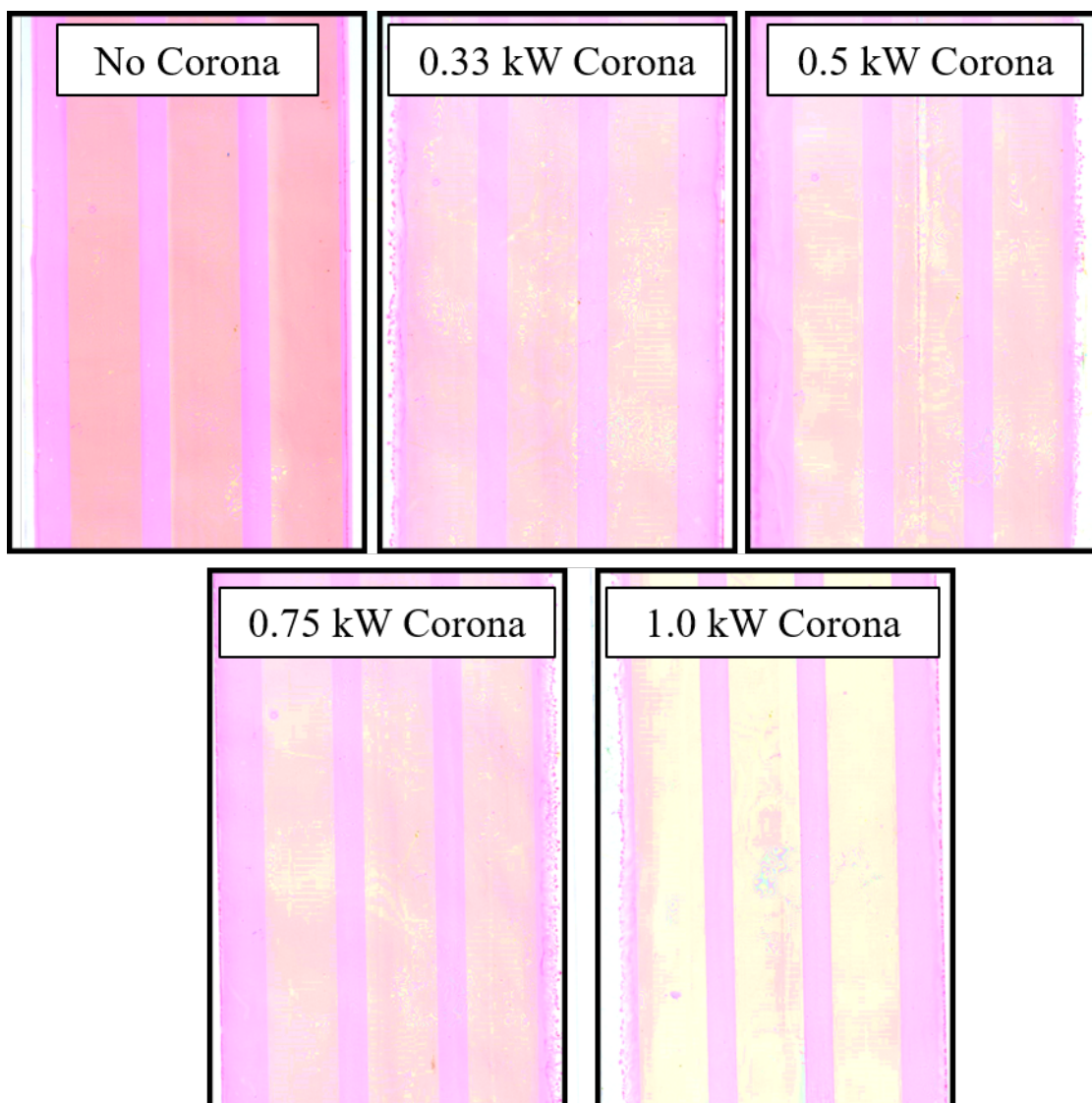


Figure 4.10: Images of roll-to-roll, slot-die coated tin oxide films with dye added to the ink. Films were subjected to various levels of corona treatment, with powers ranging from 0 - 1.0 kW

PET. By videoing and taking snapshots, the difference in wetting on the ITO and bare PET sections of the substrate were easier to identify.

Figure 4.12 compares a non-corona treated and 1.0 kW corona-treated PET/ITO substrate with the ITO and PET films annotated. Inks including the dye were dropped onto the PET and ITO sections using a pipette whilst being filmed. Snapshots were taken immediately as the ink was dropped onto the PET and 1 second after the drop. With both the corona and non-corona treated films, the drops onto the ITO remained stable, however when dropping onto the bare PET it was clear that after corona treatment the ink spreads very quickly and is unstable. This shows that there is a difference in surface energy between the ITO and PET after corona

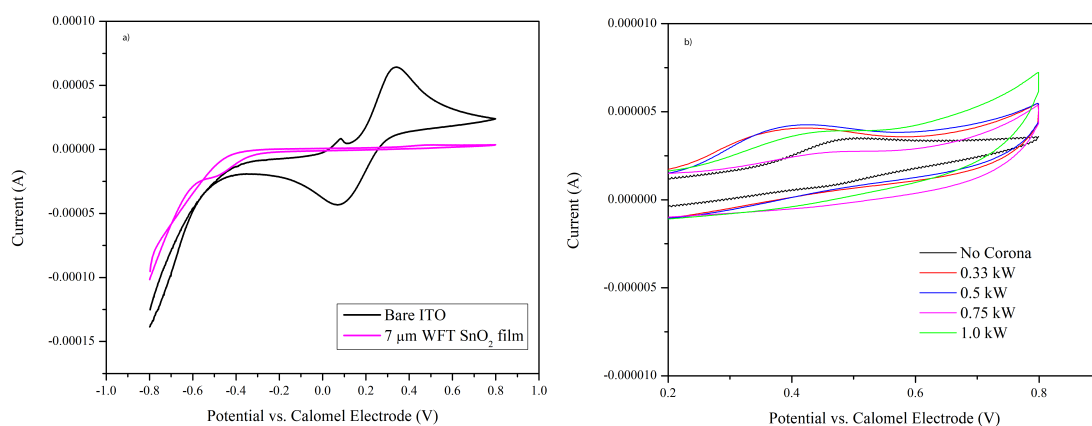


Figure 4.11: Cyclic voltammetry of a) a 7  $\mu\text{m}$  wet film of  $\text{SnO}_2$  with no corona treatment compared to bare ITO and b) a comparison of increasing corona treatment power.

treatment, with the PET being higher and leading to over wetting. Although the ink is stable on the ITO section, the over wetting of the PET would lead to an unstable region, inevitably affecting the edges of the ITO and leading to coating defects. This is in agreement with the scanned images of the coatings in Figure 4.10 and the CV results concluding the reason for the loss in coating quality when employing corona treatment. To summarise, corona treatment leads to a surface energy disparity between the ITO and bare PET on the substrate, with the surface energy of the bare PET being effected more than the ITO.

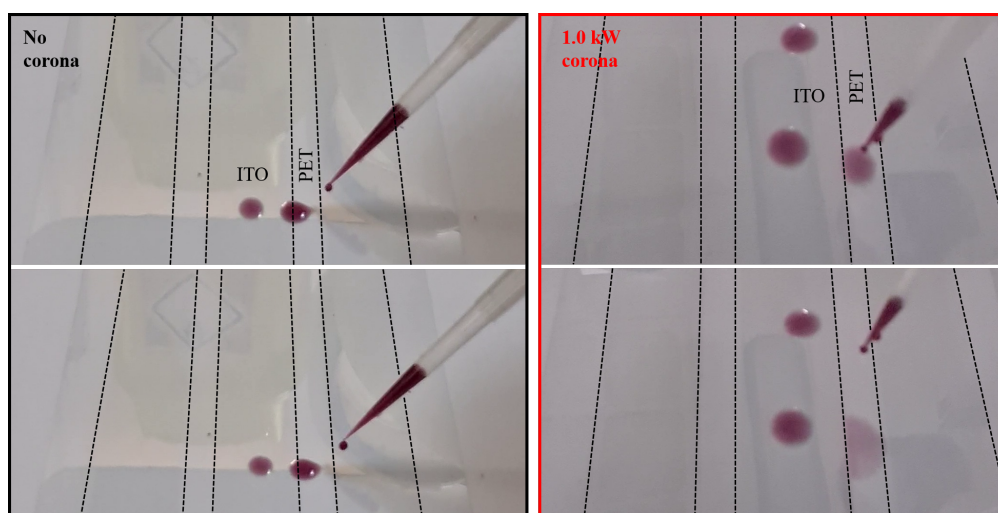


Figure 4.12: Snapshots from videos taken of dropping  $\text{SnO}_2$  ink formulations onto non-treated and corona-treated PET/ITO substrates

### 4.3.2 Film optimisation

Due to the CV results showing a reduction in film quality after corona treatment, the method was omitted from further investigation. Therefore, films were deposited onto an untreated substrate. Three wet film thicknesses were trialled; 5, 7 and 9  $\mu\text{m}$ . Although 5  $\mu\text{m}$  was predicted by the viscocapillary model to be unstable, it was included to further prove the accuracy of the model with poor or erratic device data expected from this film thickness.

Each wet film was coated in one trial at 1 m/min with the oven temperature set at 160  $^{\circ}\text{C}$ . Once the trial was completed the PET roll was removed from the smart coater and unwound, separating each section by the wet film coated. Sections of each film were then cut into 28 x 28 cm squares and the rest of the perovskite device stack spin coated on top. 5 devices (40 pixels) from each film thickness were then tested under a solar simulator and the results presented in Figure 4.13.

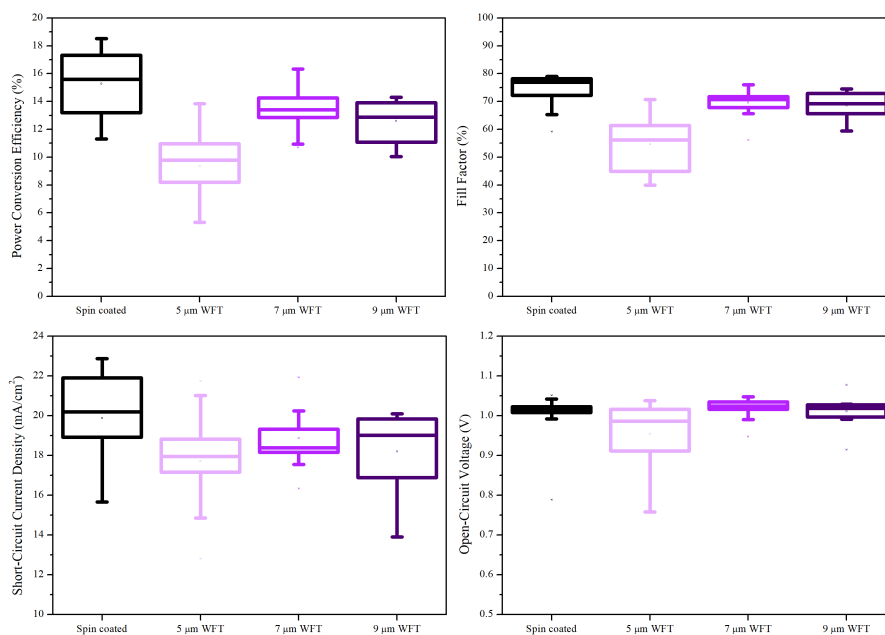


Figure 4.13: Statistical analysis of J-V data from slot-die coating of a tin oxide nanoparticle solution in a roll-to-roll setting. Data presented from 20 devices.

Results from the roll-to-roll trial were in agreement with the sheet-to-sheet optimisation, in which the optimum performance was achieved by the 7  $\mu\text{m}$  wet film. A champion efficiency of 16.34% was achieved from the slot-die coated film compared to 18.52% for the spin-coated control device. Parameters from the champion device can be found in Table 4.1 Results also proved the validity of the viscocapillary model, which as suggested the 5  $\mu\text{m}$  wet film had a large variation in performance owing to coating stability issues.



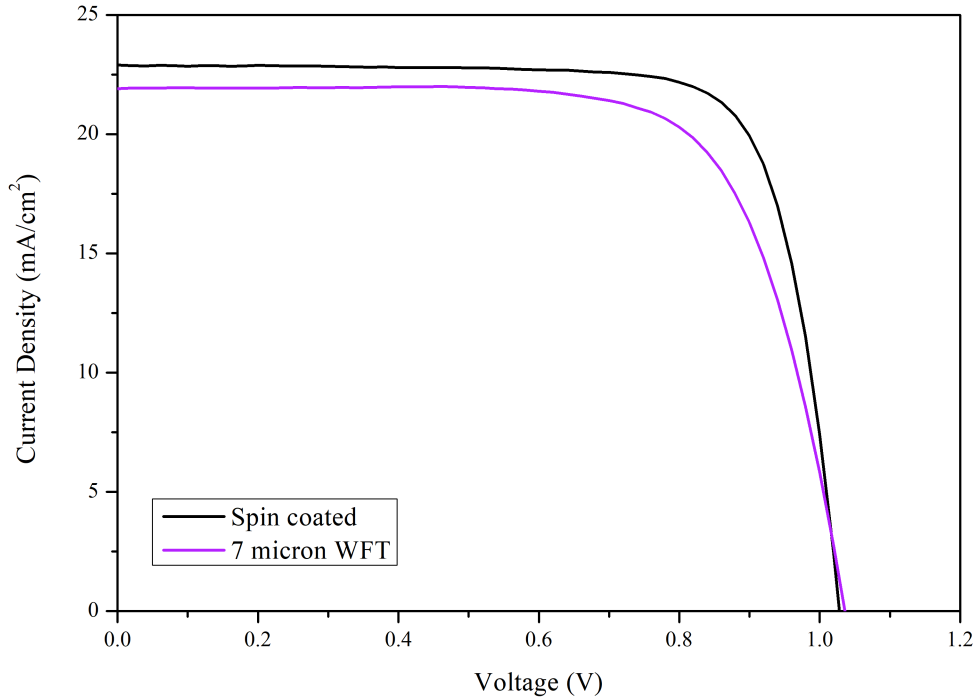


Figure 4.14: Hero device J-V data comparing a roll-to-roll slot die coated tin oxide ETL on a PET substrate compared to a spin coated control device on glass.

Table 4.1: Hero device J-V characteristics comparing a roll-to-roll, slot-die coated tin oxide ETL to a spin-coated equivalent (Reverse scans). Corresponding J-V curves plotted in Figure 4.14

Deposition Method	$J_{SC}(mA/cm^2)$	$V_{OC}(V)$	FF(%)	PCE(%)	$R_{Series}(Ohms/cm^2)$
Spin-coated	22.88	1.03	78.95	18.52	40.6
Slot-die coated	21.94	1.03	71.94	16.34	72.6

Stabilised efficiency measurements were made on the hero devices for spin-coating and slot-die coating and presented in Figure 4.15. A small amount of hysteresis was present in both coating methods with average stabilised efficiencies of 13.9% for the spin-coated device and 11.81% for slot-die. An overall difference in PCE of 2.1% between the two coating methods showed that the slot-die coated film gave similar performances, albeit slightly lower. This was suggested to be caused by the lower conductivity of the ITO coated PET compared to the ITO coated glass, which resulted in a higher series resistance value for the slot-die coated film in Table 4.1. Further improvements could be made by using a lower resistance substrate and the hysteresis reduced/removed by using a surface passivation layer. Nonetheless, it was proven that a high performance roll-to-roll  $SnO_2$  film can be deposited via slot-die coating at reasonable coating speeds.

In addition to this, the stabilised efficiency was almost identical to the benchtop slot-die

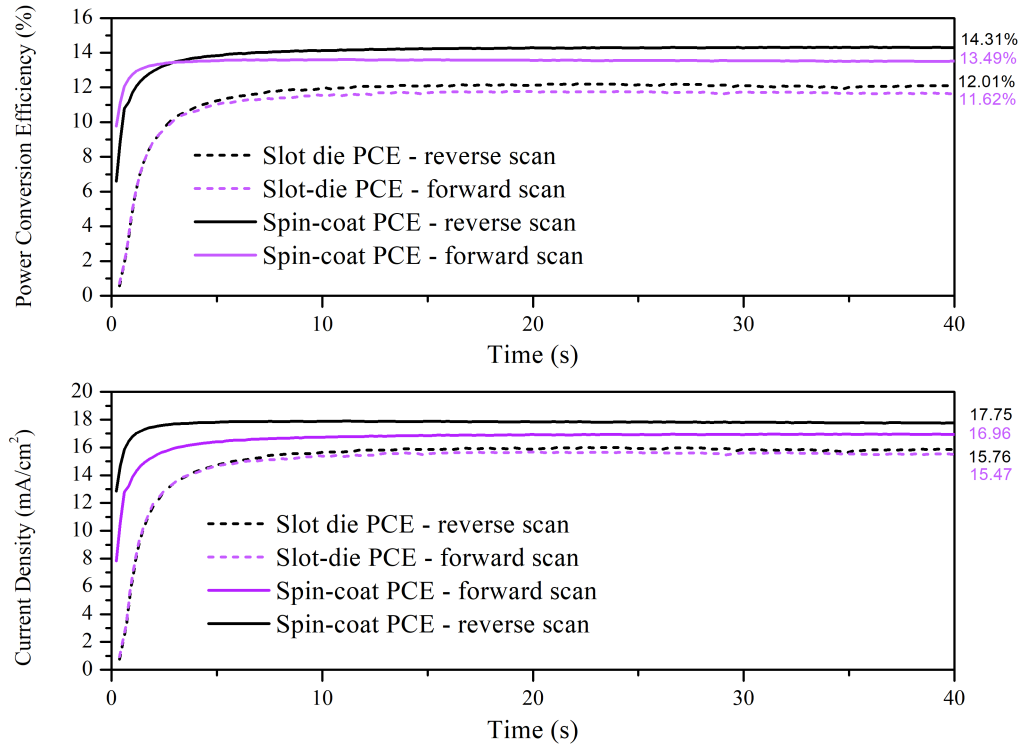


Figure 4.15: Stabilised efficiency measurements for spin-coated SnO<sub>2</sub> and roll-to-roll slot-die coated SnO<sub>2</sub>.

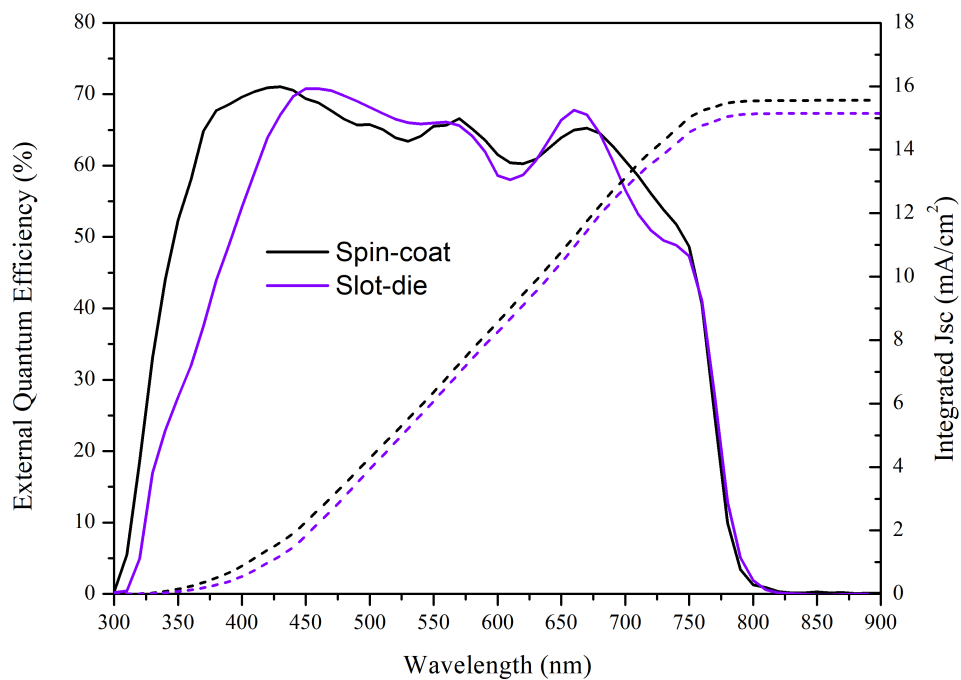


Figure 4.16: External Quantum efficiency measurements comparing the slot-die and spin-coated films. Also included is the integrated Jsc

coated film, and infact slightly higher, confirming that the upscaling from sheet-to-sheet to roll-to-roll coating is a relatively simple procedure and allows for reliable "proof of concept"

type experiments without the material wastage from a roll-to-roll coating trial.

Measurement of external quantum efficiency (EQE) was performed to compare the two deposition methods. Figure 4.16 shows the EQE results with integrated Jsc values. Both EQE traces reach a maximum EQE of 70%, albeit with the slot-die coated film reaching this at a longer wavelength. Integrated Jsc calculations give a Jsc of 15.1 mA/cm<sup>2</sup> for the slot-die coated film which is in agreement with the stabilised efficiency measurements. However, a Jsc of 15.56 mA/cm<sup>2</sup> was measured for the spin-coated film which was lower than the 17 mA/cm<sup>2</sup> measured under the stabilised efficiency measurements. The reason for this difference was not found, however, measurements of flexible devices in an EQE setup was difficult due to the small illumination spot size which can lead to discrepancies between JV and EQE results. This could also suggest hysteresis is more prevalent in the spin-coated film, perhaps due to poor morphology and is in agreement with the larger difference between the reverse and forward scans in the stabilised measurements. To conclude, slot-die coating of the tin oxide film led to little difference in performance, and perhaps if the PET/ITO films were as conductive as the glass/ITO substrates, the efficiencies would be similar.

## 4.4 Conclusions

This work demonstrates a R2R fabrication process for a tin oxide electron transport layer on flexible PET/ITO substrates. A coating speed of 1 m/min was used and demonstrates the potential for high-throughput processing of this layer. Coating of the tin oxide film was made possible through solvent engineering to manipulate the rheology of the precursor material producing homogenous, defect free coatings. It was discovered that pre-treatment of the PET/ITO substrate was not necessary and the rheology manipulation was sufficient enough to provide the conditions required for high quality coatings. An estimated surface coverage of 95% was achieved by the addition of 10 volume% 1-butanol to aid in the wetting of the substrate and to remove drying defects from the water-based precursor. Fabrication of perovskite solar cells atop of the slot-die coated SnO<sub>2</sub> led to a champion PCE of 16.34% in the reverse direction. Stabilised efficiency measurements were made and compared to a spin-coated control device with the PCE's being 11.81 and 13.9% respectively. The slightly lower stabilised efficiency for the slot-die coated film was attributed to the higher resistance of the PET/ITO (50 Ohms/sq) compared to the control glass/ITO substrates (15 Ohms/sq).

## Chapter 5

# Nickel Oxide Hole Transport Layer, Optimisation, Coating and Device Characterisation

### 5.1 Introduction

Although some organic Hole Transport Layers (HTLs) such as PEDOT have successfully been employed in large scale roll-to-roll perovskite and organic solar cell applications, they suffer from severe instability issues, especially PEDOT in perovskite-based devices [1, 2]. Further details on these issues are discussed in more detail in Chapter 1.4.6. It is therefore important to find a more stable alternative, with inorganic HTLs known to be more stable than their organic counterparts due to their superior thermal and moisture stability [3, 4]. Inorganic HTLs do however, suffer with more intensive processing conditions, usually being processed from a sol-gel precursor at high temperatures for relatively long annealing times. Common examples of inorganic HTLs in the literature include: Nickel Oxide (NiOx)[5], Cuprous Oxide (Cu<sub>2</sub>O)[6], Cupric Oxide (CuO) [7] and Copper Thiocyanate (CuSCN) [8], with NiOx being the most common. NiOx has been the most common inorganic HTL employed in perovskite solar cells in the literature due to it having good chemical stability and a convenient energy alignment with perovskite. Figure 5.1 shows the energy alignment of the most common organic and inorganic found in the literature for reference. NiOx can also be deposited via various methods such as spray pyrolysis [9], spin coating [10], sputtering [11] and atomic layer deposition (ALD) [12], with all reaching excellent efficiencies. Most commonly, NiOx is deposited by spin coating a

sol-gel such as Nickel Acetate Tetrahydrate (NiAc) dissolved in 2-methoxyethanol onto a glass substrate and annealing at 300 °C for 30 minutes, which is clearly not suitable for roll-to-roll deposition onto temperature sensitive substrates. Other methods such as ALD and sputtering could be compatible with roll-to-roll processing, but not without significant capital costs. NiOx was chosen as the target HTL for use in a roll-to-roll perovskite device stack, with the aim to reduce processing temperatures to a more suitable 150 °C or below. Although the most common method for NiOx deposition is the high-temperature sol-gel method, the next section was focussed on reducing the processing temperature of this precursor.

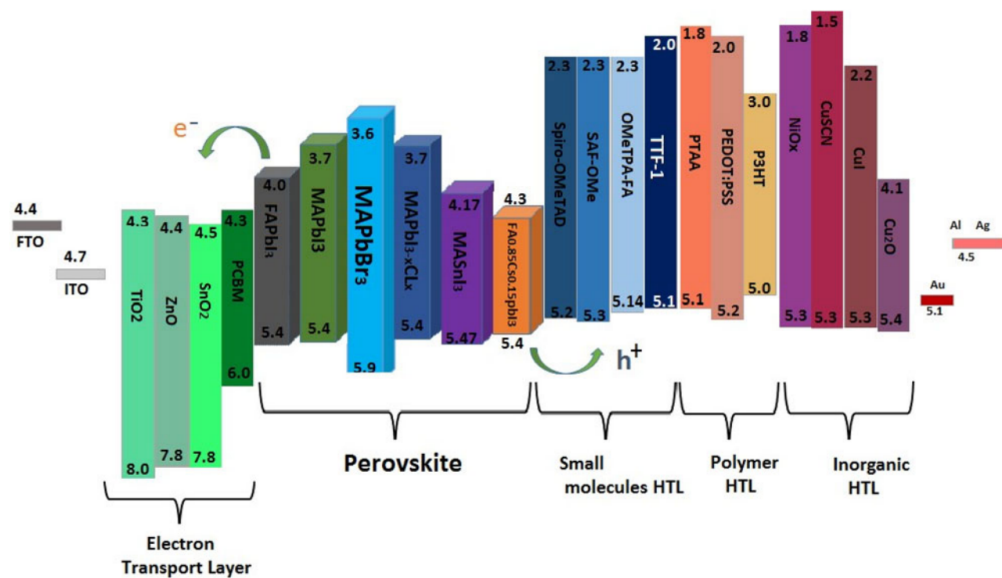


Figure 5.1: Schematic diagram of the energy level alignments of perovskite absorbers and various common HTLs, ETLs, and electrodes [13]

## 5.2 Experimental Methods

Spin coating of perovskite devices was conducted as described in Chapter 2.1. Subsequent characterisation of the device performance parameters were carried out as described in Chapter 2.7. The NiOx layer itself was characterised using various techniques including: Scanning Electron Microscopy (Chapter 2.6.1), Thermogravimetric Analysis (Chapter 2.6.4), Differential Scanning Calorimetry (Chapter 2.6.4), Transmission Electron Microscopy (Chapter 2.6.2), X-Ray Photoelectron Spectroscopy (Chapter 2.6.6), Atomic Force Microscopy (Chapter 2.6.5), Fourier Transform Infrared Spectroscopy (Chapter 2.5.2) and UV-Vis Spectroscopy (Chapter 2.5.1)

As detailed in Chapter 2.1 The full device stack was finished using the standard fabrication

method via spin coating and was made up of the following: Glass/ITO/NiOx/Perovskite/PCBM /BCP/Silver (Figure 5.2).

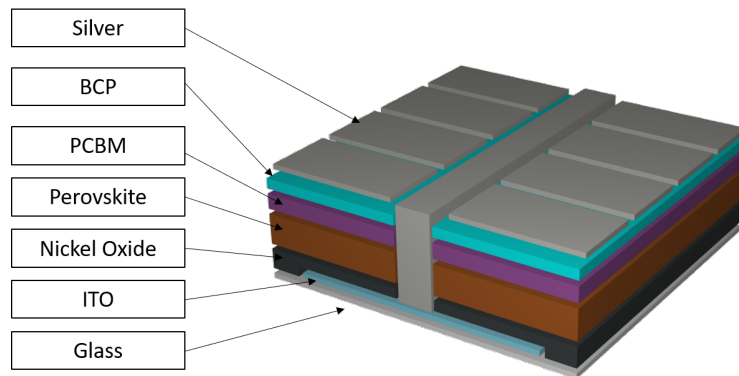


Figure 5.2: Nickel oxide based perovskite device structure.

## 5.3 Results and Discussion

### 5.3.1 Sol-Gel Based Nickel Oxide

In the literature, NiOx is usually formed from a sol-gel precursor containing Nickel acetate tetrahydrate ( $C_4H_{14}NiO_8$ ) dissolved in 2-methoxy ethanol with a small amount of ethanolamine ligand as a stabilising agent to stabilise the Nickel ions [14]. This is then spin coated onto a substrate and annealed at 300 °C for 30 minutes to convert the NiAc into NiOx by thermal decomposition. Firstly, attempts at reducing this processing temperature to 150 °C were conducted to see if the conversion could take place at lower temperatures. Films were made by spin coating the sol-gel onto ITO coated glass and annealing at 150 °C for 30 minutes and 10 minutes, with a standard film annealed at 300 °C for 30 minutes as a comparison. Firstly, perovskite devices were built on top using the method outlined in Chapter 2.1 (Glass/ITO/NiOx/Perovskite/PCBM/BCP/Ag), as this was a quick way to determine whether the NiAc annealed at lower temperatures was acting as a HTL, thus confirming whether or not the NiAc had converted into NiOx. Images were taken of the devices prior to testing under a solar simulator and shown in Figure 5.3

The NiAc film annealed at 150 °C for 10 minutes appeared to impact the morphology of the perovskite layer spun on top, most likely due to retained solvent in the film and unconverted NiAc. However, the film annealed at 150 °C for 30 minutes was visually comparable to the 300 °C equivalent. Solar simulator testing revealed that both NiAc films annealed at 150 °C

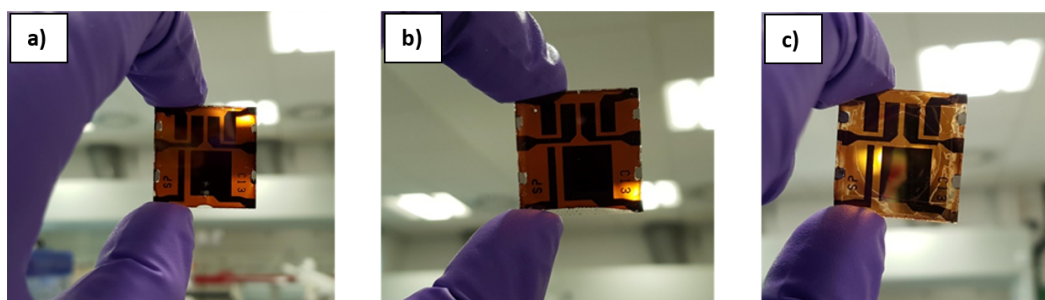


Figure 5.3: Images of full perovskite device stacks built on top of annealed NiAc films at: a) 300 °C for 30 minutes, b) 150 °C for 30 minutes, and c) 150 °C for 10 minutes.

produced non-working perovskite devices, with the subsequent Current-Voltage (JV) curves presented in Figure 5.4.

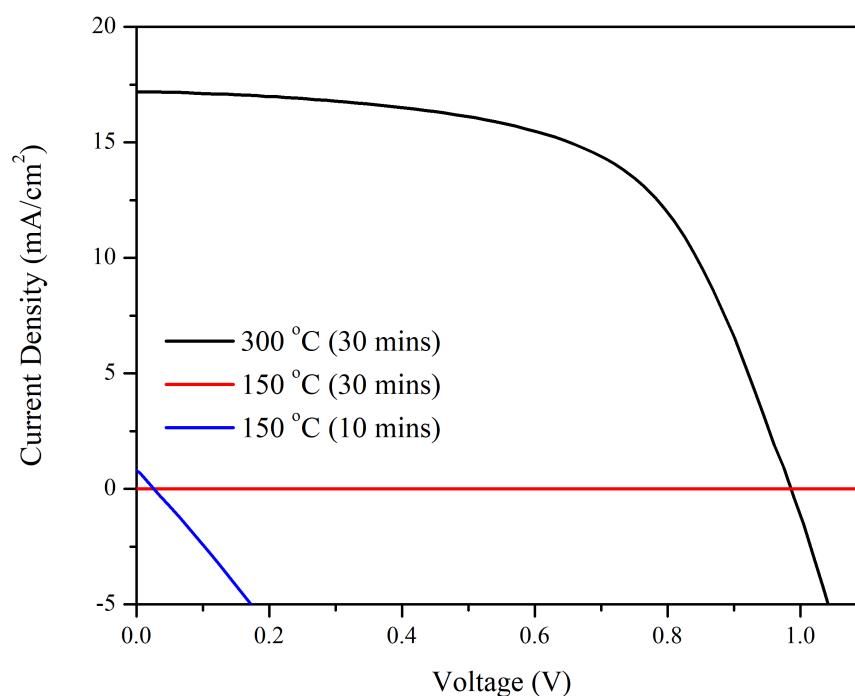


Figure 5.4: Typical JV curves comparing the device performances of NiAc films annealed at 300 °C (30 mins) and 150 °C (30 mins and 10 mins). (Reverse scans)

It was clear from the JV curves that neither of the low-temperature annealed NiAc were acting as HTLs, with no current produced by the devices, suggesting the NiAc had not converted into NiOx. Conversion to stoichiometric NiOx may have occurred, but this is naturally insulating which would prevent movement of current. Annealing for a longer period at 150 °C may be enough to convert to NiOx, but this was not explored as the time constraint would be a major bottleneck in a roll-to-roll coating line.

To confirm whether the NiAc had converted into NiOx, Fourier-Transform Infrared Spec-

troscopy (FTIR) was performed on the film annealed at 150 °C for 30 minutes and compared to the 300 °C equivalent. A neat solution of NiAc was also included for comparison to determine whether any residual solvent was present in the annealed films. Figure 5.5 shows the spectra obtained, with the neat NiAc solution showing a broad peak between 3600–3000  $\text{cm}^{-1}$  which is due to the O-H stretching from the 2-methoxy ethanol solvent. This peak is not present in both the annealed NiAc films confirming that the solvent had been removed. Also, the strong peak at 2900  $\text{cm}^{-1}$  shows a C-H stretch, again from the 2-methoxyethanol solvent which had been removed in both annealed films. A broad peak from approximately 1250-800  $\text{cm}^{-1}$  was present for the film annealed at 300 °C suggesting the presence of a Ni-O or Ni-O-H bond, which was not present in the film annealed at 150 °C.

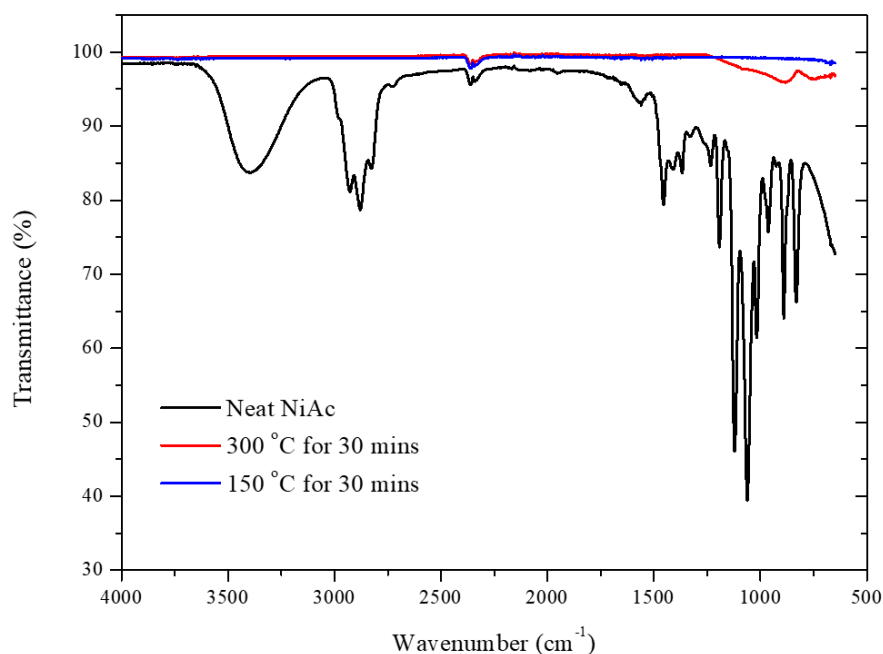


Figure 5.5: FTIR spectra showing the difference between a NiAc film annealed at 300 °C for 30 minutes and at 150 °C for 30 minutes. Also included is the FTIR spectra for a neat NiAc solution

To further establish that conversion from NiAc to NiOx had not occurred in the film annealed at 150 °C, Thermogravimetric Analysis (TGA) coupled with differential Scanning Calorimetry (DSC) was performed on the neat NiAc solution to discover the point at which conversion occurs.

A neat NiAc solution was placed into the furnace of the TGA-DSC in an alumina crucible and subjected to a temperature ramp from 30 °C to 300 °C at a rate of 10 °C/minute in air, and then held at 300 °C for 50 minutes. Weight loss as a percentage and heat flow in mW were



recorded and presented in Figures 5.6 and 5.7 respectively. Weight of the solution dropped quickly to 4.2 weight% due to evaporation of the solvent, and then plateaued until the temperature reached 300 °C. Upon the sample reaching 300 °C a drop-in weight to 1.53% occurred which is attributed to the decomposition of the NiAc into NiOx. In addition to this, the heat flow curve also showed an endothermic peak confirming that this is the point at which NiAc starts converting into NiOx. Therefore, it was confirmed that conversion of a NiAc precursor on a temperature-sensitive substrate was not possible on a hot plate, so other avenues were explored.

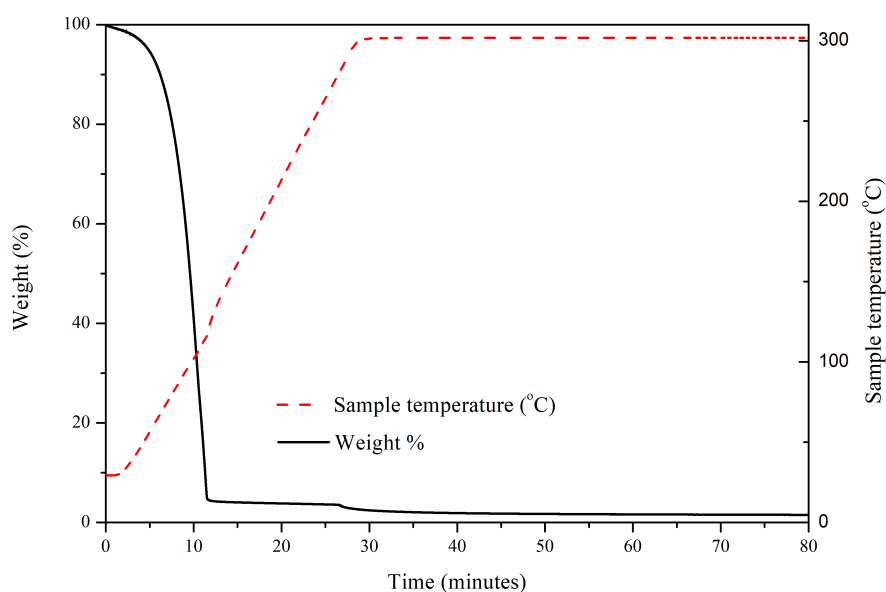


Figure 5.6: TGA analysis of neat NiAc solution with a ramp rate of 10 °C/minute up to 300 °C and held for 50 minutes.

### 5.3.2 Photonic Curing of NiAc

For conversion of the NiAc precursor into NiOx on a temperature-sensitive substrate the annealing would have to be significantly fast to prevent damage. Photonic curing is a proven technique for annealing/sintering materials with high temperature requirements on temperature sensitive substrates, mainly due to its extremely short exposure times, and the ability for it to heat the layer in question without transferring too much heat into the underlying substrate. In this work a Novacentrix Pulseforge 1300 system was used with spectral output from 200 - 1000 nm. Figure 5.9 shows the spectral output from the photonic lamps with a peak output at approximately 480 nm. Increasing the power of the lamp leads to an increase in intensity in all bands with the peak intensity shifting slightly to the shorter wavelengths. Combining a

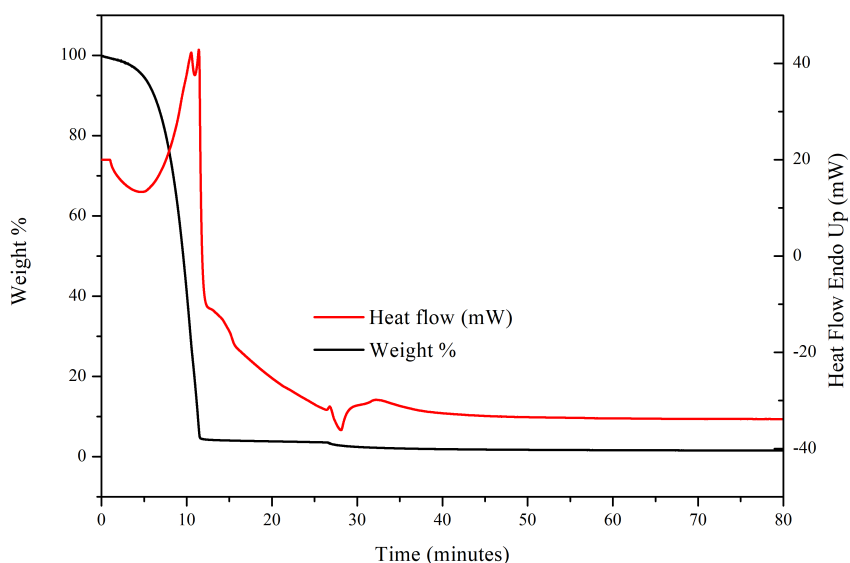


Figure 5.7: DSC analysis of neat NiAc solution with a ramp rate of 10 °C/minute up to 300 °C and held for 50 minutes.

normalised intensity spectra from the Pulseforge with the absorbance spectra of a NiAc film on ITO glass it is clear that the film does not absorb much light in the UV-Vis-NIR region. However, a small amount is absorbed around the 250 - 450 nm wavelengths which coincides with a portion of the spectral output from the Pulseforge and may facilitate sufficient heating via absorption to convert the NiAc into NiOx.

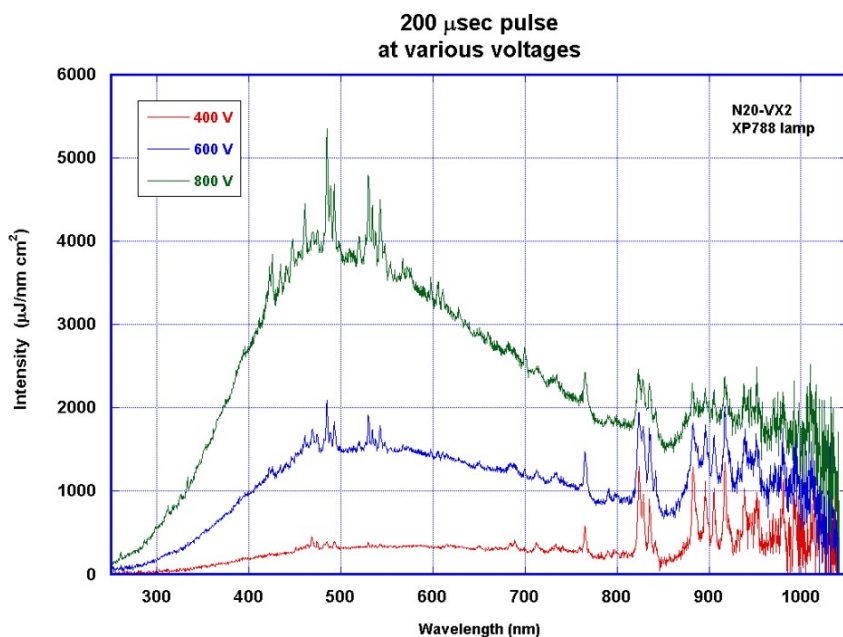


Figure 5.8: Intensity spectra for Novacentrix Pulseforge 1300 photonic lamps using a 200 μs pulse at three lamp voltages. @Novacentrix 2021.

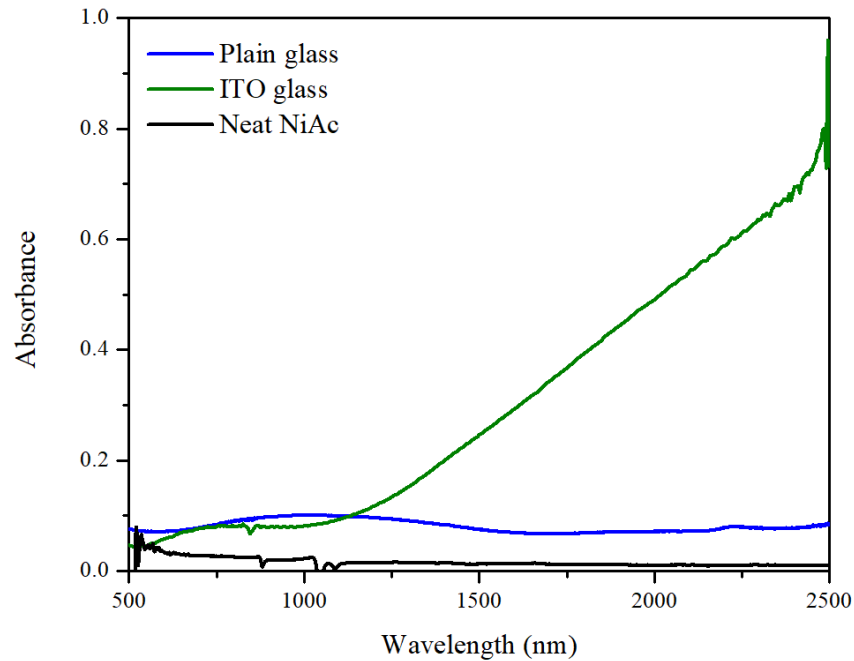


Figure 5.9: Comparison of the PulseForge white light intensity to the absorbance spectra of NiAc on glass/ITO substrate.

The Novacentrix Pulseforge 1300 is controlled by varying the voltage, thus intensity of the lamp, and duration of exposure. As the exposure times are so brief ( $\approx 1$  ms) the top film can be heated whilst the bulk of the substrate is kept relatively cool. A vast amount of parameters can be programmed into the photonic curing process such as being able to perform multiple flashes at different voltages and exposure times, as well as having the ability to perform continuous pulses which would be compatible with a roll-to-roll coating line. A schematic representation of the photonic curing system is shown in Figure 5.10

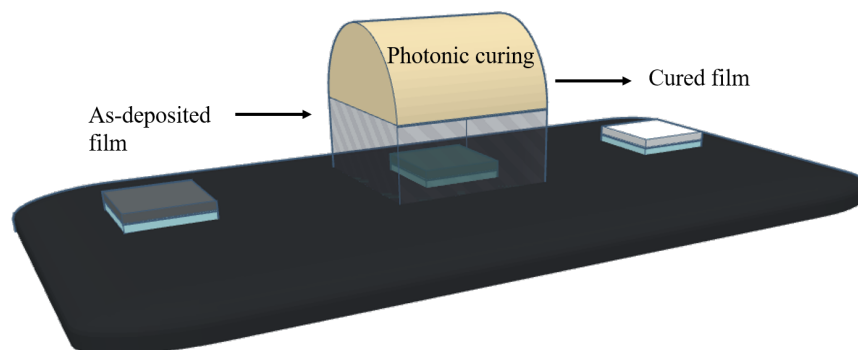


Figure 5.10: Schematic illustration of the photonic system used in this work.

Due to the vast amount of power and exposure settings available, a simple matrix of settings was chosen and outlined in Table 5.1 which was suggested by the machine operator. Spin

coated films of NiAc on ITO coated glass were subjected to each of the settings in Table 5.1, with perovskite devices then built on top. Each of the devices were then tested under a solar simulator, with the best performing devices from each lamp power setting summarised in Figure 5.11. Data collected from the devices showed that the NiAc film had converted into a film which worked as a HTL, albeit with much lower performance than the thermally annealed control device. All the photonicallly cured device data was significantly worse than the control device with the best performing device exhibiting a champion efficiency of 3.01%, which was processed with 10 pulses at 350 V. Efficiencies dropped off after this when higher voltages were used, albeit with a smaller amount of pulses. However, increasing the number of pulses at 400 V and above had a detrimental effect on the device performances. Poor current densities of 9 mA/cm<sup>2</sup> and below was the main cause of the reduced device performances, as well as low fill factors of 40%, most likely being due to the NiAc not being fully converted into NiOx, which was expected due to the short exposure time. This would cause many issues related to the poor device performances such as; poor HTL conductivity, problems with the NiOx/perovskite interface and poor morphology of the NiOx.

Table 5.1: Parameters for photonic curing exposures on NiAc.

No. Pulses	Lamp power (V)					
1	250	300	350	400	450	
2	250	300	350	400	450	
5	250	300	350	400	450	
10	250	300	350	400	450	

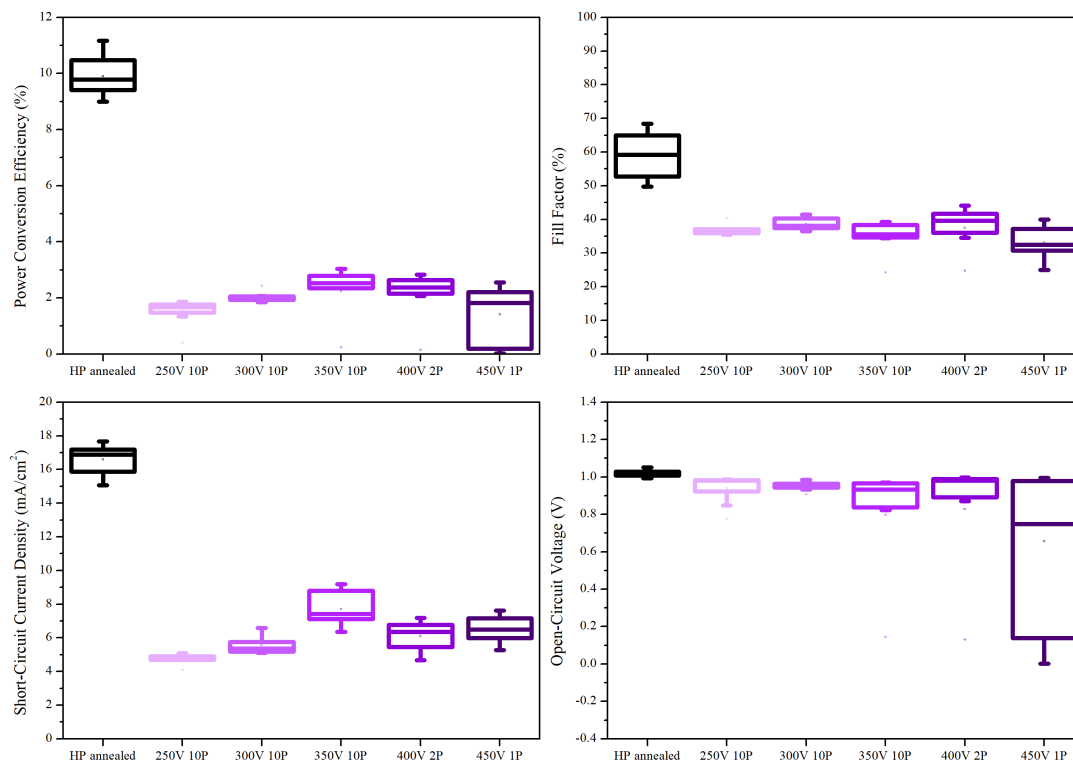


Figure 5.11: Statistical analysis of J-V data for the best performing photonicallly cured NiOx devices from each power setting. Data presented from 24 devices.

X-ray photoelectron spectroscopy (XPS) was performed on each of the best performing photonicallly cured NiAc films and compared to a film annealed at 300 °C for 30 minutes to distinguish the differences in elemental composition of the films. Figure 5.12 shows the oxygen and nitrogen peaks for a typical photonic sample and the thermally annealed sample. Both samples clearly contain oxygen, however, the peak at 529 eV is a classic metal oxide peak confirming that the thermally annealed sample contains NiOx. This peak was not present on the photonicallly cured samples, although the oxygen peaks that are present (531.1 – 531.3 eV) could be due to a range of different NiOx species such as Ni(OH)<sub>2</sub> and Ni<sub>2</sub>O<sub>3</sub>. It was suggested that some of the NiAc had converted into NiOx, however, most of it was most likely still NiAc preventing current passing through, explaining the low Jsc values.

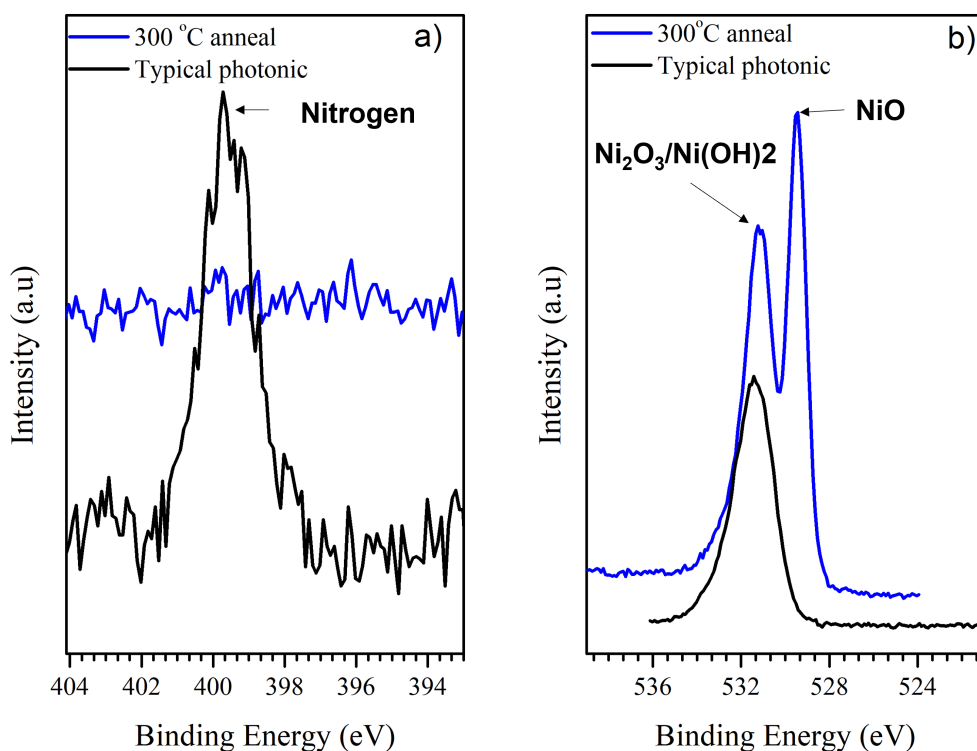


Figure 5.12: XPS data showing a) Nitrogen peaks, and b) Oxygen peaks. Data collated by Dr James McGettrick

With regards to the strong nitrogen peak found in the photonic sample, it is most likely due to the ethanolamine ligand used in the precursor solution for stabilisation, and it makes sense that this would be difficult to remove, especially with such short curing times.

Table 5.2 contains the compositional data collected from the XPS analysis and shows that the thermally annealed sample has a significantly higher proportion of nickel compared to the photonic cured samples, explaining the difference in efficiencies. An O:Ni ratio of around 1.09 is typical for a NiOx film used at a HTL in perovskite devices [15], with the ratio of the hotplate annealed NiOx film having a O:Ni ratio of 1.08, whereas the ratios for the photonic cured samples was significantly higher than this, with an average of around 3.5.

There was also a lot more carbon present in the photonic cured samples showing that a significant amount of the precursor had not been converted into NiOx. This proved that photonic curing does have the potential to convert the NiAc into NiOx but would require a larger amount of pulses. Interestingly, the films subjected to 450V for 1 pulse lead to larger amounts of nickel, but had worse efficiencies, perhaps due to the high amount of power causing

Table 5.2: XPS compositional data of the best performing photonic NiAc films at each voltage compared to a hot-plate annealed NiAc film. (p) refers to the number of pulses

Device	Amount (Atom %)			
	Nickel	Oxygen	Nitrogen	Carbon
300 °C	35.7	38.4	0	25.2
250 V (10p)	8.4	29.7	4.5	57.4
300 V (10p)	6.3	27.2	3.8	62.7
350 V (10p)	8.9	31.2	4.2	55.8
400 V (2p)	8.9	30.6	4.6	55.9
450 V (1p)	10.8	31.6	4.1	53.5

some damage to the underlying substrate.

Results from the XPS experiment suggested that a larger amount of pulses could lead to further conversion into NiOx and thus increase the efficiency of the devices, and was therefore tested. Figure 5.13 shows images of the perovskite films spin coated on top of each photonicly cured NiAc film, and immediately showed that there was an issue with the film morphologies. As to be expected the devices had extremely poor performance (less than 2%).

It was hypothesised the poor perovskite film morphology was due to the ITO absorbing the photonic light more than the bare glass, thus leading to a thermal difference between the two, and in turn a difference in the NiAc conversion between them. This was occurring in the second test as the number of pulses and power had been increased allowing the ITO more time to absorb the photonic energy. Although photonic curing is a method for alleviating temperature rises of the underlying substrate, the amount of pulses required for further NiAc conversion seemed to lead to the ITO absorbing energy and heating up. This would lead to a difference in morphology on the ITO compared to the bare glass, subsequently effecting the perovskite morphology.

Further optimisation of the photonic curing of NiAc could be performed by using the smallest power output, and increasing the number of pulses, until a suitable setting was found. However, the aim of this research is to find a method of producing these layers via a roll-to-roll fabrication method and increasing the number of pulses will exponentially increase the production time. If the layer needs to be exposed to say 20 pulses, it would be difficult to implement this into a roll-to-roll coating unit without multiple photonic units and high capital costs. Ideally the number of pulses needs to be as low as possible.

During the experimentation and planning of this first phase and preparation for potential scale up, risk assessments identified a major difficulty with the toxicity aspects of the precursor

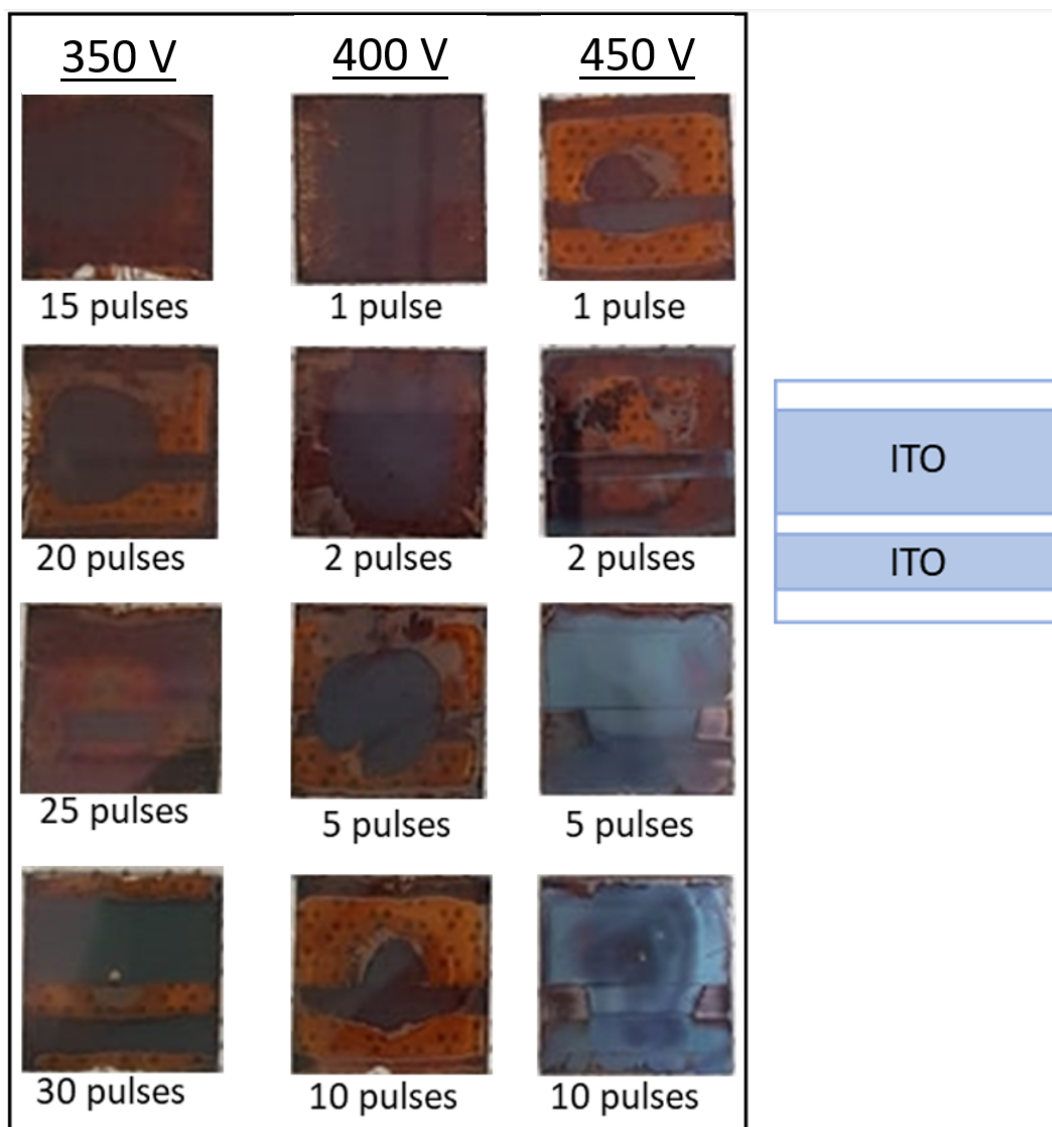


Figure 5.13: Images of perovskite films deposited on top of photonicly cured NiAc at different power and pulses. Included diagram is the ITO pattern on the glass used for illustration of damaged areas

material, in particular the 2-methoxyethanol solvent. Therefore, it was decided to abandon the use of NiAc as a precursor for NiOx and move on to alternative precursor materials.

### 5.3.3 Nickel Oxide Nanoparticles

The next logical step for realising a method for the deposition of a low-temperature nickel oxide layer was to use a nanoparticle suspension, as this should not require post annealing, only drying. This is due to the fact that the nanoparticles are already formed into NiOx prior to dispersion in a solvent, thus not requiring a decomposition step. A product called N-31 was purchased from Avantama, which consisted of a 2.5 weight% NiOx nanoparticle suspension in



ethanol, stated as a suitable hole-transport layer in a perovskite device. Initially, optimisation of the layer via spin coating was carried out by simply varying the thickness of the NiOx layer by changing the spin speed. Perovskite devices were then built on top and tested under a solar simulator and compared to a “control” device employing the high-temperature nickel acetate based NiOx layer (HT-NiOx). Firstly, spin speeds were optimised with 4000, 6000 and 8000 rpm being used, with thicknesses of these layers being approximately; 50, 35 and 30 nm respectively. Subsequent perovskite solar cell JV data for devices built on top of these layers is summarised in Figure 5.14. Recommendation from Avantama was to dry the nanoparticle films for 15 minutes at 110 °C or above to remove the solvent, so to be safe the films were dried on a hot plate for 15 minutes at 150 °C.

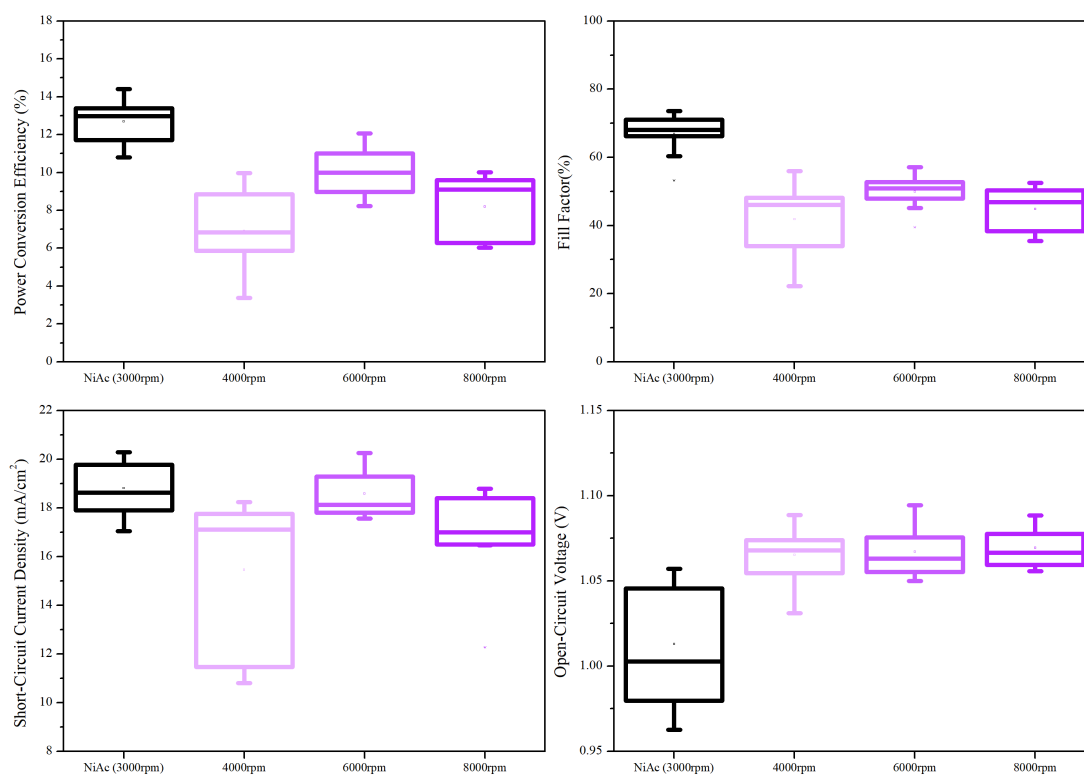


Figure 5.14: statistical JV analysis of the spin speed optimisation of NiOx nanoparticles. Data presented from 16 devices.

Clearly, the films spun at 6000 rpm lead to the best performance, with a champion efficiency of 12.2%. Average efficiencies of this film thickness were slightly lower than the HT-NiOx, but initial results were promising. It was evident the lower performances were due to a drop in fill factor, averaging around 50% for the nanoparticle film, compared to around 70% for the HT-NiOx, however,  $J_{SC}$  values were similar to the HT-NiOx, and  $V_{OC}$ 's were better, and more

consistent than the HT-NiOx. Good  $V_{OC}$  and  $J_{SC}$  values for the nanoparticle films suggested that the films were of good quality and homogenous, otherwise a drop in these would be expected. Investigating the JV curves for the nanoparticle and HT-NiOx based devices in Figure 5.15 revealed that the loss in fill factor was down to a much higher series resistance in the nanoparticle films, which was almost four times higher than that of the HT-NiOx. Shunt resistances were not too dissimilar between the two films, although slightly higher for the HT-NiOx. Averages for the series and shunt resistances are summarised in Table 5.3

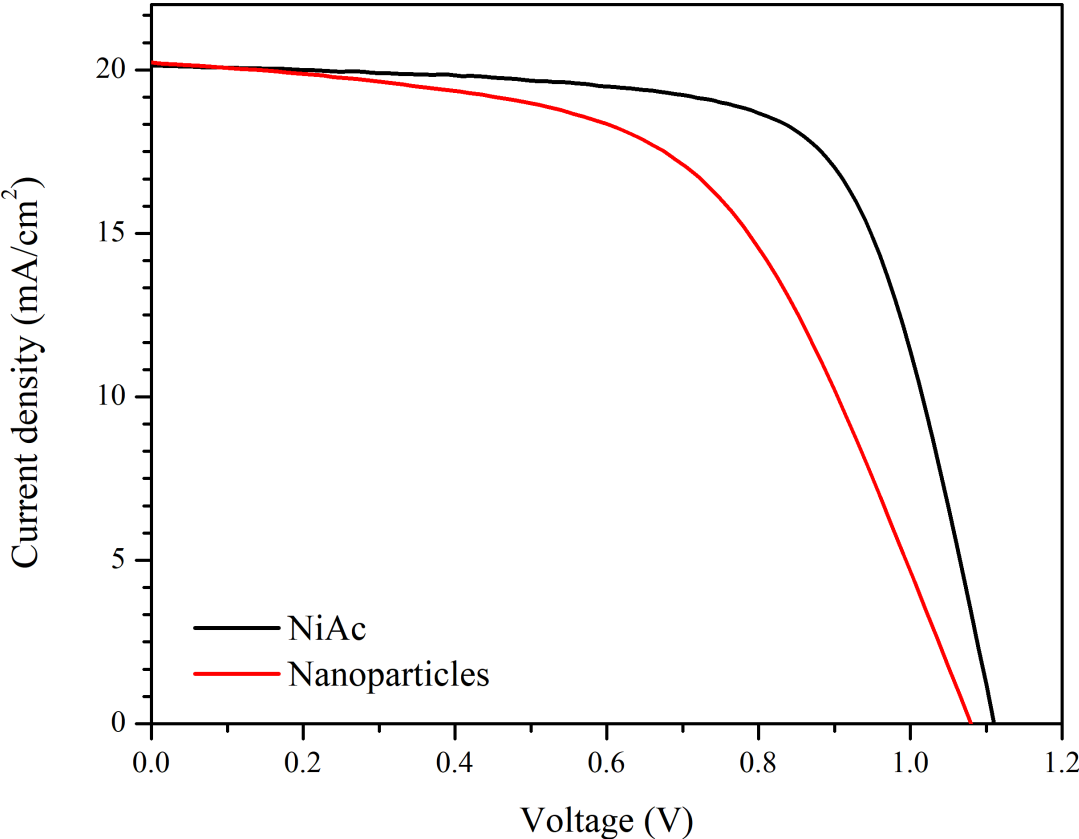


Figure 5.15: Hero JV curves for the nanoparticle-based perovskite solar cell compared to HT-NiOx.

Table 5.3: Average values for series and shunt resistances of the nanoparticle and HT-NiOx based perovskite devices.

Film	Series resistance (Ohms/cm <sup>2</sup> )	Shunt resistance (Ohms/cm <sup>2</sup> )
HT-NiOx	42	7864
Nanoparticles	158	6447

Increase in series resistances was most likely down to low conductivity of the nanoparticle

layer, but could have been due to poor interfaces. Another potential cause could have been due to residual organic species in the film, as the nanoparticle suspension is stabilised by organic material, however, the nature of this was not included in the MSDS of the product. To find out the cause of the high series resistance, the nanoparticle films were investigated by various characterisation techniques. All analysis from here on was conducted on the nanoparticle film spun at 6000 rpm and compared to the HT-NiOx film for reference. Firstly, roughness measurements of the two films were taken to see if the interface was a contributing factor to the series resistance. Roughness measurements were taken using profilometry and Atomic Force Microscopy (AFM) for large and small area resolutions. Ra and Rz parameters were taken using profilometry initially over a 5 mm long strip, both on the nanoparticle (NP's) films, as well as on perovskite films spun on top of each (Figure 5.16). Each measurement was repeated five times on separate areas for each film and the average of these presented.

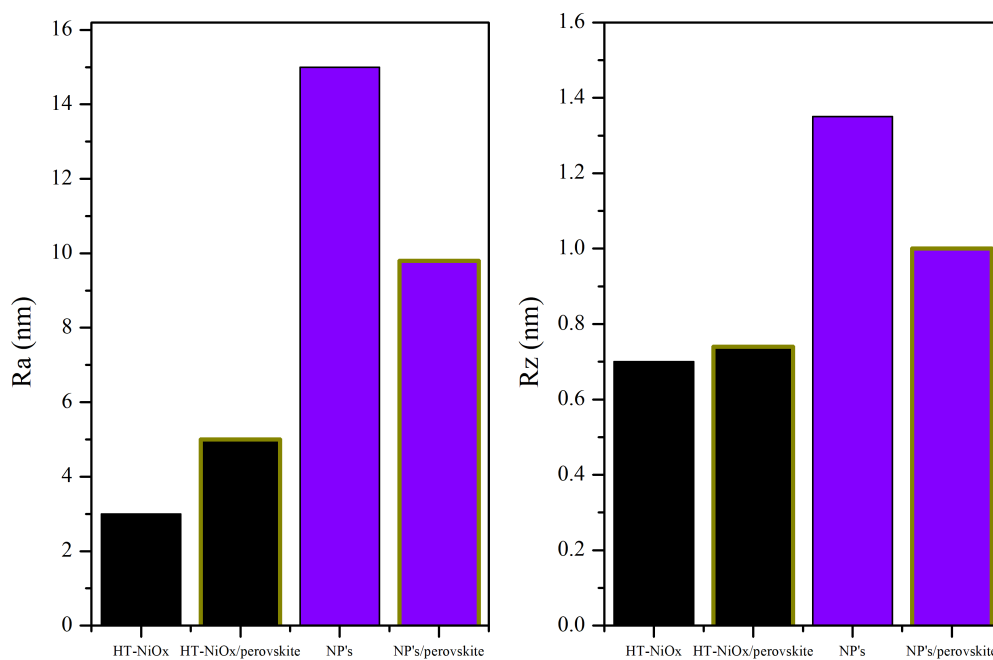


Figure 5.16: Average roughness measurements comparing HT-NiOx and NiOx nanoparticles, as well as a perovskite layer on top of each. (Each measurement was made five times over separate areas).

Overall, the nanoparticle film was clearly more rough than the HT-NiOx, which was inevitable due to the nature of the precursors, nanoparticle films are bound to produce rougher

films than a thermally degraded film. More importantly, the addition of a perovskite film on top of the nanoparticles reduces the average roughness, whereas it makes the film more rough on top of the HT-NiOx. This is good for the nanoparticle film with respect to the Electron Transport Layer (ETL) being deposited on top having a smoother surface to be coated onto. Similar results are seen for the Rz measurements, with it being reduced for the perovskite film on top of the nanoparticles and increased on the HT-NiOx film. An Rz of 1 nm over a stretch of 5mm should not produce any issues on the layer deposited on top so was excluded from being an issue. The roughness of the nanoparticle film itself could lead to poor interfaces between itself and the perovskite film and required further analysis. AFM images are shown in Figure 5.17 and show a similar story to the profilometry measurements, albeit on a much smaller area ( $1.5 \times 1.5 \mu\text{m}$ ).

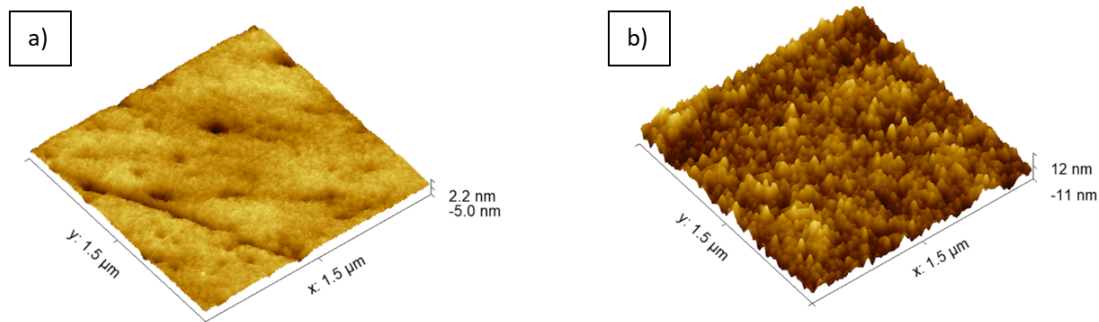


Figure 5.17: AFM images of a) NiAc based NiOx layer and b) NiOx nanoparticles.

AFM images supported the roughness measurements and illustrate the clear difference in film morphologies. Although there was an obvious difference between the films, reducing the roughness of the nanoparticle films would be difficult without the addition of a planarizing layer or a high temperature treatment to sinter the particles together.

SEM images were taken of perovskite films on top of each of the NiOx films to determine if any morphology issues were present between the two. If the roughness of the nanoparticle layer was an issue, some defects in the SEM images would confirm this. Figure 5.18 shows the two perovskite films, with not much difference between the two. The nanoparticle HTL does appear to lead to slightly smaller perovskite crystal sizes, most likely due to providing more nucleation sites for the perovskite to crystallise upon. However, the SEM images show no obvious pinholes in either of the films, and both look to be compact and homogenous with good crystal sizes. In addition to this, if there was an issue with the perovskite film then a

drop in  $J_{SC}$  would be expected, whereas the  $J_{SC}$  values were comparable to the HT-NiOx based devices.

It was suspected that the conductivity of the nanoparticles was the main issue leading to the poor fill factors, and was either due to some residual organic species left in the film which do not degrade at 150 °C, or that the nanoparticles themselves were just inherently less conductive than the HT-NiOx film. To measure the conductivity of the layers, metal-insulator-metal (m-i-m) devices were made, as using a 4-point probe would make conductivity problematic due to how thin the films were. A schematic diagram of how the m-i-m devices were made is shown in Figure 5.19

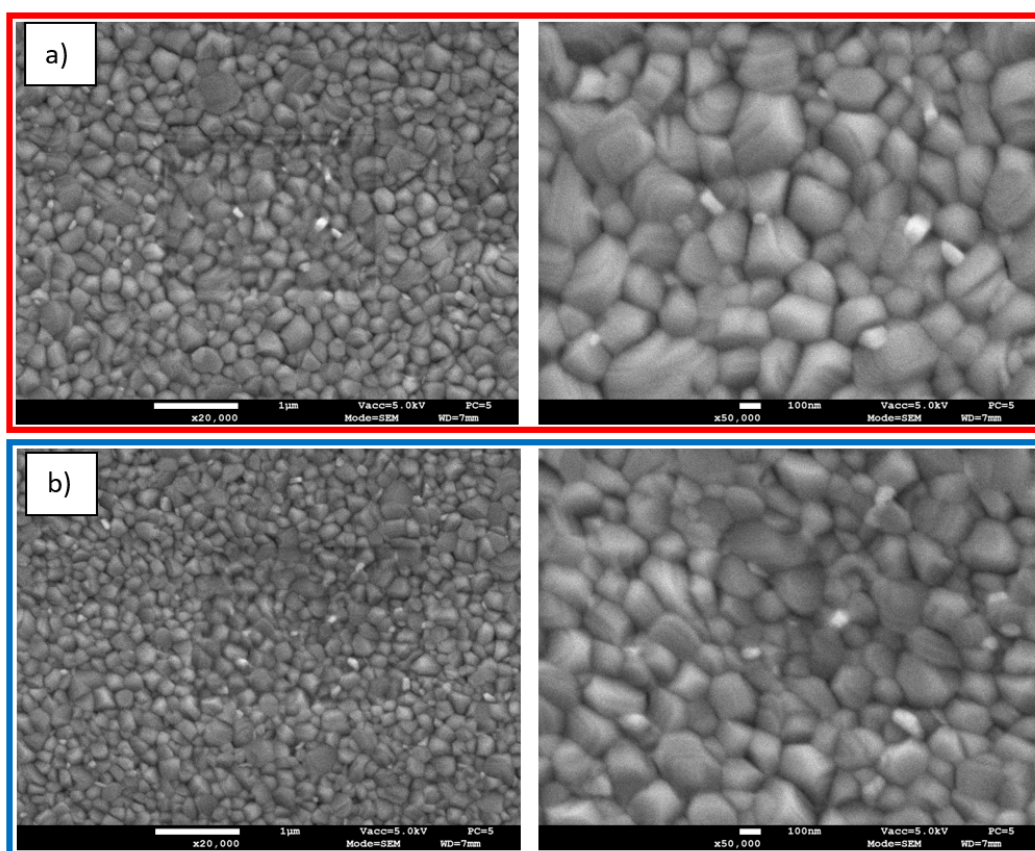


Figure 5.18: SEM images of a perovskite layer on top of a) HT-NiOx, and b) a NiOx nanoparticle layer.

To measure the conductivity, the m-i-m devices were made up from spin coated NiOx on top of ITO coated glass, with a 1 cm<sup>2</sup> evaporated silver contact on top. JV measurements were then made under dark conditions to determine the resistances of the two NiOx layers, and thus the conductivity.

Linear J-V curves in Figure 5.20 show perfect ohmic contact between both NiOx films and

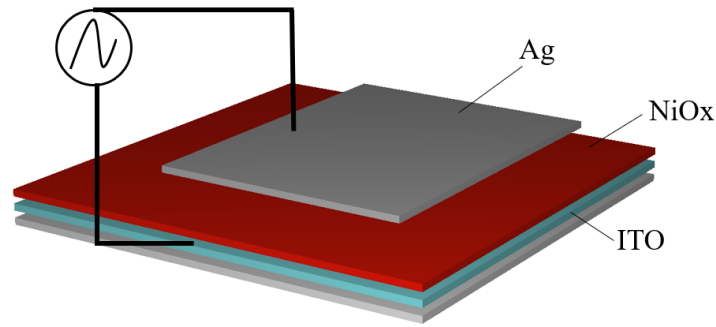


Figure 5.19: Schematic diagram of m-i-m device structure for measuring conductivity.

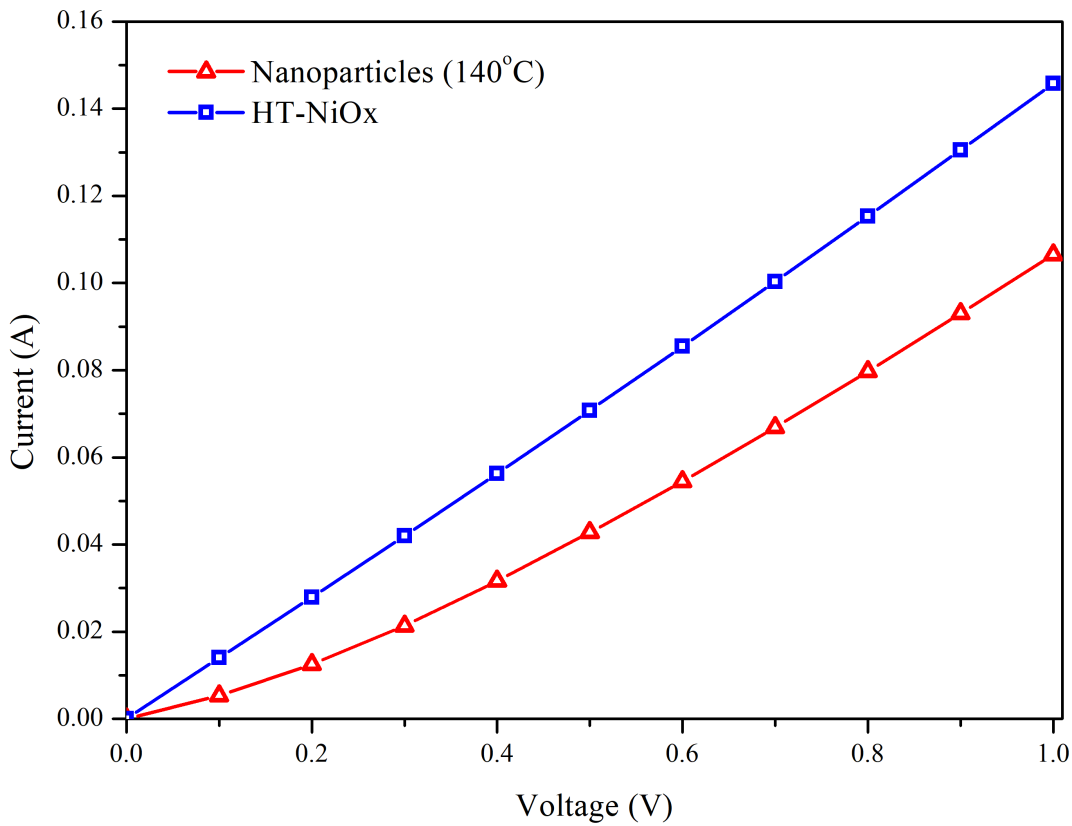


Figure 5.20: J-V Curves for conductivity measurements on HT-NiOx, compared to nanoparticles.

the silver electrode, and the electrical conductivity can be found from these, as it is proportional to the tangent of the J-V curve. Hence, the device results directly correlate to the J-V curves, concluding that the HT-NiOx film has a higher electrical conductivity than the nanoparticle film. Conductivities were calculated using the following equation:

$$\sigma = t/(AxR) \quad (5.1)$$

Where  $\sigma$  is the conductivity,  $t$  is the thickness of the NiOx film ( 35 nm),  $A$  is the active area of the films ( $2.5 \text{ cm}^2$ ) and  $R$  is the resistance of the films calculated from the J-V curves in Figure 5.20 using Ohms Law. Conductivities calculated were  $2.04 \times 10^{-6} \text{ S/cm}$  (HT-NiOx) and  $1.63 \times 10^{-6} \text{ S/cm}$  (nanoparticles) suggesting the lower conductivity was having a direct impact on the device performances.

In an attempt to increase the conductivity of the nanoparticle film, it was dried on a hot plate for 30 minutes at  $250 \text{ }^\circ\text{C}$  as the elevated temperature would remove any residual organic species. A m-i-m device was made to measure the conductivity, with the J-V curve measured added to the previous J-V measurements and summarised in Figure 5.21

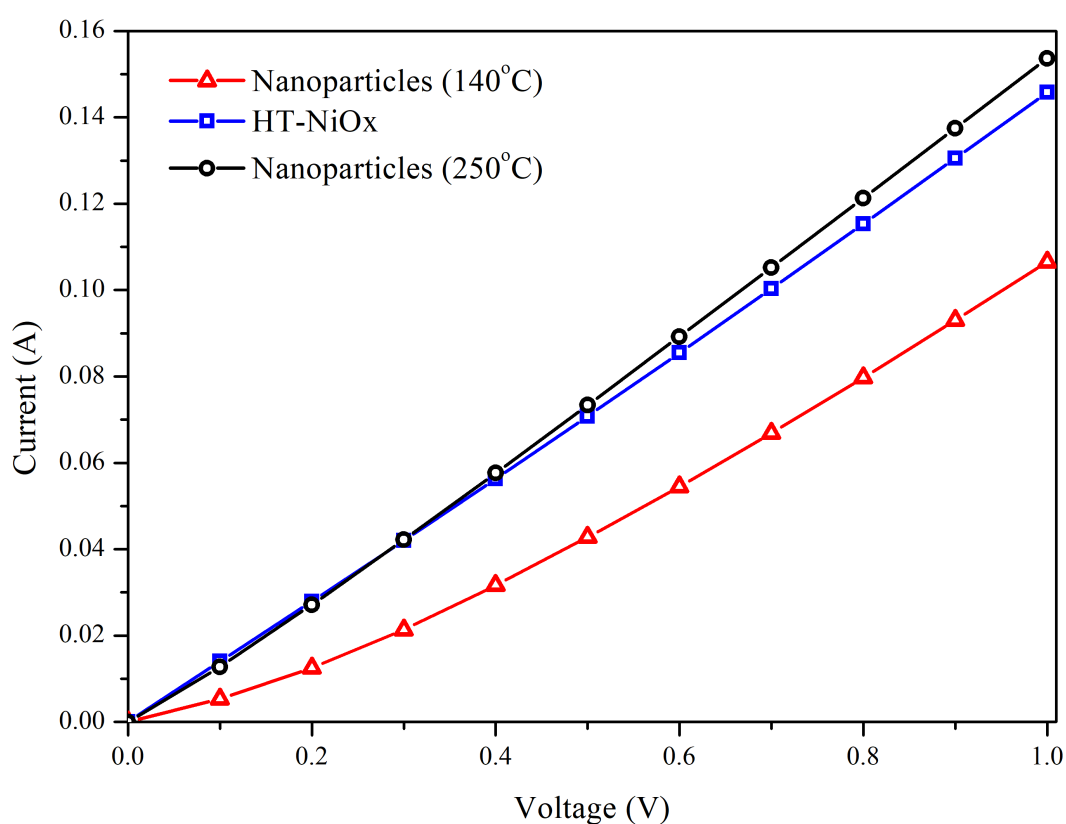


Figure 5.21: J-V Curves for conductivity measurements on HT-NiOx, compared to nanoparticles annealed at 150 and  $250 \text{ }^\circ\text{C}$  for 30 minutes.

Annealing the nanoparticles at  $250 \text{ }^\circ\text{C}$  for 30 minutes clearly increased their conductivity, even higher than that of the HT-NiOx. A conductivity of  $2.15 \times 10^{-6} \text{ S/cm}$  was calculated for the nanoparticles annealed at  $250 \text{ }^\circ\text{C}$ , which was slightly higher than the  $2.04 \times 10^{-6} \text{ S/cm}$  for the HT-NiOx. Due to this rise in conductivity, perovskite solar cells were built on top of films annealed at  $250 \text{ }^\circ\text{C}$  and compared to the HT-NiOx and the nanoparticles annealed at  $150 \text{ }^\circ\text{C}$  to

determine whether the increases in conductivity would lead to a decrease in series resistance, thus an increase in device efficiency.

Figure 5.22 summarises the JV data from these perovskite devices and shows a distinct rise in efficiencies for the nanoparticles annealed at 250 °C with a champion efficiency of 16.74%. With regards to the HT-NiOx and the nanoparticles annealed at 150 °C, efficiencies were very similar due to a higher short-circuit current density for the nanoparticle-based devices. For the nanoparticle films annealed at 250 °C, all device characteristics were superior to the HT-NiOx and the nanoparticles annealed at 150 °C, with excellent fill factors ( 80%) and short-circuit current densities ( 20 mA/cm<sup>2</sup>). As predicted from the conductivity measurements, the more conductive films produced higher efficiency devices, confirming that conductivity is a crucial parameter for these nanoparticles. This was also confirmed by much lower series resistance values for the nanoparticles annealed at 250 °C, leading to higher fill factors.

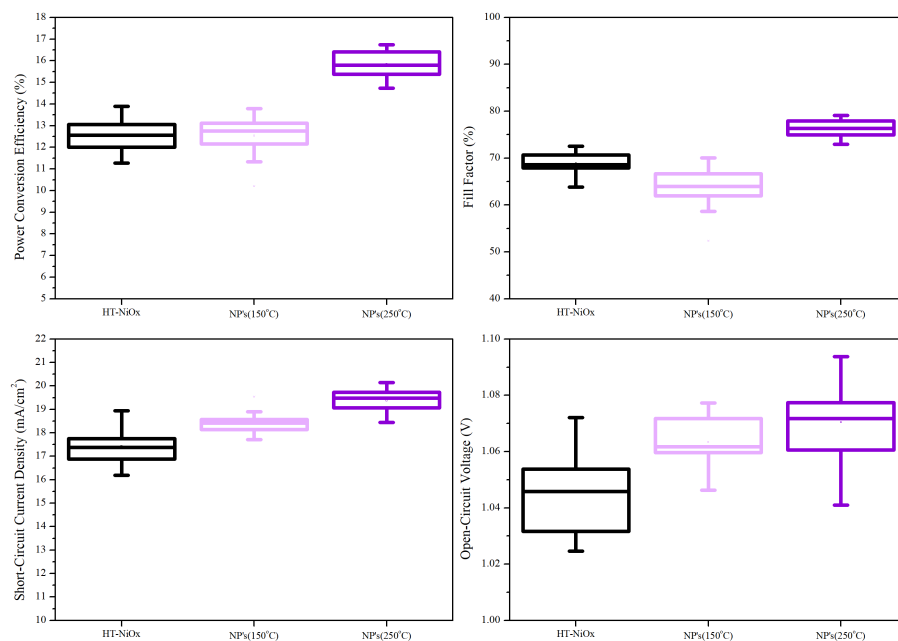


Figure 5.22: Statistical J-V analysis for NiOx nanoparticles annealed at 150 °C and 250 °C for 30 minutes compared to a HT-NiOx device. Data presented from 12 devices.

As the nanoparticles annealed at 250 °C provided much better efficiencies compared to the HT-NiOx, these films would now be used as control devices to see whether the efficiencies of the nanoparticles annealed at 150 °C could be improved upon. This efficiency improvement at



lower temperatures was important due to the focus on scale up of this layer on a PET substrate in which a maximum processing temperature of 150 °C was imposed. Comparing the averages of the series resistances of the two nanoparticle films, the film annealed at 150 °C gave an average of 84 Ohms/cm<sup>2</sup>, whereas, the film annealed at 250 °C gave an average of just 34 Ohms/cm<sup>2</sup>. In addition to this, the short-circuit current densities for the film annealed at 250 °C were higher, suggesting an improvement in the NiOx/perovskite interface, confirmed by higher V<sub>OC</sub> values. It was therefore essential to understand why the film annealed at the higher temperature gave such rises in device performance.

Although the increase in conductivity had been confirmed at the higher temperature, the reason for this was not understood. It was assumed it could be down to two reasons; the nanoparticles were sintering together at higher temperatures, or the organic binder/ligands used to stabilise the nanoparticles in suspension were only removed at elevated temperatures. However, it was unlikely that the nanoparticles were sintering at a temperature as low as 250 °C, and more likely that it was leftover binder/ligands. If the binder/ligands were still present in the low temperature film, it would cause poor inter-connectivity between the particles, thus reducing the conductivity, and if removed at higher temperatures, particle interconnectivity would be improved, effectively increasing the surface area of the NiOx film, thus conductivity.

Thermo Gravimetric Analysis (TGA) and Differential Scanning Calorimetry (DSC) were performed on the nanoparticle suspension to see if any further weight loss was observed when annealing temperature was increased to 250 °C, and to see if any peaks were present in the heat flow curves to signify any sintering occurring.

With respect to the TGA curves in Figure 5.23, initially the two solutions appeared to follow the same weight loss regime at both 150 and 250 °C, albeit with the solution annealed at 250 °C losing weight slightly quicker. However, upon closer inspection by reducing the y-axis, a second weight loss of around 0.3% was observed for the solution annealed at 250 °C most likely relating to removal of residual binder/ligands. The solution annealed at 150 °C reached a final weight of 2.8%, whereas the solution annealed at 250 °C reached a final weight of 2.5% which was the advertised weight percent of NiOx in the solution provided from Avantama. This confirmed that annealing the NiOx nanoparticles at 250 °C rather than 150 °C led to further weight reduction, thus removal of organic species, most likely to be binder/ligands. To confirm this, the DSC curves from both annealing temperatures were investigated and shown in Figure 5.24. No peaks indicative of sintering were present in either of the DSC curves, however it is

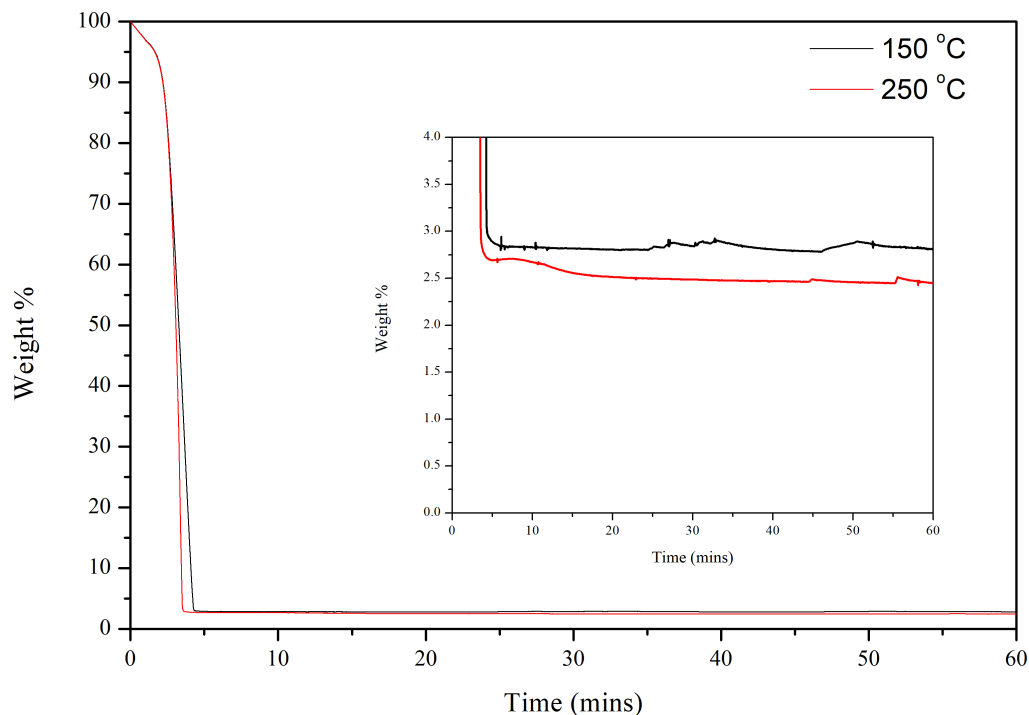


Figure 5.23: TGA of Avantama NiOx nanoparticle suspension held at 150 °C and 250 °C, with the insert showing the weight losses with a reduced x-axis.

worth mentioning some small broad peaks present in the 150 °C hold were present, relating to some small movements in the TGA graph, which was most likely caused by movement of the sample in the crucible.

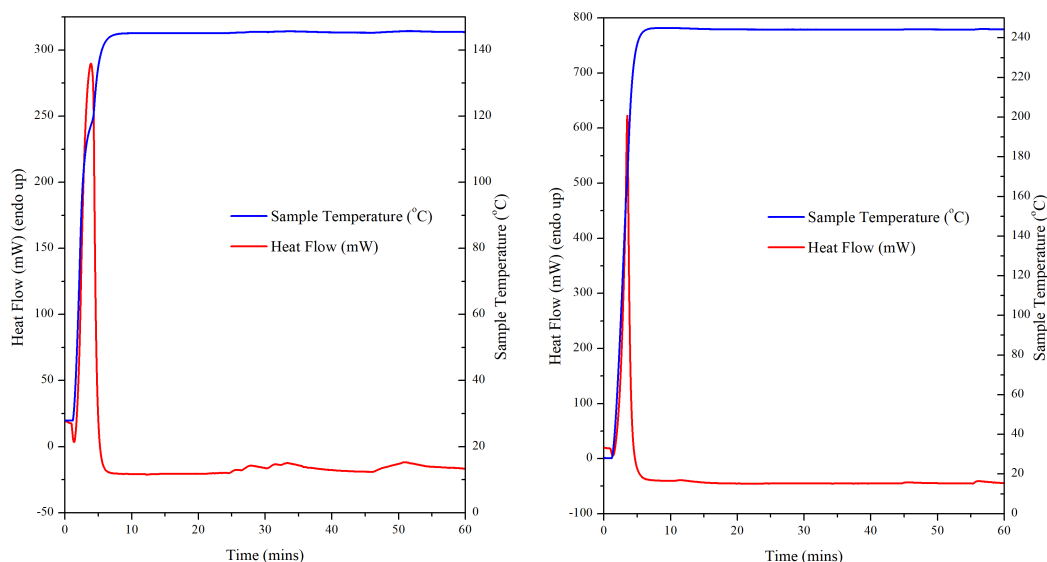


Figure 5.24: DSC curves of Avantama NiOx nanoparticle suspension held at 150 °C and 250 °C.

TGA and DSC analysis of both annealing temperatures confirmed that no sintering was

taking place at the higher temperature, and a second weight loss at 250 °C was attributed to loss of organic species in the solution, most likely binder/ligands.

Further analysis on the two annealing temperatures was conducted to solidify the theory of ligand removal. If ligand removal was occurring at the higher temperature, the roughness of the film would most likely decrease due to better nanoparticle connectivity. AFM images were taken and presented in Figure 5.25

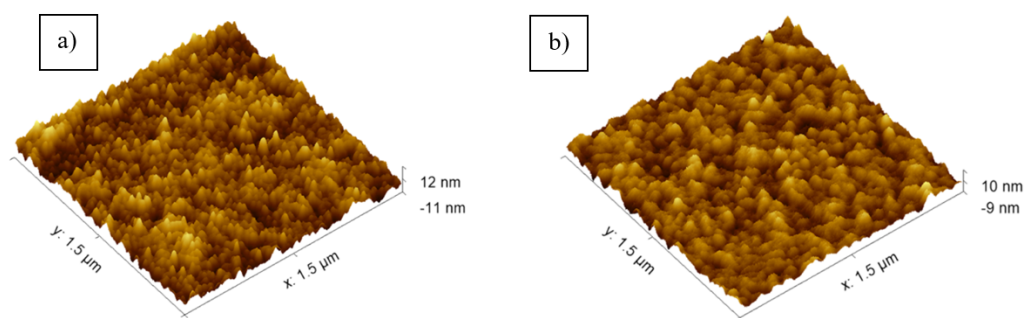


Figure 5.25: AFM images of Avantama NiOx nanoparticle films annealed at a) 150 °C and b) 250 °C . Images taken by Dr Vasil Stoichkov.

Images from the AFM measurements were visually different, with the film annealed at 250 °C appearing smoother than the low temperature film. The film annealed at 150 °C was much “spikier” in appearance, whereas the high temperature film looks as if the nanoparticles are larger, owing to the increased particle interconnectivity. Ra and Rq values for both films are shown in Table 5.4 Ra and Rq values confirmed that the film annealed at 250 °C was smoother and more homogenous than the low temperature annealed film, fitting in with the results from the TGA and the theory of binder/ligand removal decreasing surface roughness.

Table 5.4: Roughness values measured by AFM on Avantama NiOx nanoparticle films annealed at 150 °C and 250 °C.

Annealing temperature (°C)	Ra (nm)	Rq (nm)
150	2.3	2.88
250	1.99	2.52

SEM images were also taken of both films, with similar results to the AFM images. Images with 20,000x zoom are shown in Figure 5.26, which was the closest possible zoom for reasonable imaging. The film annealed at 150 °C looked to be relatively compact but appeared to have several voids or pinholes present. Imaging of the film annealed at 250 °C was more

difficult suggesting a smoother film, complying with the AFM images.

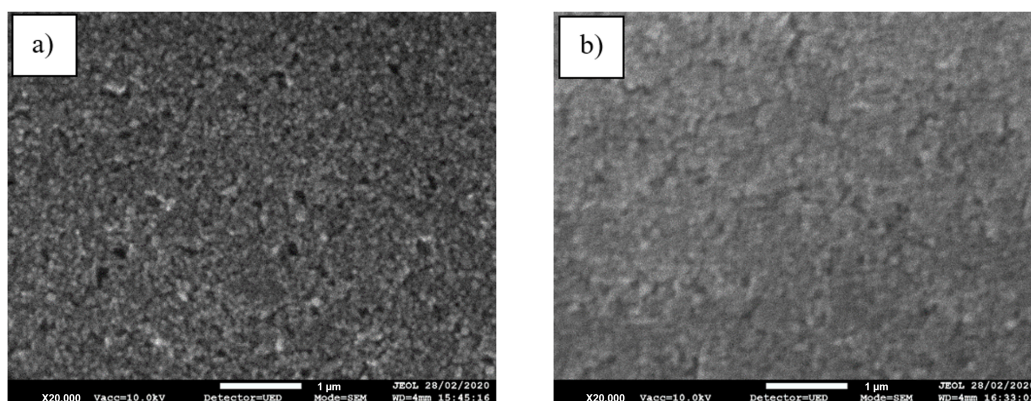


Figure 5.26: SEM images of Avantama NiOx nanoparticle films annealed at a) 150 °C and b) 250 °C. Images taken by Rahul Patidar

It was difficult to tell whether the film annealed at 250 °C contained as many voids/pinholes as the low temperature film due to the image quality, but it gave a good inclination that the film was smoother.

TEM images were also taken to conclude whether sintering was taking place as nanoparticles could be imaged individually. Samples were prepared by spin coating the nanoparticles, annealing at either 150 or 250 °C and then scraped off onto copper sample grid coupons for imaging. Images taken of each of these are shown in Figure 5.27 which showed no obvious difference in the particles annealed at both temperatures, but did however confirm that the nanoparticles were the advertised size of around 7nm.

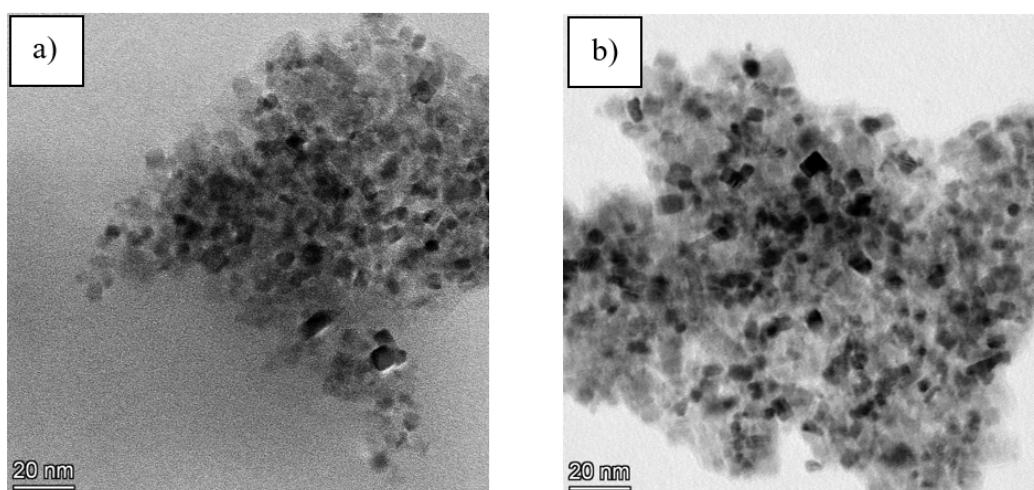


Figure 5.27: TEM images of Avantama NiOx nanoparticle films annealed at a) 150 °C and b) 250 °C. Image taken by Dr Matt Burton.

In conclusion, the analysis performed via TGA, DSC, AFM, SEM and TEM gave solid

evidence that the nanoparticle films annealed at 250 °C were smoother, and more homogenous. Results also showed that increasing the annealing temperature from 150 to 250 °C led to a secondary weight loss of the nanoparticle sample in the TGA which was attributed to removal of organic species most likely being the binder/ligands used to stabilise the nanoparticles in suspension. It was evident that by increasing the annealing temperature, the conductivity of the film increased, thus reducing the series resistance in the perovskite solar cells built on top, with this drop in series resistance being essential for good performances.

Finally, the optimum annealing time at each of the two temperatures was found by making perovskite devices on top of films annealed at 150 and 250 °C, each with increasing annealing times. Instead of showing box plots for each of these parameters, the averages for each device parameter are summarised in Figure 5.28 for ease of comparison.

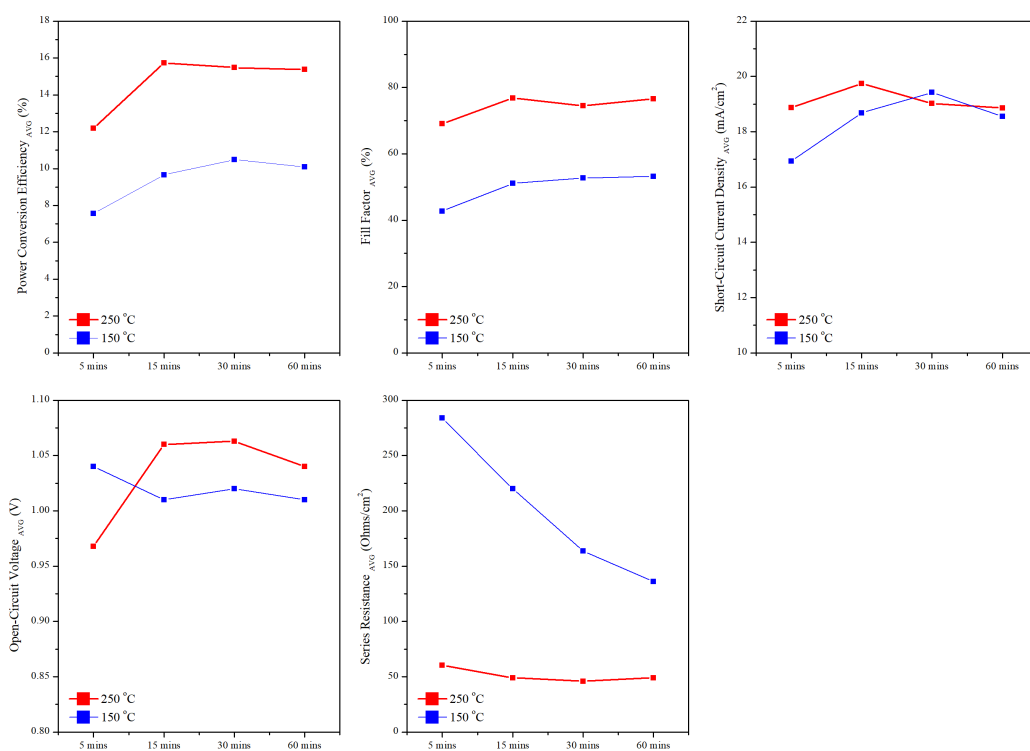


Figure 5.28: Average device parameters for perovskite solar cells built on top of NiOx nanoparticle films annealed at 150 and 250 °C at increasing times (averages of 12 pixels per annealing time).

Devices show a general increase in performance parameters the longer they are annealed for, which is attributed to the longer time for binder/ligand removal. For the films annealed at 250 °C the device performances appear to maintain 16% efficiency from 15 minutes annealing and above suggesting 15 minutes is sufficient enough to fully remove the binder/ligands from

the film, which is also confirmed by the low series resistance, which does not decrease any further as the annealing time is increased. Fill factors also stay at a similar value from 15 minutes and onwards with very little variation, which confirmed that 15 minutes was long enough for high performance devices and any further increase in annealing time was not necessary.

With regards to the films annealed at 150 °C the most obvious and important parameter change was the large drop in series resistances as the annealing time increased. A steep drop in average series resistance is observed as the annealing time is increased, suggesting that something is being removed from the film as time increases. This could have been due to a slow breaking down of the binder/ligands although unlikely as it was thought that a sufficient temperature would be required to break down the organic bonds. Perhaps a portion of the organic species was being broken down over time, but the temperature was not significant enough to remove them entirely, hence the difference between the film annealed at 250 °C. Another potential cause was due to trapped solvent being released slowly as the annealing time increased. However, no evidence was found from the TGA analysis in Figure 5.23 that weight loss increased over time at 150 C. Nonetheless, even after 1 hour of annealing at 150 °C, the series resistances do not reach values as low as the films annealed for even 5 minutes at 250 °C. This further concludes that removal of the binder/ligands is essential for high performance NiOx films.

Although an average series resistance drop of 50 Ohms/cm<sup>2</sup> between 30 minutes and 60 minutes annealing, no further increase in performance was observed. Negligible changes in V<sub>OC</sub> and J<sub>SC</sub> were seen but was most likely down to small differences in film qualities of the subsequent layers. The drop in series resistance did lead to slight increases in fill factors, but a much larger drop in series resistance to at least 50 ohms/cm<sup>2</sup> was compulsory for high efficiencies. Longer annealing times at 150 °C were not investigated as it would certainly be too long for roll-to-roll processing, therefore, other methods for removing the binder/ligands at low temperature were explored.

For further insight into the reason for the drop in series resistance as the annealing time is increased at 150 °C, TGA was performed again, but this time the sample crucible was filled with the NiOx nanoparticle solution on a hot plate at 100 °C to remove the solvent. Solution was continually added as the solvent evaporated until a sufficient amount of nanoparticles were left over; this would allow for a better observation of the weight loss occurring due to the ligands/binder as a much larger sample weight was present in the crucible.

Approximately 50 mg of nanoparticles were present in the crucible and subjected to a thermal treatment in the STA under air. The sample was heated from room temperature to 100 °C and held for 10 minutes to remove any retained solvent, then held at 150 °C for 30 minutes to replicate the anneal at 150 °C and finally held at 250 °C for another 30 minutes to replicate the anneal at 250 °C.

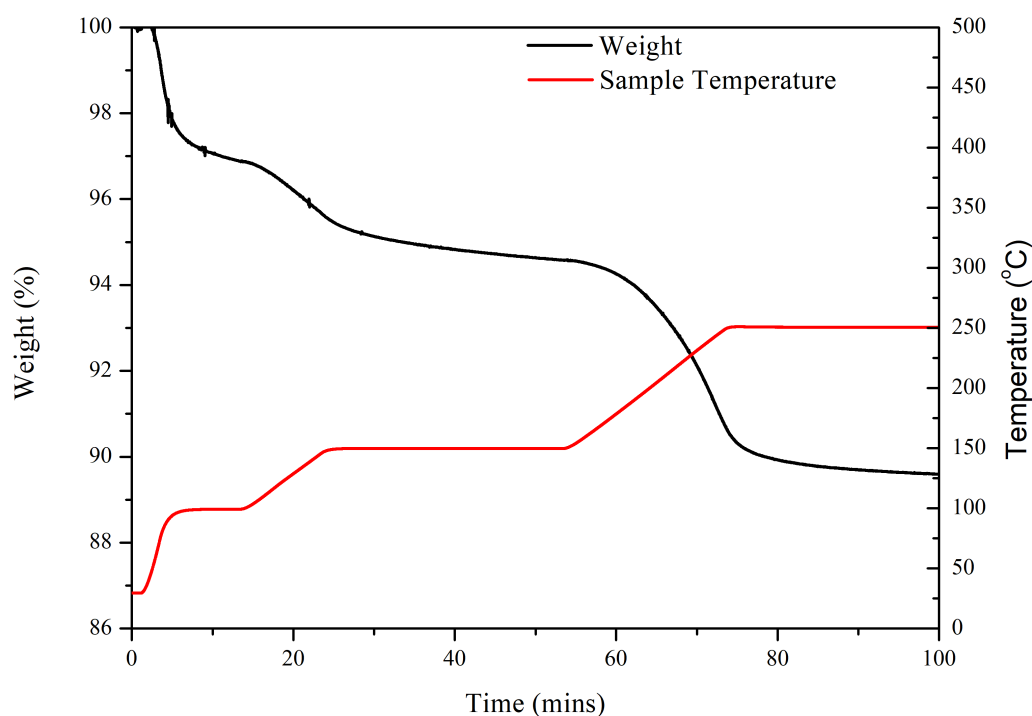


Figure 5.29: Thermogravimetric analysis of NiOx nanoparticles pre-dried on a hot plate to remove solvent.

Figure 5.29 clearly shows three separate weight losses throughout the thermal treatment: firstly during the 100 °C hold where the retained solvent is being removed. A second gradual weight loss is observed as the temperature is increased to 150 °C and leads to a overall weight loss of 2.4% during the 30 minute hold. This weight loss at 150 °C coincided with the previous results on the annealing time in which the series resistance drops as the nanoparticles annealing time is increased and suggests that some of the binder/ligands are being removed at this temperature, but not fully. Finally a much larger weight% drop of 5% is observed as the temperature is increased to 250 °C.

Combining the TGA graph with PCE box plots at 100, 150 and 250 °C outlines the significance of the annealing temperature, with each mass loss coinciding with an increase in device performance concluding that a higher temperature anneal is essential for optimal device performance (Figure 5.30).

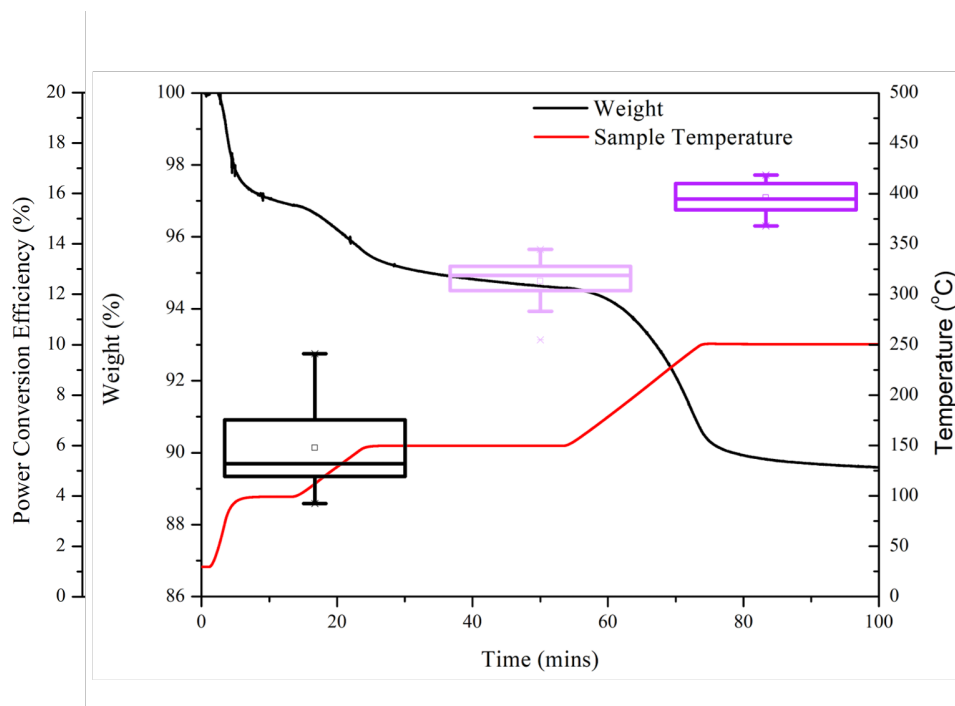


Figure 5.30: Thermogravimetric analysis of NiOx nanoparticles combined with PCE box plots at each corresponding annealing temperature.

Removal of any organic species in the film would also be expected to improve the interface between the NiOx and perovskite films with photoluminescence spectroscopy (PL) used to confirm this. Figure 5.31 shows the PL spectra for a bare perovskite film and is compared to perovskite on top of NiOx annealed at 150 and 250 °C. Clearly from the PL spectra, the NiOx film annealed at 250 °C exhibits far more efficient PL quenching than the film annealed at 150 °C, indicating its better hole extraction capability and agreeing with the JV results, further concluding that removal of the organic species in the film is crucial for high performance.

Finally XPS was employed to study any bond/elemental changes in the NiOx material. It is well known that XPS analysis of the first-row transition metals is difficult due to the complexity of their 2p spectra [16] and distinguishing each Nickel state would be difficult. NiOx films annealed at 150 °C and 250 °C were compared to determine whether there were any noticeable differences. Figure 5.32 shows the XPS results for the two annealed samples, highlighting the Ni 2p<sub>3/2</sub> and O 1s core levels. For the Nickel peaks, a model by Biesinger [17] was fitted to compare the NiOx nanoparticles to a confirmed NiOx spectra, and for the oxygen peaks, constituents were fitted using XPS software (CASAXPS). When comparing the two annealed films, the NiOx annealed at 250 °C looks very similar to the Biesinger model, whereas the sample annealed at 150 °C shows a peak increase at 855.5 eV which could be



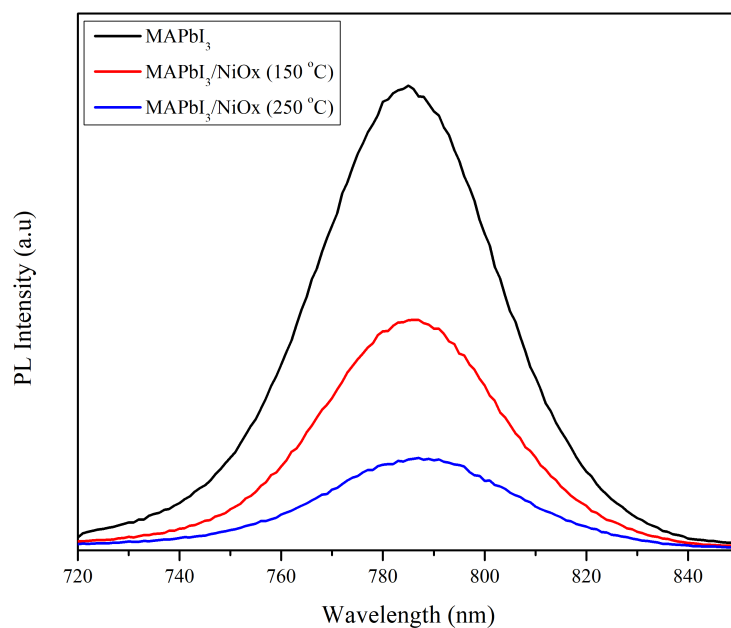


Figure 5.31: PL spectroscopy comparing NiOx annealed at 150 and 250 °C.

attributed to either Ni<sub>2</sub>O<sub>3</sub>, Ni(OH)<sub>2</sub> or NiOOH, or a combination of the three. Similarly, in the O 1s spectra, a larger peak at 531 eV is observed for the 150 °C annealed film attributed to Ni<sub>2</sub>O<sub>3</sub>, Ni(OH)<sub>2</sub> or NiOOH. In the literature, an increase in this peak has been correlated with a rise in NiOx film conductivity and suggested to be caused by an increase in Ni<sup>3+</sup> vacancies, thus an increase in p-type selectivity. However, with regards to the NiOx nanoparticles in this work, the peak increase does not appear to be attributed to an increase in Ni<sub>2</sub>O<sub>3</sub> as the conductivity of the film annealed at 150 °C is much less than that of the film annealed at 250 °C which shows a smaller “Ni<sub>2</sub>O<sub>3</sub> peak”. Most likely, the reduction in this peak for the 250 °C annealed sample is due to removal of organic species in the film, which correlates well with the removal of binder/ligands. In addition to this, as the annealing temperature increases, there is a reduction of the peak attributed to NiOOH at 523 eV, solidifying the suggestion that the peak changes are due to removal of organic species.

When comparing XPS spectra for NiOx in the literature, peak assignment is conflicting, with some groups attributing the peak at 855 eV solely to Ni<sub>2</sub>O<sub>3</sub> and others stating it is due to NiOOH. However, it would be reasonable to say that the sample annealed at 150 °C contains more OH than the 250 °C annealed sample.

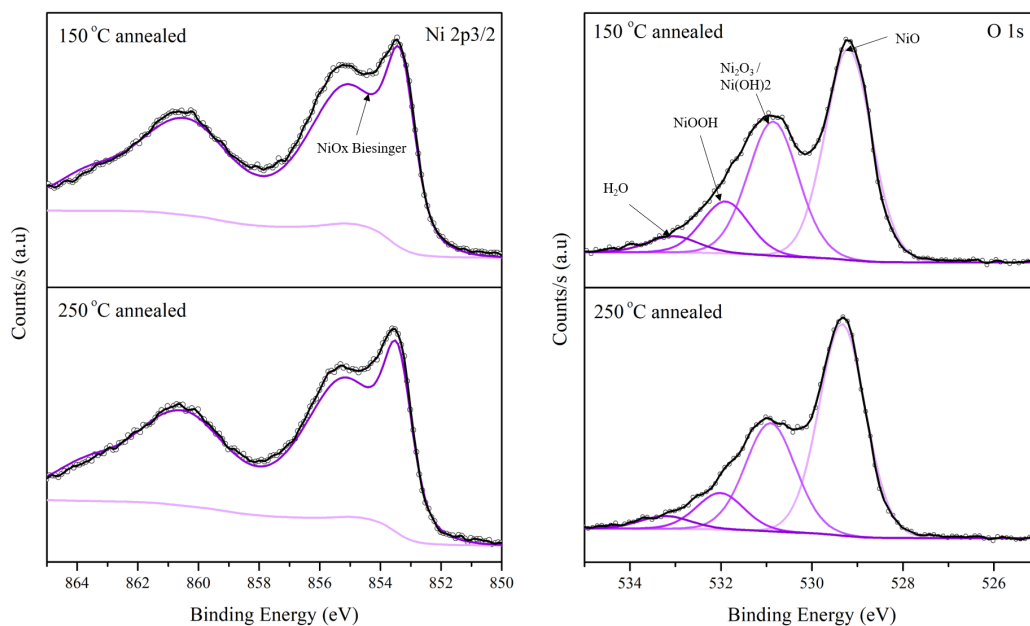


Figure 5.32: XPS spectra for the Ni 2p<sub>3/2</sub> and O 1s orbitals comparing NiOx nanoparticle films annealed at 150 and 250 °C.

### 5.3.4 Stability of NiOx nanoparticles

As NiOx was being investigated as being a replacement for unstable HTLs such as PEDOT, the stability of the NiOx nanoparticles needed examining. It was decided to compare the stability to a PEDOT layer as PEDOT is the most common HTL used in the literature in a p-i-n device stack, especially in R2R based devices. Firstly, full devices employing both HTLs were built and placed in a lightbox for 7 days in ambient conditions under 3580 lux or 0.5 mW/cm<sup>2</sup> and an image taken each day (Figure 5.33).

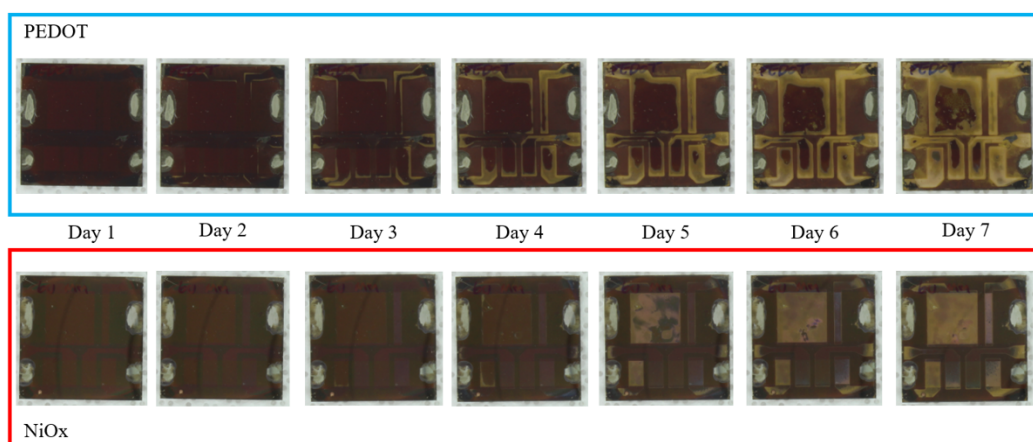


Figure 5.33: Images of perovskite devices employing a PEDOT HTL and a NiOx nanoparticle (annealed at 150 °C) HTL under constant illumination in a lightbox.

Clearly, the PEDOT based device shows signs of degradation as soon as day 2, indicated

by the yellow colours appearing around the silver top contacts which becomes progressively worse as time goes on, eventually turning the majority of the film yellow by the seventh day. This degradation in the PEDOT based device is due to the hygroscopic nature of the PEDOT leading to water absorption, thus deterioration of the perovskite film [18]. With regards to the NiOx nanoparticle-based device, discolouration of the perovskite film is observed but does not become apparent until day 4 and appears to be localised to the silver electrodes. The colour change does not seem to be the same as in the PEDOT based device after 7 days suggesting a different degradation mechanism other than water absorption. As discovered by Yang et al, residual ligands and surface hydroxyl groups accelerated the degradation of perovskite films when employing ZnO NP ETLs [19]. The group discovered that the basic nature of the ZnO surface leads to proton-transfer reactions at the perovskite interface, resulting in decomposition. They also found that the decomposition process is accelerated by the presence of surface hydroxyl groups and/or residual ligands. This suggests a similar degradation mechanism with the NiOx nanoparticles due to the residual binder/ligands in the film. Therefore, removal of the ligands should lead to a more stable perovskite device.

Stabilised efficiency measurements were made on the NiOx films annealed at 150 and 250 °C and compared to a PEDOT based device. Stability measurements were made under constant illumination at AM1.5G, 25 °C and in ambient conditions. Normalised efficiency data over the course of 140 hours are summarised in Figure 5.34.

Normalised efficiency data shows a clear severe degradation of the PEDOT device, losing almost 100% efficiency in a matter of hours. Both NiOx devices show an initial steady rise in efficiency under illumination which has been attributed to ion and defect migration within the perovskite layer. When the NiOx nanoparticles are annealed at 150 °C a large loss in efficiency of around 60% is observed after 150 hours. Stability measurements for the PEDOT and NiOx film annealed at 150 °C coincide with the images in Figure 5.33. However, in the case of the NiOx film annealed at 250 °C the stability is vastly improved, retaining 100% of its efficiency after 140 hours. This confirms that the residual binder/ligands assist in the degradation of the perovskite, much like in Yang et al's work on ZnO nanoparticles where the hydroxyls groups of the ligands accelerate the perovskite degradation [19], and upon removal at higher temperatures the devices become significantly more stable. Although the NiOx based devices annealed at 150 °C are more stable than PEDOT equivalents, annealing at elevated temperatures to remove the binder/ligands is not only essential for improved efficiencies, but

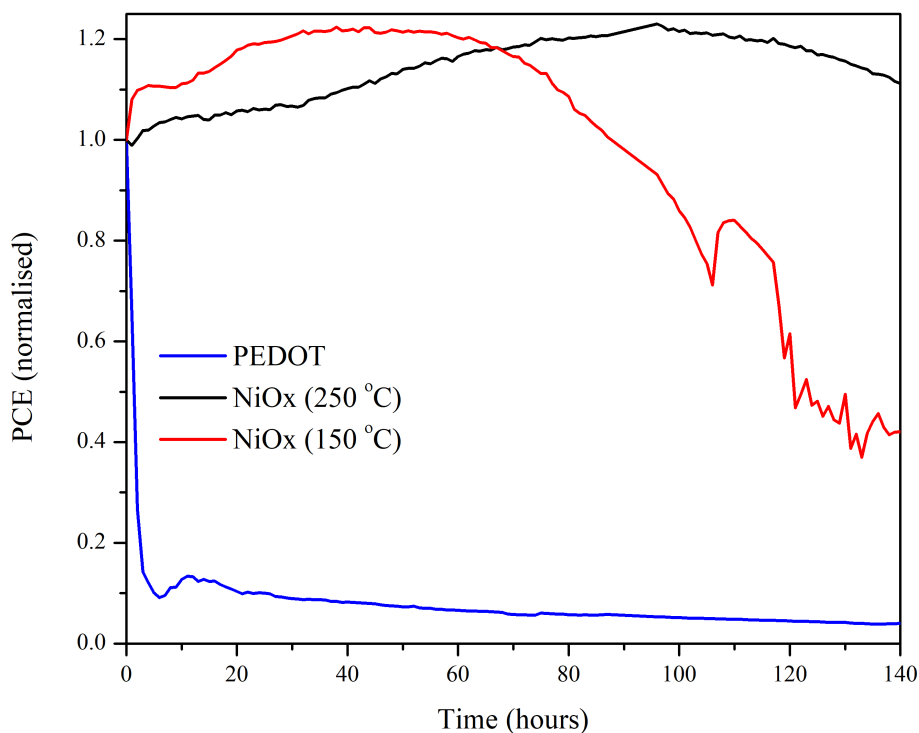


Figure 5.34: Normalised efficiency stability measurements for a PEDOT (Blue) based perovskite device compared to perovskite devices employing NiOx nanoparticle HTLs annealed at 150 °C (Red) and 250 °C (Black).

also contributes to a significant rise in stability.

### 5.3.5 Slot-die coating of NiOx nanoparticles

Due to the nanoparticles being suspended in ethanol, slot-die coating was straightforward. To achieve a dry film thickness of 35 nm, an estimated wet film thickness of around 9 micron was necessary as calculated from equation 1.2. Substrate speed was set at 0.25 m/min and the overall predicted coating stability for three wet film thicknesses (5,7 and 9 micorn) was modelled using the viscocapillary model and shown in figure 5.35.

Using an overall head-substrate gap height of 1200 um (including the meniscus guide protrusions) each of the coating thicknesses were well within the stable range of the model. Initially, to determine the compatibility of the NiOx nanoparticles with slot-die coating, they were coated on glass and annealed on a hot plate at 250 °C for 15 minutes and compared with a spin-coated equivalent.

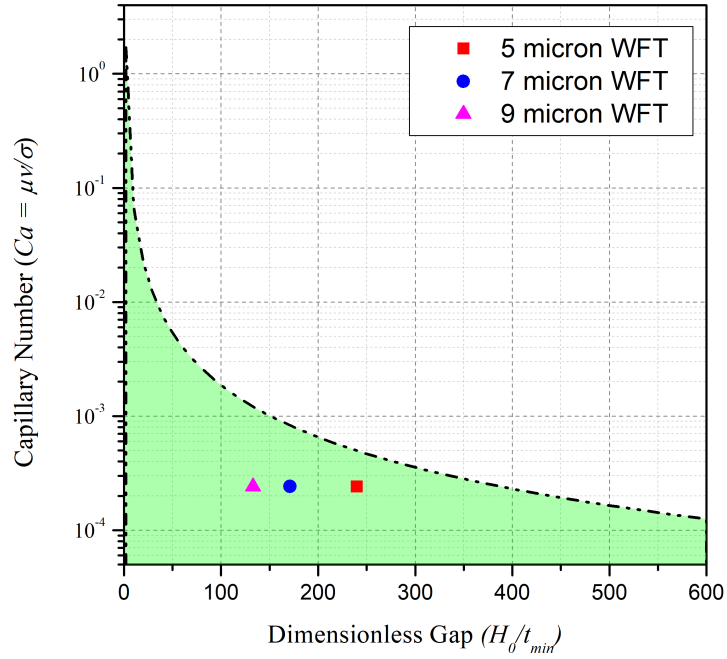


Figure 5.35: Viscocapillary model for NiOx nanoparticles at 3 wet film thicknesses (5,7 and 9 micron) and with an overall head-substrate gap height set at 1200 micron.

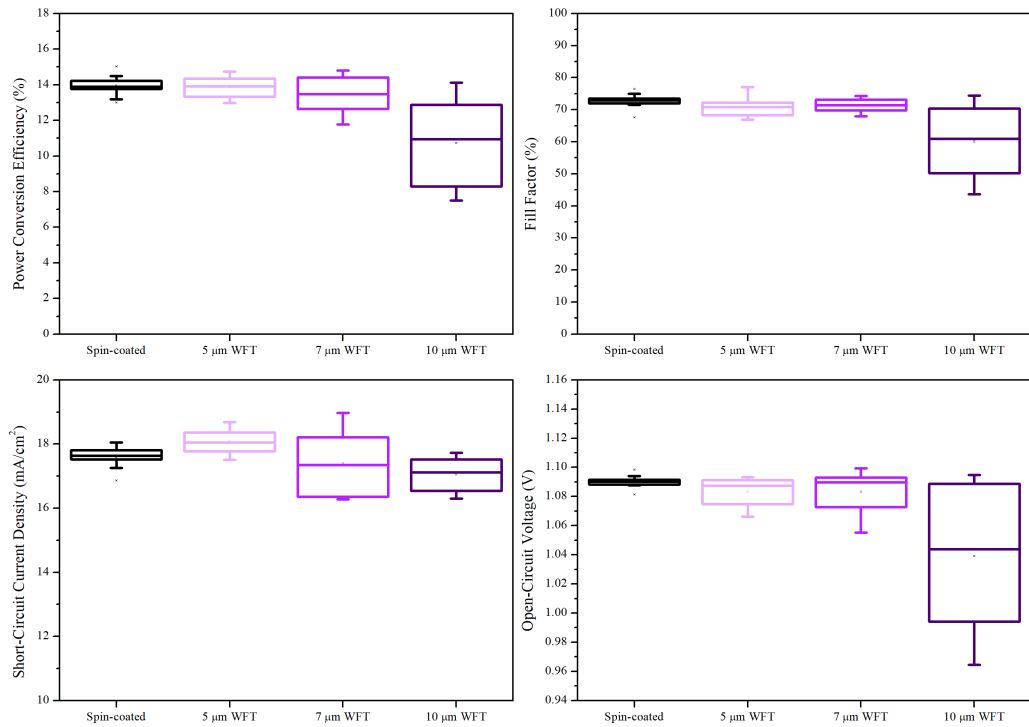


Figure 5.36: Statistical JV data for slot-die coated NiOx nanoparticles with increasing wet film thickness and annealed at 250 °C, compared to a spin-coated control device. Data presented from 16 devices.

From the JV box plots in figure 5.36 the efficiency of the slot-die coated NiOx was equivalent to the spin-coated control devices. A wet film thickness of 5 microns achieved the best and

most consistent results and was deemed optimised. A summary of the hero device data from slot-die coating can be found in table 5.5. The main difference between the two champion pixels is the fill factor and corresponding series resistance, however the average series resistance for the spin-coated devices was 41.2 ohms/cm<sup>2</sup> compared to 43.3 ohms/cm<sup>2</sup> for slot-die coated.

Table 5.5: Hero device data for slot-die coated NiOx nanoparticles annealed at 250 °C compared to a spin coated equivalent.

Device	Voc (V)	Jsc (mA/cm <sup>2</sup> )	FF (%)	Rsh (Ω/cm <sup>2</sup> )	PCE (%)
Spin-coated	1.08	18.05	76.5	29.66	15.03
Slot-die coated	1.09	18.57	71.41	47.78	14.45

Optimisation of the NiOx nanoparticles at 250 °C had been achieved with a champion PCE of 14.45 % and similar PCE distribution to a spin-coated control device. Although this produced high efficiency devices, the temperature was too high for transfer to flexible substrates. Nonetheless, this did prove the compatibility of the NiOx nanoparticles with slot-die coating.

Until now the testing was conducted on ITO coated glass, however in order to demonstrate the scalable potential of the NiOx nanoparticles further coating trials were made on ITO coated PET and compared to spin-coated equivalents, both annealed on a hot plate for 30 minutes at 150 °C. Parameters for the coating were kept the same as the previous trial. Slot-die coated films were cut up into smaller 28 x 28 cm squares and the remainder of the device stack spun on top. JV results are presented via box plots in figure 5.37.

A champion PCE of 11.16% was achieved for the flexible slot-die coated device compared to a 12.86% for the spin-coated equivalent. Although the efficiencies were slightly lower than the spin-coated devices, they were still promising for a low-temperature NiOx film on flexible substrates to be realised. A larger series resistance was the main contributor to the loss of performance which was an average of 208 Ohms/cm<sup>2</sup> compared to 160 Ohms/cm<sup>2</sup> for the spin-coated films and was attributed to the flexible substrates being more resistive than the glass substrates (50 Ohms/sq and 15 Ohms/sq respectively), which was also seen when coating the tin oxide ETL in Chapter 3. Despite the lower efficiencies on PET, the results prove that slot-die coating of NiOx onto flexible substrates with reasonable efficiencies are simple to achieve. Coating of a thinner layer of NiOx may improve the efficiencies slightly, but this could also be detrimental to performance by introducing defects such as pinholes inevitably leading to recombination reactions and reducing the PCE. Developing a method to anneal the

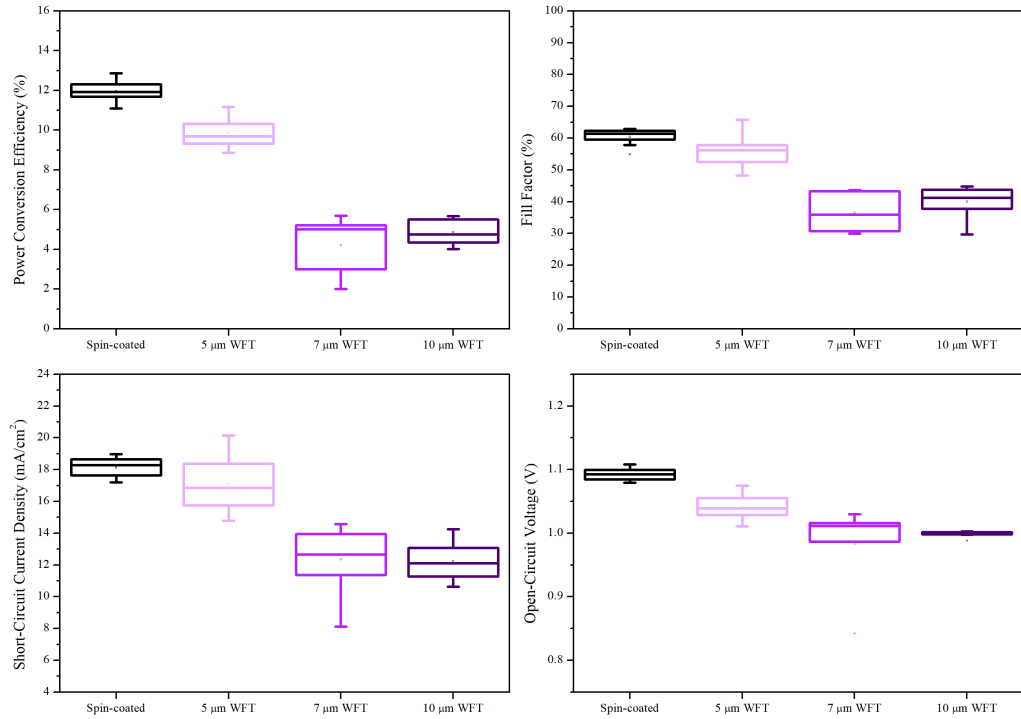


Figure 5.37: Statistical JV data for slot-die coated NiOx nanoparticles on PET/ITO with increasing wet film thickness and annealed at 150 °C, compared to a spin-coated control device. Data presented from 16 devices.

nanoparticles at elevated temperatures without damaging the PET was more important.

## 5.4 Conclusions

A method for depositing high performing and repeatable NiOx HTLs was discovered by using a nanoparticle suspension. Initial trials consisted of using a well studied sol-gel precursor consisting of NiAc dissolved in 2-methoxy ethanol but it was found that reducing the annealing temperature from 300 °C to a more suitable 150 °C was not possible. Photonic curing of the sol-gel films did lead to working devices, albeit much lower performing compared to a heat treatment. Photonic curing did however show promise, but it is suspected that for high performance, the films would need to be subjected to a significantly large amount of pulses creating a bottleneck in production in terms of time and capital cost. In addition to this, the 2-methoxy ethanol solvent that the NiAc is dissolved in is extremely toxic and deemed unsuitable for large scale manufacture unless costly enclosures and extraction facilities are included. A NiOx nanoparticle suspension was then optimised at low processing temperatures of 150 °C with modest performance. Increasing the annealing temperature to 250 °C saw a significant

rise in performance and was discovered to be due to removal of organic species in the film, thus decreasing the series resistance of the subsequent perovskite device. Although good efficiencies of 10-12% were achieved at the low annealing temperature, the higher processing temperature not only led to efficiencies approaching 17% but also improved the stability of the finished devices. In addition, the nanoparticle suspension was proven as slot die coating compatible. Slot die coated films annealed at 250 °C on glass substrates were comparable to a spin coated equivalent, and slot die coated films efficiencies annealed at 150 °C on PET films were only marginally lower than a spin coated film on glass. This chapter confirmed that low-temperature NiOx films can be deposited onto flexible PET substrates via slot die coating with generally good efficiencies, however, further work was required to match the efficiencies of the high temperature annealed counterpart.

## 5.5 References

- [1] Qin Wang et al. “Modulation of PEDOT:PSS pH for efficient inverted perovskite solar cells with reduced potential loss and enhanced stability”. In: *ACS Applied Materials and Interfaces* 8.46 (2016), pp. 32068–32076. ISSN: 19448252. DOI: 10.1021/acsami.6b11757.
- [2] Lijun Hu et al. “PEDOT:PSS monolayers to enhance the hole extraction and stability of perovskite solar cells”. In: *Journal of Materials Chemistry A* 6.34 (2018), pp. 16583–16589. ISSN: 20507496. DOI: 10.1039/c8ta05234d.
- [3] Jiangzhao Chen and Wallace C.H. Choy. “Efficient and Stable All-Inorganic Perovskite Solar Cells”. In: *Solar RRL* (2020). ISSN: 2367198X. DOI: 10.1002/solr.202000408.
- [4] Zijun Yi et al. “Will organic-inorganic hybrid halide lead perovskites be eliminated from optoelectronic applications?” In: *Nanoscale Advances* 1.4 (2019), pp. 1276–1289. ISSN: 25160230. DOI: 10.1039/c8na00416a.
- [5] Xingtian Yin et al. “Nickel Oxide as Efficient Hole Transport Materials for Perovskite Solar Cells”. In: *Solar RRL* 3.5 (2019), p. 1900001. ISSN: 2367-198X. DOI: 10.1002/solr.201900001.



- [6] Bahram Abdollahi Nejand et al. “Cuprous Oxide as a Potential Low-Cost Hole-Transport Material for Stable Perovskite Solar Cells”. In: *ChemSusChem* 9.3 (2016), pp. 302–313. ISSN: 1864564X. DOI: 10.1002/cssc.201501273.
- [7] Ahmed Mourtada Elseman et al. “Recent progress concerning inorganic hole transport layers for efficient perovskite solar cells”. In: *Applied Physics A: Materials Science and Processing* 125.7 (2019), pp. 1–12. ISSN: 14320630. DOI: 10.1007/s00339-019-2766-7. URL: <https://doi.org/10.1007/s00339-019-2766-7>.
- [8] Neha Arora et al. “Perovskite solar cells with CuSCN hole extraction layers yield stabilized efficiencies greater than 20%”. In: *Science* 358.6364 (2017), pp. 768–771. ISSN: 10959203. DOI: 10.1126/science.aam5655.
- [9] Neetesh Kumar et al. “Large-area, green solvent spray deposited nickel oxide films for scalable fabrication of triple-cation perovskite solar cells”. In: *Journal of Materials Chemistry A* 8.6 (2020), pp. 3357–3368. ISSN: 20507496. DOI: 10.1039/c9ta13528f.
- [10] Su Kyung Kim et al. “Comparison of NiO: Xthin film deposited by spin-coating or thermal evaporation for application as a hole transport layer of perovskite solar cells”. In: *RSC Advances* 10.71 (2020), pp. 43847–43852. ISSN: 20462069. DOI: 10.1039/d0ra08776a.
- [11] Xin Yan et al. “Optimization of sputtering NiOx films for perovskite solar cell applications”. In: *Materials Research Bulletin* 103 (2018), pp. 150–157. ISSN: 00255408. DOI: 10.1016/j.materresbull.2018.03.027. URL: <https://doi.org/10.1016/j.materresbull.2018.03.027>.
- [12] Dibyashree Koushik et al. “Plasma-assisted atomic layer deposition of nickel oxide as hole transport layer for hybrid perovskite solar cells”. In: *Journal of Materials Chemistry C* 7.40 (2019), pp. 12532–12543. ISSN: 20507526. DOI: 10.1039/c9tc04282b.
- [13] Mohammed S.G. Hamed and Genene Tessema Mola. “Mixed Halide Perovskite Solar Cells: Progress and Challenges”. In: *Critical Reviews in Solid State and Materials Sciences* 45.2 (2020), pp. 85–112. ISSN: 15476561. DOI: 10.1080/10408436.2018.1549976. URL: <https://doi.org/10.1080/10408436.2018.1549976>.
- [14] Wanyi Nie et al. “Critical Role of Interface and Crystallinity on the Performance and Photostability of Perovskite Solar Cell on Nickel Oxide”. In: *Advanced Materials* 30.5 (2018), pp. 1–9. ISSN: 15214095. DOI: 10.1002/adma.201703879.

- [15] Tun Wang et al. “Efficient Inverted Planar Perovskite Solar Cells Using Ultraviolet/Ozone-Treated NiO<sub>x</sub> as the Hole Transport Layer”. In: *Solar RRL* 3.6 (2019), p. 1900045. ISSN: 2367-198X. DOI: 10.1002/solr.201900045.
- [16] Seongrok Seo et al. “An ultra-thin, un-doped NiO hole transporting layer of highly efficient (16.4%) organic-inorganic hybrid perovskite solar cells”. In: *Nanoscale* 8.22 (2016), pp. 11403–11412. ISSN: 20403372. DOI: 10.1039/c6nr01601d.
- [17] Mark C. Biesinger et al. “X-ray photoelectron spectroscopic chemical state Quantification of mixed nickel metal, oxide and hydroxide systems”. In: *Surface and Interface Analysis* 41.4 (2009), pp. 324–332. ISSN: 01422421. DOI: 10.1002/sia.3026.
- [18] Ju Huang et al. “Improving the efficiency and stability of inverted perovskite solar cells with dopamine-copolymerized PEDOT:PSS as a hole extraction layer”. In: *Journal of Materials Chemistry A* 5.26 (2017), pp. 13817–13822. ISSN: 20507496. DOI: 10.1039/c7ta02670f.
- [19] Jinli Yang et al. “Origin of the Thermal Instability in CH<sub>3</sub>NH<sub>3</sub>PbI<sub>3</sub> Thin Films Deposited on ZnO”. In: *Chemistry of Materials* 27.12 (2015), pp. 4229–4236. ISSN: 15205002. DOI: 10.1021/acs.chemmater.5b01598.

## **Chapter 6**

# **Low-temperature processing options for NiO<sub>x</sub> HTL**

### **6.1 Introduction**

Deposition of a low-temperature NiO<sub>x</sub> HTL had been achieved in Chapter 5 with reasonable performance, however, it was discovered that elevating the annealing temperature to 250 °C saw a significant improvement in performance. Clearly, increasing this temperature on flexible substrates leads to damage and deformation thus being incompatible with roll-to-roll coating. In order to improve the efficiency without causing damage to the underlying substrate, rapid processing techniques in the form of Near-infrared annealing (NIR), photonic pulse annealing and Ultraviolet-Ozone (UVO) treatment are investigated.

### **6.2 Experimental Methods**

NiO<sub>x</sub> films were spin coated onto ITO coated glass substrates at 6000 rpm using a 2.5 weight% nanoparticle suspension in ethanol. Control films were annealed on a hot plate at 150 and 250 °C with the annealing stage replaced by the respective processing method used in each section. Remaining layers of the perovskite devices were processed by the standard method described in Chapter 2.1. NIR annealing was achieved using a Heraeus system as described in Chapter 2.8.1, UVO treatment using a Jelight UVO cleaner system (Chapter 2.8.2) and photonic curing using a PulseForge system (Chapter 2.8.3).

## 6.3 Results and Discussion

### 6.3.1 Near-infrared annealing of NiOx nanoparticles

In this section, the possibility of using Near-Infrared Radiation (NIR) to rapidly anneal the NiOx films is explored. Driving tungsten halogen bulbs at high powers causes irradiation in the NIR region of the light spectrum. This irradiation directly heats the underlying ITO substrate rapidly and leaves the glass at a relatively cool temperature preventing breaking of the glass. This heated ITO acts as a hot plate for the annealing of NiOx deposited on top, which should enable full removal of the binder/ligands as high temperatures can be achieved in a short space of time.

As the final objective was to deposit the nanoparticles via slot-die coating in a roll-to-roll coater, drying would be performed in a convection oven, not on a hot-plate. This is where NIR annealing has a significant advantage, as the ITO acts as a hot plate driving solvent and organics upwards and out of the layer, whereas convection drying does not heat the substrate like a hot plate would and does not assist in solvent removal up and out of the layer as illustrated in Figure 6.1

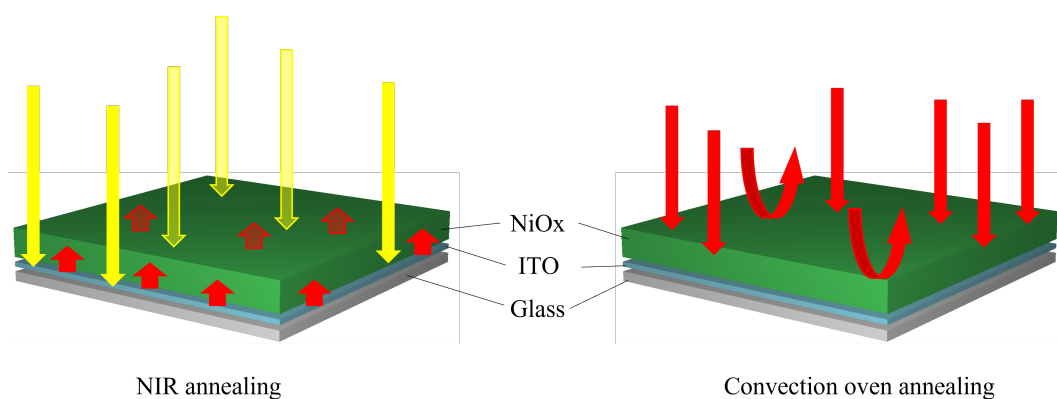


Figure 6.1: Schematic illustration of the difference in NIR and convection oven annealing.

Firstly, the absorption spectra for the glass, ITO and NiOx layers were measured to confirm whether the ITO would be the layer to absorb the majority of the NIR light. The NIR lamps emit light over a broad range of wavelengths well into the infrared region, but most of the light is in the NIR range shown in Figure 6.2 with the peak intensity at around 1250 nm.

Absorbance spectra measured using UV-Vis spectrometry of the ITO coated glass, plain glass and neat NiOx nanoparticle solution showed that the ITO absorbs NIR light from around 1000 nm and above which coincided with the wavelength output from the NIR lamps. Plain

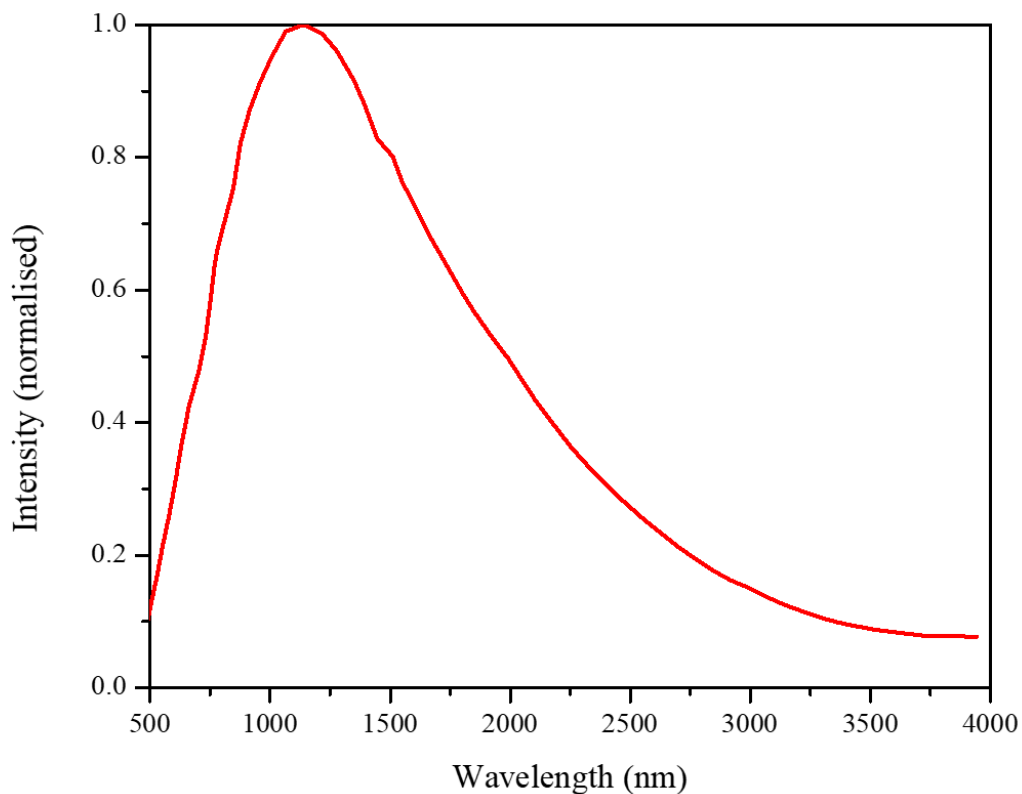


Figure 6.2: Intensity spectra for the Heraeus NIR emitters. Data from manufacturer

glass absorbs very little across the NIR range and will therefore stay relatively cool during NIR exposure, apart from the thermal transfer from the ITO. Also, although the NiOx nanoparticles have a distinct dark colour to the naked eye, they barely absorb any NIR light allowing it to pass through and be absorbed by the ITO preventing direct heating of the nanoparticles themselves as suggested in 6.3. The lack of heating of the glass may also allow higher thermal ramp rates than would usually be possible which could potentially allow the use of NIR annealing on temperature sensitive substrates.

In a study performed by Troughton et al [1] on the NIR annealing of perovskite, infrared thermal imaging of the substrate directly after heating was used to estimate the substrate temperatures. However, a different NIR system was used for the study in which the unit was not enclosed allowing direct imaging of the substrate, whereas the Heraeus system used in this work is a fully enclosed system preventing measurements of substrate temperature. To gain an idea of the temperatures reached upon NIR exposure, IR imaging was used once the substrate had passed under the emitters. Significant cooling was expected to occur after exposure and movement of the sample from under the unit so the measured temperature was expected to be less than the peak temperature reached.

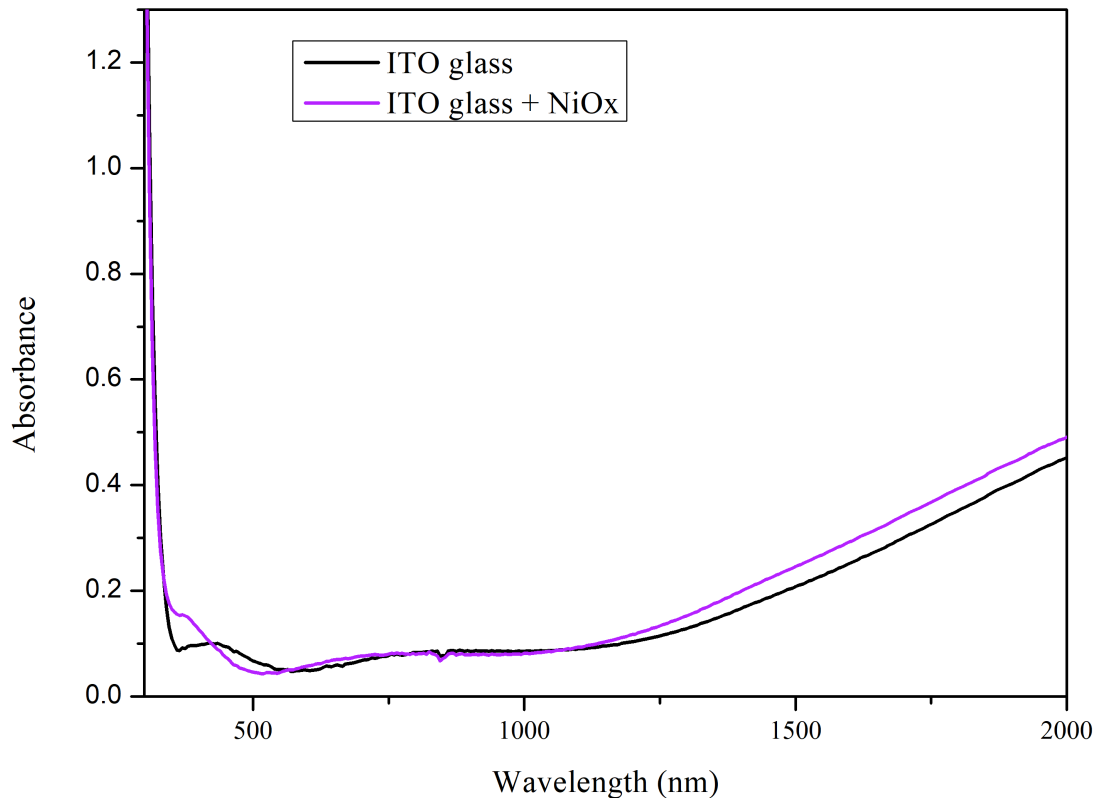


Figure 6.3: Absorbance spectra for ITO glass and ITO glass + NiOx.

Calibration of the IR camera software was achieved by placing a glass/ITO substrate onto a hot plate at 100 °C with the temperature monitored using a thermocouple (Figure 6.4). Emissivity values were then changed in the imaging software to match the temperature of the ITO film and was found to be 0.23 which was in agreement with values in the literature. IR imaging could then be used to measure the temperature of the ITO upon exiting the NIR oven with the setup as depicted in Figure 6.5.

In Troughtons study, an FTO substrate was measured at 200 °C after only 2.47 s of exposure, but the power output from that NIR emitter was significantly higher than that possible from the Heraeus system. Without accurate temperature measurements, optimisation of the NIR exposure was conducted by making perovskite devices on the NIR annealed samples with the subsequent performance used as a guide for optimal exposure times. Another issue with the Heraeus system was that the conveyor belt was unreliable at low speeds and sometimes completely stopped during operation, so prior to exposure the NIR lamps were turned on and allowed to heat up with the samples then moved underneath manually for specified periods of times before the lamps were turned off again.

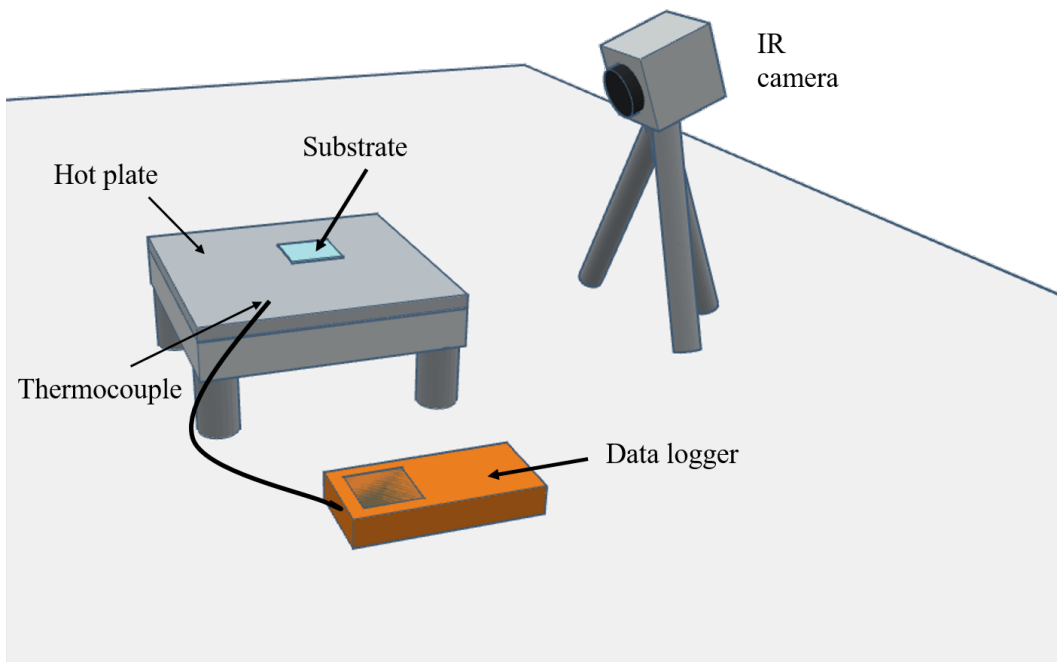


Figure 6.4: Schematic illustration of the method used to calibrate the IR camera.

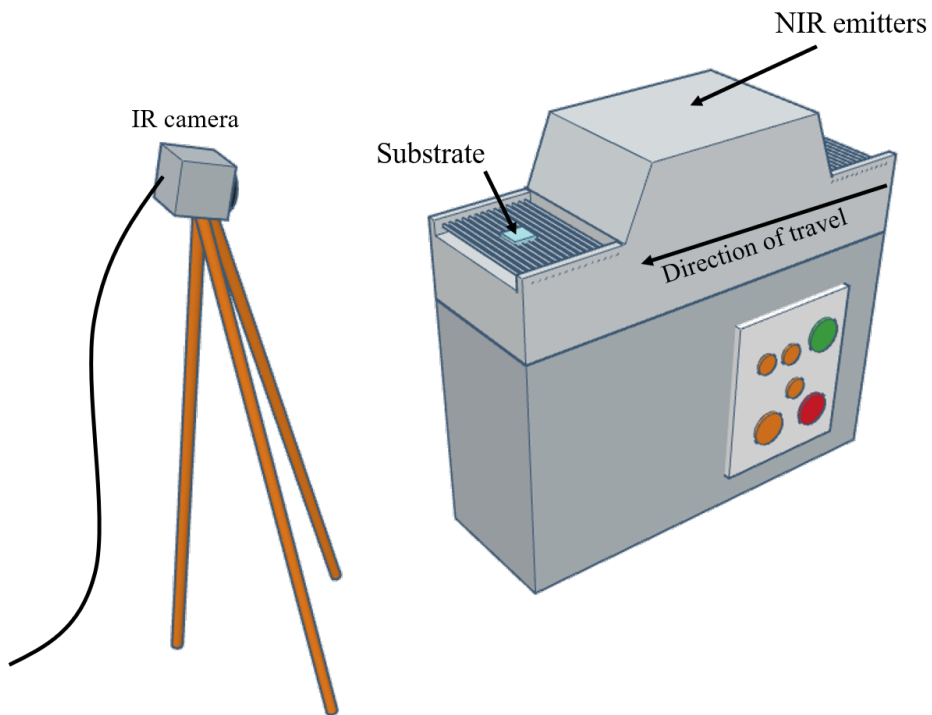


Figure 6.5: Schematic illustration of the method used to measure the temperature of the ITO film on exit

NiOx films were spin coated onto ITO coated glass as usual at 6000 rpm and put straight onto a metal plate to be taken under the NIR lamps. Exposure times were initially, relatively long and started at 60 seconds with increments of 30 seconds up to 120 seconds. Substrates were then allowed to cool down and perovskite devices built on top ready for solar simulation testing. In addition to this, films hotplate annealed at 150 and 250 °C for 30 minutes and 15 minutes respectively were used for comparison. Statistical JV analysis of the devices made in this experiment are summarised in Figure 6.6

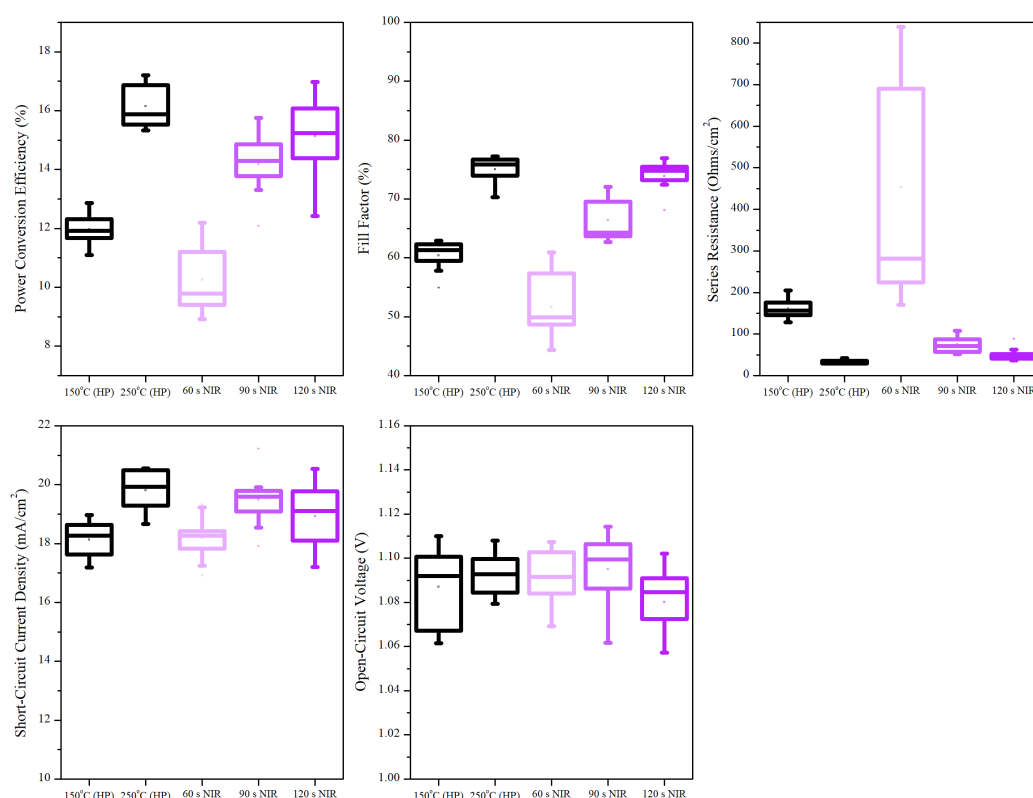


Figure 6.6: Statistical J-V analysis of NIR annealed NiOx nanoparticle films on a metal plate, compared to hot plate annealed films at 150 and 250 °C. Data presented from 20 devices.

As the NIR exposure time increases, the fill factors increase which is directly related to the series resistances as observed with the increase in temperature in previous studies. Series resistances for the samples exposed for 60 seconds are very sporadic with values as high as 800 Ohms/cm<sup>2</sup> most likely due to retained solvents in the film. This was surprising as 60 seconds is a relatively long exposure time for NIR annealing, but shows the difference in the Heraeus lamps effect on heating compared to the unit used by Troughton et al (Heraeus lamps are 6 kW compared to 25 kW used in Troughtons work). However, upon reaching 90 seconds of exposure, the series resistances reach close values to that of the 250 °C hot plate annealed sample



and lower to comparable values after 120 seconds of exposure. This suggests that the substrates were reaching temperatures similar to 250 °C and therefore burning off the binder/ligands. 120 seconds exposure gave the best results in terms of efficiency which was shown by a rise in fill factor and had very similar performance characteristics to the sample annealed at 250 °C. This in itself was an achievement as the annealing time had been reduced from 15 minutes to a mere 2 minutes, however, ideally this time could be reduced even further as it was unlikely that a PET substrate would be able to withstand 2 minutes exposure. Samples were also exposed to 150 seconds of NIR, which caused the glass to break which was not expected to be an issue when using NIR, but the exposure time was significantly longer than usually used for NIR sintering allowing sufficient heating of the glass by thermal transfer from the ITO causing it to break.

It was suggested that a lot of heat produced by the absorption of NIR in the ITO layer was being dissipated through the large metal substrate plate used to transport the substrates through the NIR system, reducing the peak temperature of the ITO. This is usually overcome by using a polytetrafluoroethylene (PTFE) block, but the small opening to the Heraeus prevented the use of the PTFE blocks available. Therefore, it was decided to place the samples directly onto the NIR conveyor belt without a metal plate to see if the samples would anneal faster due to more retained heat. The experiment was repeated as before and JV analysis presented in Figure 6.7

This time, the film exposed to 60 seconds of NIR light had a significant increase in performance compared to the same amount of exposure on a metal plate, confirming the theory that the metal was dissipating some heat from the substrate. Device performances increased as the exposure time increased from 60 to 120 seconds, coinciding with a rise in fill factor. Most importantly, all exposure times led to performances far exceeding that of the films annealed on a hot plate at 150 °C due to the samples reaching higher temperatures and burning off the binder/ligands, confirmed by a large drop in series resistance. NIR annealed films also gave comparable performances to the sample annealed at 250 °C for 15 minutes proving that NIR annealing was certainly capable of removing the organic species from the films, and in a much faster time. A champion efficiency of 17.57% in the reverse direction was achieved for an NIR film exposed for 2 minutes compared to 17.21% for a 15 minute anneal at 250 °C. Current-voltage curves for the NIR champion device is shown in Figure 6.8 along with the champion devices from the hotplate annealed films at 150 and 250 °C, with the corresponding key data summarised in Table 6.1. IR images of the films upon exiting the NIR system were

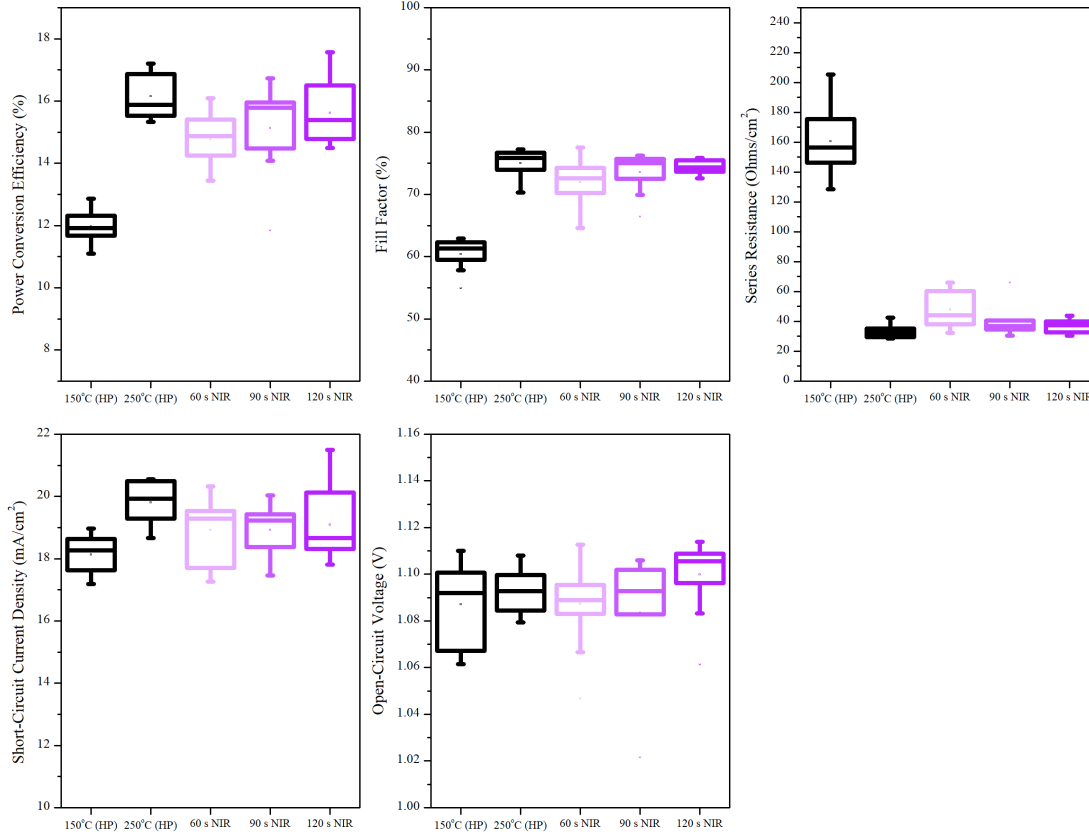


Figure 6.7: Statistical J-V analysis of NIR annealed NiOx nanoparticle films without a metal plate, compared to hot plate annealed films at 150 and 250 °C. Data presented from 20 devices.

taken and the corresponding temperatures plotted in Figure 6.9. The temperatures recorded were less than the peak temperatures reached under exposure due to cooling during the time taken for the samples to exit the NIR enclosure. However, the temperatures measured were in good agreement with the JV results with the 2 minute exposure showing a temperature of around 255 °C.

Table 6.1: J-V curves for highest performing perovskite solar cells employing hot plate annealed NiOx nanoparticles as well as an NIR annealed film.

Device	Voc (V)	Jsc (mA/cm <sup>2</sup> )	FF (%)	Rsh (Ω/cm <sup>2</sup> )	PCE (%)
150 °C (HP)	1.11	18.64	62.28	128.49	12.86
250 °C (HP)	1.09	20.55	76.92	29.21	17.21
120 s (NIR)	1.08	21.49	75.48	32.05	17.57

To conclude, NIR annealing was employed to rapidly anneal the NiOx nanoparticle layer with 2 minutes exposure to NIR light being sufficient enough to reach comparable efficiencies

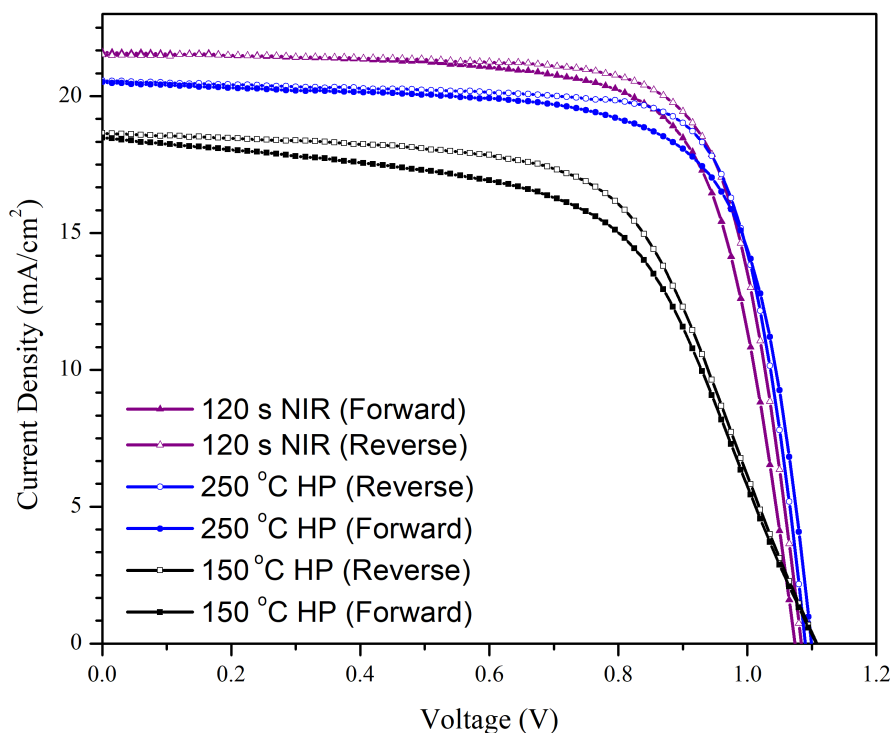


Figure 6.8: J-V curves for highest performing perovskite solar cells employing hot plate annealed NiOx nanoparticles as well as an NIR annealed film.

to the hot plate annealed sample at 250 °C for 15 minutes. In addition to the processing time being reduced, the main aim was to find a process capable of improving upon the efficiencies achieved at the lower temperature hot plate anneal for integration into a roll-to-roll processing method. However, this process had only been used on glass substrates which are much less susceptible to thermal degradation, and measurement of the peak temperature of the ITO during the NIR annealing was expected to be well over the 255 °C measured on exit. Due to the low power output of this particular NIR unit, the exposure times required to reach high temperatures was particularly excessive in NIR annealing terms. PET was not expected to withstand this long exposure time but was tested to confirm. Therefore, plain ITO coated PET substrates were subjected to NIR annealing starting with very low exposure times increasing from 1s and upwards. The PET substrate appeared to cope with the NIR exposure up until 7 seconds in which it started deforming. An image of a PET substrate after 7 seconds of NIR exposure is shown in Figure 6.10

Clearly the PET substrate is not capable of withstanding the NIR radiation for very long,

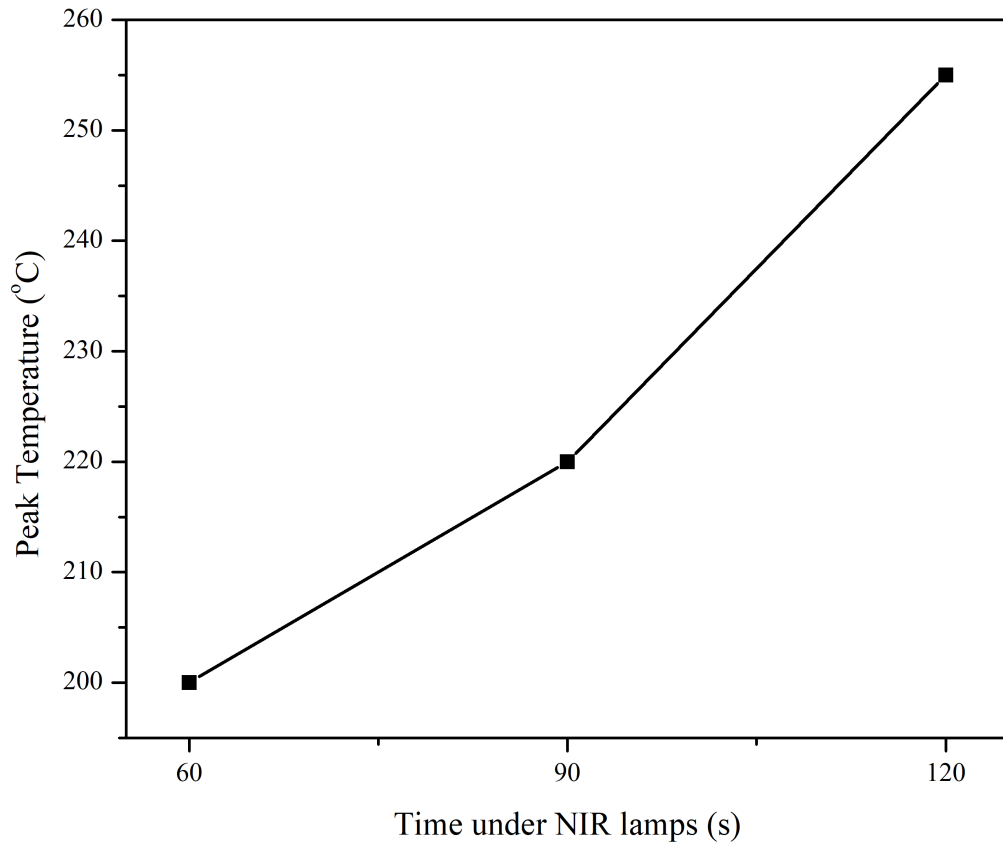


Figure 6.9: IR measured temperatures of ITO substrates upon exiting the NIR oven at each residence exposure time.



Figure 6.10: Image of an ITO coated PET film exposed to 7 seconds of NIR radiation.

especially the 2 minutes which was required for the glass substrates. The degradation temperature of PET is much lower than that of glass, meaning that the thermal transfer from the ITO has a much more profound effect on the underlying substrate. This obviously created a hindrance for the use of NIR in a roll-to-roll coater as the tension the substrate is subjected to

would cause various issues such as stretching of the PET or even complete breakage. It was concluded that NIR annealing of the NiOx on PET was not possible using the Heraeus NIR unit due to the substrates sensitivity to heat. Perhaps using an NIR unit with much higher light intensities would be able to heat the ITO more rapidly and suppress the heating of the PET for long enough to prevent damaging it. Unfortunately, an NIR unit with these capabilities was unavailable for this work.

### **6.3.2 UltraViolet-Ozone treatment of NiOx nanoparticles**

Research focus moved on to removing the binder/ligands from the films at low temperatures. It was thought that UltraViolet-Ozone (UVO) treatment may be able to break down the organic ligands, thus removing them from the film. UVO is usually employed as a method for cleaning sample surfaces which removes contaminants and subsequently improves the wetting of a subsequent deposited layer. During UVO treatment, atmospheric oxygen is irradiated with UltraViolet (UV) rays with wavelengths of 184.9 nm, which produces Ozone ( $O^3$ ). Ozone is a strong oxidiser leading to decomposition of organic materials into volatile substances such as water, carbon dioxide and nitrogen. In addition to this, the  $O^3$  created is irradiated with UV light at a wavelength of 253.7 nm causing it to decompose into atomic oxygen ( $O(^1D)$ ) which also has a strong oxidising ability leading to further surface contamination decomposition [2].

Several papers have been published on the use of UVO to increase the performance of NiOx films, however, these were all conducted on NiAc based NiOx precursor films and not nanoparticles. Wang et al reported an efficiency increase of their NiOx based devices after exposure to UVO and attributed it to an increase in NiOx conductivity and enhanced wettability of the perovskite precursor [3]. An increase in conductivity after UVO exposure was confirmed by Islam et al and suggested to be caused by a change in the film stoichiometry by introducing Ni vacancy defects [4]. In summary, exposure to UVO leads to an oxygen-rich stoichiometry, producing Ni vacancy defects, and it is the O:Ni ratio that allows NiOx to behave as a p-type semiconductor, therefore UVO allows for simple doping of NiOx to enhance p-type conductivity. Although these papers have successfully improved NiOx based perovskite devices by increasing the NiOx conductivity, the underlying reason for doing so was not to remove organic species from the films. However, it was thought that UVO had the potential to remove organics from the NiOx nanoparticle film due to its oxidising ability, thus increasing the conductivity and more importantly, the performance. It was also possible that UVO could

further increase the conductivity by introducing Ni vacancy defects.

To determine whether UVO could remove the ligands from the film, samples which had already been annealed at 150 °C for 30 minutes were placed under the UVO lamps for specified times and subsequently characterised. Exposure times were kept relatively low to begin with and were as follows: 5 s, 20 s, 40 s, 60 s and 5 minutes. After UVO exposure a darkening of the NiOx films was apparent and became darker as the exposure increased. Figure 6.11 shows the UV-Vis spectra for each exposure length and confirmed that the transparency of the films decreased as the UVO exposure lengthened.

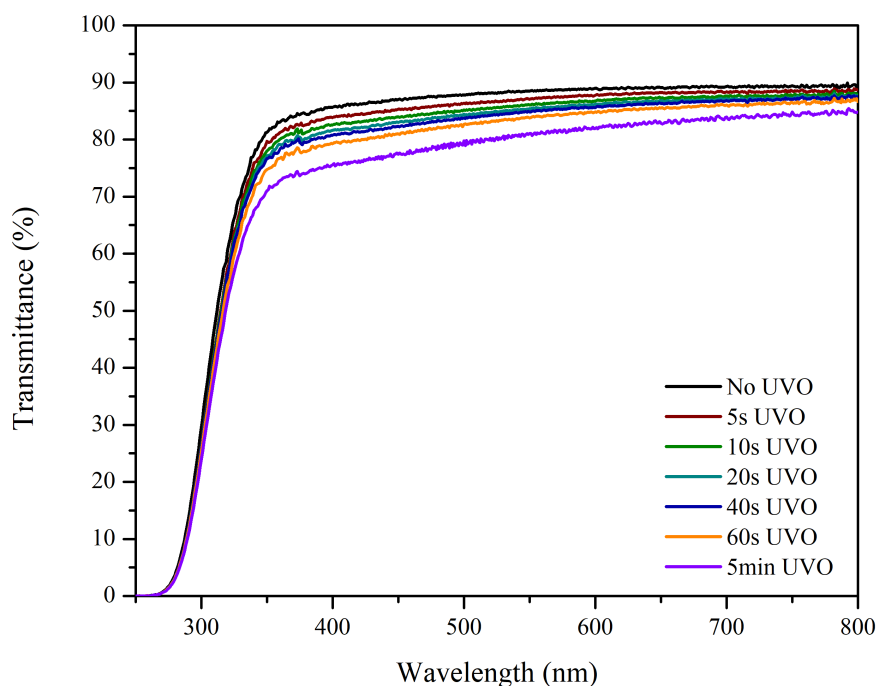


Figure 6.11: UV-Vis spectra for Avantama NiOx nanoparticle films with increasing UVO exposure times.

Perovskite devices were then built on top of each film and tested under a solar simulator. Figure 6.12 summarises the results and shows a linear drop in performance as the exposure increased when compared to a control device annealed at 150 °C for 30 minutes. Most notably, the main contributing factor to the drop in performance was a decrease in current density as exposure increased, most likely caused by the films being less transparent and therefore reducing the amount of light absorbed by the perovskite. Fill factors remained consistent until the exposure reached 60 seconds, and dropped by 10% after 5 minutes exposure suggesting that UVO had not increased the conductivity of the NiOx. However, this could have been wholly

due to the large reduction in current density.

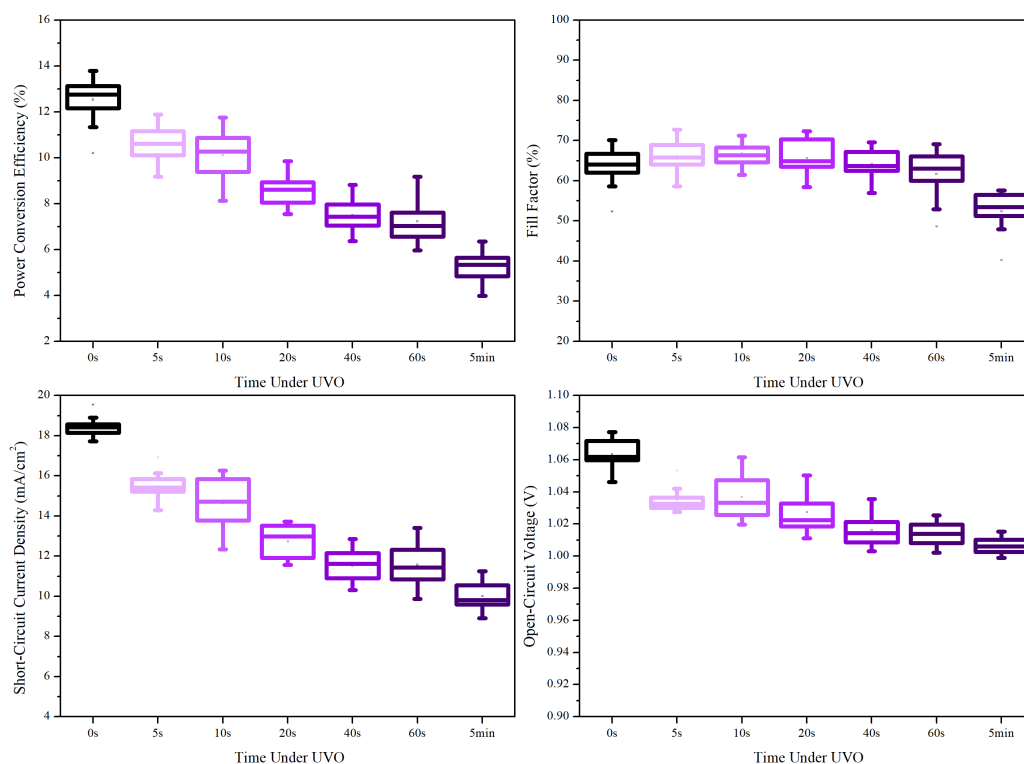


Figure 6.12: Summary of JV characteristics from perovskite solar cells built on top of Avanta NiOx nanoparticles subjected to increasing UVO exposure. Data presented from 28 devices.

It was important to discover the cause of the darkening of the films after UVO exposure. Main candidates for this were thought to be Nickel(III) Oxide ( $\text{Ni}_2\text{O}_3$ ), Nickel Oxide Hydroxide ( $\text{Ni(III)OOH}$ ) or Nickel(II) hydroxide ( $\text{Ni(II)(OH)}_2$ ), all being black in colour and being the most likely cause. XPS analysis was performed on bare NiOx samples before and after exposure to UVO to determine whether any elemental compositional changes were occurring.

Investigating the XPS spectra for the NiOx films exposed to 40 seconds and 5 minutes of UVO in Figure 6.13 revealed a definite chemical change between the films. With respect to the Nickel peaks, as the UVO exposure increased the peak at 855.5 eV also increased which correlates well with literature reports, however, device performance was not increasing. In addition to this, the peaks at 531 and 523 eV also increased with UVO exposure suggesting an increase in  $\text{Ni}_2\text{O}_3/\text{Ni(OH)}_2$  and NiOOH respectively. Darkening of the films could be due to an increase in  $\text{Ni}^{3+}$  forming  $\text{Ni(III)OOH}$  or  $\text{Ni}_2\text{O}_3$  which are both black in colour. Regardless, the apparent increase in  $\text{Ni}^{3+}$  did not lead to a decrease in series resistance, thus rise in p-type conductivity as the literature suggests. Using XPS alone makes it very difficult to distinguish

between Ni(II) and Ni(III), but the Ni(OH)<sub>2</sub> content as a percentage of total nickel can be compared and is summarised in Table 6.2

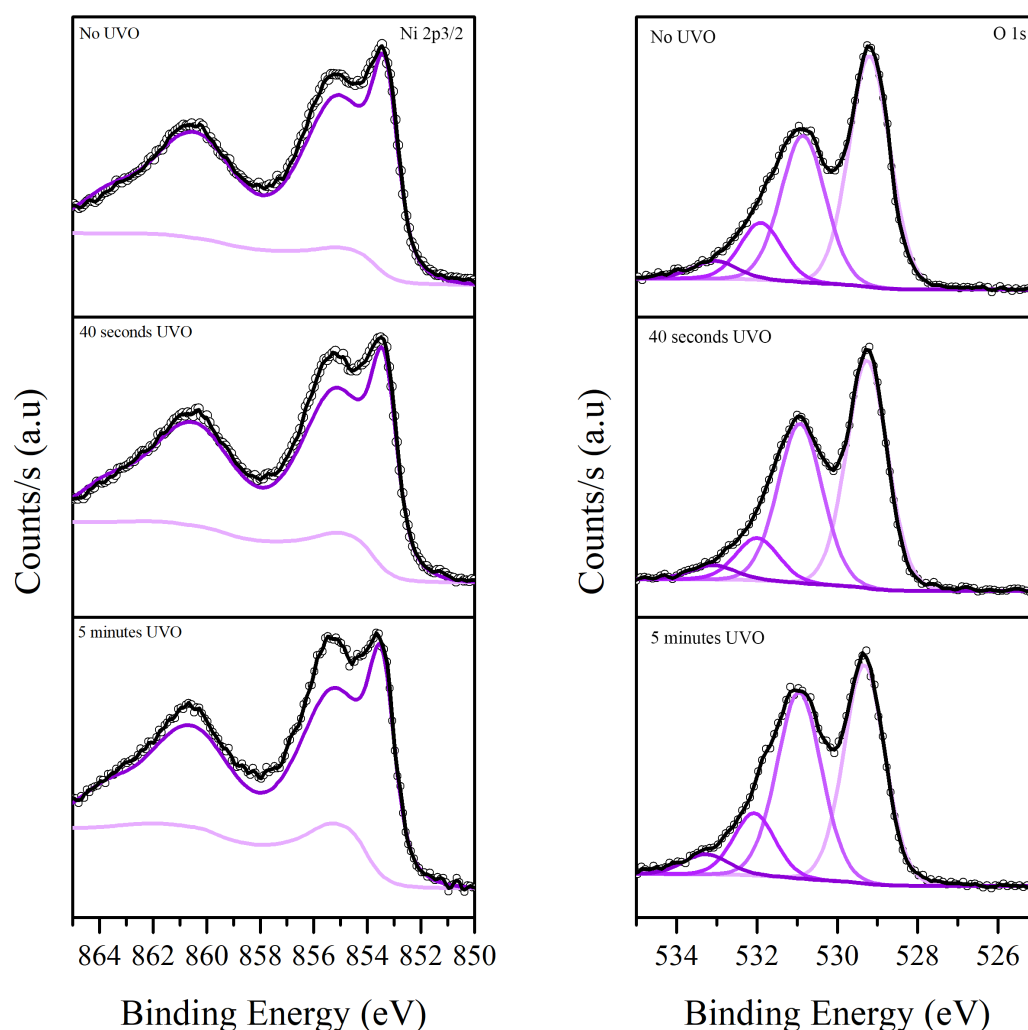


Figure 6.13: XPS spectra for the Ni 2p<sub>3/2</sub> and O 1s orbitals comparing NiOx nanoparticle films annealed at 150 °C and exposed to 40 seconds and 5 minutes of UVO.

Table 6.2: Table comparing the amount of Ni(OH)<sub>2</sub> as a % of total nickel, and carbon content of NiOx films annealed on a hot plate, and exposed to UVO

Sample	Ni(OH) <sub>2</sub>	error +/-	Carbon	error +/-
150 °C anneal	7.3	0.2	20.8	0.2
40 s UVO	10.0	0.5	19	3.0
60 s UVO	14.0	0.6	20.8	0.9

It can be concluded that an increase in hydroxide presence is occurring in the films when exposed to UVO, which correlates well with the darkening of the films. However, it is also likely that Ni<sup>3+</sup> is increasing with respect to Ni<sup>2+</sup>, and the hydroxyls are negatively affecting



the NiOx/perovskite interface.

A paper by Noonuruk et al reported that the colour change of UVO treated nickel oxide films is induced by an increase in hydroxyl groups on the surface through a combination of Ozone and absorbed water molecules [5]. Interestingly, they stated that after heat treatment at 150 °C the colour change can be reversed. This would explain the main reason behind the loss in device performances inducing poor contact between the perovskite and NiOx layers. To confirm this theory, films post UVO treatment were placed on a hot plate at 150 °C for 10 minutes and the transmittance measured. Figure 6.14 shows an image of UVO treated NiOx films before and after heat treatments. The longer UVO treatments show a clear darkening of the film, but not as obvious with the low residence times. Heat treatment after UVO certainly showed a reduction of the darkening effect and was confirmed by UV-Vis spectroscopy (Figure 6.15).

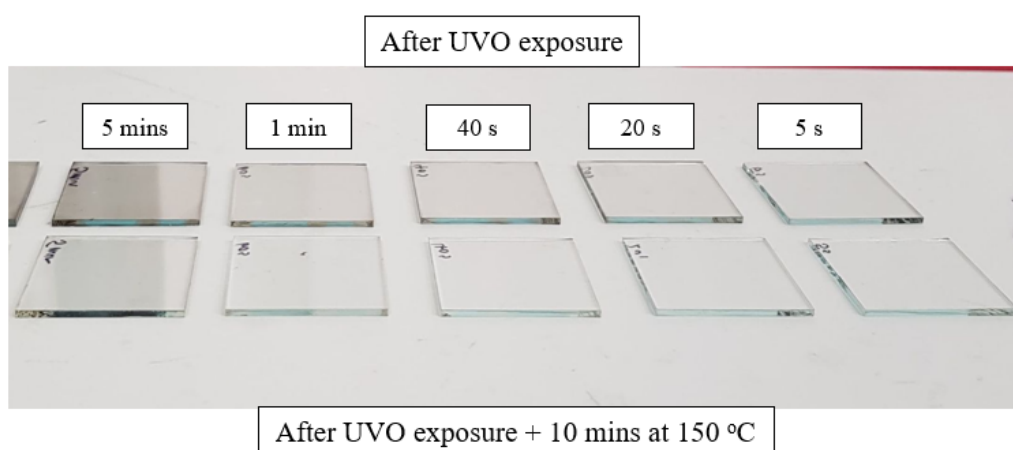


Figure 6.14: Image of UVO treated NiOx films with UVO treatment, as well as a heat treatment of 150 °C post UVO treatment.

Investigating the XPS spectra of the post UVO heat treated films revealed that the heat treatment appeared to reverse the effects of the UVO (As summarised in Figure 6.16). Both the Nickel and Oxygen peaks for the post UVO treated films return to the same profiles as the film annealed at 150 °C with no UVO exposure. Table 6.3 contains the Ni(OH)<sub>2</sub> as a total % of nickel before and after the heat treatment and confirms that the heat treatment reduces the amount. Therefore it is highly likely that the UVO treatment introduces hydroxyls onto the surface of the NiOx film causing the film darkening and poor device performance. With regards to ligand/binder removal, UVO does not achieve this, even after a heat treatment post UVO the XPS spectra replicate that of the 150 °C annealed sample and does not lead to a further reduction in OH peaks. Perovskite devices were fabricated on films exposed to UVO

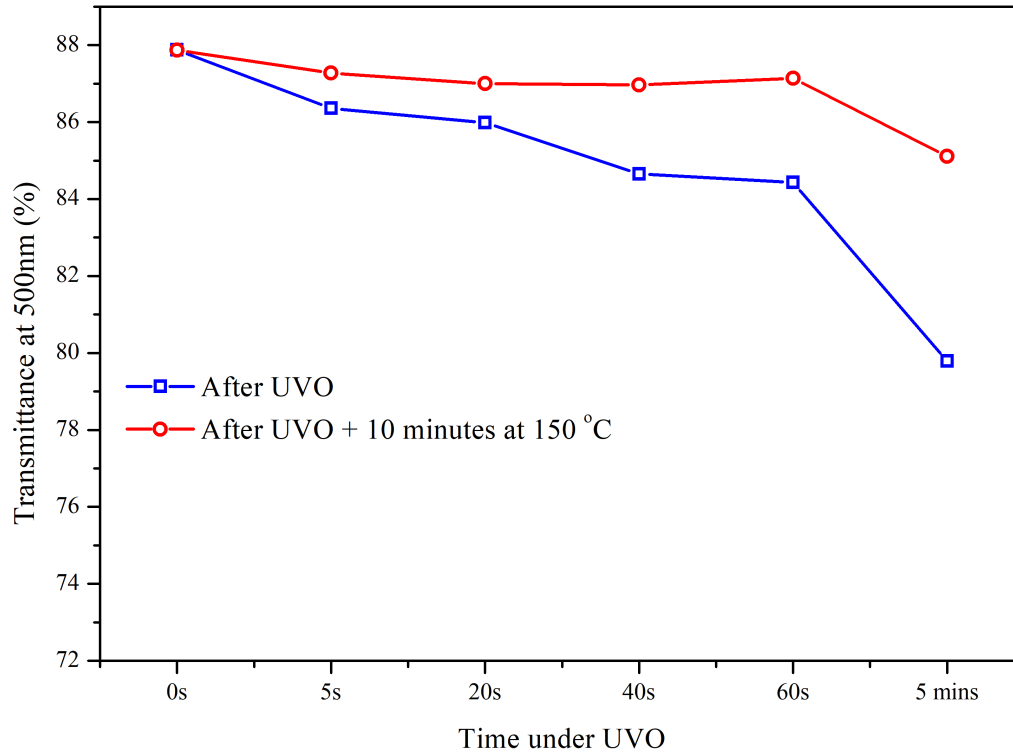


Figure 6.15: UV-Vis transmittance at 500 nm for UVO treated NiOx films as well as post UVO heat treatment at 140 °C for 10 minute.

with a post thermal treatment and summarised in Figure 6.17

Table 6.3: Table comparing the amount of Ni(OH<sub>2</sub>) as a % of total nickel, and carbon content of NiOx films annealed on a hot plate, treated with UVO as well as UVO treated films with a post heat treatment at 150 °C for 10 minutes

Sample	Ni(OH <sub>2</sub> )	error +/-	Carbon	error +/-
150 °C anneal	7.3	0.2	20.8	0.2
250 °C anneal	7.0	1.0	16.4	0.8
40 s UVO	10.0	0.5	19	3.0
40 s UVO + heat	7.0	1.0	21	1.0
60 s UVO	14.0	0.6	20.8	0.9
60 s UVO + heat	9.0	1.0	20.3	0.9

After the heat treatment post UVO there is a subtle increase in the device efficiencies attributed to a small increase in fill factor. This could be caused by an improvement in the NiOx/perovskite interface due to UVO induced surface cleaning, or there could be a small increase in Ni<sup>3+</sup> associated with Ni<sub>2</sub>O<sub>3</sub> increasing the p-type conductivity. Unfortunately, this could not be concluded from the XPS data alone. A champion device efficiency of 13.1% was achieved after a 5 second UVO exposure and 10-minute post anneal, but still did not compare to the higher temperature thermal anneal. In conclusion, UVO treatment alone has a signifi-

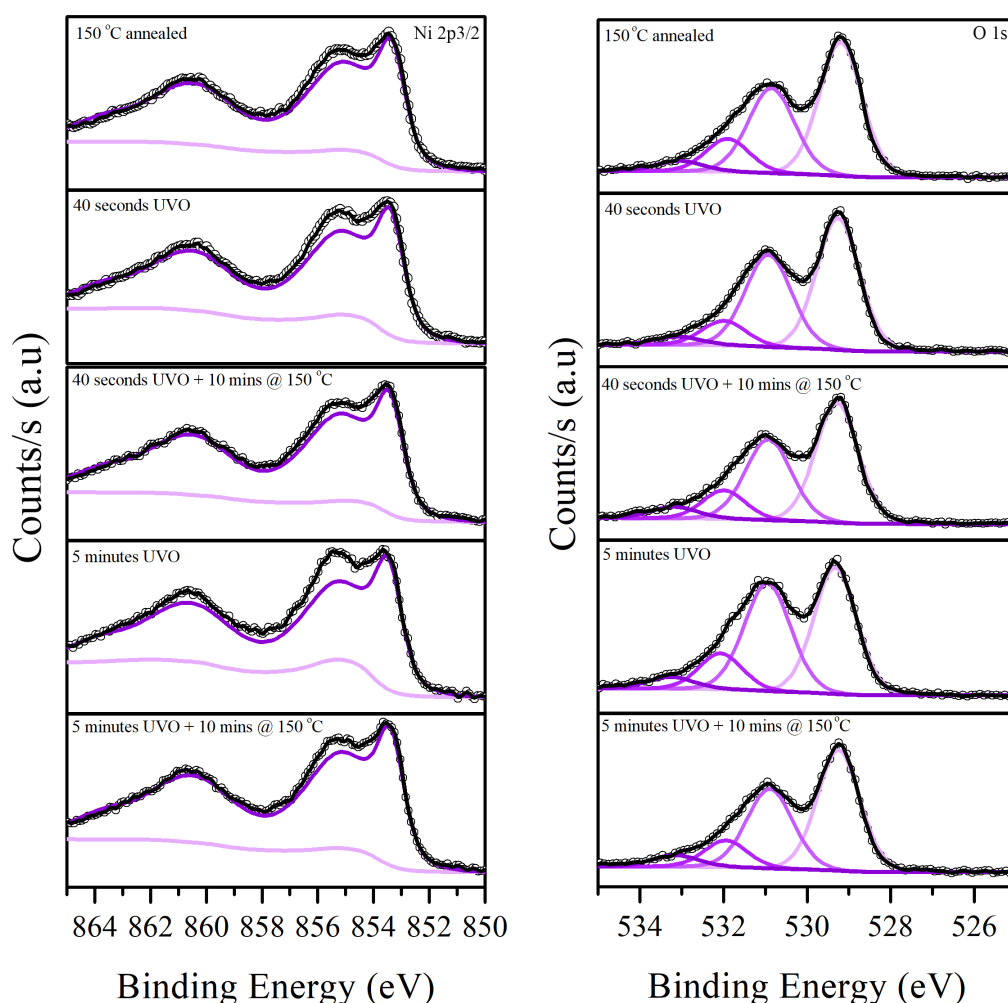


Figure 6.16: XPS spectra for the Ni  $2p_{3/2}$  and O  $1s$  orbitals comparing NiOx nanoparticle films annealed at 150 °C and exposed to 40 seconds and 5 minutes of UVO. Also included are the same XPS spectra for the films placed on a hot plate at 150 °C for 10 minutes post UVO exposure

cant detrimental effect on the device efficiencies and was attributed to an increase in hydroxyl species in the film. A heat treatment after the UVO exposure leads to the removal of the OH species and subsequently leads to subtle improvement in device efficiencies. When comparing the performance of the post UVO annealed films to just a thermally annealed sample at 150 °C, a small increase is observed and was thought to be either due to a small increase in p-type conductivity by means of more  $Ni^{3+}$  vacancies introduced by the UVO, or an improvement in the NiOx/perovskite interface via UVO cleaning. It was not thought that the UVO was removing any of the ligands/binder present in the original film as the XPS spectra were not comparable to the high temperature annealed film (250 °C). Perhaps a longer UVO exposure of 30 minutes could lead to further device improvements, however, the post anneal would inevitably be significantly longer to remove the increased presence OH species and would lead to an undesirably

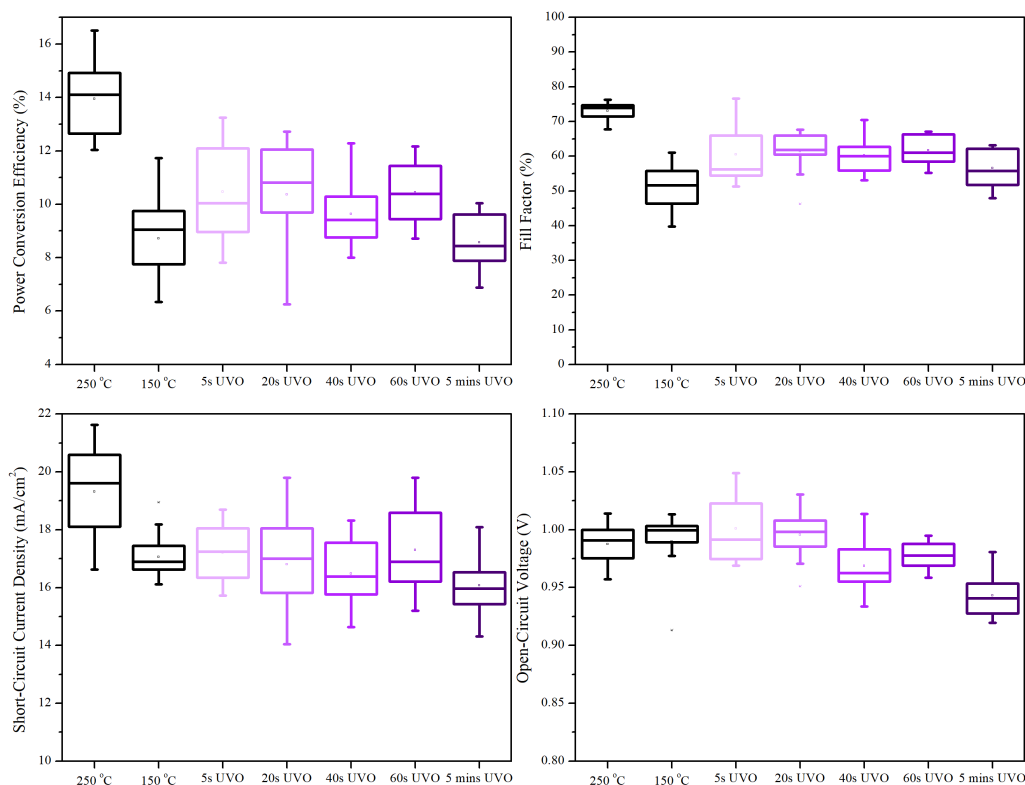


Figure 6.17: Summary of JV characteristics from perovskite solar cells built on top of Avanta nanoparticles subjected to increasing UVO exposure with a 10 minute heat treatment at 150 °C post UVO. Data presented from 28 devices.

long processing time which would not be suitable for roll-to-roll coating.

### 6.3.3 Photonic curing of NiOx nanoparticles

Finally, photonic curing was assessed for its ability to remove the organic species in the NiOx films. The equipment used was the same as in Chapter 5.3.2. Absorption characteristics of the ITO glass and a film of NiOx on ITO glass (Figure 6.3) were compared to the spectral output from the photonic flash lamp. Figure 6.18 shows the normalised spectral output for the Novacentrix Pulseforge 1300 photonic lamp with the peak output at approximately 480 nm. This spectral output is mainly in the Uv-visible-NIR region and is notably not well matched with the absorbance spectra of ITO glass and NiOx. However looking at the absorbance spectra of the substrate and NiOx film in Figure 6.19 absorbance is slightly increased at the lower wavelengths especially between 350 and 450 nm which matches nicely with the higher intensity wavelengths of the Pulsed light and may promote effective heating of the NiOx layer.

Parameters available for photonic pulsing are numerous as the exposure time and power output can be manipulated to a high degree. Initially, for simplicity, samples were subjected

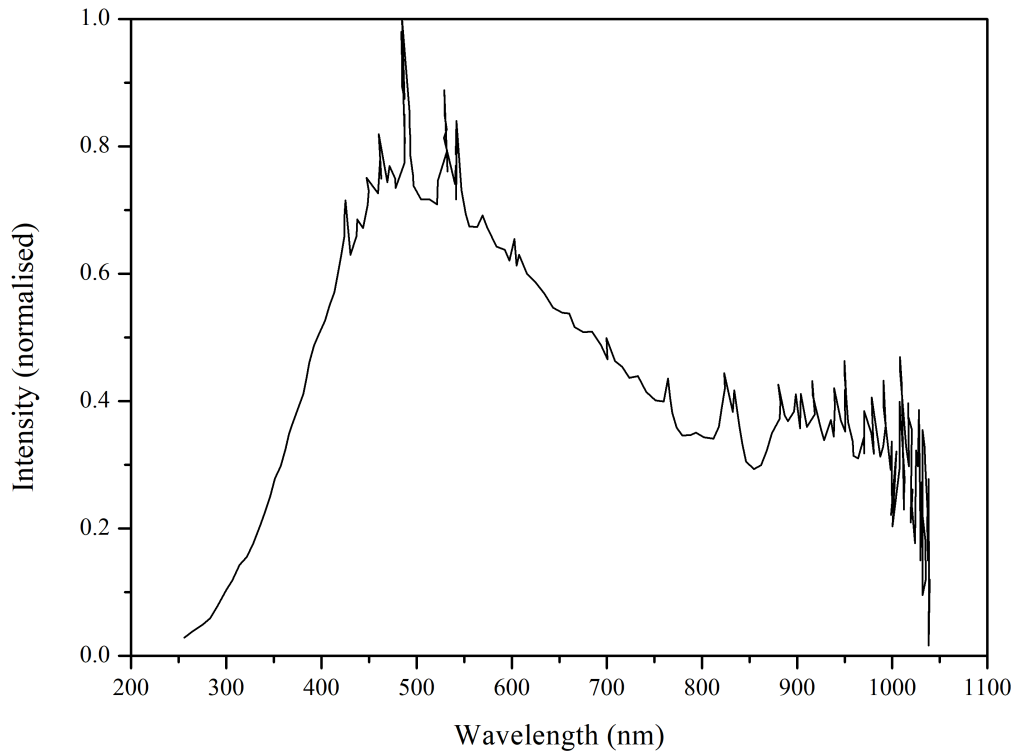


Figure 6.18: Intensity spectra for Novacentrix Pulseforge 1300 photonic lamp.

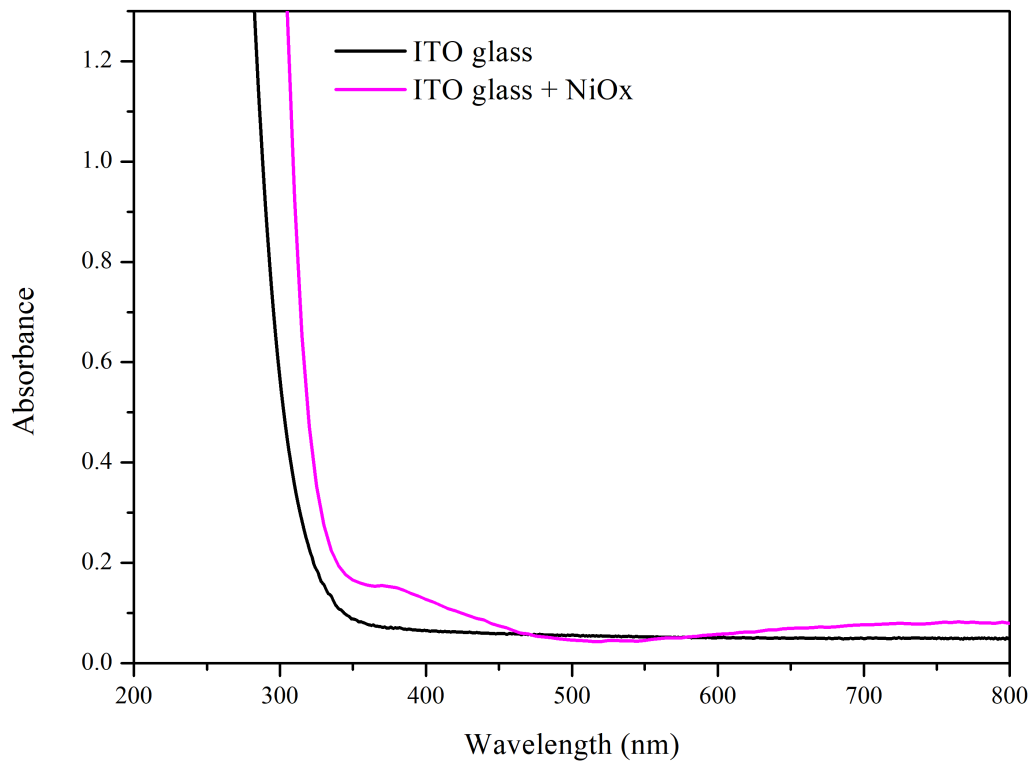


Figure 6.19: Absorbance spectra for ITO glass as well as ITO glass + NiOx up to 800 nm.

to one pulse and the pulse time was kept constant at 20000  $\mu$ s, with the voltage increasing in 50 V increments from 200 to 450 V. NiOx films were prepared using the normal parameters,

and dried on a hot plate for 5 minutes to remove the solvent prior to photonic curing. The PulseForge system also has built in software for the estimation of the peak temperature of the film and the results summarised in Table 6.4. After photonic exposure perovskite devices were built on top of each film and their related JV parameters presented in Figure 6.20, with samples hot plate-annealed at 150 and 250 °C for comparison.

Table 6.4: Estimated peak temperature for NiOx films subjected to increasing photonic pulse power.

Voltage (V)	Estimated temperature (°C)
200	156
250	256
300	391
350	564
400	778
450	1030

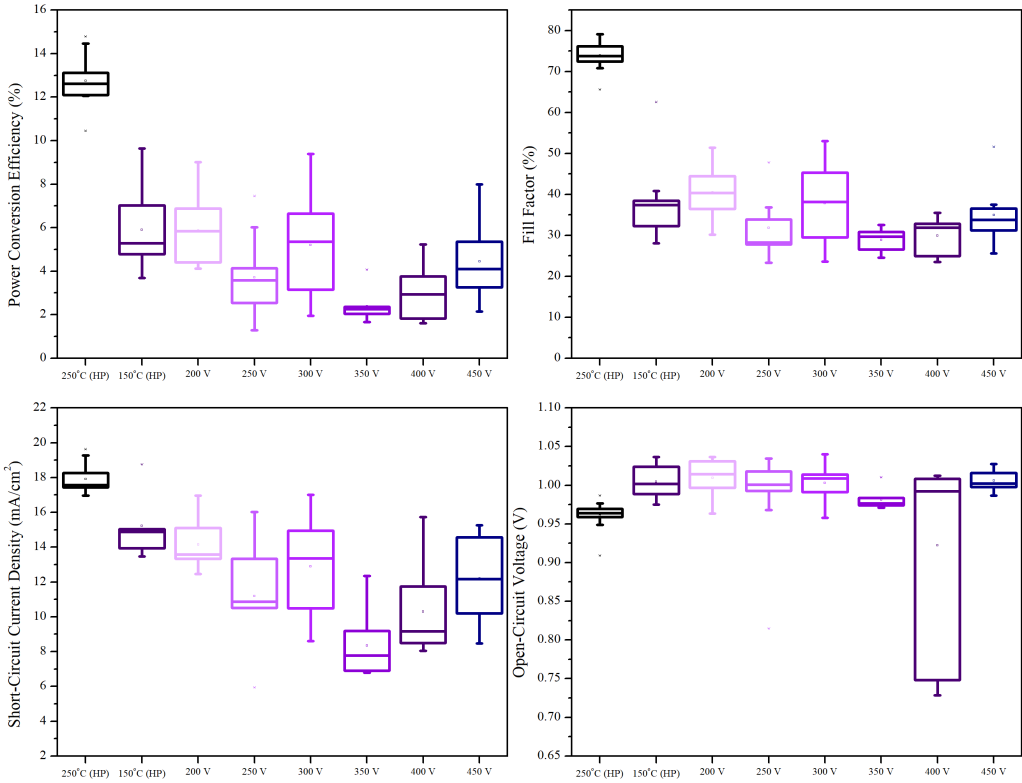


Figure 6.20: JV data for photonicallly cured NiOx nanoparticle films subjected to one pulse with increasing voltage, compared to films hot plate annealed at 150 and 250 °C. Data presented from 32 devices.

Results from the perovskite devices on the photonicallly cured NiOx films did not perform as expected. It was suggested that an increase in power would lead to higher performance due

to the increase in estimated peak temperature. However, the best performance was achieved from the lowest power of 200 V with an average PCE comparable to that of the film annealed at 150 °C. This did prove that photonic curing can provide the same performance as a hot plate annealed film with a substantial reduction in processing time, but did not enhance the efficiency to that of a high-temperature annealed hot plate equivalent. A lack of improvement to the fill factor of each photonicallly cured film suggested that the organic species had not been removed from the film, thus not reducing the series resistances. Fill factors for each voltage remained similar throughout, with poor current density proving to be the main contributing factor for poor device performances. No observable trend was apparent as the voltage increased and could be due to variance in device making so a conclusion was not reached with this optimisation.

J-V curves for the best performing photonic based NiOx device and the two hot-plate annealed control devices are summarised in Figure 6.21. It is clear from the JV curves that the series resistance is the limiting factor for device performance, with the photonic based device having a series resistance of 308 Ohms/cm<sup>2</sup> compared to 185 Ohms/cm<sup>2</sup> for the 150 °C hot-plate annealed device. Although the device performance for the photonicallly cured films did not reach that of the high-temperature annealed controls, the fact that a film comparable to that of a hot-plate annealed sample (150 °C) can be produced in 20000  $\mu$ s rather than 30 minutes shows promising potential for photonic curing to be employed for rapid processing. Unfortunately, further optimisation of the photonic curing process was not achieved due to time restraints and equipment down time. Nonetheless, when taking into account the vast number of settings available on the photonic curing system, as well as the ability to perform multiple pulses there is strong potential for photonic curing to be employed to reach efficiencies comparable to that of a high-temperature annealed film.

## 6.4 Conclusions

In conclusion, removal of the organic species in the NiOx film required for high-performance was achieved using NIR annealing. A champion efficiency of 17.57% was obtained on a glass substrate after only 2 minutes of NIR exposure and compared to a maximum efficiency of 17.21% for a hot plate annealed equivalent. Although high-efficiencies were achieved, NIR exposure on PET substrates caused the substrate to melt after only 7 seconds exposure deeming this NIR system incapable of flexible substrate processing. Using a higher powered NIR

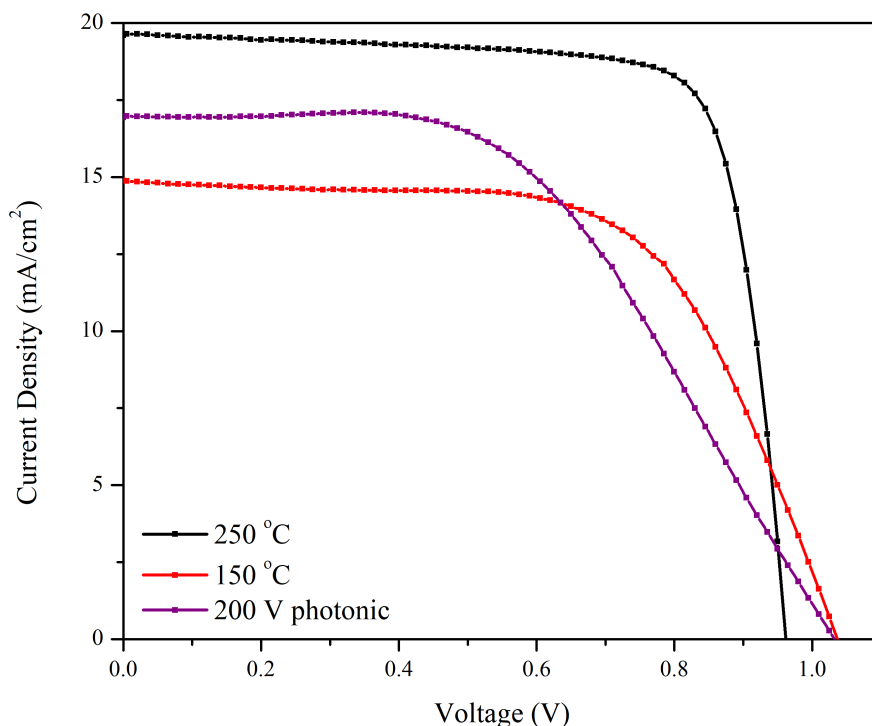


Figure 6.21: JV curves for best performing photonicallly cured NiOx film compared to hot-plate annealed control devices at 150 and 250 °C.

system may prevent excessive heating of the substrate by smaller exposure times, however, a high-powered system was unavailable for this work. Focus then moved onto using UVO to remove the organic species, however, it was quickly noticed that UVO exposure led to darkening of the NiOx films which subsequently reduced the efficiencies of the perovskite devices due to less absorption of incident photons leading to low current densities. Darkening of the films was caused by an increase in OH species in the films, either by absorption of OH from the surrounding air or introduction of NiOOH or Ni(OH)<sub>2</sub> both being black in colour. Placing the films on a hot plate after UVO exposure reversed the darkening of the films and arguably led to a small increase in device efficiency compared to a hot-plate annealed film at 150 °C. Nonetheless, reversal of the darkening did not improve the efficiencies significantly enough to warrant the extra processing time associated with UVO treatment, and was not capable of efficiencies comparable to a high-temperature hot-plate anneal. UVO did not remove the organic species in the film and in fact appeared to introduce more, inhibiting the device performance. Finally, photonic curing using white light was attempted and led to some potentially promising results. Exposing a NiOx film to pulsed white light for 20000  $\mu$ s at 200 Volts led to efficiencies comparable to that of a hot-plate annealed film at 150 °C for 30 minutes. This result was promising as the processing time had been significantly reduced whilst maintaining efficiency,



however, increasing the power of the photonic system did not lead to an improvement in performance. The main issue with photonic curing is the vast amount of settings available, with significant optimisation required to determine the most favourable conditions. Unfortunately due to time constraints and equipment downtime, further exploration of photonic curing was not completed. Despite efficiencies not reaching that of a high-temperature annealed film, this work proves that photonic curing has the potential to rapidly process the NiOx nanoparticles and should not lead to damage of the underlying substrate due to such short exposure.

## 6.5 References

- [1] Joel Troughton et al. “Rapid processing of perovskite solar cells in under 2.5 seconds”. In: *Journal of Materials Chemistry A* 3.17 (2015), pp. 9123–9127. ISSN: 20507496. DOI: 10.1039/c5ta00568j.
- [2] Rajiv Kohli. *UV-Ozone Cleaning for Removal of Surface Contaminants*. Vol. 8. Elsevier Inc., 2015, pp. 71–104. ISBN: 9780323299619. DOI: 10.1016/b978-0-323-29961-9.00002-8. URL: <http://dx.doi.org/10.1016/B978-0-323-29961-9.00002-8>.
- [3] Kaijie Wang et al. “Surface Treatment on Nickel Oxide to Enhance the Efficiency of Inverted Perovskite Solar Cells”. In: *International Journal of Photoenergy* 2019 (2019). ISSN: 1687529X. DOI: 10.1155/2019/4360816.
- [4] Raisul Islam et al. “Investigation of the changes in electronic properties of nickel oxide (NiO) due to UV/Ozone treatment”. In: (2017). DOI: 10.1021/acsami.7b01629.
- [5] R. Noonuruk et al. “Ozone-induced optical density change of NiO thin films and their applicability as neutral optical density filter”. In: *Procedia Engineering* 8 (2011), pp. 212–216. ISSN: 18777058. DOI: 10.1016/j.proeng.2011.03.039. URL: <http://dx.doi.org/10.1016/j.proeng.2011.03.039>.

## Chapter 7

# Conclusions and Future Work

In Chapter 3 a method for depositing a low-temperature (140 °C) tin oxide electron transport layer was developed, both on small spin-coated glass substrates as well as bench top slot-die coated flexible PET substrates. A tin oxide nanoparticle suspension from Alfa Aesar was used for the deposition and was supplied as a 15 weight% suspension in DI water. Spin coated samples were optimised by dilution of the precursor in DI water and a 4.2 weight% was found to provide the best performance. Films were characterised using JV data, cyclic voltammetry and SEM, showing excellent electron transport properties and high device efficiencies. This tin oxide precursor was then used to perform slot-die coatings onto flexible PET substrates. It was discovered that a 1.2 weight% solution with an addition of 10 volume% 1-butanol was required to provide stable coatings due to the reticulation and poor drying behaviour of a neat DI water solution on PET. In addition to this, the viscocapillary model was utilised to determine coating stabilities and was also proven to be accurate by imaging theoretical stable and unstable coatings. Through rheological manipulation of the tin oxide precursor, 30 x 10 cm PET substrates were coated with a 7  $\mu\text{m}$  wet film thickness at 0.25 m/min, producing a low temperature, homogenous layer of tin oxide. Films were dried for 4 minutes at 140 °C and a champion efficiency of 14.38% was achieved compared to 15.99% for a spin coated equivalent.

Utilising these results, slot-die coating was scaled up using a roll-to-roll coater, in which several metres of substrate were coated. In Chapter 3 it was discovered that a small dose of plasma lead to improved efficiencies, however, this capability was not available on the roll-to-roll coater. Corona treatment was available, but was discovered to negatively effect the coating qualities due to a difference in surface energy between the ITO electrode and the PET film itself. Corona treatment, even at its lowest power setting led to particularly poor film qualities and was

deemed to be unsuitable for this particular coating. To demonstrate large scale coatings, the coating speed was increased to 1 m/min which led to a drying time of only 1 minute at 140 °C, and had no effect on the coating performance. As discovered in Chapter 3, the optimal wet film coating thickness was 7  $\mu\text{m}$  producing a champion efficiency of 16.34% compared to 18.52% for a spin coated equivalent. Efficiencies were slightly lower for the slot-die coated films compared with spin-coating due to the increased resistance of the ITO/PET at 50 Ohms/sq (ITO/glass was 15 Ohms/sq). Lower resistance PET substrates were unavailable for this work, however, using a more conductive substrate would provide higher efficiencies comparable to that of spin coating. Work completed in Chapters 3 and 4 prove that high-performance electron transport layers can be deposited on a large scale at low-temperatures, providing a path for potential large scale manufacture.

In Chapter 5 methods for depositing a low-temperature nickel oxide hole transport layer were examined. Initially, techniques to reduce the annealing temperature of a well known nickel acetate precursor were attempted with photonic curing being the most promising method. Precursors were successfully converted into NiOx in a matter of milliseconds using the pulsed white light, but device efficiencies were significantly reduced when compared to a hot plate annealed sample. Further work on this was not undertaken due to the highly toxic nature of the precursors, which would make it difficult and dangerous to incorporate into a mass manufacturing process. Focus then moved onto a NiOx nanoparticle suspension from Avantama; these were provided as a 2.5 weight% suspension in ethanol. Initial optimisation on spin-coated substrates gave promising results with champion efficiencies of 12% when annealed at 150 °C. It was then discovered that annealing the nanoparticles at 250 °C led to significant improvements in device performance and was due to a large reduction in series resistance owed to the increased conductivity of the nanoparticle layer. Using thermogravimetric analysis, AFM, SEM and XPS the reason for the increased conductivity was down to removal of organic species at the higher annealing temperature which were most likely residual ligands/binder which keep the nanoparticles suspended in solution. Nickel oxide films were also discovered to be significantly more stable than their common counterpart, PEDOT. Removal of the residual organic species in the film also led to increased stability compared to the lower temperature annealed films. Slot-die coating of the NiOx nanoparticles was also performed at the lower temperature of 150 °C to compare with spin-coating. Using a wet film thickness of 5  $\mu\text{m}$  on glass led to efficiencies comparable to that of spin-coating, and films slot-die coated on flexible PET

films reached efficiencies of 10% compared to 12% for spin-coating. This was again due to the higher resistance of the ITO/PET substrates. This chapter proved that reasonable efficiencies could be achieved at low-temperatures on flexible substrates.

In Chapter 6, methods for the removal of the residual organic materials from the film were investigated. Firstly, near infrared annealing was trialled as a potential processing method. Exposing the films to NIR light for 2 minutes on glass substrates provided efficiencies equal to that of film annealed for 15 minutes at 250 °C on a hot-plate. This result was an achievement as the annealing time was significantly reduced with no loss in performance, but unfortunately the intense heat from the absorbance of NIR by PET substrates led to deformation after only 7 seconds of exposure. Use of a much higher powered NIR system could allow for the annealing of NiOx nanoparticles on PET by substantially reducing the exposure time, however, access to a higher powered NIR was unavailable.

UV-Ozone treatments were also investigated as a method for removal of residual organics. In the literature, UVO has been employed to increase the performance on nickel acetate based NiOx layers which leads to increased p-type conductivity by introduction of nickel vacancies. In this work UVO was detrimental to device performance due to a darkening of the films, reducing current density and increasing series resistance. This was discovered to be caused by an increase in OH species on the films confirmed by XPS analysis. It is likely that the darkening is caused by introduction of OH from the surrounding air as well as introduction of NiOOH and Ni(OH)<sub>2</sub> from the harsh environment in the UVO chamber. By Placing the UVO exposed films on a hot plate for 10 minutes at 150 °C the transparency of the films was restored, thus removal of the absorbed organic species, which was also confirmed by XPS analysis. Device performances of the films after heat treatment were restored, with a slight increase in performance compared untreated films. Devices did not however approach the efficiencies of NiOx films annealed at 250 °C. Perhaps an extensive UVO exposure followed by heat treatment could remove the organic species in the films, but this would lead to excessive processing times which would inevitably create a bottleneck in large scale production and was not pursued any further. Finally, photonic curing was used as a potential method for low-temperature, rapid annealing of the NiOx nanoparticles. It was discovered that the nanoparticles absorbed a portion of the light output from the photonic unit causing them to increase in temperature. Films were subjected to pulses of white light at varying intensities controlled via the power input. Direct measurement of the peak film temperatures was not possible due to the enclosed

nature of the system but efficiencies comparable to that of a 150 °C annealed film were achieved in 20000  $\mu$ s rather than 30 minutes. Photonic curing appears to be a very promising method to process the NiOx nanoparticles with higher efficiencies once the curing exposures have been optimised, but equipment downtime hindered this optimisation.

If a high-performance nickel oxide HTL is to be realised on a flexible substrate such as PET, further work on the reduction of processing temperature is required. In addition to this, for large scale deposition the annealing time may also benefit from being reduced. Heat alone will not remove the ligands required for high-performance, so alternative methods need further interrogation. However, manipulation of the ligands in the nanoparticle suspension may also alleviate the requirement for a high-temperature anneal. Future work may also involve developing a method for depositing the nickel oxide nanoparticles directly on top of the perovskite layer in an n-i-p structure, where tin oxide is the ETL and nickel oxide the HTL, resulting in an in-organic stack. This should lead to higher overall stability when compared to using an organic HTL such as spiro-MeOTAD.

Although the results in Chapter 6 were not necessarily positive in the overall theme of the thesis, it did reveal the potential problems associated with low-temperature deposition of metal oxide semiconductors. Attempts at reducing the deposition temperature of an otherwise "high-temperature" deposited material are not trivial and come with unexpected hindrances. The thesis did however discover these hindrances and found potential methods to alleviate them. Further optimisation of the processing conditions should lead to much higher efficiencies and stability of NiO based perovskite devices. In addition to this, the knowledge and experience gained on the slot-die coating process will allow for successful scale up in a roll-to-roll setting once the temperature limitations are solved.

On a positive note, the thesis developed a method for the deposition of a low-temperature ETL in a roll-to-roll setting which is a big step in the right direction for the realisation of a fully roll-to-roll coated perovskite solar cell. Key understanding of what is involved when scaling from a small spin coated film to a large area slot-die coated layer was crucial in the move towards roll-to-roll processing. In order to reach the milestone of a fully printed roll-to-roll perovskite solar cell/module for mass manufacture, significant progress must be made. The majority of papers being published are focused on improving the cell efficiencies which is healthy for the overall recognition of perovskites and their potential, however, these usually employ deposition methods which are either not scalable, or would be expensive to manufacture at

scale. Champion efficiency cells that use scalable deposition methods usually consist of more expensive materials or high-temperature processing, again not suitable for mass manufacture. As the main attraction for perovskites is cheap manufacture capability and earth abundant materials it is important for the community to focus on scalable materials and methods. Recently, significant progress is being made in the scale up of perovskites shown by the increase of publications in this area. Increasing numbers of research groups are reporting roll-to-roll deposition of perovskite device stacks and achieving impressive efficiencies. For mass manufacture via roll-to-roll deposition to be commercialised a number of milestones must be reached. Most importantly, the overall stability needs to be competitive with current technologies and significant work is required to achieve this. Also, the reduction, or preferably the complete removal of toxic substances would be extremely advantageous, as this would greatly reduce the cost of manufacture. Although a perovskite product would be encapsulated, the removal of lead from the precursor would be hugely advantageous as this could be seen as a potential danger due to its widely known toxicity. Finally, coating speeds also need to be compatible with high-throughput roll-to-roll coating. It was shown in this thesis that a coating speed of 1 m/min was possible, however, large scale manufacture would most likely require coating speeds in the tens of metres per minute. Increasing the speed to this would not necessarily be a big problem with respect to the coating quality, but the drying conditions may be a bottleneck. For instance, if a layer required 5 minutes of drying/annealing at a coating speed of 10 metres per minute a total oven length of 50 metres would be needed. In addition to this, if a whole device stack was to be deposited in one go through multiple coating stages, the speed would need to be consistent throughout, and with a perovskite device having at least 4 layers, the coating machine would be enormous if the drying/annealing times were relatively long. Clearly, significant advancements are required for a commercialised roll-to-roll perovskite solar cell to be achieved, but the overall outlook is very promising and certainly has the potential to become a realisation.